UNIVERSITY OF CALIFORNIA, SAN DIEGO

Engineered Silica Nanoparticles for Enhancing Circulation

A dissertation submitted in partial satisfaction of the
requirements for the degree
Doctor of Philosophy

in

Bioengineering
with a Specialization in Multi-Scale Biology

by

Ya-San Yeh

Committee in charge:

Professor Karen L Christman, Chair
Professor Sadik C Esener, Co-Chair
Professor Gaurav Arya
Professor Michael W Berns
Professor John T Watson

2017

The dissertation of Ya-San Yeh is approved, and it is acceptable in quality and form for publication on microfilm and electronically:

_____

_____

_____

_____
Co-Chair

_____
Chair

University of California, San Diego

2017

DEDICATION

I dedicate this dissertation to my mother and father for their support in everything I do, my sisters for their encouragements, and my partner Zach for his positivity and help through the stressful times.

TABLE OF CONTENTS

LIST OF FIGURES

ACKNOWLEDGEMENTS

I would like to acknowledge my advisor, Professor Sadik Esener, for his guidance and support throughout my graduate career. His emphasis on encouraging all his students to innovate and explore a broad range of research subjects allowed me to develop independent thinking and skills to design and execute experiments to test hypotheses. I would also like to thank the members of my committee: Professors Karen Christman, Gaurav Arya, Michael Berns, and John Watson. They have provided invaluable suggestions and advice for my project and my future career.

In addition, I would like to acknowledge the support of the senior graduate students in the Esener Lab and my post-doc collaborators, namely, Michael Benchimol, PhD; Inanc Ortac, PhD; Stuart Ibsen, PhD; Gen Yong, PhD; Carolyn Schutt-Ibsen, PhD; Hazem Ali, PhD; Laura Ruff, PhD; Alok Singh, PhD; and Jared Fischer, PhD. I am especially grateful to Inanc for his mentorship in synthesizing the 200-nm spherical silica nanoparticles and navigating graduate school. My dissertation would not be completed without the help from Jared, who went above and beyond to support my experiments in the last few months before my defense. I was also very fortunate to be mentored by Dr. Yu-Tsueng Liu, Dr. Dennis Carson, and Brad Messmer, PhD. They have been generous with their feedback and suggestions for my project throughout my graduate career.

My graduate school experience was fulfilling, rewarding, and fun because of my fellow graduate students in the Esener Lab. Mukanth Vaidyanathan, Negin

Mokhtari, Ajay Sapre, Justin Plaut, and Saharnaz Baghdadchi were extremely encouraging and supportive labmates. Several very talented undergraduates and staff members played significant roles in the completion of my project. Wayne Neilson was involved in the design and manufacture of the stretching device. Ryan Adams and Gor Sardarian were involved in the synthesis of the 100-nm spherical silica nanoparticles. Shawn Chen was involved in the development of calcium phosphate coated silica nanoparticles. Ebru Erdal was involved in the synthesis of enzyme-encapsulated silica nanoparticles that are activated by ultrasound. Jan Lenington and Pam Murphy of the Bioengineering department have been instrumental in ensuring all administrative issues were resolved in advanced for my graduation.

Chapter 4, in part, is currently being prepared for submission for publication of the material. Yeh, Ya-San; Sadik, Esener C. "Synthesis of Spherical and Elongated Hollow Mesoporous Silica Nanoparticles with Controlled Pore Size." The dissertation author is the primary investigator and author of this material.

Chapter 5, in part, is currently being prepared for submission for publication of the material. Yeh, Ya-San; Vaidyanathan, Mukanth; Sadik, Esener C. "Synthesis of Ultrasound-Activated Enzyme-Loaded Silica Nanoparticles for Targeted Cancer Therapy." The dissertation author is the co-investigator and co-author of this material.

VITA

B. S. in Chemical Engineering, *highest honors*, The University of Texas at Austin

M. S. in Bioengineering, University of California, San Diego

Ph. D. in Bioengineering with a Specialization in Multi-Scale Biology, University of California, San Diego

ABSTRACT OF THE DISSERTATION

Engineered Silica Nanoparticles for Enhancing Circulation

by

Ya-San Yeh

Doctor of Philosophy in Bioengineering

with a Specialization in Multi-Scale Biology

University of California San Diego, 2017

Professor Karen L Christman, Chair

Professor Sadik C Esener, Co-Chair

Cancer is the second leading cause of death in the United States and remains a complex disease to treat. The conventional chemotherapies taken at the dosage necessary to kill cancer cells often have unacceptable toxicities towards normal cells. Therefore, there is a critical need for therapeutics that are better at targeting cancer cells to minimize toxicity to normal cells.

One possible targeting strategy is to exploit the alterations in amino acid synthesis or salvage pathways displayed by cancer cells. Cancer cells that are aux-

otrophic for a particular amino acid can be targeted with amino acid deprivation with enzymes that convert the targeted amino acid to other harmless biomolecules. Unfortunately, most of the enzymes with the potential for amino acid depletion therapy are derived from non-human sources, which makes them highly immunogenic. Therefore, for non-human enzymes to have clinical efficacy, they must be delivered in a non-immunogenic manner.

Another possible targeting strategy is to exploit the enhanced permeability and retention (EPR) effect to target solid tumors. However, for therapeutics to exploit the EPR effects, they must be small enough (<100 nm) to penetrate the tumor vasculature and remain in circulation for a sufficient amount of time to accumulate in the tumor.

The scientific significance of this dissertation is the engineering of a novel nanoparticle-assisted delivery vehicle that (1) protects non-human enzymes from the immune systems to eliminate the problem of immunogenicity, (2) enhances the circulation half-life of the enzymes in order to exploit the EPR effect displayed in solid tumors, and (3) increases the accumulation of the enzymes at the targeted site through active targeting with ligands and/or ultrasound. All three goals are achieved without modifications to the enzymes, which usually reduce the activity of the enzymes.

Chapter 1

Introduction

Nanomedicine, which is the application of nanotechnology to medicine, has experienced an increased interest in the recent decades due to its potential to target drugs to a diseased location. Targeting drugs to tumor sites can minimize off-target adverse side effects and reduce the required dosage. So far, the main focus of nanomedicine has been on cancer diagnostics and therapies. A wide variety of nanostructures have been engineered and studied for detection and treatment of cancers. These nanostructures are made from diverse materials such as metals, lipids, polymers, and silica. They are also made of diverse shapes and arrangements such as solid spheres, solid rods, hollow shells, and tubes.

This dissertation explores the application of nanotechnology to the delivery of therapeutic agents for cancer treatment. The next chapter provides the relevant background information on nanotechnology and its applications to cancer medicine. The potential advantages and the current clinical successes of cancer nanomedicine

are discussed. Next, the different types of biomaterials suitable for nanotechnology utilization are introduced. Then the current challenges of delivering anti-cancer therapeutic agents using nanotechnology are considered. Finally, the biological barriers preventing nanoparticles from prolonged circulation and the characteristics of long-circulating nanoparticles are presented in detail.

The third chapter focuses on a disease-driven approach to design and develop a nanotechnology-based delivery system. This approach exploits a specific difference between cancer cells and normal cells for a specific cancer patient population. Specifically, the different approaches and limitations of amino acid depletion therapy for cancer treatment are discussed. These limitations drive the design of a silica-based nanoparticle for the delivery of therapeutic enzymes for amino acid depletion therapy.

Using a disease-driven approach outlined in the previous chapter, a new type of hollow mesoporous silica nanoparticle (HMSNP) is introduced in the fourth chapter. To take into account the lessons learned from other nanoparticles described in the second chapter and the limitations of the current enzyme delivery systems described in the third chapter, the proposed long-circulating HMSNP is designed to have size below 200 nm, ellipsoidal shape, and PEGylated. The general approach to the HMSNP synthesis method is first outlined in this chapter, then the development and optimization of the intermediate steps are described in detail in the subsequent sections. Specifically, three types of HMSNPs are developed, namely, 200-nm hollow mesoporous silica nanospheres (HMSNS), 100-nm HMSNS, and hollow mesoporous

silica nanorods (HMSNR).

With the synthesis of HMSNS and HSMNR optimized, the next steps are to optimize the loading of enzymes, sealing of the mesopores, and conjugating of polyethylene glycol molecules onto the surface of the final enzyme-encapsulated HMSNP. The fifth chapter describes the development and optimization of these steps and the *in vitro* evaluation of the effect of the silica nanoparticles on cells. In addition, a feasibility test on using ultrasound as an external trigger to activate the enzymes encapsulated in these silica nanoparticles is also briefly explored.

The sixth chapter presents the results of *in vivo* enzyme protection, circulation, and biodistribution of the three types of HMSNP that differ in size (i.e. 100-nm and 200-nm) and shape (i.e. spherical and ellipsoidal) for therapeutic enzyme delivery. All three types of silica nanoparticles will be PEGylated in order to study the effects of size and shape on circulation and biodistribution. The hypothesis is that the silica nanoparticles will be able to protect the enzymes from neutralizing antibodies, but the ellipsoidal silica nanorods will have the longest time in circulation. Since nanoparticles have the tendency to accumulate in the liver and the spleen, the experimental results presented in this chapter will confirm if the biodistribution of these silica nanoparticles is also concentrated to the liver and spleen.

The final chapter summarizes all the results and discusses some of the future directions.

Chapter 2

Background of Nanotechnology in Medicine

This chapter provides the relevant background information on nanotechnology and its applications to cancer medicine. First, the potential advantages and the current clinical successes of cancer nanomedicine are discussed. Next, the different types of biomaterials suitable for nanotechnology utilization are introduced. Then the current challenges of delivering anti-cancer therapeutic agents using nanotechnology are considered. Finally, the biological barriers preventing nanoparticles from prolonged circulation and the characteristics of long-circulating nanoparticles are presented in detail.

2.1 Nanotechnology in Cancer Medicine

According to the World Health Organization, cancer is one of the leading causes of morbidity and mortality worldwide. Statistics reported by the National Cancer Institute at the National Institute of Health and the American Cancer Society estimate 1.69 million new cases of cancer will be diagnosed in the United States and almost 600,000 people will die from the disease in 2017. The cost of cancer care in the United States totaled nearly $125 billion in 2010 and could reach $156 billion in 2020. According to the most recent SEER (Surveillance, Epidemiology, and End Results Program) Cancer Statistics Review, the overall cancer death rate has declined by 13% from 2004 to 2013. The downward trend shows that progress is being made against cancer, but much work remains to further decrease cancer mortality rates, improve quality of life for cancer patients, and reduce the cost of cancer care.

Although substantial progress has advanced fundamental cancer biology research in the recent years, the translation from research to the clinic has been less significant. The main driving factor for the discrepancy between research progress and clinical advancement is the inability to deliver administered therapeutic agents such as small molecules, nucleic acids, peptides, or proteins to the targeted sites with minimal off-target adverse effects [1]. Many therapeutic agents become insoluble, unstable, or unavailable once they are given to cancer patients regardless of the route of administration due to the enzymatic and degradative environment *in vivo* [2]. Even if the therapeutic agents are bioavailable, they eventually spread throughout the cir-

culatory system to all organs and tissues, healthy or diseased. This non-preferential delivery of cancer therapeutic agents results in toxicity to healthy cells and reduction of therapeutic dose to diseased cells, which manifest as adverse side-effects and reduced efficacy in the treatment of cancer patients.

In vivo studies found that when anti-cancer drugs such as cytarabine, methotrexate, and interferon α-2b are administered in a single bolus injection, their plasma or serum elimination half-lives range from only 10 minutes to 7.2 hours, depending on the route of administration [3]. Furthermore, it was reported that even in the ideal case, only 10 to 100 parts per million of monoclonal antibodies administered intravenously will reach their parenchymal targets *in vivo* [4]. Therefore, there is a need to reduce the high elimination rate and off-target delivery of therapeutic agents with a better delivery system.

A successful delivery of therapeutic agents requires the agents to be bioactive and released at a specific rate and at a specific site [5]. Therefore, an ideal therapeutic delivery system should achieve the following four goals: (1) protect the therapeutic agents from aggregation, inactivation, or degradation during circulation, (2) provide the therapeutic agents with ways to overcome the biological barriers that prevent them from being delivered to their target by means of increased blood circulation time, (3) possess an increased targeting selectivity to improve distribution of the therapeutic agents in the targeted tissues, and (4) release the therapeutic agents in a controlled manner. Increased targeting selectively to localize delivery will inherently result in a reduced dosage of the therapeutic agents that is still efficacious, thereby

reducing dose-dependent adverse side effects [6], [7].

Nanotechnology may be the solution to overcome the challenges of delivering therapeutic agents to treat cancer patients by addressing the four goals. Nanotechnology is generally defined as the study of nanoparticles, which are fabricated using natural or synthetic materials and have at least one dimension in the 1 to 1,000 nm size range. Nanoparticles can protect therapeutic agents with encapsulation, prolong circulation, improve targeting, and control release of these agents [1], [8].

2.1.1 Protection with Nanotechnology

In theory, a nanoparticle can protect therapeutic agents from aggregation and inactivation and delay their degradation to improve their bioavailability [9]. Protection of therapeutic agents may be achieved by physically shielding the therapeutic agents within the nanoparticles to prevent inactivation by the acidic environment of the lysosomes in a cell, degradation by enzymes in the blood, and recognition by the immune system. Therapeutic agents may be small molecules, proteins, nucleic acids (i.e. RNA and DNA), or viruses. Small molecules are typically cleared by the renal system. Proteins, RNA, and DNA are degraded by proteases, ribonucleases, and deoxyribonucleases, respectively, in the body. Viruses may be recognized and cleared by the immune system. By protecting these therapeutic agents, the nanoparticles may reduce the dosage required for therapeutic efficacy and minimize dose-related adverse side effects.

In addition, nanoparticles can improve the solubility of poorly soluble thera-

peutic agents to protect them from aggregation and diminished bioavailability. Most chemotherapeutics are hydrophobic and use solvents in their formulations to keep the drugs from aggregating in an aqueous solution [10]. One example of a poorly soluble chemotherapeutic is paclitaxel, which is approved by the Food and Drug Administration (FDA) for treating certain patients with breast cancer, non-small cell lung cancer in combination with carboplatin, and pancreatic cancer in combination with gemcitabine. Paclitaxel is formulated using 50% Cremophor EL and 50% dehydrated ethanol in order to solubilize the hydrophobic drug. The use of Cremophor EL in the formulation causes acute hypersensitivity reaction, hyperlipidaemia, and neurotoxicity in patients [11]. Nanotechnology is able to overcome the solubility issue of paclitaxel with Abraxane® and Genexol®-PM. The FDA-approved Abraxane® is an albumin-bounded nanoparticle formulation of paclitaxel. Genexol®-PM, a micelle formulation of paclitaxel, is approved in South Korea to treat refractory ovarian cancer and metastatic breast cancer. Since both formulations eliminate the need for solvents to solubilize paclitaxel, they are able to avoid the adverse side-effects associated with Cremophor EL and allow for significantly higher dosage of paclitaxel to be administered to the patients [10], [12].

2.1.2 Evading Biological Barriers with Nanotechnology

Most of the therapeutic agents are given in high dosage to compensate for their clearance by either the renal system due to their small sizes or by the mononuclear phagocytic system (MPS) and the immune system due to their immunogenicity.

Although nanotechnology-based delivery systems face the same clearance challenge, they can be designed to overcome the biological barriers more easily than modifying the therapeutic agents. For nanoparticles to accumulate in the tumor, they have to prolong their circulation time to allow for multiple passes by the tumor site. Prolonged circulation requires the nanoparticles to evade physiological and biological barriers. Therefore, nanoparticles must be able to escape filtration by the splenic red pulp, bone marrow, lymph nodes, and kidney; overcome phagocytosis by the complex system of Kupffer cells lining the sinusoids of the liver and other macrophages; and recognition by other immune cells in circulation [13]. Once they reach the tumor site, the nanoparticles have to diffuse through the interstitial space and extracellular matrix, then release the therapeutic agents either in the extracellular space after anchoring to the surface of the targeted cancer cells or intracellularly after being internalized by the targeted cancer cells. The location of the release depends on the site of action of the therapeutic agents [14]. Several parameters that influence the interaction between a nanoparticle and the biological barriers are the size, shape, surface properties, and mechanical properties of the nanoparticle.

The size of the nanoparticles carrying therapeutic agents has the most significant contribution to their circulation time. The nanoparticles must not be larger than the smallest capillaries to avoid occluding the blood vessels. Particles or aggregates of nanoparticles with sizes greater than 10 μm have been reported to form embolism in the liver and lung [15]. Particles with sizes between 3 and 4 μm have been shown to accumulate in the spleen [16]. Nanoparticles smaller than 5.5 nm may

be filtered through the fenestration in the glomerulus of the kidney, which ranges between 5 to 25 nm in size [9].

There are increasing number of studies that show the importance of nanoparticle shape on circulation time by affecting the interactions between the nanoparticles and the MPS [6]. Rod-like nanoparticles with high aspect ratio appear to extravasate into tumor sites faster than spherical nanoparticles due to their margination property. For example, elongated viral nanofilaments have increased accumulation in tumor compared to spherical viral constructs [17]. In another study, nanospheres constructed from CdSe/CdS quantum-dot cores with spherical silica shells were compared to nanorods fabricated from CdSe quantum-dot cores with seed-grown elongated CdS shells. Both nanospheres and nanorods have their surfaces modified with a layer of polyethylene glycol. The final hydrodynamic diameter and length of the nanorods was 5 nm in diameter and 54 nm in length (aspect ratio of about 10). The hydrodynamic diameter of the nanospheres was about 34 nm. Although both nanoparticles have similar blood circulation profiles, the nanorods extravasate into the interstitium four times faster and diffuse deeper into the tumor tissues to distribute across 1.7 times more tissue volume when compared to the nanospheres [18]. These observations are often attributed to the marginating property of the nanoparticles, which indirectly affects their circulation time. A marginating particle has the tendency to drift from the core of the blood vessel towards the blood vessel wall, which increases the chance of interacting with the endothelial cells lining the blood vessels and exiting out of larger blood vessels in the macro-circulation

into smaller blood vessels within the tumor micro-circulation [13]. This property is highly desirable for therapy targeting the tumor vasculatures or exploiting the enhanced permeability and retention effect. Spherical particles that are non-buoyant preferentially move along the center of the blood vessel until an external force is applied to cause the particles to drift laterally towards the blood vessel wall [19]. In contrast, non-spherical particles exhibit tumbling and rolling motion that contribute to their margination towards the blood vessel wall without application of external forces. Computer simulation suggests that a neutrally buoyant spherical particle moves to an equilibrium distance from a cylindrical wall (an idealized capillary), while an ellipsoidal particle rotates and translates from one side of the cylindrical wall to the other [20]. Although this simulated observation assumes an idealized case and fails to account for any interaction of the particles with other blood components such as the red blood cells and serum proteins, it is reasonable to assume ellipsoidal particles smaller than the red blood cells have a higher tendency towards margination to the blood vessel walls than their spherical counterparts. In addition, the particle surface curvature plays a role in antibody-binding, which leads to complement activation and clearance by macrophages. Immunoglobulin M (IgM) molecules have a cross-sectional diameter between 35 to 38 nm [21]. As the dimension of a nanoparticle approaches that of IgM, the degree of strain for an IgM to bind to the nanoparticle increases. Therefore, it is observed that particles that are 250-nm in diameter have higher IgM binding than particles that are 50-nm in diameter. Recently, non-spherical shaped particles have been successfully synthesize using silicon

[22], gold and bacteriophage [23], solid lipid [24], silica [25], nanotubes [26], and polymer [27].

Surface property such as surface charge is another physiochemical parameter of nanoparticles that affects their systemic circulation times. It has been reported experimentally that electrostatic interactions between a circulating particle and the charged components of the extracellular matrix can slow down diffusion of the particle significantly [28]. Circulating nanoparticles with positively-charged surface are attracted in a non-specific manner to negatively-charged endothelial cells lining the blood vessels and may be internalized, which leads to reduced circulation time. However, positively-charged nanoparticles may be good candidates for targeting the tumor vasculatures [29]. A cationic liposomal formulation of embedded paclitaxel, EndoTAG^{TM}-1, is currently recruiting patients for phase III clinical trial in combination with gemcitabine as the first-line therapy for patients with visceral metastatic triple-negative breast cancer. EndoTAG^{TM}-1 targets delivery of paclitaxel to negatively-charged, activated endothelial cells of the tumor vasculature [30]. Nanoparticles with negatively-charged surface can either increase, decrease, or have no effect on the circulation time of the nanoparticles [6]. Nanoparticles with neutral or slightly negative surface can diffuse faster than charged nanoparticles [28]. Hence, neutral to slightly negatively-charged nanoparticles are preferred if extended circulation is required. Many clinically approved nanoparticles use polyethylene glycol to neutralize the surface charge in order to extend the circulation time of the nanoparticles. Examples of neutral nanoparticles in clinical use are Doxil® and Oncaspar®,

with many more in clinical trials [29].

Finally, the mechanical property is another parameter that affects the interaction between nanoparticles and the biological barriers. It has been reported that macrophages have a stronger preference to phagocytose rigid particles compared to soft and flexible particles even when the chemical properties are identical [31]. Using hydrogel nanoparticles with different elastic modulus to compare a range of soft to rigid nanoparticles of similar size, shape, and charge, it was observed that softer nanoparticles were able to resist phagocytosis for a longer period of time as compared to more rigid nanoparticles [32]. Consequently, softer nanoparticles are able to circulate longer in blood.

Because of the importance of the size, shape, and surface property of nanoparticles in prolonging their blood circulation time, a later section on "Nanoparticles and Circulation" will explore the effects of these three parameters in more details.

2.1.3 Targeting with Nanotechnology

In addition to protecting the therapeutic agents, multiple targeting strategies may be incorporated into the nanoparticle design to improve the accumulation, biodistribution, and absorption of therapeutic agents in tumor sites. Deeper penetration of the nanoparticles into the tumor tissues is preferred for better biodistribution. The penetration of the nanoparticles is a diffusion-mediated process that is inversely correlated with the size of the nanoparticles [33]. However, accumulation and distribution of therapeutic agents in the tumor tissue will not occur if the nanoparticles are

unable to reach the tumor site. Therefore, targeting strategies will only be successful with long-circulating nanoparticles. So far, three main targeting strategies have been developed, which are passive targeting, active targeting, and external targeting.

A passive targeting strategy is to exploit the increased endothelial fenestration (i.e. the intercellular openings between endothelial cells) and structural disorder of the vasculature associated with rapid angiogenesis within tumor tissues. Rapid formation of new blood vessels is necessary when the existing normal vasculatures become inadequate in supplying oxygen and nutrients to a solid tumor beyond a certain size. The formation of these large openings between endothelial cells [34] occurs because of impaired recruitment of pericytes to support the endothelial cells that line the tumor vasculature [35], thereby enhancing the permeability of the tumor vasculature [36]. Depending on the tumor type, the tumor stage, the tumor environment, and its location within the tumor, the fenestration in the tumor capillaries may range from 100 nm and 780 nm as compared with 2 to 6 nm in normal blood vessels [6], [34], [35], [37], [38]. Nanoparticles with size smaller than these openings can extravasate through this "leaky" vasculature into the tumor tissues. Furthermore, the intratumoral lymphatics are highly compressed due to the physical forces exerting from the proliferation of cancer and stromal cells [39]. This dysfunctional lymphatic drainage system within a tumor prevents any nanoparticles from draining back into the circulation and helps retain and accumulate nanoparticles in the tumor interstitium. The combination of permeable vasculature and poor lymphatic drainage allow nanoparticles to accumulate in the tumor by the enhanced

permeability and retention (EPR) effect [5], [6], [40], [41]. One of the first FDA-approved nanotechnology-based anti-cancer drug, Doxil® (a liposomal formulation of doxorubicin), has clinically shown up to six times improvement in drug retention via the EPR effect and enhanced circulation time when compared to the free drug, doxorubicin [5].

Small tumors or metastatic cancers do not exhibit strong angiogenesis, so passive targeting based on the EPR effect or vasculature targeting may not be sufficient. In these cases, active targeting in addition to passive targeting may enhance the selectivity of the nanoparticles to tumor tissues. An active targeting strategy employs mechanism beyond size-dependent biodistribution to further enhance preferential delivery to a specific tissue [42]. Active targeting strategy requires the conjugation of active recognition moieties to the surface of a nanoparticle to recognize biomarkers overexpressed by cancer cells. This strategy has several advantages such as delivering higher therapeutic payloads to the target, conjugating multiple different recognition moieties, and colocalizing delivery of multiple therapeutic agents for combination therapy [1]. These active recognition moieties or ligands can be classified as proteins (e.g. antibodies and their fragments, peptides), nucleic acids (e.g. aptamers), or other high-affinity small molecules (e.g. vitamins and carbohydrates) that selectively bind to a specific type of receptors on the targeted cell [41].

The most commonly used proteins as targeting ligands are antibodies. Antibodies are widely used because of their high affinity and specificity for their targeted receptors. Examples of antibodies as targeting ligands include the FDA-approved

Herceptin and Avastin. Herceptin, approved for treating breast cancer, is an anti-HER2 monoclonal antibody that binds to ERBB2 receptor. Avastin, approved for treating colorectal cancer, is an anti-VEGF monoclonal antibody that inhibits VEGF that is responsible for angiogenesis. In fact, more than 30 types of monoclonal antibodies have been approved for clinical use [6]. The challenges with conjugating antibodies to nanoparticles is the size of the antibodies and recognition by immune cells. At 150 kDa and a hydrodynamic radius of 15 to 20 nm, antibodies are considered large proteins. Conjugating such large proteins onto a nanoparticle effectively increases its size. In addition, the antibodies may bind to antigens in circulation that are recognized and cleared by the immune cells. Both challenges may be addressed by using fragments of the antibodies [6]. Single-chain variable fragments are fusion proteins that consist of the variable regions of the heavy and light chains of an antibody connected with a short linker peptide. These fragments are significantly smaller in size at about 27 kDa and less immunogenic [33]. Small proteins such as epidermal growth factor (EGF) conjugated to nanoparticles to target EGF receptors that are overexpressed in head and neck, ovarian, cervical, bladder, and oesophageal cancers have been successfully tested in pre-clinical settings [43]. Targeting peptides are even smaller at about 1kDa. These peptides have better tissue penetration properties, no immunogenicity, and are easy to conjugate onto nanoparticles. An example of peptides used as targeting agents is RGD (arginine-glycine-aspartate) peptide. In pre-clinical studies, RGD peptides have been conjugated to nanoparticles to target $\alpha_{\mathrm{v}}\beta_3$-integrin. $\alpha_{\mathrm{v}}\beta_3$-integrin plays an important role in angiogenesis

and is overexpressed on tumoral endothelial cells [44].

Another class of recognition moiety is nucleic acid-based aptamers. Nucleic acid aptamers are short single-stranded oligonucleotides such as DNA or RNA that are screened to have high affinity and specificity for specific nucleic acid sequences. They are usually around 10 to 20 kDa with size around 3 to 10 nm. Preclinical studies of aptamers designed to target the prostate-specific membrane antigen cancer biomarker have shown efficacy in slowing tumor growth [45], [46]. The main challenge with using nucleic acid aptamers is their stability. Nucleic acids are quickly degraded by nucleases in the biological environment. One proposed solution is to use nucleic acids modified with fluoro amino or methoxy groups to delay their degradation [47]. Another concern with using nucleic acids is the negative charge attributed to the phosphodiester backbone of nucleic acids. Conjugated at a high density, the nucleic acids may contribute to an overall negative charge on the nanoparticle surface [48].

The last class of recognition moiety is the high-affinity small molecules. A common small molecule targeting moiety is folic acid. Folic acids have very high affinity for folate receptors which are often overexpressed on the surface of several cancer cells including epithelial, ovarian, breast, colorectal, brain, renal, and lung cancers [49]. However, the overexpression of folate receptors is patient-dependent and folate receptors are also constitutively expressed in healthy cells, which limit their selectivity for cancer cells [6]. Carbohydrates are another class of small molecules used as targeting ligands. Carbohydrates such as mannose, glucose, and galactose have been studied as targeting ligands to bind to lectins, which are cellular membrane

proteins [50].

So far, no actively-targeted nanoparticles have been approved for clinical use. However, several actively-targeted liposomes and polymeric nanoparticles are in clinical trial. In general, the ligands selected for conjugation onto the nanoparticles should bind with high selectivity to receptors that are uniquely expressed or overexpressed on the targeted cancer cell surface.

External targeting strategy is the use of external energy to trigger localized activation or release of cytotoxic therapeutic agents in the pathological tissue while avoiding cytotoxicity in healthy tissues. Some examples of external energy include light, heat, ultrasound, electric field, and magnetic field.

The ability of light to remotely trigger the release of therapeutic agents is accomplished through the use of photosensitive chemical groups. Photosensitive chemical groups change their structural conformation or other properties when exposed to light at a specific wavelength. Azobenzene, for example, changes from *trans* to *cis* isomer when exposed to ultraviolet light (wavelength between 300 to 380 nm) and reverses its conformation with blue light. By incorporating azobenzene in the lipid bilayers of liposomes, encapsulated therapeutic agents may be released by photo-isomerization when the steric effect and the increased polarity of the *cis* isomer destabilizes the lipid bilayer [51]. Photo-cleavable amphiphilic molecules are another type of photosensitive molecules that can be incorporated into the liposomal membrane for light-triggered release. By exposing these molecules to specific wavelength of light, the molecules are cleaved, causing their polar and nonpolar moi-

eties to separate. Once the amphiphilic property of the molecules is lost, the lipid membrane destabilizes and the encapsulated therapeutic agents are released [52]. Photo-induced crosslinking of polymers or photo-polymerization is another method to destabilize a lipid membrane. Unfortunately, most of the photosensitive molecules function with ultraviolet light which has a shallow tissue penetration depth of less than 200 μm due to scattering of the soft tissues and may cause cell damage by DNA mutation. Near-infrared light between 700 to 900 nm in wavelength is preferred since the penetration depth in soft tissue is deeper and the cell damage or heating of the exposed area is less significant than ultraviolet and visible light.

The use of heat on thermo-responsive nanoparticles to target the release of therapeutic agents is more promising. ThermoDox® is an example of externally-triggered nanoparticles in clinical trials for treating hepatocellular carcinoma, breast cancer recurrence at the chest wall, and liver metastasis [29]. ThermoDox® is a thermo-sensitive liposomal formulation of doxorubicin. The liposome is composed of heat sensitive lipids that have a gel-to-liquid crystalline phase transition temperature around 40°C. At temperature above 40°C, the liposome membrane integrity breaks down and releases the doxorubicin within the liposome. The thermal trigger is delivered using radio-frequency ablation [53].

In addition, therapeutic agents may be bound to magnetic nanoparticles such as iron oxide and concentrated to the tumor site by applying magnetic field to the tumor tissue [5].

A schematic diagram that summarizes the different strategies mediated by

nanoparticles to deliver and target therapeutic agents to tumor tissues is shown in Figure 2.1. In theory, nanoparticles carrying therapeutic agents may be designed to have a size of approximately 100 nm to exploit the enhanced permeability and retention effect observed in tumor tissues. Once the nanoparticles have extravasated into the tumor, the active targeting moieties conjugated on the surface of nanoparticles may interact with targeted molecules in the extracellular matrix or on the cancer cells to either anchor to the targeted molecules or be internalized by the cancer cells. Finally, regardless if the nanoparticles are within the tumor environment, on the surface of cancer cells, or internalized by the cancer cells, the nanoparticles may be designed to release their contents with different release profiles based on the therapeutic requirements.

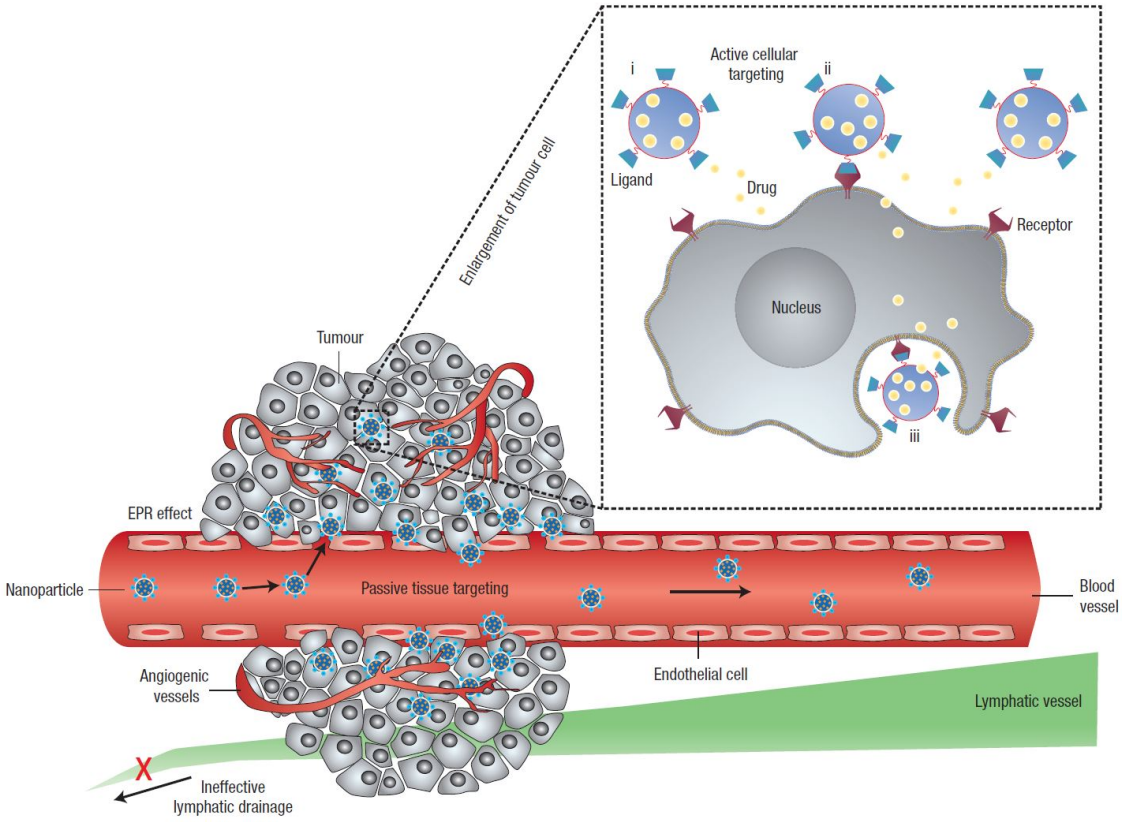

Figure 2.1: A schematic diagram of different mechanisms by which nanoparticles can deliver drugs to tumors. Nanoparticles in the range of 100 nm may passively target tumor tissues by extravasating into tumors through increased permeability of the tumor vasculature and dysfunctional tumor lymphatic draining (EPR effect). Once in the tumor environment, nanoparticles may actively target tumor cells (inset) by functionalizing the surface of nanoparticles with ligands that recognize and bind to targeted cancer cells. The nanoparticles can (i) release their contents in close proximity to the targeted cells; (ii) bind to the membrane of the targeted cell and act as an extracellular sustained-release drug depot; or (iii) internalize into the targeted cell. Reprinted with permission from [41], copyright 2007 Nature Publishing Group.

2.1.4 Controlled Release with Nanotechnology

Once the nanoparticles reach the targeted tumor site, they may be designed to release the therapeutic agents intracellularly, locally in tumor tissues, or return to systemic blood circulation depending on the site of action of the therapeutic agents.

Cellular uptake may be required for therapeutic agents targeting intracellular components such as nucleic acids. The internalization rate of nanoparticles by cells can be controlled by their size and shape. Using 10 to 100-nm spherical gold nanoparticles, a maximum cellular internalization of 50-nm nanoparticles was reported. Comparing 14-nm and 74-nm spherical gold nanoparticles with 14 x 40-nm (aspect ratio of 3) and 14 x 74-nm (aspect ratio of 5), the internalization rate of the nanoparticles ranked from highest to lowest was 74-nm spheres, 14-nm spheres, 14 x 40-nm rods, and 14 x 74-nm rods [54]. Therefore, the size and shape of nanoparticles designed to carry therapeutic agents directed at the cytosol or nucleus should be around 50-nm and spherical to increase internalization. Once internalized, there are different strategies to release the therapeutic agents from the nanoparticles. One strategy is to co-encapsulate listeriolysin O with the drugs in liposomes [55]. After internalized into endosomes, listeriolysin O is able to permeabilize the endosomal membranes to release the contents of the liposomes into the cytosols. This type of nanoparticles is useful for delivery of protein antigens for vaccines. Another strategy for intracellular delivery is to target internalizing receptors. For example, conjugating anti-CD19 ligands to the surface of liposomes can target B-cell lymphoma to internalize the liposomes. Using internalizing anti-CD19 ligands resulted in a more significant therapeutic outcome than using non-internalizing anti-CD20 ligands, even though B cells express both CD19 and CD20 molecules on their surface [56].

For nanoparticles designed to serve as drug-releasing depots in the tumor environment, cellular internalization may not be necessary. Doxorubicin, for instance,

is capable of crossing the cell membrane by passive diffusion when released near targeted cancer cells [7]. The optimal nanoparticle design should have a high probability of adhering selectively to the targeted cells via different methods of targeting. Such design requires short margination time and fast interaction with the endothelium of the tumor vasculature via targeting ligands to receptors on the endothelial cells. Once the nanoparticles adhere to the targeted cells or extracellular matrix, they should also resist internalization and begin to release their therapeutic payload in a controlled manner. Therefore, the size and shape of nanoparticles designed to serve as drug-releasing depots in the tumor environment should be greater than 50-nm and ellipsoidal shaped with high aspect ratio.

Similarly, nanoparticles designed for systemic delivery should have an optimal design that prolongs circulating time in order to interact with metastatic cancer cells or leukemic cells without being internalized by non-targeted cells or trapped within the interstitium. Such design should possess long margination time or minimum interaction with the endothelium via neutral surface charge. By modulating the geometry and surface properties of the nanoparticles, the margination speed can be tuned. Considering buoyancy, hemodynamic forces and van der Waals interaction, it is reported that a theoretical critical radius (in the range of 100 nm) exists at which the particle margination time is maximum [57]. Particle with radius smaller or larger than the critical radius has a shorter margination time. However, to exploit the enhanced permeability and retention effect, the optimal nanoparticles shape may be ellipsoidal with high aspect ratio in order to exit the main systemic circulation

into the micro-circulation within a tumor.

Besides engineering the nanoparticles for intracellular, localized, or systemic delivery, nanoparticles may be further designed to control the release profiles of their therapeutic agents (e.g. no release, slow release, or fast release) to tailor to the different types of therapy. The design of the release profile is highly dependent on the material of the nanoparticles. In fact, materials may be selected to be responsive to certain stimuli *in vivo* such as pH-responsive liposomes.

For the delivery of therapeutic enzymes, it might be beneficial for the nanoparticles to keep the enzymes encapsulated and not released to protect them from degradation or clearance by the MPS. For the delivery of therapeutic drugs, it might be beneficial for the nanoparticles to release the drugs in a slow and controlled manner at the tumor site to reduce dosing frequency, while protecting the unreleased drugs from inactivation or degradation. There are two main mechanisms for releasing therapeutic agents from nanoparticles, namely diffusion and erosion [3].

For slow-release by diffusion, the nanoparticle number remains constant but the amount of drug retained within the nanoparticles decreases over time. In general, there are two designs for diffusion-controlled release, namely the reservoir-based design and the matrix-based design [58]. The reservoir-based design utilizes nanoparticles with an outer shell composed of a lipid membrane, a polymeric material, or an inorganic material. Therapeutic agents loaded within the core of the nanoparticles are unable to escape all at once due to the outer shell layer acting as a barrier slowing the release. Depending on the porosity and thickness of the outer layer and

the size of the therapeutic agents, the rate of diffusion of the therapeutic agents out of the nanoparticles may be tuned. In the matrix-based design, therapeutic agents are homogeneously distributed throughout a water-insoluble polymeric matrix which forms a nanoparticle [59]. Examples of water-insoluble polymers include polyurethane and poly(methyl methacrylate). This design usually exhibits an initial burst release when therapeutic agents adsorbed on the surface of the nanoparticles are released, followed by a slow release as the therapeutic agents diffuse out of the polymeric matrix. Again, the rate of diffusion may be tuned by varying the porosity of the polymeric matrix.

For slow-release by erosion, the concentration of both the nanoparticle and the internal drug remain constant but the nanoparticle size decreases. In this case, the nanoparticle is made of degradable polymers that form a matrix with the therapeutic agents distributed uniformly throughout the nanoparticle. Examples of degradable polymers include poly(lactic acid), poly(glycolic acid), and poly(lactic-*co*-glycolic acid), which undergo hydrolytic cleavage of their ester bond between lactic and glycolic acid during degradation. Since these polymers are degraded via hydrolysis reaction, their hydrophilicity and the surrounding pH determine the nanoparticle erosion rate and the drug release rate [60]. In addition, the erosion may take place from the surface inwards or throughout the bulk of the nanoparticles to provide two different release profiles. Surface erosion occurs when the rate of erosion is faster than the rate of water permeation into the bulk of the nanoparticle [61]. This type of erosion is achieved by selecting a more hydrophobic polymer where its hydrophobicity slows

water permeation [62]. Surface erosion is generally preferred since it produces a more steady-state release of the therapeutic agents. Bulk erosion, in contrast, occurs when water molecules are absorbed into the nanoparticles faster than the rate of erosion. The release profile is more complex for bulk erosion. Initially, there is a fast release of therapeutic agents from the surface. Next, the therapeutic agents are released at a slower rate as the polymer gradually degrades. Finally, the therapeutic agents are burst released when the polymer matrix is completely degraded from all direction.

An example of controlled slow-released nanotechnology-based delivery vehicle using both diffusion and erosion mechanisms is the multivesicular liposome. The increased stability and extended drug-release duration of multivesicular liposomes are attributed to their composition of multiple non-concentric lipid layers. Therapeutic agents are released constantly by diffusion through the lipid membranes. In addition, the outer bilayer membrane degrades over time to release its content, while the internal space that is divided into numerous compartments by bilayer septa rearranges through fusion and division without any release of their encapsulated drugs. This process repeats until all the therapeutic agents encapsulated within the multivesicular liposomes are released [3]. DepoCyt® is an example of multivesicular liposomes for controlled released of cytarabine that is approved by the FDA. This design is an improvement over single-vesicle liposomes and concentric multivesicular liposomes.

For the delivery of diagnostic imaging agents or high dose of therapeutic agents, it might be beneficial for fast release of the agents from the nanoparticles at the tumor site. Internal or external stimuli is generally used to trigger fast release

of diagnostic or therapeutic agents. Internal stimuli usually refers to low pH or high level of certain enzymes associated with the tumor environment. Many pH-sensitive nanoparticles have been developed for fast release of their contents when they encounter an acidic environment. The most commonly studied pH-sensitive nanoparticles are polymer micelle, liposome, and hydrogel nanoparticles [63]. The design of a pH-sensitive polymer micelle involves electrostatically attracting positively-charged therapeutic agents such as doxorubicin to negatively-charged block copolymer with carboxylate groups to form nanoparticles. When the pH of the surrounding decreases, the carboxylate groups become protonated, the electrostatic attraction breaks down, and the therapeutic agents are released [64]. Similarly, pH-sensitive polymers may be incorporated into liposomes such that the polymers collapse when the surrounding pH drops, thereby creating instability within the liposomal shells that results in the efflux of the encapsulated therapeutic agents [65]. Likewise, hydrogels may also incorporate pH-sensitive polymers such as polyamine that protonates when the pH drops 1 to 2 units from the physiological pH of 7.4. Protonation of the polymer core leads to swelling of the nanoparticle and the release of its content [66]. Exploiting overexpression of certain enzymes associated with the tumor environment is another strategy for using internal stimuli to trigger the release of therapeutic agents. Enzyme-sensitive nanoparticles are usually designed to be susceptible to enzymatic cleavage of a linker between the therapeutic agent and the nanoparticle or the bonds holding the nanoparticle intact [67]. Since matrix metalloproteinases (MMPs) level are typically elevated in the tumor environment, short peptides with

sequences designed to be cleaved by MMPs have been developed as linkers between polyethylene glycol (PEG) and liposomes [68], polymeric nanoparticles [69], or iron oxide nanoparticles [70] to trigger the removal of the PEG layers from the nanoparticles in the tumor tissue. With the removal of the protective PEG layer, the active surface of the nanoparticles are exposed to aid in the internalization of the nanoparticles by the cancer cells [33]. External stimuli such as light, heat, ultrasound, electric field, and magnetic field are another form of targeting and are discussed in more details under the "Targeting with Nanotechnology" section.

2.2 Biomaterials in Nanotechnology

Other important considerations in using nanotechnology to develop drug delivery systems include selecting a nanoparticle material that is biocompatible, biodegradable, and easy to perform surface modification and functionalization. Biocompatibility can be achieved by selecting biomaterials that are inert or non-toxic to the biological environment [71]. A biocompatible nanoparticle should not elicit unacceptable toxicity, immunogenicity, thrombogenicity, and carcinogenicity responses in human. Biodegradability is the ability of the body to breakdown nanoparticles into harmless metabolic products for excretion through the renal system or the biliary system [72]. Ease of surface modification is the ability to perform chemical reactions on the surface of the nanoparticles in order to conjugate moieties for targeting or to evade the immune system. Common types of biomaterials used to synthe-

size nanoparticles that are biocompatible, biodegradable, and easily functionalized include polymers, lipids, inorganic materials, and dendrimers [73].

2.2.1 Polymer Conjugates

Polymer-protein and polymer-drug conjugates are usually 6-nm to 15-nm nanoparticles designed to target tumor vasculatures [41]. The advantages of polymer-protein conjugates include increased protein solubility and stability, reduced protein immunogenicity, decreased degradation of small proteins, and reduced clearance of receptor-mediated clearance by the MPS. All these advantages support prolong circulation of the therapeutic proteins, which leads to reduced dosing frequency and dose-related adverse side effects. In fact, polymer-protein conjugate is one of the few classes of nanoparticles that have several therapeutic products approved for clinical use to treat cancer patients. The most common polymer used for protein conjugation is poly(ethylene glycol) due to its biocompatibility, low immunogenicity, ease of conjugation, and high degree of hydration to create a water solvation layer around the conjugates to mask the protein from the body [8]. An example of a FDA-approved polymer-protein conjugate is Oncaspar®. Oncaspar® is the enzyme asparaginase conjugated to poly(ethylene glycol). It is used to treat acute lymphoblastic leukemia and lymphoma. The circulation half-life of Oncaspar® is significantly increased to almost 6 days compared to the circulation half-life of about 30 hours with native asparaginase. In addition, there is a decrease in hypersensitivity reactions in patients treated with Oncaspar® versus native asparaginase [74]. Zinostatin Stimalamer is a

polymer-protein conjugate approved in Japan for treating primary unresectable hepatocellular carcinoma [29]. It is a conjugate of a copolymer of styrene-maleic acid (SMA) and an antitumor protein NeoCarzinoStatin (NCS).

The motivations for designing polymer-drug conjugates are to increase solubility of hydrophobic drugs such as doxorubicin and paclitaxel with hydrophilic polymers, improve drug targeting to tumor site usually via enhanced permeability and retention effect, prolong circulation of the therapeutic drugs to reduce dosage and dose-related toxicity, and limit intracellular uptake through the endocytic route [8]. Currently, there are several polymer-drug conjugates in clinical trials, but none have been approved as cancer therapy [75]. One promising polymer-drug conjugate in Phase III clinical trial is etirinotecan pegol (NKTR-102). It is a long-acting topoisomerase-I inhibitor that consists of the topoisomerase-I inhibitor irinotecan bound to a proprietary poly(ethylene glycol) core by a biodegradable linker. As the linker slowly hydrolyzes *in vivo*, the active metabolite SN-38 is released from etirinotecan pegol. SN-38 molecules bind to the topoisomerase I-DNA complex and prevent religation of single-stranded DNA breaks to induce cytotoxicity. For the drug to be safe and efficacious, the cancer cells will need to be exposed to SN-38 molecules continuously, while reducing the dose-related toxicities reported in patients who receive irinotecan directly. The half-life of irinotecan and SN-38 are approximately 9 hours and 47 hours in human [76]. Clinical trials showed that the polymer-drug conjugate etirinotecan pegol can achieve a sustained and controlled release of SN-38, leading to a mean half-life of about 50 days [77].

2.2.2 Polymeric Nanoparticles

Polymeric nanoparticles are typically 50 to 200 nm and synthesized from synthetic polymers such as poly(lactic-co-glycolic acid), poly(ethylene glycol), poly-L-lactic acid, polycaprolactone, and hyaluronic acid; or from natural polymers such as dextran, albumin, sodium alginate, collagen, and chitosan. Therapeutic agents may be encapsulated within polymeric nanoparticles without chemical modification. The therapeutic agents are typically released in a slow and controlled fashion through mechanisms such as surface or bulk erosion, diffusion through the polymer matrix with or without swelling of the matrix, or in response to local stimuli [41]. Abraxane® is an example of polymeric nanoparticle approved by the FDA to treat metastatic breast cancer. Abraxane® is an albumin-bounded nanoparticle formulation of paclitaxel that is around 130 nm. Paclitaxel is a cytoskeletal drug that targets tubulin by stabilizing the microtubule polymer and inhibits it from disassembly. As a result, chromosomes are unable to attain a metaphase spindle configuration, which inhibits mitosis progression. Delayed activation of the mitotic checkpoint induces apoptosis or reversion to the G-phase of the cell cycle without cell division. The clinical toxicity of paclitaxel is associated with the solvent Cremophor EL in which paclitaxel is dissolved for injection. Clinical trial with breast cancer patients showed greater efficacy and better safety profile with Abraxane® when compared to paclitaxel. The response rate and time to tumor progression of Abraxane® treated patients (33% and 23 weeks) is significantly higher than paclitaxel treated patients (19% and 17

weeks). Furthermore, there was no hypersensitivity reaction with Abraxane® treated patients despite without pre-treatment with steroidal anti-inflammatory drugs, which are required in paclitaxel treated patients [78]. An example of polymeric nanoparticles in clinical trial is CALAA-01. CALAA-01 is a polymer-based nanoparticle about 75 nm in diameter. It consists of a linear cationic cyclodextrin-based polymer (adamantane polyethylene glycol) for surface stabilization, the human protein transferrin as targeting ligands on its surface to target transferrin receptors that are typically overexpressed on cancer cells, and a small interfering RNA (siRNA) as the therapeutic agent. The siRNA targets the M2 subunit of ribonucleotide reductase, a clinically-validated cancer target. Ribonucleotide reductase is a crucial enzyme for cell proliferation because it catalyzes the conversion of ribonucleosides to deoxyribonucleosides during DNA synthesis and replication. By suppressing ribonucleotide reductases with siRNA, CALAA-01 has demonstrated potent anti-proliferative activity across multiple types of cancer cells [79]. In fact, tumor biopsies from clinical trials on melanoma patients have shown intracellular localization of CALAA-01 in tumors correlating with the dose levels of the nanoparticles administered and reduction of ribonucleotide reductase expression as evidence in the decrease of intact mRNA level for ribonucleotide reductase and the protein itself when compared to untreated samples. More importantly, the presence of mRNA fragments were detected in a patient given the highest dose of CALAA-01, which demonstrates the occurrence of siRNA-mediated mRNA cleavage at the predicted site. These data suggest that systemic administration of siRNA can produce a specific gene inhibition, with

reduction in mRNA and protein, by an RNAi mechanism of action in humans [80].

2.2.3 Liposomes

Liposomes are probably the most successful nanotechnology-based delivery system to date, with several FDA-approved liposomal formulations for clinical use to treat cancer patients. Liposomes are spherical nanoparticles synthesized from cholesterol and non-toxic phospholipids to form one or more concentric lipid bilayers with an inner aqueous phase compartment [14]. Unilamellar liposomes are formed by a single lipid bilayer and have a size range of 85 nm to 200 nm. Besides being biocompatible and biodegradable, liposomes have the advantages of being able to entrap hydrophilic therapeutic agents in the inner aqueous phase and hydrophobic therapeutic agents within the lipid bilayers; to protect therapeutic agents from chemical and enzymatic degradation; and to easily functionalize the surface to prolong circulation, improve targeting, or induce cell internalization [81]. However, liposomes has the challenge of being unstable *in vivo* and may result in drug leakage or fast burst release of their contents.

One example of chemotherapeutics delivered using liposomes that is approved by the FDA for treating refractory Kaposi's sarcoma, recurrent breast cancer, and ovarian cancer is Doxil®. Doxil® is a doxorubicin-encapsulated liposome in a size range of 80 to 90 nm and with polyethylene glycol polymers attached to the outer lipids. A single Doxil® liposome is capable of encapsulating 10,000 to 15,000 doxorubicin molecules [82]. Doxorubicin is an approved cytotoxic anthracycline chemother-

apy drug that intercalates DNA to prevent DNA transcription, thereby halting replication. Comparing free doxorubicin to Doxil® in clinical trial, the initial distribution half-life of doxorubicin is increased from 5 minutes to between 1 and 3 hours, respectively. The second distribution phase has the half-life extended from between 20 and 48 hours for free doxorubicin to 30 and 90 hours for Doxil®. The doxorubicin concentration (not differentiated between free and encapsulated) in blood plasma is approximately 300-fold greater with Doxil® when compared with free doxorubicin. In addition, Doxil® can target certain tumors via EPR effect, which significantly increases the amount of encapsulated doxorubicin that accumulates in the tumors when compared to free doxorubicin [83]. Finally, there is a decrease in cardiotoxicity with Doxil® compared with free doxorubicin, which enables a higher cumulative dose to be administered than allowed for free doxorubicin [84]. Other liposomal formulations approved by the FDA include DaunoXome® (daunorubicin citrate liposome) for treating Kaposi's sarcoma, DepoCyt® (cytarabine liposome) for treating lymphoma associated with meningitis, Marqibo® (vincristine liposome) for treating Philadelphia chromosome negative acute lymphoblastic leukemia, and Onivyde® (irinotecan liposome) for treating metastatic pancreatic cancer [12].

2.2.4 Inorganic Materials

Inorganic materials such as ceramics and metals are widely studied as materials for making nanoparticles. Ceramic nanoparticles are synthesized from inorganic materials with porous characteristics such as alumina, silica, and titania. The ad-

vantages of using ceramic materials are their small size for evading the MPS and their resistance to swelling or changes in porosity with varying physiological pH [5]. In addition, ceramic materials are inert, highly biocompatible, and easily functionalized for conjugation to targeting ligands. Metal nanoparticles such as gold or silver nanoparticles also have the advantages of being extremely small in size (less than 50 nm), easily functionalized due to their negative surface charge, and biocompatible. In addition, metal nanoparticles have the added capability to be triggered by external excitation sources such as an infrared light or a magnetic field [41]. Solid metal nanoparticles such as gold and iron oxide nanoparticles are extensively studied for photothermal therapy and magnetic resonance imaging, respectively. Currently, no nanoparticles using inorganic materials have been approved by the FDA for cancer treatment or diagnostic. However, there are several inorganic nanoparticles in clinical trials, including Aurimmune, AuroShell, and Combidex [5]. Aurimmune are colloidal gold nanoparticles with tumor necrosis factor alpha (TNFα) bound to their surface via a poly(ethylene glycol) linker to treat pancreatic cancer patients. The small size of the nanoparticles may evade the MPS to deliver TNFα to the tumor vasculature via EPR effect. TNFα is capable of destroying the endothelial cells lining the tumor vasculature to destroy the protective pressure barrier of tumor tissues. Clinical results have shown that Aurimmune can be delivered systemically at doses of TNFα that were previously shown to be toxic and that Aurimmune can target to tumors. Future clinical studies will focus on combining Aurimmune with approved chemotherapy drugs for the systemic treatment of non-resectable cancers such as pancreatic

cancer [85]. AuroShell is a gold-coated silica nanoparticle designed to accumulate in solid tumor via EPR effect due to its small size. After the AuroShell nanoparticles accumulate in the tumor, the tumor site is exposed to near-infrared laser at selected wavelengths for maximum penetration of light through the tissue. The AuroShell nanoparticles are specifically designed to absorb this wavelength and convert the laser light into heat, resulting in the thermal ablation of the tumor. The clinical safety profile of AuroShell nanoparticles is shown to be excellent, so the clinical trial for efficacy of combining AuroShell infusion with laser ablation in treating prostate cancer will be evaluated in future studies [86]. Combidex is a solution of dextran-coated iron oxide nanoparticles in the size range of 20 to 50 nm. It is designed to be administered intravenously and phagocytosed by macrophages. Macrophages accumulate in normal lymph nodes throughout the body, but less in metastatic lymph nodes. As a results, benign lymph nodes may be differentiated from metastatic lymph nodes on an iron-sensitive (T2*-weighted) magnetic resonance imaging (MRI) sequence at 24 to 36 hours after administration of Combidex. Normal lymph nodes appear black on these MR-images, whereas nodes with metastases retain MR signal and appear white [87].

2.2.5 Dendrimers

Dendrimers are spherical structures composed of multiple synthetic and hyperbranched monomers that radiate outward from a central core [5]. They are biocompatible, hydrophilic, and easily conjugated to therapeutic agents and target-

ing moieties. Dendrimers studied by researchers includes polyamidoamine dendrimers, polypropylenimine dendrimers, polyarylether dendrimers, polyester dendrimers based on 2,2-bis(hydroxymethyl)propionic acid, and polyester dendrimers based on glycerol and succinic acid [88]. The three important structural domains of a dendrimer are the multivalent surface, the interior shells surrounding the core, and the core where the dendrons attached. The three domains are routinely modified to customize the dendrimers for different purposes such as dendritic sensors or drug carriers. The multivalent surface is extremely useful because it contains a large number of reactive sites for high-concentration drug or ligand conjugation. The interior shells are suitable for encapsulating therapeutic agents and protecting the agents from direct interaction with biochemicals or enzymes. Finally, the inner core can be designed to degrade at different rates for different drug release profiles. Most studies on dendrimers are still pre-clinical. An animal study comparing the delivery of free systemic methotrexate with dendrimer-methotrexate conjugates showed ten-fold reduction in tumor size when treated with the conjugates [89].

Figure 2.2 summarizes the different types of nanoparticle for delivering and targeting therapeutic agents to tumors.

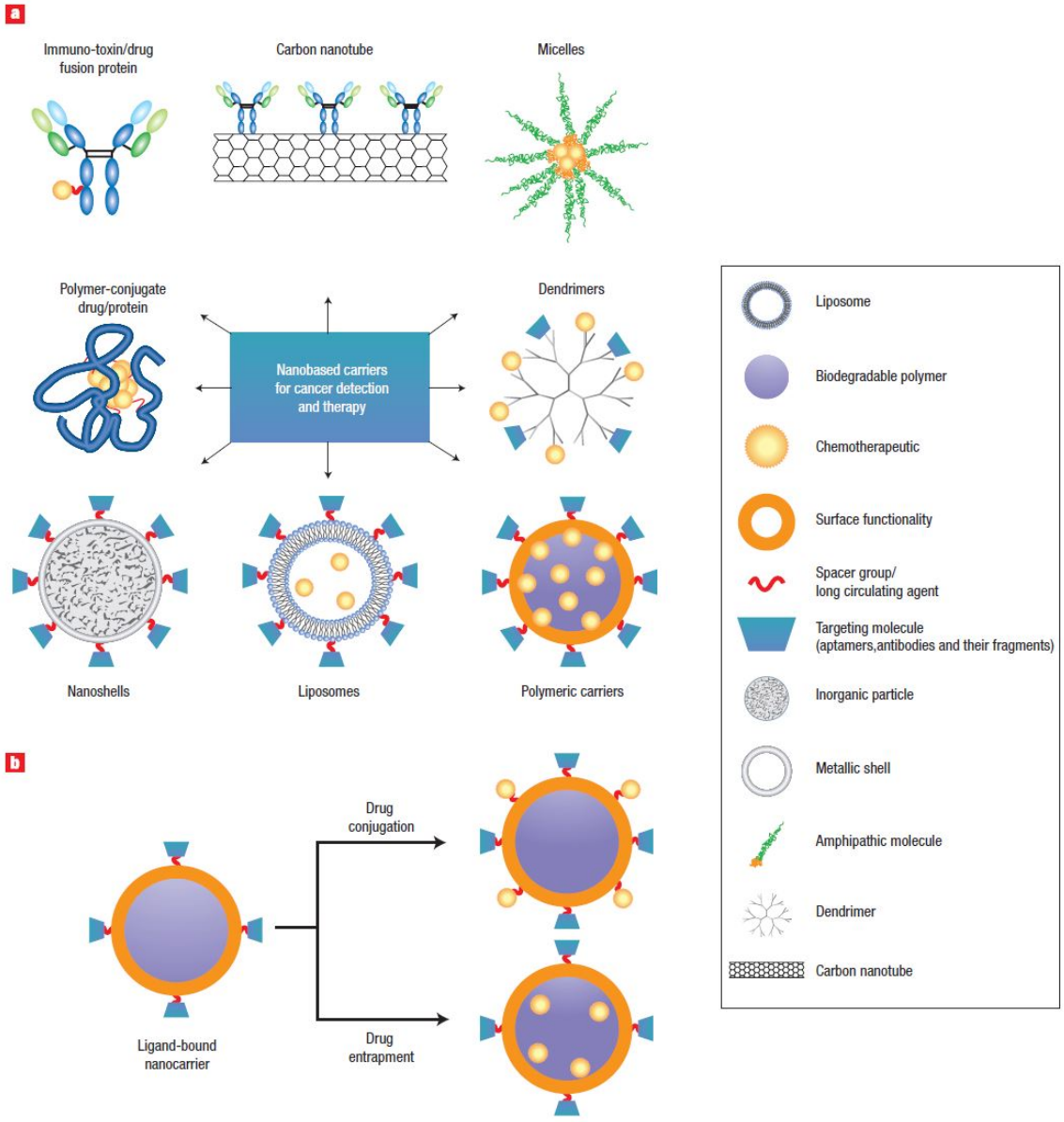

Figure 2.2: A schematic diagram of different types of nanoparticle for delivering and targeting therapeutic agents to tumors. (a) Different types of nanoparticle for delivering therapeutic agents. A typical delivery system design consists of a nanoparticle, a targeting moiety conjugated to the surface of the nanoparticle, and the desired therapeutic agents. (b) Different methods of conjugating and entrapping therapeutic agents. The therapeutic agents could be bound to the surface of the nanoparticle such as in the use of polymer-drug conjugates, or they could be entrapped inside the nanoparticle such as in the use of drug-encapsulated liposomes. Reprinted with permission from [41], copyright 2007 Nature Publishing Group.

2.3 Nanotechnology and its Challenges in Cancer Medicine

The previous section describes the advantages and current state of nanotechnology as applied to cancer medicine. Nanotechnology has been successful in improving the delivery of poorly water-soluble drugs as in the case of Abraxane®, targeting delivery of therapeutic agents to tumor sites via enhanced permeability and retention effect as in the case of Doxil®, and extending the circulation half-life of therapeutic agents while reducing their immunogenicity as in the case of Oncaspar®. In addition, nanoparticles have the potential to deliver intracellular drugs to the cytoplasm via targeting internalizing receptors on cancer cells, co-deliver two or more therapeutic agents for combination therapy, and image sites of drug delivery by combining therapeutic agents with imaging agents [90].

Despite some successes and the potential advantages of applying nanotechnology to cancer medicine, there are still significant clinical challenges to overcome. Specifically, there are three major components in using nanotechnology for the delivery of anti-cancer therapeutic agents that must be addressed for a successful clinical translation, namely, the cancer, the therapeutic agents, and the delivery vehicle (i.e. nanoparticles) [90].

2.3.1 Cancer Biology and Tumor Environment

The first and most important factor for a successful clinical outcome is the understanding of the disease itself. Malignant cancer cells are abnormal cells that divide uncontrollably and have the ability to invade other tissues to cause destruction of surrounding healthy tissues. Cancer cells may also metastasize by disseminating through blood or lymphatic circulation to form secondary tumors in other organs or tissues. Since cancer is a complex disease, it is important to understand the biology of the cancer and its environment in order to design an effective treatment enhanced by nanotechnology. Currently, the three general strategies for killing cancer cells are to remove them by surgery, poison them with chemotherapy drugs or radiotherapy, or starve them with nutrients deprivation. A combination of any two or all three strategies are typically employed in the clinic. Surgery may be successful at treating early stage solid tumors, but is not useful in treating metastatic cancers or unresectable cancers. The conventional chemotherapy drugs such as doxorubicin and paclitaxel taken at the doses necessary to kill cancer cells often have unacceptable off-target toxicities such as nephrotoxicity and cardiotoxicity due to non-ideal biodistribution to normal cells and indiscrimination between healthy and diseased cells. In addition, chemotherapy drugs often cause hypersensitivity and cancer cells to develop multi-drug resistance [14]. Radiotherapy, which utilizes ionizing radiation such as high-energy X-ray, gamma rays, or particle beam radiations to kill tumor tissue by damaging DNA, often has severe side effects and secondary malignancies

since radiation also causes DNA mutation in healthy cells that may lead to cancer [72]. Depriving cancer cells of the nutrients they need to survive and proliferate may also adversely affect normal cells.

With the inadequacy of the current cancer treatment regimes, there are critical needs to detect cancer during its early stage for surgery to be effective, identify unique cancer biomarkers and associated ligands in order to actively and specifically target cancer cells in different disease states with cytotoxic agents, and determine unique cancer nutrient requirements to selectively starve cancer cells while sparing normal cells.

Unfortunately, many of the unique phenomena and features observed in tumor environment or cancer cells do not always translate into successful strategies in the clinic. One example is the enhanced permeability and retention effect (EPR) observed in tumors. As discussed previously, the enhanced permeability of tumor vasculature is the result of the structural disorder of the vasculature associated with rapid angiogenesis within cancer lesions. The retention of nanoparticles within the tumor vasculature is the result of the dysfunctional lymphatic drainage system within the tumor environment. However, recent studies have reported increased osmotic pressure within cancer lesions during later stages of cancer development. The increased pressure may act as a counter force against extravasation and diffusion of therapeutic agents into the tumor [1]. In addition, there is significant heterogeneity within and among tumor types. The openings in the endothelial fenestration in the tumor vasculature vary with different tumor types, locations within a given tumor

type, and stages of a tumor [91]. Furthermore, the blood flow is low and unevenly distributed in tumor tissues, which limit the penetration and distribution of nanoparticles in tumors. Finally, there is a gap in understanding which pre-clinical tumor models recapitulate patients with solid tumors. This gap in knowledge makes it difficult to predict the biodistribution of nanoparticles and to develop modeling tools. As a result, prediction of the behavior of these nanoparticles in human patients is still inaccurate even with large number of *in vitro* and *in vivo* screening tests [29].

There are several solutions proposed to overcome the increased osmotic pressure and different gap sizes in the tumor vasculature. One solution to overcome the increased osmotic pressure within tumor tissue is to increase the blood pressure of the patient during infusion of the nanoparticles with angiotensin-II. In fact, it has been observed in animal models that the blood flow volume in tumor tissue increases when angiotensin-II is infused to achieve higher blood pressure, while the blood flow volume in normal tissue remains consistent regardless of the change in blood pressure [92]. A solution to improve extravasation of nanoparticles into the tumor tissue is to use vasodilators such as an angiotensin-converting enzyme inhibitor to increase the vascular permeability [6] and to design nanoparticles with size much smaller than the largest gap dimension of the endothelial fenestration in the targeted type of tumor vasculature [36]. The lower size limit is suggested to be 5.5 nm in hydrodynamic diameter, which is the cut-off size for rapid clearance by the renal and biliary system [93]. However, reducing the nanoparticle size will reduce the amount of the therapeutic agents a nanoparticle can carry, and increasing the nanoparticle size will increase

its clearance by the MPS. Therefore, the optimal nanoparticle size should be the size that maximizes extravasation into the tumor vasculature and minimizes clearance by the MPS. Although these solutions appear to be promising in pre-clinical studies, more studies are needed to understand if modulating the tumor biology to improve the EPR effect will translate clinically.

Following extravasation into the tumor vasculature, the nanoparticles will need to navigate the dense interstitial matrix, composed of an assembly of collagen, glycosaminoglycans, and proteoglycans that further obstruct the delivery of the drugs throughout the entire tumor in an adequate concentration [94]. Furthermore, the tumor center is typically unperfused, which limits the delivery of therapeutic agents to this region.

The possible solutions to overcome this poor biodistribution of therapeutic agents in the tumor tissue may come from the tumor hostile micro-environment. The tumor micro-environment is plagued with low pH, low partial oxygen pressure, and high concentrations of matrix metalloproteinases (MMPs) [94]. Tumor environment is more acidic (pH 6.5 to 6.8) as compared to healthy tissues (pH 7.4) due to the high metabolic turnover in order to meet their high energy usage for rapid cell proliferation [33]. Increase in aerobic and anaerobic respiration lead to increase in the release of respiratory by-products such as lactic acid and carbonic acid into the tumor environment. Since the lymphatic drainage system is defective as mentioned before, the accumulation of these respiratory by-products results in an acidic pH within the tumor environment. Different types of pH-sensitive liposomes have been developed

to take advantage of this acidic pH environment. Therapeutic agents are designed to be released from the liposomes when the lower pH triggers structural destabilization of the lipid bilayer or hydrolysis of pH-responsive lipids [72]. Regions of the tumor tissue that are far from the blood vessels tend to have low partial oxygen pressure and become hypoxic. The hypoxic region has elevated level of reductive agents that can be exploited by redox-responsive nanoparticles. Nanoparticles may be designed to have disulfide linkages to hold the therapeutic agents within them. When these nanoparticles encounter increased level of glutathione that is characteristic of a hypoxic tumor environment, the disulfide bonds will be cleaved by the glutathione and the therapeutic agents will be released [95]. In addition, the hypoxic regions also have high level of MMPs, particularly MMP-2 and MMP-9, which are effectors of angiogenesis, invasion, and metastasis. Nanoparticles may be designed with a gelatin core loaded with therapeutic agents. Both MMP-2 and MMP-9 are highly efficient enzymes in hydrolyzing gelatin (or denatured collagen). When these nanoparticles encounter the MMPs, therapeutic agents loaded within are released during the degradation of the gelatin. As the size of the nanoparticles decreases with the degradation, the smaller nanoparticles can penetrate further into the tumor tissue and continue to release therapeutic agents within [94]. The pH-sensitive, redox-responsive, and MMP-triggered nanoparticle formulations for delivering therapeutic agents are still in the research stage.

2.3.2 Therapeutic Agents

Once a unique cancer signature is identified, the selection of the therapeutic agents to target the cancer cells will need to address and exploit this difference between healthy and cancer cells. The therapeutic agents may be chemical compounds, nucleic acids such as siRNA or DNA, proteins, or viruses.

The most common cancer therapy is chemotherapy using cytotoxic drugs. They may be administered prior to surgery to shrink the tumor, post-surgery to prevent metastasis, or concurrently with radiotherapy. These drugs are usually alkylating agents, anthracyclines, anti-metabolites, and microtubule inhibitors [96]. Alkylating agents attach an alkyl group to DNA to cause DNA damages and prevent normal DNA replication. A few examples of FDA-approved alkylating agents are cyclophosphamide and mechlorethamine. Platinum-based chemotherapeutic drugs such as cisplatin, carboplatin, and oxaliplatin are considered alkylating-like since they also causes DNA damages by crosslinking them. Anthracyclines intercalate between DNA base pairs thereby inhibiting DNA replication. Daunorubicin and doxorubicin are two examples of FDA-approved anthracyclines. Anti-metabolites interfere with DNA replication either by incorporating chemically altered nucleotides or by depleting the supply of deoxynucleotides needed for DNA replication. Some examples of FDA-approved anti-metabolites are capecitabine, cytarabine, gemcitabine, and pemetrexed. Microtubule inhibitors bind to the protein tubulin in the mitotic spindle and prevent polymerization or depolymerization into the microtubules during

cell mitosis. A few examples of FDA-approved microtubule inhibitors are paclitaxel and vincristine. All these chemotherapeutic agents affect DNA replication or cell division to target fast proliferating cancer cells. Unfortunately, these agents do not distinguish between proliferating cancer cells and healthy cells that divide frequently such as cells in the gastrointestinal tract, bone marrow, testicles, and ovaries [82]. Since the mechanisms of action of these chemotherapeutic drugs are directed at intracellular components, they must be internalized by cancer cells and escape from the endosomes after endocytosis to be effective.

Unfortunately, these chemotherapeutic agents often could not be given at a dose and frequency high enough to be efficacious against cancerous tumor without unacceptable off-target toxicity in patients. Some of the common adverse side effects include myelosuppression (e.g. aplastic anemia, thrombocytopenia, and neutropenia), nausea, diarrhea, vomiting, prone to infection, mucositis, and alopecia [97]. These dose-limiting toxicities interfere with effective treatment because patient adherence to treatment drops and dosage is reduced in response to the adverse side effects of these drugs [98]. Other more serious side effects include cardiotoxicity [97], nephrotoxicity [99], and neurotoxicity [100]. Many established chemotherapeutic drugs such as doxorubicin, camptothecin, paclitaxel, and carboplatin have been developed into second generation drugs using nanoparticle formulations to address issues with the free drugs such as insolubility, toxicity, and low bioavailability [5].

Another class of therapeutic agents for cancer treatment are regulatory nucleic acids involved in RNA interference such as small interfering RNA (siRNA) and

microRNA (miRNA) to silence oncogenes (e.g. c-Myc, c-Raf, or Bcl-2) or to enhance tumor suppressors (e.g. p53 or Fus 1) [7]. A siRNA is a double-stranded RNA that is generally 20 to 25 base-pairs long and possesses complementary sequences to its target mRNA. siRNA requires other proteins to form an active RNA-Induced Silencing Complex (RISC). One strand of the unwound siRNA stays as part of the active RISC, binds to its complementary mRNA, and induces cleavage of the bound mRNA. Cleavage and degradation of the target mRNA prevent downstream translation of the mRNA into proteins [101]. Several siRNA targets have been identified for gene silencing in cancer therapy. For example, the cell cycle effector, cyclin B1, is found to be overexpressed in various cancers such as prostate and lung cancers. siRNAs suppressing cyclin B1 production have shown success in significant tumor reduction in animal models [102]. A miRNA is a small non-coding RNA that is about 22 nucleotides long that is complementary to its target mRNA. Similar to siRNA, miRNA also requires other proteins to form an active microRNA ribonucleoprotein complex (miRNP). When a miRNA is a complete complementarity to its target mRNA, the miRNP induces cleavage of the mRNA, leading to degradation of the mRNA and prevention of the translation of the mRNA into proteins. For partial complementarity, the miRNP suppresses translation of the mRNA. miRNA-24, for example, has been found to inhibit cancer cell proliferation by targeting oncogenes such as c-Myc, E2F1, and other transcription factor genes. Conversely, anti-sense oligonucleotides to silence oncogenic miRNA-21 leads to pro-apoptotic and anti-proliferative responses in cell cultures and tumor reduction in animal models [103]. There are a few chal-

lenges involving delivery of siRNA or miRNA to cancer cells. First, ribonucleic acids are rapidly degraded by ribonucleases in circulation. Second, these ribonucleic acids acts on cytoplasmic components, so they must be internalized by the target cell. Nanoparticles may be suited as ribonucleic acids delivery system if they can encapsulate them to protect them from ribonucleases, target cancer cells to internalize them, and escape endosomal vesicle to deliver the ribonucleic acids into the cytoplasm [104]. There are no FDA-approved cancer therapy based on regulatory nucleic acids yet.

The next class of therapeutic agents are proteins. Therapeutic proteins for treating cancers are generally enzymes. Enzymes have two unique features that distinguish them from other types of therapeutic agents. First, enzymes have high affinity and specificity for their target substrates. Second, the catalytic feature of enzymes allows them to convert multiple target molecules to products. Because of their specificity and high potency, therapeutic enzymes have become attractive therapeutic agents for treating a wide range of diseases [105]. Since cancers are defined by their uncontrolled proliferation, one major strategy for suppressing the growth and inducing apoptosis of cancer cells is depleting their nutrients. Certain cancers are auxotrophic for specific non-essential amino acids. Acute lymphoblastic leukemia, for example, is auxotrophic for asparagine because of a lack of asparagine synthetase activity. Asparagine synthetase catalyzes the synthesis of asparagine from aspartate. Oncaspar®, an enzyme asparaginase conjugated to poly(ethylene glycol), is an FDA-approved therapeutic enzyme to treat acute lymphoblastic leukemia by

depleting asparagine [105]. Poly(ethylene glycol)-conjugated arginine deiminase is another therapeutic enzyme in clinical trials to treat melanoma and hepatocellular carcinomas by depleting arginine. Some melanoma and hepatocellular carcinomas are auxotrophic for arginine because of a lack of argininosuccinate synthetase activity [106]. Argininosuccinate synthetase is an enzyme that catalyzes the synthesis of argininosuccinate from citrulline and aspartate. The transformation of citrulline into argininosuccinate is the rate-limiting step in arginine synthesis. The major challenges with enzyme therapeutics are their immunogenicity due to their derivation from non-human sources such as bacteria and degradation in blood due to the presence of proteases. Nanoparticles may be designed to protect therapeutic enzymes from the immune system and proteases.

Virus is the last type of therapeutic agents use for cancer treatment. Viruses may be engineered to produce therapeutic proteins selectively in cancer cells. For example, the oncolytic immunotherapy talimogene laherparepvec (IMLYGIC®) is the first FDA-approved oncolytic viral therapy. It is approved for the local treatment of unresectable cutaneous, subcutaneous, and nodal lesions in patients with melanoma. IMLYGIC® is a herpes simplex virus type-1 genetically engineered to selectively replicate within cancer cells and produce granulocyte macrophage colony-stimulating factor (GM-CSF) to enhance systemic anti-tumor immune responses [107]. In addition, some pox viruses preferentially replicate in cancer cells. An engineered vaccinia virus currently in Phase I/II clinical trial, JX-594, is designed to selectively replicate in cancer cells and kill them by activating replication-dependent cell lysis pathway

and expressing GM-CSF to stimulate immunological anti-tumoral response [108]. However, administration of oncolytic virus is mostly restricted to intratumoral delivery. For treatment of metastatic cancer, systemic delivery is required. Nanotechnology may provide the solution to minimize sequestration of oncolytic virus in the liver and spleen, evade neutralization by opsonization, target viruses to the endothelial cells lining tumor vasculature, and selectively enhance vessel permeability [109].

The methods for loading therapeutic agents in a nanoparticle will need to be optimized to be compatible with the therapeutic agents. Understanding the properties of the therapeutic agents is important for optimizing encapsulation efficiency and designing the desirable release profile [33]. Different loading methods include covalent conjugation, encapsulation, absorption, or suspension in the nanoparticle matrix [72]. The appropriate method to achieve high loading efficiency of therapeutic agents in a nanoparticles depends on the properties of the therapeutic agents and the nanoparticles.

Therapeutic agents may be classified as hydrophobic or hydrophilic. Hydrophobic drugs such as paclitaxel are challenging to deliver in circulation. Since they have poor water solubility, they aggregate upon intravenous administration into the aqueous environment of blood circulation. These drug aggregates are not able to penetrate cell membranes to reach their intracellular targets. Large aggregates may lead to embolisms [110]. The issue with aggregation in blood may be solved by using amphiphilic polymer. The lipophilic end of the polymer will interact with the hydrophobic drugs to form the core of the nanoparticles, while the

hydrophilic end of the polymer will interact with the surrounding aqueous environment. By using nanoparticles to deliver poorly soluble drugs, the bioavailability of the drug is significantly increased [33]. Although hydrophilic therapeutic agents such as proteins, peptides, nucleic acids and some small molecules are less likely to aggregate in blood, they may have other stability issues. Peptides and nucleic acids may be degraded in the proteolytic and hydrolytic blood environment. Encapsulating therapeutic agents within nanoparticles may be able to protect and shield them from their harsh environment, improve their cellular uptake, and evade clearance *in vivo*. At its isoelectric point, a therapeutic protein is at its minimum solubility and maximum absorption to a nanoparticle, leading to the highest loading efficiency. Another challenge some hydrophilic therapeutic agents may face is their high charge density. Nucleic acids, for examples, are negatively charged due to their phosphate backbone. Negatively charged macromolecules usually have poor cellular uptake and rapid clearance by the MPS. Since the target of nucleic acid-based therapeutics are intracellular, poor cellular uptake renders the therapy ineffective even if they survived clearance. Cationic polymers or liposomes may be utilized to encapsulate these negatively charged nucleic acids via electrostatic interactions to increase loading efficiency. Similarly, therapeutic small molecules are usually charged; therefore, the use of electrostatic interactions to attract the small molecules to oppositely charged nanoparticle material can increase the loading efficiency.

2.3.3 Nanoparticles as Delivery Vehicle

Finally, with the therapeutic agents selected to target a specific signature of the cancer of interest, the delivery vehicle in the form of a nanoparticle will need to be developed to meet the needs of the therapy. The considerations in designing the delivery nanoparticles are the method of loading the therapeutic agents of interest, the targeting strategy for delivering the therapeutic agents to the site of interest, and the design of the release profile of the therapeutic agents. In addition, the physiochemical properties of the nanoparticle play important roles in their ability to reach their targets and their interactions with cancer cells.

There are various methods for loading therapeutic agents onto a nanoparticle to create therapeutic nanoparticles. Therapeutic agents may be loaded on the surface of the nanoparticles by adsorption or covalent bonds, suspended within the nanoparticles, or encapsulated inside the nanoparticles [5].

The therapeutic agents may be encapsulated inside polymeric nanoparticles using the double emulsion and solvent evaporation process. This process requires the therapeutic agents to be first dissolved in an aqueous phase and the polymer in an organic solvent separately. Then the two phases are emulsified to form the first water-in-oil emulsion. Next, the first emulsion is mixed with a second aqueous phase with dissolved surfactant to form the second water-in-oil-in-water emulsion. The final evaporation step involves the organic solvent diffusing out from the polymer phase and evaporating from the aqueous phase to form the final polymeric nanoparticles

loaded with the therapeutic agents [111].

Next, the nanoparticle may need to have active targeting moieties for cellular uptake if the targets of the therapeutic agents are intracellular. In some cases, the site of action of the therapeutic agents may be extracellular and requires the nanoparticles to serve as a depot for the therapeutic agents within the tumor environment. In other cases, the therapeutic agents may need to be delivered systemically in a prolonged manner. The design of the delivery vehicle will need to be adjusted to meet the requirements of the different type of delivery mechanisms.

If the target of a therapeutic agent is located intracellularly, then active targeting may be necessary. Active targeting increases the affinity of nanoparticles for cancer cells, which leads to increased residence time of the nanoparticles on the cancer cells and facilitates the nanoparticles to be internalized by the cancer cells. There are five main pathways identified for cellular internalization of nanoparticles: phagocytosis, macropinocytosis, caveolar-mediate endocytosis, clathrin-mediated endocytosis, and clathrin-independent and caveolar-independent endocytosis. A schematic diagram of the different mechanisms of cellular internalization of nanoparticles is shown in Figure 2.3. The pathway activated by a cell is dependent on the cell type and the size and surface properties of the nanoparticles. After internalization, the nanoparticles are trafficked through the endolysosomal network to other cytosolic organelles that use hydrolytic enzymes to degrade their contents [33].

Phagocytosis is primarily carried out by macrophages, monocytes, and neutrophils to clear large pathogens (e.g. bacteria or yeast), large debris (e.g. remnant

of apoptotic cells), or other foreign objects (e.g. nanoparticles) larger than 100 nm in size. Antibodies bound to surface antigens on pathogens or other foreign objects are recognized by the Fc receptors on macrophages. Phosphatidylserine on the surface of damaged or apoptotic cells are recognized by phosphatidylserine receptors on macrophages. Complement proteins on the surface of nanoparticles are recognized by complement receptors on macrophages. Binding of the receptors to the antibodies, phosphatidylserine, or complement proteins initiates different signaling cascades that eventually triggers actin re-arrangements to form a protrusion of the macrophage membrane around the object that leads to engulfment of the object into a phagosome. Phagosomes contain acids, free oxygen radicals, and hydrolases to degrade their contents [112]. Nanoparticles larger than 100 nm have been reported to be internalized by phagocytosis [33].

Macropinocytosis is also known as cell drinking because the invagination of the cell membrane generates a large vesicle between 0.5 and 5 μm in size that is filled with a large volume of extracellular fluid and other substances and small particles present in the fluid to be internalized. This process occurs in all cell types and appears to be stimulated by growth factors [112]. A wide range of nanoparticle sizes have been reported to be internalized by macropinocytosis [33].

Caveolar-mediated endocytosis is first observed in endothelial cells to mediate transcellular transport of serum proteins from the blood into tissues across the endothelial cell layer. Caveolar-mediated endocytosis is now known to occur in many cell types. Caveolar are flask-shaped invaginations of the plasma membrane that

slowly internalized macromolecules to form a vesicles around 60 nm in size with little fluid-phase volume [112]. Ligands such as folic acid, albumin, and cholesterol have been reported to induce caveolar-mediated endocytosis [113]. Anionic dendrimers have also been reported to be internalized by caveolar-mediated endocytosis [33].

Clathrin-mediated endocytosis is also known as receptor-mediated endocytosis because it is initiated when surface receptors on the plasma membrane recognize the specific ligands on the nanoparticles to induce the inward budding of plasma membrane vesicles to internalize the nanoparticles. These vesicles are usually about 120 nm in size and coated with a protein complex associated with the cytosolic protein clathrin [112]. Charged mesoporous silica nanoparticles have been reported to be internalized by clathrin-mediated endocytosis [33].

Clathrin-independent endocytosis and caveolar-independent endocytosis are the most poorly understood types of endocytosis. An example of clathrin-independent and caveolar-independent endocytosis is the IL-2 receptor-mediated endocytosis. It has been reported that concentration of IL-2 receptors on a cell membrane initiates endocytosis via small non-coated invaginations and formation of endocytic vesicles ranging from 50 to 100 nm in size. Similar endocytosis process is observed with concentrated epidermal growth factor receptors on cell membranes [114].

Once internalized by the target cells, the nanoparticles must be able to escape from the endolysosomal network in order to enter the cytosol and release the therapeutic agents to act on their appropriate targets in the cytoplasm. Several strategies have been developed for the endocytosed nanoparticles to escape the endosomes or

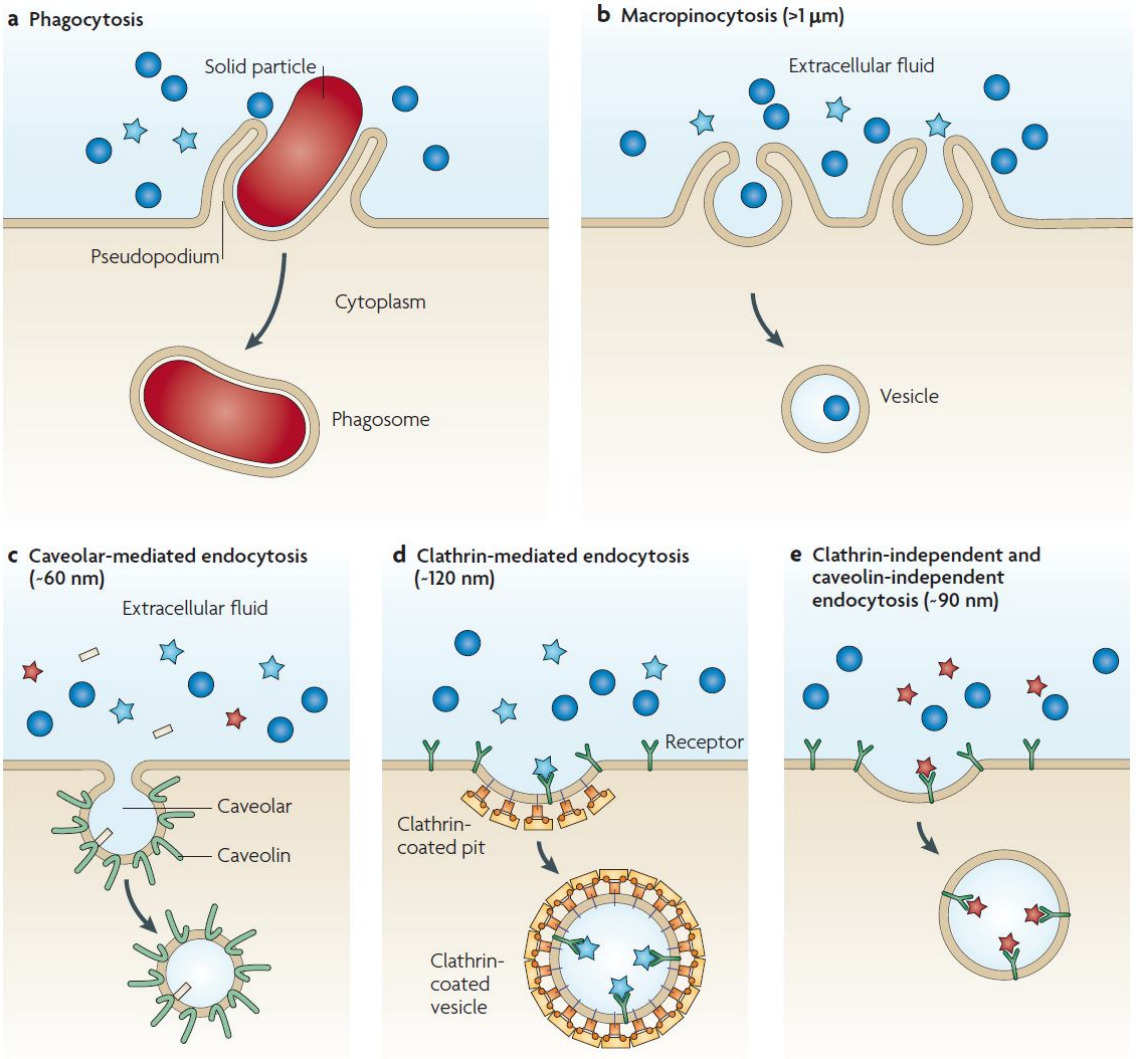

Figure 2.3: A schematic diagram of different mechanisms of cellular internalization of nanoparticles. (a) Phagocytosis (b) Macropinocytosis (c) Caveolar-mediated endocytosis (d) Clathrin-mediated endocytosis (e) Clathrin-independent and caveolin-independent endocytosis. Different sizes of nanoparticles are represented by blue circles (>1 μm), blue stars (about 120 nm), red stars (about 90 nm), and yellow rods (about 60 nm). Reprinted with permission from [113], copyright 2010 Nature Publishing Group.

lysosomes. It is reported that nanoparticles coated with polycations are able to sequester the protons pumped into an endosome that are normally intended to create an acidic environment. As more protons are pumped into the endosome, water

molecules begins to accumulate. Eventually the swelling of the endosome leads to its rupture and the escape of the therapeutic agents into the cytoplasm [115]. Another strategy for nanoparticles to escape the endolysosomes is to use pH-sensitive peptides designed to disrupt the endolysosomal membranes. GALA is a pH-sensitive peptides composed of 30 amino acids with repeating sequence of glutamate-alanine-leucine-alanine. When the peptide encounters the acidic environment in an endosome, the peptide loses its negative charges due to protonation. The drop in charge causes a conformational change of the peptide from random coil to amphipathic α-helix that binds to and disrupts the endosomal membrane [116].

The major challenge for active targeting via ligand-antigen interaction is the requirement that the ligands on the nanoparticles be in close vicinity of the antigens they are targeting. The probability of the ligands on the nanoparticles encountering their target antigens increases with the blood circulation time of the nanoparticles. Therefore, actively targeted nanoparticles will need to have extended blood circulation time.

Targeting ligands may be attached to nanoparticles either by physical adsorption or covalent attachment. Covalent attachment is usually the preferred method since nanoparticles are more likely to shed ligands that are adsorbed by electrostatic or hydrophobic/hydrophilic interactions. There are generally two strategies to conjugate targeting ligands to the surface of nanoparticles. Pre-conjugation is more useful when the targeting ligands are small molecules, peptides, or aptamers. It usually involves organic solvents during conjugation of the targeting ligands to monomers

such as lipids or polymers that are the building blocks of the final liposomes or polymeric nanoparticles. The benefits of pre-conjugation is the ability to synthesize nanoparticles with a one-step process that reduces side reactions. Post-conjugation is preferred when the targeting ligands are proteins with complex structures. In this case, targeting ligands are conjugated after the nanoparticles are synthesized. This process is compatible with all types of targeting ligands since organic solvents are not used during conjugation [6]. Nanoparticle surface expressing maleimide groups may react with proteins expressing thiol groups such as cysteine to form a stable thioether bond. Alternatively, nanoparticles surface expressing carboxylic groups may react with proteins expressing amine groups such as lysine using N-hydroxysuccinimide and 1-Ethyl-3-(3-dimethylaminopropyl) carbodiimide hydrochloride to form a stable amide bond. Recently, a bioconjugation method called "clicked chemistry" was developed to react alkyne groups on peptides or small molecules with azide groups on the nanoparticle surface in a single reaction step without side reactions.

The next issue with active targeting with ligands is the optimization of the ligand density in order to bind targeted cancer cell with high efficiency and also avoid rapid clearance by the MPS [7]. Binding of a ligand on a nanoparticle to its receptor on a targeted cell enhances the subsequent binding of its surrounding ligands to other receptors nearby [117]. This process causes clustering and local concentration of receptors on the cell, which induces the cell membrane to wrap around the nanoparticle and initiates internalization of the nanoparticle by the cell [118]. In general, increasing ligand density on a nanoparticle usually improves uptake of the

nanoparticle by targeted cells. However, if the ligands are charged molecules, then a high ligand density may change the surface charge of the nanoparticles such that the nanoparticles may become recognized and cleared by the MPS [6]. Therefore the ligand density must be balanced to maximize binding to targeted cells and minimize clearance by the liver and spleen.

Finally, the therapeutic agents may be released through controlled release by diffusion, erosion, or environment-triggered release. Regardless of the strategies for targeting and release, the first requirement of nanoparticles is the ability to circulate for an extended period of time. More studies will need to be conducted to understand the influences of size, shape, surface properties, material properties, delivery method, and active targeting of nanoparticles have on the delivery of the nanoparticles. Major focuses have been placed on developing strategies to avoid premature clearance of the nanoparticles by the MPS, while preventing accumulation of the nanoparticles through eventual degradation and excretion of the nanoparticles. Although all materials use in research and in clinic are biocompatible, it is still unknown if these materials persist *in vivo* and produce longer-term toxicities [42].

2.4 Nanoparticles and Circulation

The importance of long-circulating nanoparticles has driven the nanotechnology field to develop different strategies for nanoparticles to avoid capture by immune cells, endothelial cells lining the wall of blood vessels, and other mechanisms re-

moving them from the circulation. In order for a strategy to be successful, the physiological and biological barriers challenging the nanoparticle circulation must first be understood. Therefore, the main biological systems responsible for removing nanoparticles from circulation and the mechanisms by which the nanoparticles are removed are first described in this section. Next, the nanoparticle properties that have the most influence on circulation are discussed.

2.4.1 The Complement System

There is strong experimental and clinical evidence indicating that some acute allergic reactions following the administration of nanoparticles are associated with the activation of the complement system [119]. The complement system is part of the innate immune system with the biological functions of immunological protection and homeostasis. Therefore, the complement system is used to recognize foreign particles, macromolecules, and microorganisms for elimination and damaged or altered "self" components for clearance through three main processes. The first process is through lysis of foreign cells (e.g. bacteria) or host cells (e.g. tumor cells or apoptotic cells). The second process is through the production of mediators that are involved in inflammation and attraction of neutrophils. The last process is through opsonization, which is the coating of foreign entities or host components with serum molecules such as mannose-binding proteins, complement components, or antibodies. A summary of the different pathways leading to the activating of the complement system is shown in Figure 2.4.

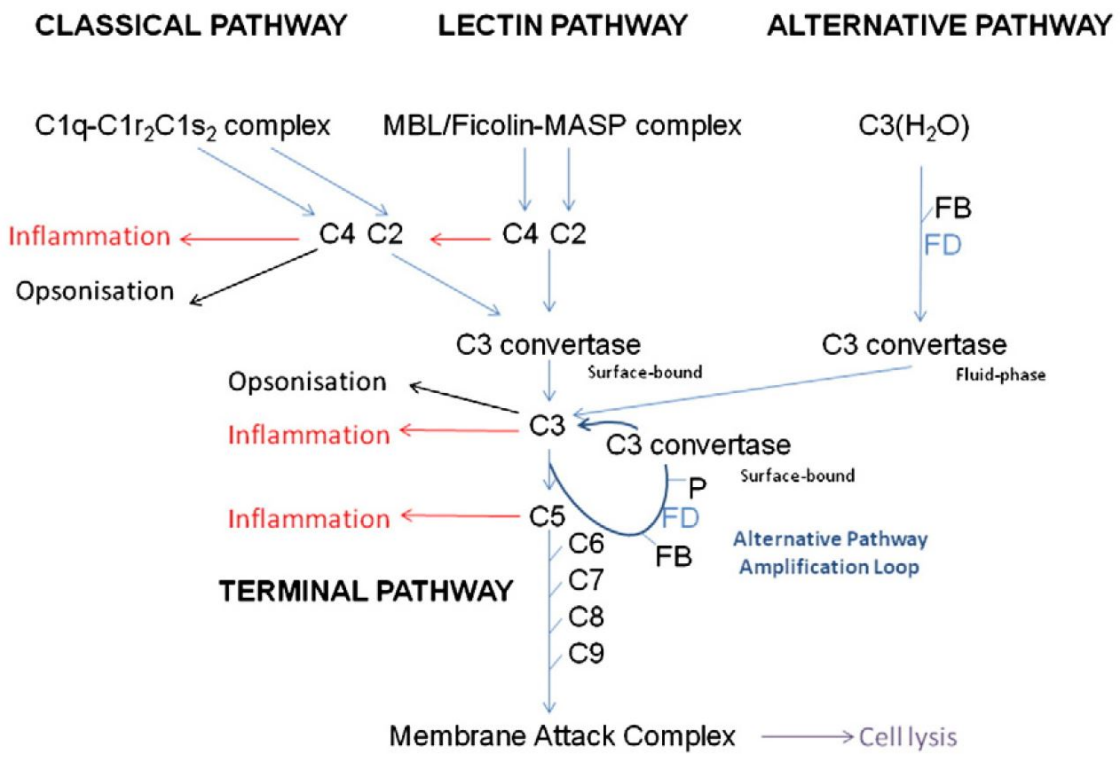

Figure 2.4: The complement system consists of three activation pathways: classical, alternative, and lectin. All pathways lead to the terminal pathway, causing cell lysis and inflammation. Reprinted with permission from [120], copyright 2011 Elsevier.

The complement system consists of a set of 35 to 40 proteins and glycoproteins that are present in blood plasma or on cell surfaces in inactive forms. There are three pathways to activate the complement system: the classical pathway, the alternative pathway, and the lectin pathway. Regardless of the pathway, the initial steps of complement system activation involve the cleavage of an inactive protein into two fragments: a smaller fragment and a larger fragment. The larger fragment is capable of cleaving other proteins to initiate a cascade of protein activation. Since one activated protein is capable of cleaving and activating many molecules, the cascade activation of complement proteins is amplified.

The classical pathway for activating the complement system is initiated by the attachment of C1q to an antibody-antigen complex. The intact C1 is inactive and composed of C1q, C1r, and C1s. The C1q molecule consists of six identical globular heads extending from a central stalk. The globular heads bind to the complement-binding regions on the heavy chains of IgG and IgM antibodies. For IgG to bind to C1q, IgG must have bound antigen to have the proper configuration to bind to C1q. For IgM to bind to C1q, IgM must also have bound antigen to have access to C1q binding site. When two or more of the globular heads of C1q bind to IgG or IgM antibodies, the serine protease proenzyme C1r is activated. Activated C1r is a protease that can cleave and activate another serine protease proenzyme C1s. Activated C1s is a protease that cleaves C4 into C4a (smaller fragment) and C4b (larger fragment). C4b contains an exposed thioester group that can react with hydroxyl groups on any surface to bind to it. C2 then binds to bound C4b. C2 is then cleaved to generate C2a (larger fragment, an exception to the naming nomenclature) and C2b (smaller fragment), where the C2b fragment remains bound to C4b. The C4bC2b complex is known as the classical pathway C3 convertase, which is capable of cleaving C3 into C3a (smaller fragment) and C3b (larger fragment). The C3b fragment may activate the alternative pathway, which is described next, or bind to the C4bC2b complex to form the C4bC2bC3b complex, which is known as the classical pathway C5 convertase. The C5 convertase in turn cleaves C5 into C5a and C5b to initiate the final steps in activating the complement system which will be described later. Since the classical pathway to activate the complement system requires the specific recognition

of antigen by antibodies, it is a more specific pathway. Finally, additional structures such as C-reactive proteins, apoptotic bodies, and serum amyloid P may also activate this pathway [121], [122], [123], [124], [125], [126]. A schematic diagram of the classical pathway for activating the complement system is shown in Figure 2.5.

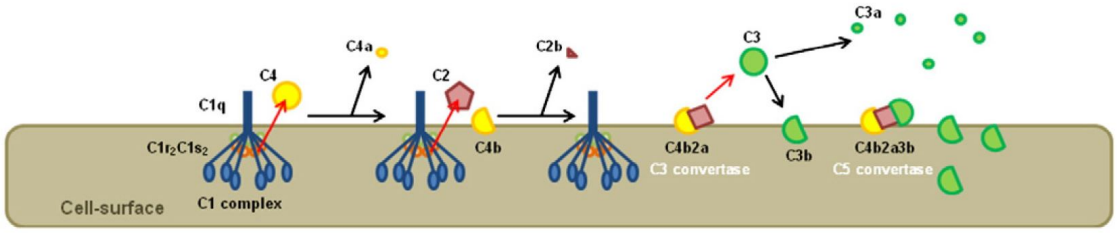

Figure 2.5: A schematic diagram of the classical pathway for activating the complement system. First, C1q of the circulating C1 complex binds to a target (shown as the cell surface) and activates C1r and C1s. Next, C1s cleaves C4 and C2 in circulation to generate C4b and C2a, which form the C3 convertase (i.e. C4b2a complex). Finally, C3 convertase cleaves circulating C3 to generate C3b, which form the C5 convertase (i.e. C4b2a3b complex). Reprinted with permission from [120], copyright 2011 Elsevier.

The alternative pathway for activating the complement system is initiated by the attachment of C3b to a microbial cell surface. The intact C3 is inactive because its reactive thioester domain on C3b is protected by hydrophobic residues to prevent the hydrolysis of the thioester group. This inactive configuration is stabilized by the anaphylatoxin domain of C3. When the anaphylatoxin domain is cleaved to release C3a (smaller fragment) and C3b (larger fragment), the thioester group is exposed on C3b. The exposure of the thioester group results in a configurational change in C3b and facilitates the binding of C3b to a cell surface such as a bacterial cell surface. If there is no foreign cell surface to bind, the thioester group becomes hydrolyzed which inactivates C3b. There is a low-level of spontaneous cleavage of C3 into C3a and

C3b in the plasma to maintain a surveillance for microbes and other foreign particles. Once C3b is attached to a foreign cell or particle surface, the plasma protein Factor B binds to C3b. Factor B is then cleaved by Factor D to generate Ba and Bb fragments, where the Bb fragment remains bound to C3b and the Ba fragment is released. The C3b and Bb complex is stabilized by the plasma protein properdin. This stabilized complex is known as the alternative pathway C3 convertase, which is capable of cleaving more C3 into C3a and C3b to amplify the alternative pathway cascade. More formation of C3b results in the formation of the C3bBbC3b complex, which is known as the alternative pathway C5 convertase. The C5 convertase in turn cleaves C5 into C5a and C5b to initiate the final steps in activating the complement system. Since the alternative pathway to activate the complement system does not require specific recognition of antigen, it is considered a part of the innate immunity. Without antigen recognition, the alternative pathway may lead to the binding of not just foreign cells, but also host cells. This undesirable binding of host cells for clearance is prevented by rapid intervention of regulatory proteins on the surface of host cells to protect them from unnecessary attack. Therefore, the alternative pathway is able to attack foreign cells such as bacteria, fungi, and virus. It is also able to attack altered "host" cells such as tumor cells. Finally, additional structures such as IgA immune complexes and endotoxin may also activate this pathway [121], [122], [123], [124], [125], [126]. A schematic diagram of the alternative pathway for activating the complement system is shown in Figure 2.6.

The lectin pathway is identical to the classical pathway with the exception

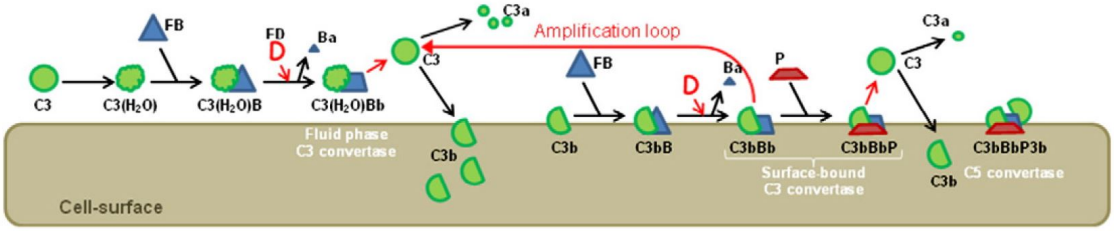

Figure 2.6: A schematic diagram of the alternative pathway for activating the complement system. The circulating C3 is cleaved in the plasma into C3a and C3b. C3b then binds to the surface of a foreign cell. Plasma protein Factor B then binds to C3b and gets cleaved by Factor D to generate Bb, which forms C3 convertase (i.e. C3bBb complex). C3bBb is capable of cleaving more C3 to form more C3bBb, which are stabilized by binding to properdin to form C3bBbP complexes. Finally, C3bBbP cleaves C3 to generate C3b, which form C5 convertase (i.e. C3bBbP3b complex). Reprinted with permission from [120], copyright 2011 Elsevier.

of the initiating steps. The first step in the activation of complement via the lectin pathway is the binding for a plasma lectin called the mannose-binding lectin (MBL) to polysaccharides on microbial cell surfaces. Because the structure of the MBL is very similar to C1q, it can associate with C1r and C1s. Therefore, the binding of MBL to a microbe can activate C1r and C1s in a cascading manner. In additional, MBL also interacts with MBL-associated serine proteases (MASPs), which similar to C1r and C1s, can cleave C4 to generate C4a and C4b to continue the process to form C5 convertase. The C5 convertase in turn cleaves C5 into C5a and C5b to initiate the final steps in activating the complement system. Based on the recognition by the MBL, the lectin pathway is capable of attacking microbes with terminal mannose groups. Finally, additional structures such as serum ficolins, which are lectins that bind to N-acetylglucosamine, may also activate this pathway [121], [122], [123], [124], [125], [126].

The final steps of all three pathways converge to the cleavage of C5 into C5a (smaller fragment) and C5b (larger fragment). The C5b fragment remains bound to the microbe surface. C5b sequentially binds to C6, C7, C8, and C9 to form a complex which is an active membrane attack complex (MAC). C9 polymerizes around the complex to form pores in the cell membranes. These pores may cause cell death through osmotic rupture or the lysis process. The insertion of MAC into phagocyte cell membranes can lead to the production of inflammatory mediators, including reactive oxygen species and prostaglandins, to active phagocytes [121], [122], [123], [124], [125], [126]. A schematic diagram of the terminal pathway for activating the complement system is shown in Figure 2.7.

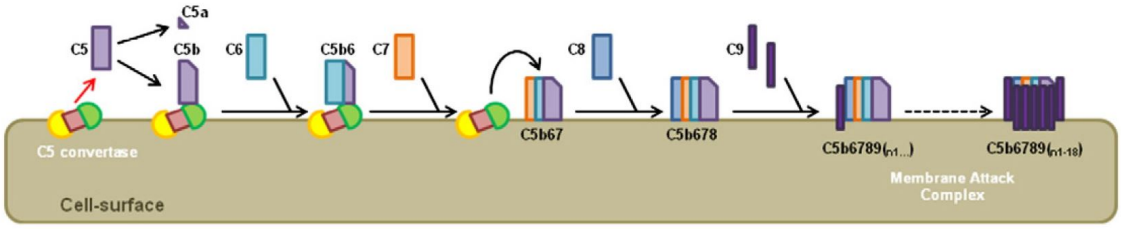

Figure 2.7: A schematic diagram of the terminal pathway for activating the complement system. The C5 convertase formed via classical, alternative, or lectin pathway cleaves C5 to generate C5b, which stays bound to the cell surface. C5b binds to C6, C7, C8, and C9 to form an active membrane attack complex (MAC). C9 polymerizes around the complex to form pores in the cell membrane, leading to cell lysis. Reprinted with permission from [120], copyright 2011 Elsevier.

2.4.2 The Mononuclear Phagocytic System

The mononuclear phagocytic system (MPS) is part of the immune system and is consist of a family of macrophages derived from monocytes in blood. Macrophages

have phagocytic ability and specialize in degradation of proteins and removal of dead cells, tissue debris, and foreign particles [127]. There are four main functions of macrophages. The first type of macrophages produce cytokines, chemotactic factors, and other molecules involved in inflammation and antigen processing and presentation. These macrophages are located in connective tissues, lymphoid organs, lungs, bone marrow, pleural and peritoneal cavities, liver, and central nervous system. The macrophages residing in liver and the central nervous system are also known as Kupffer cells and microglial cells, respectively. Another type of macrophages responsible for antigen processing and presentation are the Langerhans cells located in the skin epidermis and the dendritic cells located in the lymph nodes and spleen. The third kind of macrophages located in the bone are responsible for localized digestion of bone marrow. The fourth and final type of macrophages are the multinuclear giant cells, which are several macrophages fused together, located in the connective tissue during disease to segregate and digest foreign entities [127].

Since the macrophages are the primary cells removing nanoparticles from circulation, it is important to understand the clearance mechanism in order to engineer better nanoparticles designed to evade them. The two most important macrophages responsible for majority of the nanoparticle clearance are the Kupffer cells in the liver and the splenic macrophages. The function and mechanism of clearance by these macrophages can be elucidated by the structure of the organs they are located and the contact route with the nanoparticles, which is usually through blood.

The Kupffer cells are located in the liver. The smallest histological unit of the

liver is called a lobule. The smallest functional unit of the liver is called an acinus. Each acinus of the liver consists of the hepatic triad, which are branches of the portal vein, the hepatic artery, and the bile ducts. Blood enters via a series of sinusoids, which are lined with fenestrated endothelial cells supported by a loose connective tissue layer known as the space of Disse. Hepatocytes are sandwiched between two endothelium layers [128]. Sinusoids are low-resistance cavities that blood from the portal veins and hepatic arteries enter and drain into the central vein [129], [130]. The central veins of the lobules of the liver drain into the hepatic veins [131]. The liver macrophages known as Kupffer cells reside in the sinusoidal lumen. Stellate cells reside in the space of Disse. A schematic of a liver lobule [132] and acinus [133] are shown in Figure 2.8.

The portal vein supplies 75% of the blood entering the liver. The portal vein is formed from merging of the splenic mesenteric vein, superior mesenteric vein, and left gastric vein, which drains blood from the spleen, the small intestines, and the stomach, respectively [134]. Since blood from the large intestine also drained into the splenic mesenteric vein via the inferior mesentery vein, so the portal vein also indirectly receives blood from the large intestine [131]. Since the liver receives blood from the gastrointestinal tract, it is the initial site when ingested nutrients and other substances such as drugs and bacterial metabolites are processed by the body. Drugs administered via intravenous and intraperitoneal routes are also indirectly or directly transported by the blood to the liver for processing. Therefore, the liver is the key organ for processing useful substances while detoxifying harmful substances [129].

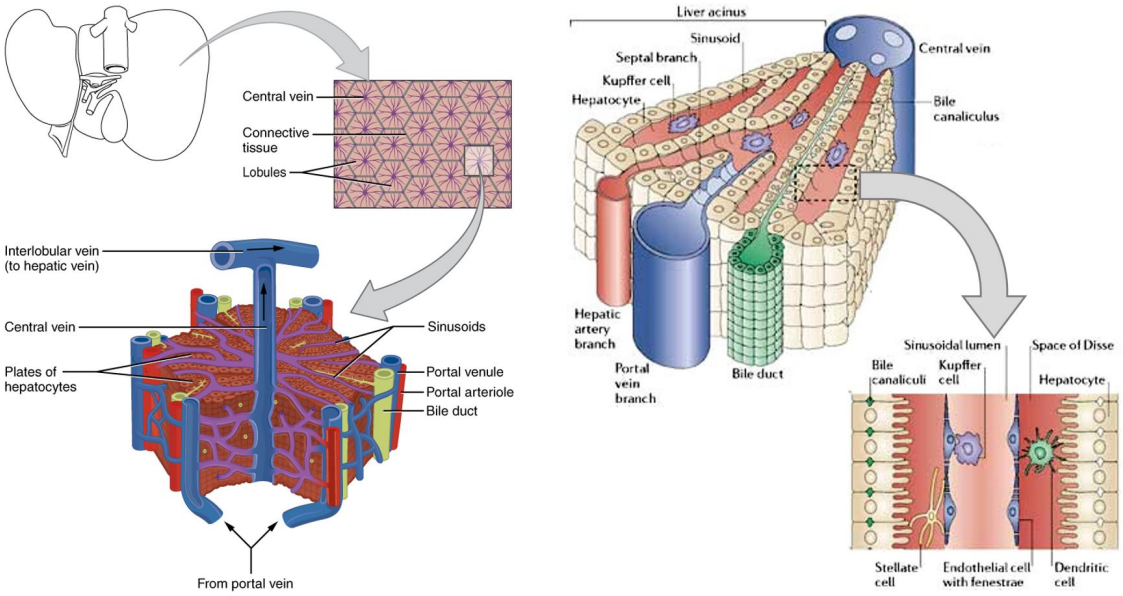

Figure 2.8: Schematic diagrams of the liver lobule (*left*) and the liver acinus (*right*). A lobule is the smallest histological unit of the liver that is made up of six acini. An acinus is the smallest functional unit of the liver that consists of the portal vein, the hepatic artery, and the bile duct. Reprinted with permission from [133], copyright 2006 Nature Publishing Group.

The elimination of harmful or foreign bioactive substances by the liver is achieved with Kupffer cells and hepatocytes. Kupffer cells are highly effective phagocytes that resides in the sinusoids of the liver lobules where they are exposed to almost all of the blood flow into the liver. These cells serve important functions such as filtering, removing, and processing antigens that arrive from the gastrointestinal tract or systemic circulation. Kupffer cells also express receptors on their surfaces for altered or foreign protein. For example, the Fc immunoglobulin receptors on a Kupffer cell can be used to initiate phagocytosis of foreign proteins or microorganisms that have been opsonized with antibodies [129]. Hepatocytes line the sinusoids of the liver lobules and express large quantities of cytochrome P450 and other en-

zymes that convert drugs and toxins into inactive and less lipophilic metabolites for excretion via the biliary system [128].

The endothelial cells that lined the sinusoids are perforated by large intracellular pores know as fenestrae. These fenestrae are 100 to 200 nm in diameter and are designed for large foreign or "self" macromolecules and nanoparticles to be transported out of the blood while allowing larger cells such as red blood cells, white blood cells, and platelets to remain in the circulation. To increase endothelial permeability to solutes from the blood, the endothelial cells are not supported with a basement membrane. Both features of the sinusoidal endothelium are to ensure minimal barrier to the flow of macromolecules from the circulation via forced sieving. Force sieving occurs when fast-moving blood cells physically force the macromolecules against the endothelial fenestrae and force them into the space of Disse towards the hepatocytes for processing [129].

The spleen has multiple functions in red blood cell clearance, innate and adaptive immunity, and blood volume regulation [130]. Structurally, the spleen is composed of three components: the red pulp, the white pulp, and the marginal zone [135]. The splenic red pulp contains dendritic cells and macrophages that are responsible for removing senescent or damaged red blood cells and other foreign substances [136]. The splenic white pulp consists of secondary lymphoid tissue where immune cells such as T cells, B cells, and dendritic cells can interact with one and another to activate adaptive immune responses to antigens in circulation. The marginal zone surrounds the white pulp and merges with the red pulp. Antigens in blood are con-

centrated in this zone for presentation to the splenic lymphocytes [135]. In short, the spleen serves as a filter of red blood cells, antigens, and antigen-coated particles from the blood [137]. In addition, the spleen is also used for storage and rapid release of monocytes to participate in wound healing and inflammation regulation [138]. A schematic diagram of the structure of the spleen is shown in Figure 2.9.

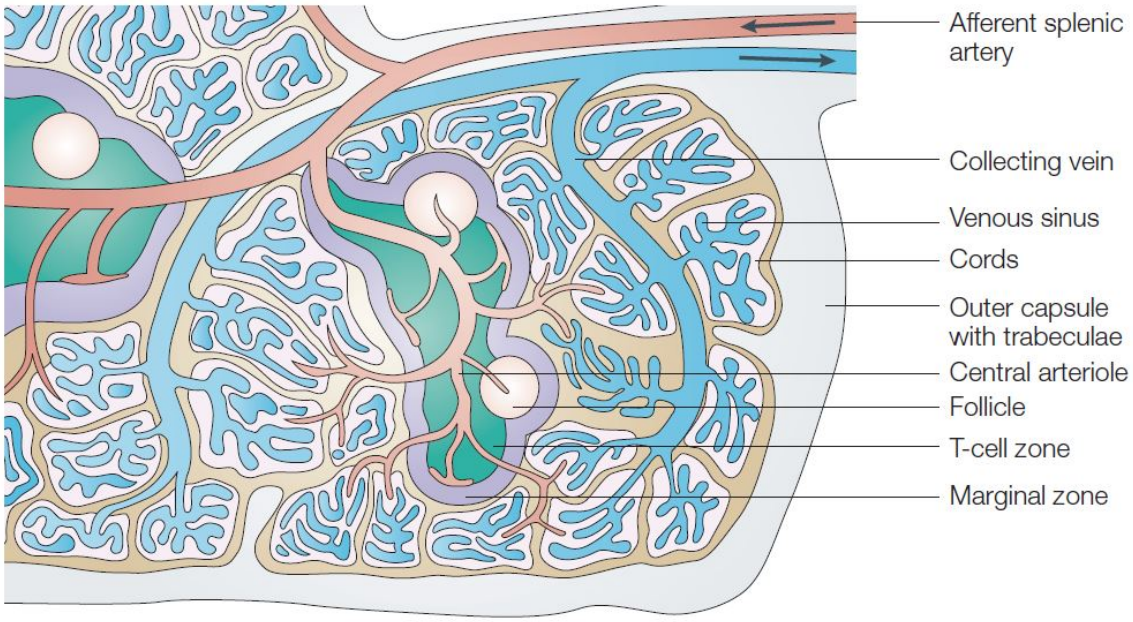

Figure 2.9: A schematic diagram of the spleen structure. Blood enters the spleen through the afferent splenic artery that branches into central arterioles sheathed by white-pulp areas. The white-pulp areas also consist of the T-cell zone and B-cell follicles. The arterioles end in cords in the red-pulp areas where the blood drains into the venous sinuses to be filtered and returned back to the venous system. Reprinted with permission from [139], copyright 2005 Nature Publishing Group.

The red blood cells are cleared within the marginal zone and the red pulp. The red blood cells must undergo changes in shape to squeeze through the physical barrier created by the sinusoidal inter-endothelial slits and the fibroblast stroma, which are about 500 nm [136]. Normal red blood cells is able to pass through this

opening as shown in Figure 2.10 [139], while damaged or altered red blood cells cannot. Particles larger than 500 nm will also be sequestered in the spleen. In addition, antibody-coated foreign particles are recognized and removed by splenic macrophages in the red pulp.

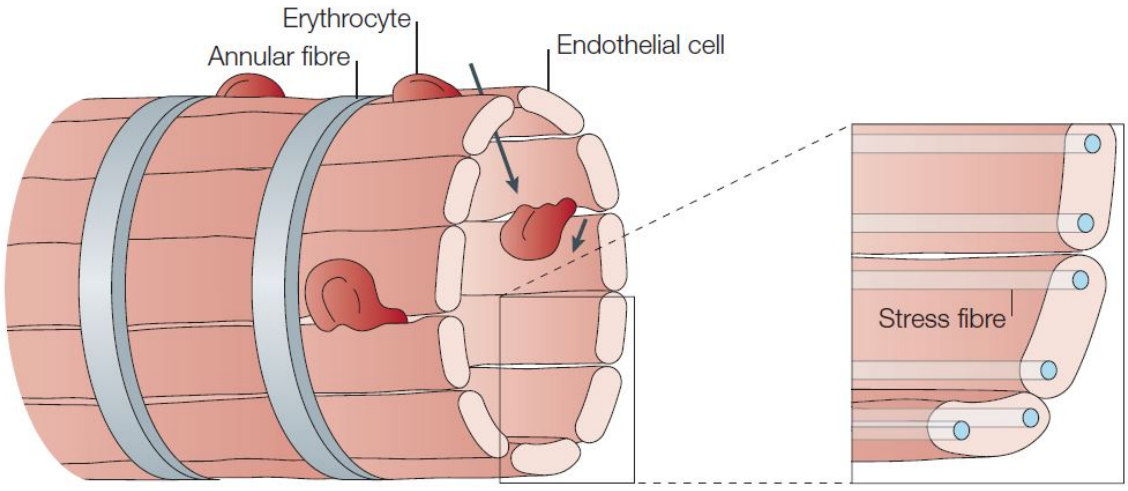

Figure 2.10: A schematic diagram of the venous sinuses in the splenic red pulp. Normal red blood cells are shown squeezing through inter-endothelial slits from the red-pulp cords into the sinuses and back into the venous system. Larger particles and ageing or damaged red blood cells that are not able to pass through the slits are phagocytosed by the red pulp macrophages. Reprinted with permission from [139], copyright 2005 Nature Publishing Group.

2.4.3 Nanoparticles Clearance by Complement and MPS

As discussed in the previous section, the main biological function of the complement system is to recognize foreign particles (e.g. bacteria, fungi, viruses) and damaged or altered "self" components (e.g. apoptotic cells, necrotic cells, tumor cells, abnormal protein assemblies such as amyloids, clots, or antibody aggregates) and facilitate their elimination by opsonization or by lysis if the particles have lipid

bilayer membrane. Opsonization is the coating of foreign particles with complement proteins to initiate phagocytosis of opsonized particles by phagocytic cells. Therefore, the complement proteins are mostly synthesized in the liver and cells of the monocyte and macrophage lineage. In addition to biological targets, the complement proteins also recognize synthetic materials as such liposomes, carbon nanotubes, and various polymers used to make drug carrier particles.

When nanoparticles are administered into circulation, they immediately and spontaneously acquire a layer of host blood proteins before interacting with any immune cells or endothelial cells. Electrostatic interactions and hydrophobic interactions are the main driving force for opsonization. Therefore, charged or hydrophobic nanoparticles are usually opsonized within minutes in the blood and cleared by the MPS [140]. The host reactions to these nanoparticles are most likely determined by the types, levels, and surface conformations of the adsorbed proteins. Conversely, the characteristics of the adsorbed proteins are dependent on the surface properties of nanoparticles. In addition, some adsorbed proteins may desorbed over time giving rise to the time-dependent variations in the type and level of proteins adsorbed on the nanoparticles *in vivo* [141].

Regardless of the dynamic changes in the adsorbed proteins, nanoparticles recognized by the complement system will have C1q molecules and many C3b molecules bound to them. Red blood cells have receptor CR1 which binds to C3b. Therefore, C3b-coated nanoparticles in the blood will bind mainly to red blood cells and circulate. CR1 on the red blood cells is a cofactor for Factor I, which cleaves C3b to iC3b.

As the C3b-coated nanoparticles circulate with the red blood cells and encounter Factor I, more C3b molecules are converted to iC3b to convert the nanoparticles from C3b-coated to mostly iC3b-coated. iC3b binds weakly to receptor CR1 on the red blood cells and strongly to receptor CR3 and CR4 on phagocytic cells. Therefore, when the red blood cells with iC3b-coated nanoparticles circulate through the liver and spleen, the iC3b-coated nanoparticles will be transferred to the resident phagocytic cells in the liver and spleen to be phagocytosed and removed from circulation [120]. After the nanoparticles are phagocytosed, the phagocytes will secrete enzymes and oxidative-reactive chemical factors such as superoxides, oxyhalide, nitric oxide, and hydrogen peroxide to assist in the degradation of the phagocytosed material [142]. Depending on the size and molecular weight of the degraded products, they are either removed by the renal system if their molecular weight is below 5000 or remained sequestered and stored in the organs of the MPS.

Even if the iC3b-coated nanoparticles are able to evade phagocytic cells in the liver and spleen, the iC3b molecules are eventually broken down into smaller C3d fragment. These C3d fragments binds to receptor CR2, which are abundant on B lymphocytes and on follicular dendritic cells (FDC). When the C3d-coated nanoparticles bind to surface immunoglobulin on B cells, the secondary C3d-CR2 interaction causes proliferation of B cells. When C3d-coated nanoparticles bind to CR2 on FDC, it promotes the germinal center reaction and B cell memory. The activation of the adaptive immune response through CR2 has the complement system functions as an adjuvant. Finally, antigen presenting dendritic cells can bind to

nanoparticles opsonized with complement proteins via other receptors such as CR3, CR4, and C1q receptors to enhance antigen presentation and transportation to the lymph nodes for clearance [120].

Alternatively, macrophage integrin may also bind to the adsorbed proteins on the surface of nanoparticles to trigger downstream signaling transduction pathways. These pathways may lead to cytoskeletal rearrangements and formation of adhesion structures to spread over the nanoparticles for internalization [141].

In addition to opsonization of nanoparticles with C1q and C3b molecules to facilitate the recognition and clearance of these nanoparticles by macrophages of the MPS bearing complement receptors (e.g. hepatic Kupffer cells, splenic marginal zone and red-pulp macrophages, blood monocytes, etc), other factors such as size can mediate particle-macrophage interaction. Nanoparticles may aggregate into larger flexible particles *in vivo*. Macrophages are capable of phagocytosing small particles that are <5 μm. For large particle sizes or aggregates that are >10 μm, multiple macrophages may adhere and fused onto the particle surface, provided that the appropriate types of adsorbed proteins are present. These macrophages then undergo phenotype changes to fuse into one foreign body giant cell that degrades foreign particles in a similar fashion as macrophages.

A literature search showed that the dominant factors of nanoparticles that affects complement activation and MPS clearance are surface properties such as charge, functional groups, and hydrophobicity/hydrophilicity, hydrodynamic size, and morphology such as shape and structure defects. A diagram illustrating the

properties of nanoparticle that may affect complement activation and clearance by the MPS is shown in Figure 2.11.

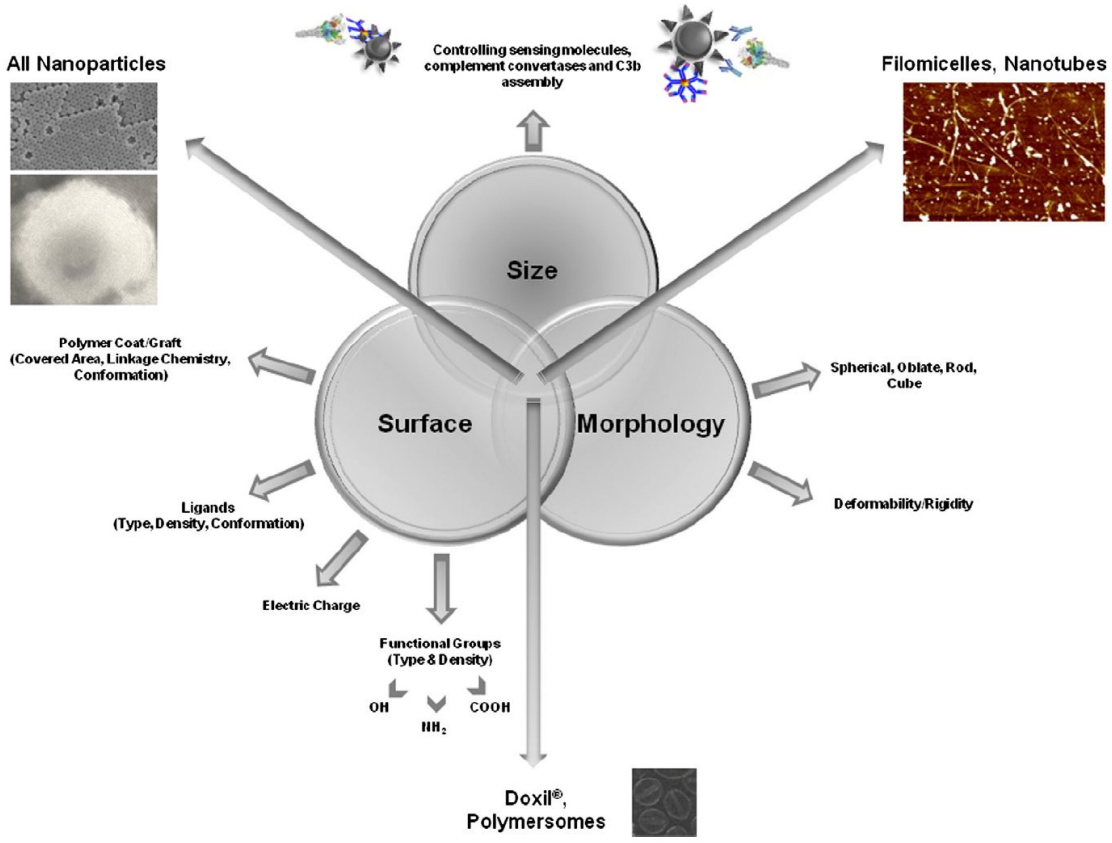

Figure 2.11: Properties of nanoparticle affecting complement activation. The three main properties are the hydrodynamic size, morphology (i.e. shape and rigidity), and surface properties (i.e. type and density of functional groups; surface charge; hydrophobicity/hydrophilicity; type, density, and conformation of ligands or polymer coatings). Reprinted with permission from [119], copyright 2011 Elsevier.

2.4.4 Nanoparticle Surface Properties and Circulation

The surface properties of the nanoparticle is one of the factors that can influence the circulation half-life of the nanoparticles. Hydrophobicity or hydrophilicity of the surface of the nanoparticles is one of the surface properties affecting circulation.

Opsonization has been reported to take place more rapidly on hydrophobic nanoparticles compared to hydrophilic nanoparticles, so the hydrophobic nanoparticles are cleared faster from circulation [143].

Another surface property that plays an important part in complement activation is the surface functional groups. Studies have found that phospholipid micelles conjugated with surface poly(ethylene glycol) do not activate complement through any of the known pathways. However, polyethylene oxide and polypropylene oxide block copolymers activate the complement system through all the three known pathways [144]. Other surface moieties such as amino and hydroxyl functional groups have been shown to induce nucleophilic attack on the thioester group of C3b to cause the activation of the complement system through the alternative pathway [145], [146]. Nanoparticles with carboxyl-functionalized surface (i.e. negatively charged) have been reported to activate the complement system through both classical and/or alternative pathways. The classical pathway may be activated through C1q binding to negatively charged surfaces since its head is highly cationic. The alternative pathway may be activated through non-specific protein deposition on the surface of these nanoparticles [147].

Surface charge is another surface property affecting circulation. Positively charged nanoparticles have a higher cell uptake due to the electrostatic attractions of the positively-charged nanoparticles to the cell membrane which is slightly negatively charged. Therefore, the circulation half-life of positively charged nanoparticles are shorter due to removal from the blood by cell uptake. Furthermore, charged

nanoparticles regardless of positive or negative interact with blood proteins such as immunoglobulin, lipoproteins, complement and coagulation factors, acute phase proteins, and metal-binding and sugar-binding proteins. The adsorbed blood proteins may cause rapid clearance of the nanoparticles by the MPS. In contrast, neutral nanoparticles that have poly(ethylene glycol) conjugated to their surfaces have the highest blood half-life due to the poly(ethylene glycol) layer attracting water molecules to form a protective layer against opsonization [148].

In fact, one of the most successful surface stabilization strategy for enhancing nanoparticles circulation in blood is with a range of non-ionic surfactants or polymeric macromolecules. These non-ionic surfactants or polymeric macromolecules may be physically adsorbed or covalently attached to the surface of the nanoparticles. One very popular polymer used for surface stabilization of nanoparticles is poly(ethylene glycol) (PEG). The process of physically adsorbing or covalently attaching PEG to a surface is often referred to as PEGylation. The circulation half-life of PEGylated liposomes such as Doxil® is about 7 to 10 times higher than non-PEGylated liposomes such as DaunoXome® [82].

Physical adsorption has the downside of the PEG molecules desorbing from the surface to leave gaps where opsonins can bind [149]. Therefore, covalently attaching the PEG molecules to the surface of the nanoparticle is the preferred method. The covalent attachment of PEG molecules may be accomplished by either the "grafting-to" or "grafting-from" approach [150], [151]. "Grafting-to" chemically reacts a preformed functionalized PEG to the surface of a nanoparticle that has the complemen-

tary functional groups [150], [152]. Higher concentration of the pre-formed PEG with reactive functional groups and longer reaction time will lead to higher PEG density on the surface of the nanoparticle with complementary reactive groups. "Grafting-from" forms the PEG chain *in situ* where polymerization occurs on a surface that is functionalized with an initiating monomer [150], [152]. Due to the simplicity of the "grafting-to" chemistry, it is the preferred method for PEGylating nanoparticles.

In theory, the presence of the surfactants or polymers on the surface of the nanoparticles will decrease the attractive Van der Waals forces between particles such as a nanoparticle and an opsonizing protein and increase the repulsive force between two approaching particles to create a steric stabilization effect. Additionally, there is an elastic component to the stabilization effect. When two surfaces approach each other, there is a reduction in the available volume for each polymer (or conformational entropy loss) and a positive heat of solution (or enthalpy increase). The entropy loss and enthalpy gain result in a gain in free energy of mixing that causes the particles to separate. Finally, there is an osmotic pressure component to the stabilization effect. When an opsonizing protein approaches a polymer-coated nanoparticle, the polymers are compressed which reduces the number of available polymer chain conformations. This loss of conformational freedom of the polymer chains is counteracted by an influx of water into the compressed polymer region to force the two surfaces to separate [144], [151].

However, there have been some *in vitro* evidence indicating opsonization and formation of iC3b on the surface of PEGylated nanoparticles [153], [154] even though

these nanoparticles circulate for prolonged period of time *in vivo*. One of the suggested explanations is the Vroman effect [155]. The Vroman effect is the observation of competitive adsorption of blood serum proteins onto a finite number of surface sites. Proteins with the highest mobility and/or abundance are generally adsorbed first and are later displaced by less motile and/or abundant proteins and have a higher affinity for the surface. Therefore, *in vitro* experimental results are highly dependent on the initial protein concentration of the plasma or serum (which is variable from patient to patient) and the length of the incubation period of the nanoparticles with the plasma or serum. The Vroman effect may partially explained why opsonization observed *in vitro* did not translate to shorter circulation time of PEGylated nanoparticles *in vivo*.

Another explanation for why opsonization of PEGylated nanoparticles and complement activation do not affect circulation times of these nanoparticles is the steric hindrance effect of the PEG layer. It has been suggested that the iC3b complement proteins attached to regions on the surface of the nanoparticles that are inaccessible by the CR3 receptors on the macrophages [156]. There are also evidence of surface binding of long-circulating particles with immunoglobulins (e.g. IgG). Again, the binding of IgG fails to enhance clearance of these nanoparticles via Fc receptors on B cells, follicular dendritic cells, and macrophages. It is plausible that IgG binds to the surface with the Fc domain hidden, which helps the nanoparticle resist recognition by macrophages [156]. It is also suggested that the free iC3b proteins may compete with iC3b proteins that are bound to nanoparticles for the

CR3 receptors on macrophages [157]. Finally, it is suggested that C3b bound to the surface of nanoparticles may interact with CR1 receptors on red blood cells such that the nanoparticles may circulate with the red blood cells for longer time [158].

Based on the many observations of opsonization and complement activation by PEGylated nanoparticles, the key observation is that these nanoparticles were still able resist clearance from circulation. So the strategy may not be to avoid opsonization which may lead to phagocytosis by macrophages, but to avoid phagocytosis instead.

One of the main factor in having an effective PEG layer that is resistant to phagocytosis by macrophages is reported to be the PEG density [159]. The two extreme levels of PEG density are simulated on the surface of nanoparticles and shown in Figure 2.12. With low PEG density on a nanoparticle surface, each PEG molecule resembles a "mushroom" configuration. With high PEG density on a nanoparticle surface, each PEG molecule resembles a "brush" configuration.

The definitions of different PEG density are described in Figure 2.13. Nanoparticles with surface grafted with low PEG density, where a single grafted PEG chain is too far to interact with its neighboring PEG chains, produce a mushroom configuration. This mushroom configuration is explained by the larger range of motion since the neighboring PEG molecules much further away from it, so the PEG chains will on average be located closer to the surface of the nanoparticle. Nanoparticles with surfaces grafted with high PEG density, where the size of the grafted PEG chain approaches the distance between two PEG chains such that the grafted chains

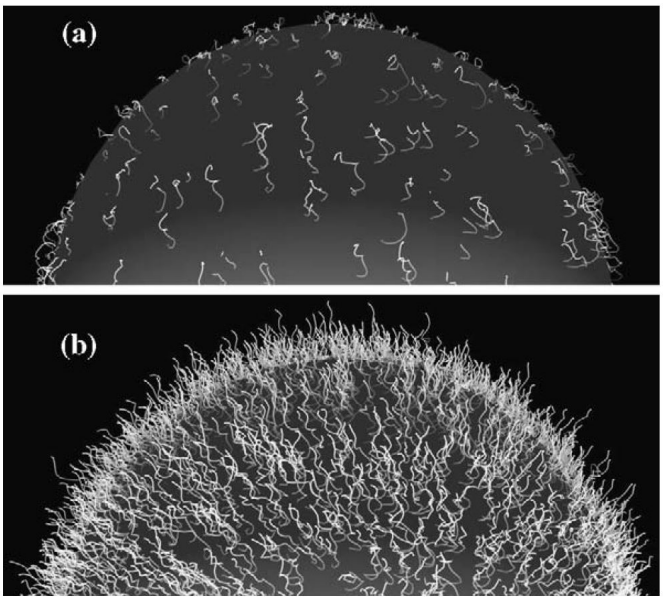

Figure 2.12: A schematic diagram of poly(ethylene glycol) (PEG) configurations on a nanoparticle. PEG molecules assume (a) the mushroom configuration due to low PEG density and (b) brush configuration due to high PEG density. Reprinted with permission from [160], copyright 2006 Elsevier.

overlap, produce the brush configuration [160]. This brush configuration is explained by the restricted range of motion due to the close proximity of the neighboring PEG molecules. Most PEG chains are extended away from the surface. The mobility of the PEG chains are severely restricted that it decreases the desirable steric hindrance properties of the PEG layer [160]. Nanoparticles with surface grafted with medium PEG density exhibit a mushroom-brush intermediate configuration.

Opsonins can mix with PEG chains grafted at low density, penetrate the PEG layer, and interact with the surface of the nanoparticles. It is reported that PEG layer with mushroom configuration is a potent activator of the complement system and susceptible to phagocytosis [160]. At high PEG density, an increase in attractive forces occurs due to poor miscibility among the surrounding solvent, PEG polymers,

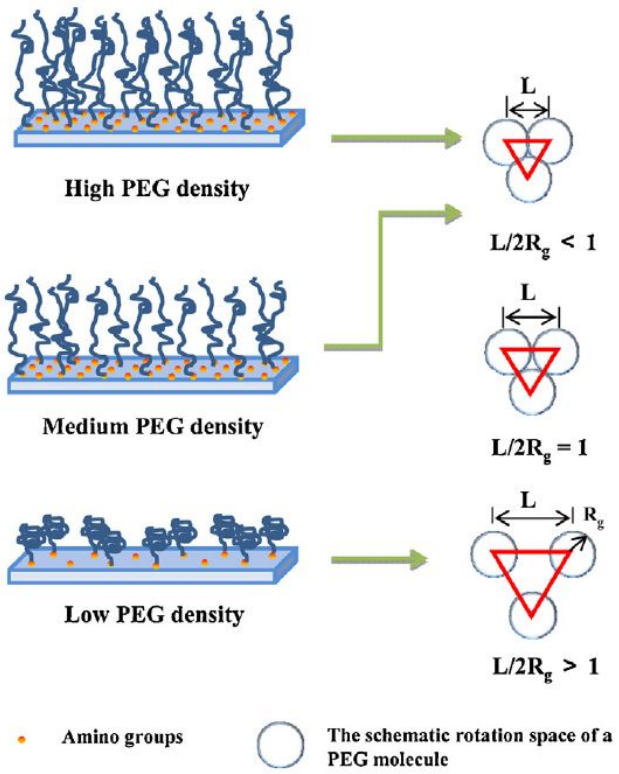

Figure 2.13: A schematic diagram of different surface density of poly(ethylene glycol) (PEG), where L is the distance between two adjacent PEG chains and R is the radius of gyration of PEG chains. A low PEG density corresponds to a mushroom configuration. A medium PEG density corresponds to a mushroom-brush configuration. A high PEG density corresponds to a brush configuration. Reprinted with permission from [161], copyright 2014 Elsevier.

and opsonins within the dense PEG brushes [150], [152]. At medium PEG density, opsonins are unable to penetrate the PEG layer and sufficient solvation occurs to expel opsonins away from the PEG layer. A schematic diagram of the interaction between proteins and different PEG density surface is shown in Figure 2.14 [150].

It was reported that nanoparticles with surface grafted with sufficient PEG density to produce a mushroom-brush configuration is the most resistant to phagocytosis and a poor activator of the human complement system [162], [163]. Therefore,

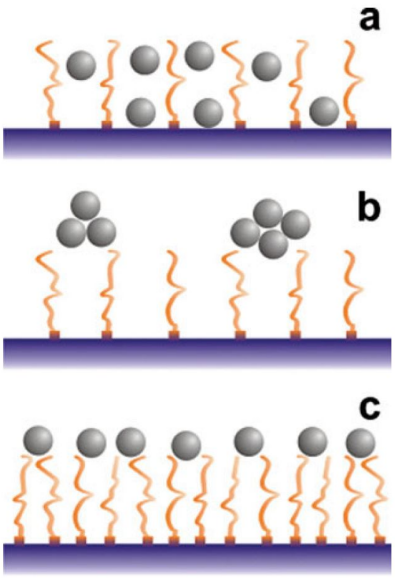

Figure 2.14: A schematic diagram of interaction between protein molecules and different poly(ethylene glycol) (PEG) density layer. (a) At low PEG density, proteins such as opsonins can penetrate into the mushroom-like PEG layer. (b) At medium PEG density, protein aggregates are expel to surface of the mushroom/brush-like PEG layer. (c) At high PEG density, proteins are attracted to the brush-like PEG layer. Reprinted with permission from [150], copyright 2007 John Wiley and Sons.

the optimal PEG layer should assume the mushroom-brush intermediate configuration, where most of the PEG chains are slightly constricted, but they are at a sufficient density to leave no gaps on the surface of the nanoparticles [150]. Since surface heterogeneity is likely to exist in any PEGylated nanoparticles population, it is feasible that a fraction of the administered nanoparticles that is cleared rapidly by macrophages in the liver and spleen did not have the mushroom-brush intermediate configuration, while those that remain in the circulation for extended time do [164].

The PEG density can also affects the stability of nanoparticles based on the interactions between the nanoparticles. At low PEG density, two nanoparticles are attracted to each other due to a bridging effect. At medium PEG density, two

nanoparticles are repelled from each other due to steric repulsion. At high PEG density, two nanoparticles are again attracted to each other due to Van der Waals interaction and depletion effect. A schematic diagram of the interaction between two nanoparticles with different PEG layer configurations is shown in Figure 2.15.

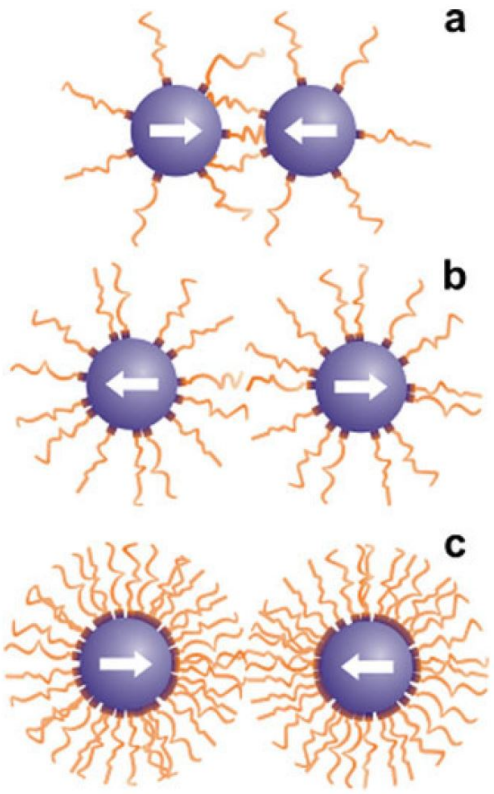

Figure 2.15: A schematic diagram of the interaction between two nanoparticles with different surface poly(ethylene glycol) (PEG) density. (a) At low PEG density or mushroom configuration, nanoparticles are attracted to each other due to a bridging effect. (b) At medium PEG density or mushroom-brush configuration, nanoparticles are repelled from each other due to steric repulsion. (c) At high PEG density or brush configuration, nanoparticles are attracted to each other due to Van der Waals interaction and depletion effect. Reprinted with permission from [150], copyright 2007 John Wiley and Sons.

Another factor affecting receptor recognition of opsonized proteins is the PEG chain length on the surface of nanoparticles. Others have reported that the minimum

molecular weight required to achieve increased resistance to clearance by the MPS is 2,000 Da due to the loss in flexibility of shorter PEG chains [165]. Increased in PEG chain molecular weight above 2,000 Da has been shown to further increase blood circulation half-life [160]. For example, the presence of 5,000 Da PEG chain significantly increases the steric repulsion of the PEG layers from other surfaces such as macrophages cell surface, resulting in poor adhesion of the macrophages to the nanoparticles [166]. Longer PEG length results in a thicker PEG layer. It has been reported that a PEG layer thickness of 12 nm has the maximum possible repulsive interaction with proteins [167]. The maximum PEG length reported to have prolonged circulation effect is 10,000 Da [159].

2.4.5 Nanoparticle Size and Circulation

Studies have shown that particle size is an important factor affecting the circulation time of nanoparticles. The hydrodynamic diameter of nanoparticles will affect their transport and adhesion in blood vessels, airways, and gastro-intestinal tract. It will also affect their interaction with the MPS. As discussed in the previous section, the MPS is a part of the immune system and includes organs such as the liver and the spleen and their associated phagocytic cells. These phagocytic cells are primarily blood monocytes, macrophages in the lymph nodes, Kupffer cells of the liver, macrophages of the splenic red pulp, and other tissue histiocytes.

Since the interendothelial cell slits of venous sinuses in the spleen are approximately 500-nm wide, nanoparticles larger than 500 nm may potentially be trapped

or taken up by the macrophages in the splenic red-pulp regions [9]. In fact, studies have shown that nanoparticles with hydrodynamic radii greater than 200 nm show a more rapid rate of clearance than nanoparticles with radii smaller than 200 nm, regardless if they are PEGylated or not [168].

Similarly, since the diameter of the fenestration in the endothelial lining of the liver is between 100 and 200 nm, particles in this size range should be able to escape capture by Kupffer cells or physically trapped in the capillary beds [169].

The kidney, although not part of the MPS, is another organ that assists in the excretion of foreign particles or waste materials. The capillary endothelium of the glomerular filter of the kidney has non-diaphragmed fenestration that is about 50 to 100 nm in diameter. Podocytes, with phagocytic function, wrap around the capillary. The podocytes have long processes or pedicels that wrap around the capillaries and leave slits between them. Blood is filtered through these slits that are approximately 10 to 25 nm. Therefore, nanoparticles that are smaller than 10 nm may be removed from blood circulation through excretion via the kidney [9].

A summary of the effect of nanoparticle size and circulation is summarized in Figure 2.16. The location where injected nanoparticles will potentially accumulate depends on the physical dimensions of the biological barriers they encounter and the different processes by which they are transported in the human body. These transport processes include passive (i.e. diffusive) and active processes ranging from extravasation out of blood vessels to transdermal uptake. Most of these processes affect the biodistribution and the clearance of microparticles and nanoparticles in

the human body and have been shown to be strongly dependent on particle size.

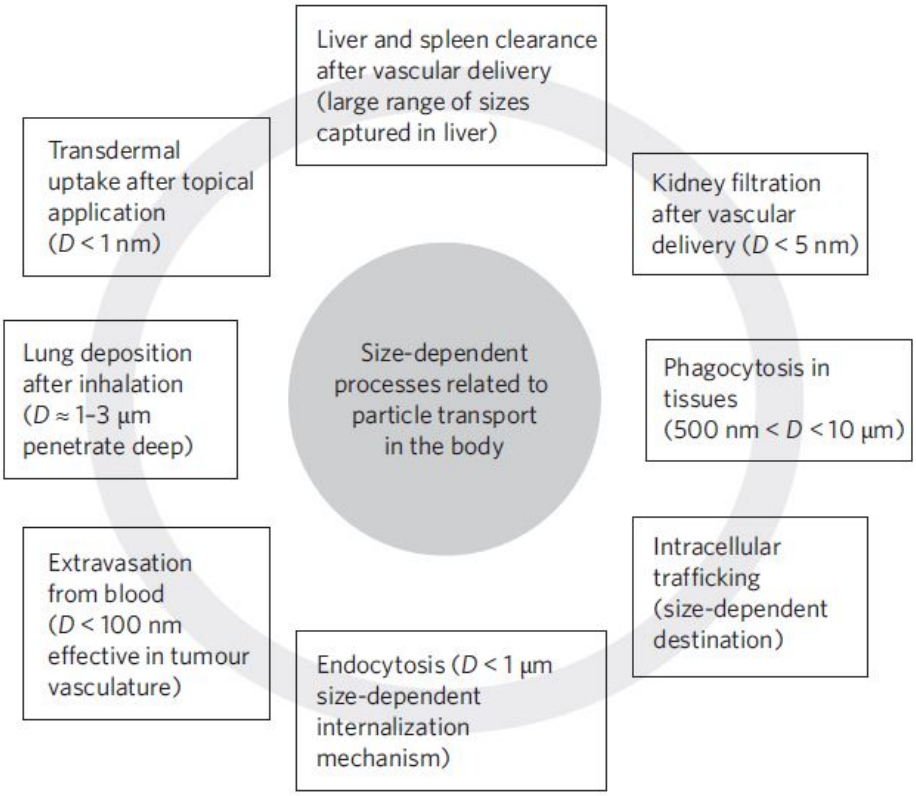

Figure 2.16: Size-dependent processes of particle transport in the human body. To achieve long circulation, a nanoparticle should have hydrodynamic diameter greater than the kidney filtration cut-off and less than the liver and spleen clearance cut-off, which is usually suggested to be between 30 and 200 nm. Reprinted with permission from [169], copyright 2009 Nature Publishing Group.

In addition to the physical barriers that long-circulating nanoparticles have to overcome, they also have to avoid activating the complement system to stay in circulation. A study on size and complement activation found that effective binding of an antibody to a surface with target antigen is not sufficient to activate the classical pathway of the complement system. For potent complement activation to occur post IgM binding, the nanoparticle surface must also meet other topological require-

ment regarding curvature. In the referenced study, the binding of IgM to 250-nm dextran-coated iron oxide nanoparticles induced potent complement activation. In contrast, complement activation was significantly lowered when corrected for surface area with 600-nm nanoparticles even though the larger nanoparticles bind IgM as effectively as the smaller nanoparticles. This observation may be explained by the particle curvature. The cross-sectional diameter of IgM is about 40 nm, so particles that are 50 nm were found to bind IgM poorly and failed to activate the complement system. The study also used peptidoglycan (PGN) which is a complement-activating macromolecule produced by bacteria to test size against complement activation. When PGN particles of varying sizes were tested for complement activation, it was found that 100-nm PGN nanoparticles showed the strongest complement activation via classical pathway as compared to 50-nm or 400-nm PGN nanoparticles. Based on the consistent observations with dextran-coated nanoparticles and PGN-coated nanoparticles, it is possible that high-affinity interaction between IgM and complement proteins such as C1q on the nanoparticles in the size range between 100 nm and 250 nm may sufficiently strain the IgM to dock with C1q and activate the classical pathway of the complement system [156]. However, it is possible to avoid complement activation by PEGylating the nanoparticles in this size range.

In order for nanoparticles to have long blood circulation life, they will have to be small enough to evade the MPS and large enough to escape filtration by the kidney. Based on the consideration of the physical size and the surface properties mentioned, the optimal size range for nanoparticles to have enhanced blood circulation is between

30 nm and 200 nm [38], [33] and the surface PEGylated.

2.4.6 Nanoparticle Morphology and Circulation

Finally, the morphology of the nanoparticles may affect their ability to activate the complement system and evade the MPS. It has been reported that PEGylated liposomes containing doxorubicin (e.g. Doxil®) activate complement more than PEGylated liposomes without the drug. This observation is explained by the change in liposome morphology from spherical without doxorubicin to oblate/disc shape with doxorubicin. The change in morphology may affect the phospholipid arrangement in the plane of the vesicular bilayer to be favorable for antibody or direct C3 binding. Another explanation may be the present of surface bound or membrane trapped doxorubicin crystals which attract complement proteins. On the other hand, drug-free PEGylated liposomes were found to induce IgM binding resulting in IgM-mediated complement activation and subsequent hepatic clearance of these liposomes. However, no IgM response was observed with doxorubicin-loaded PEGylated liposomes. This inconsistency in clearance of doxorubicin-loaded or drug-free PEGylated liposomes were speculated to be caused by doxorubicin-mediated macrophage death and inhibition of B-cell proliferation [153], [170], [171].

The morphology of the nanoparticles, particularly the shape, may affect circulating half-life of nanoparticles. The motivation of using different shapes besides spherical originate from biology itself as shown in Figure 2.17. For examples, bacteria exist in a variety of shapes including rods, spirals, and ellipsoids. Human red

blood cells possess unique discoidal shapes to avoid splenic filtration. The disc-like shape of platelets helps them to adhere and roll on vascular endothelium.

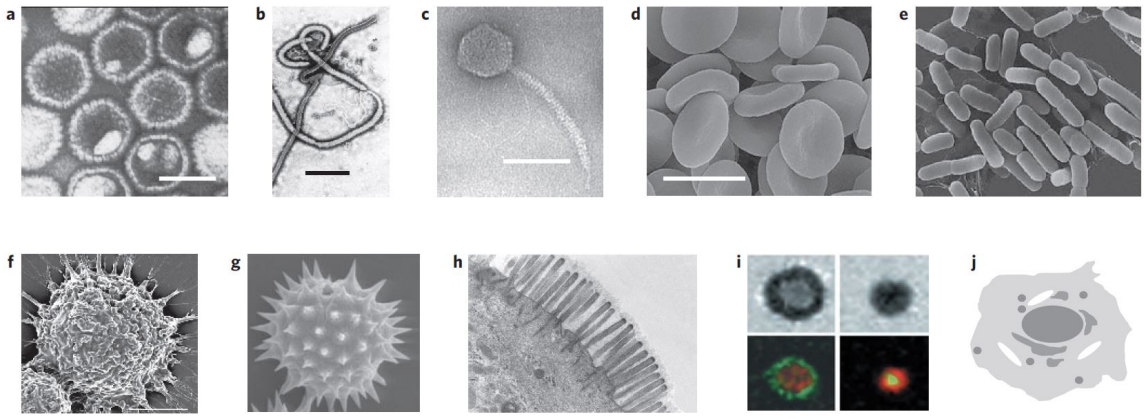

Figure 2.17: Examples of biology's diverse physical properties in terms of shape. (a) Herpesvirus, (b) Ebola virus, (c) enterobacteria phage, (d) erythrocytes, (e) *Escherichia coli*, (f) alveolar macrophage, (g) pollen, (h) intestinal villi, (i) immunological synapse, and (j) cellular compartments. Reprinted with permission from [169], copyright 2009 Nature Publishing Group.

The clearance of nanoparticles by phagocytosis is strongly dependent on the shape of the nanoparticles. Specifically, the local geometry of the nanoparticle at the point of macrophage attachment has the dominant effect on whether macrophages will initiate the phagocytosis process or not [169].

Studies using polystyrene material indicated that when the pointed end of an elliptical disc came into contact with a macrophage, the disc was phagocytosed within a few minutes. In contrast, when the flatter region of the same elliptical disc came into contact with a macrophage, the macrophage was unable to phagocytose the disc for over 12 hours. In fact, it was reported that the angle Ω as defined in Figure 2.18 and the dimensionless volume V^* defined as the volume of the particles divided by the volume of the macrophage (assuming a radius of 7.5 μm) may be used

to predict if a nanoparticle will be phagocytosed by a macrophage. At $\Omega < 45^{o}$, a cell attaches to a particle with successful internalization when $V^{*} < 1$ (Region A) and unsuccessful internalization when $V^{*} > 1$ (Region B). At $\Omega > 45^{o}$, a cell spreads over a particle without initiating internalization regardless of V^{*}. Spherical particles, by definition has $\Omega = 45^{o}$, will be phagocytosed unless they are bigger than the cell (i.e. $V^{*} > 1$). However, ellipsoids have $\Omega < 45^{o}$ when they approach the macrophage with the pointed end and $\Omega > 45^{o}$ when they approach with the flatter region.

Assuming only two approach configurations and the approach is random, then the probability is 50% phagocytosed with the pointed end approach and 50% not phagocytosed with the flatter region approach for an ellipsoid. However, the approach of a particle to a cell may be at different angles and the fluid flow of the blood may bias the approach to a specific angle.

With ellipsoids, there is another variable to consider. The aspect ratio defined as the long axis divided by the short axis will influence the phagocytosis of the particles. Studies showed gold nanospheres with diameters of 14 nm or 74 nm were internalized by HeLa cells three times more often as gold ellipsoid with 14 nm by 74 nm dimension [54].

An *in vitro* cell culture study showed that silica nanoparticle uptake is maximum for particles with an aspect ratio of 2.1 to 2.5 as compare to an aspect ratio of 1.5 to 1.7 [172]. An *in vivo* study with silica material showed that nanorods with aspect ratio of 1.5 is able to circulate longer in blood when PEGylated [173]. Comparing the silicon contents of organs at 2 hours, 24 hours, and 7 days post in-

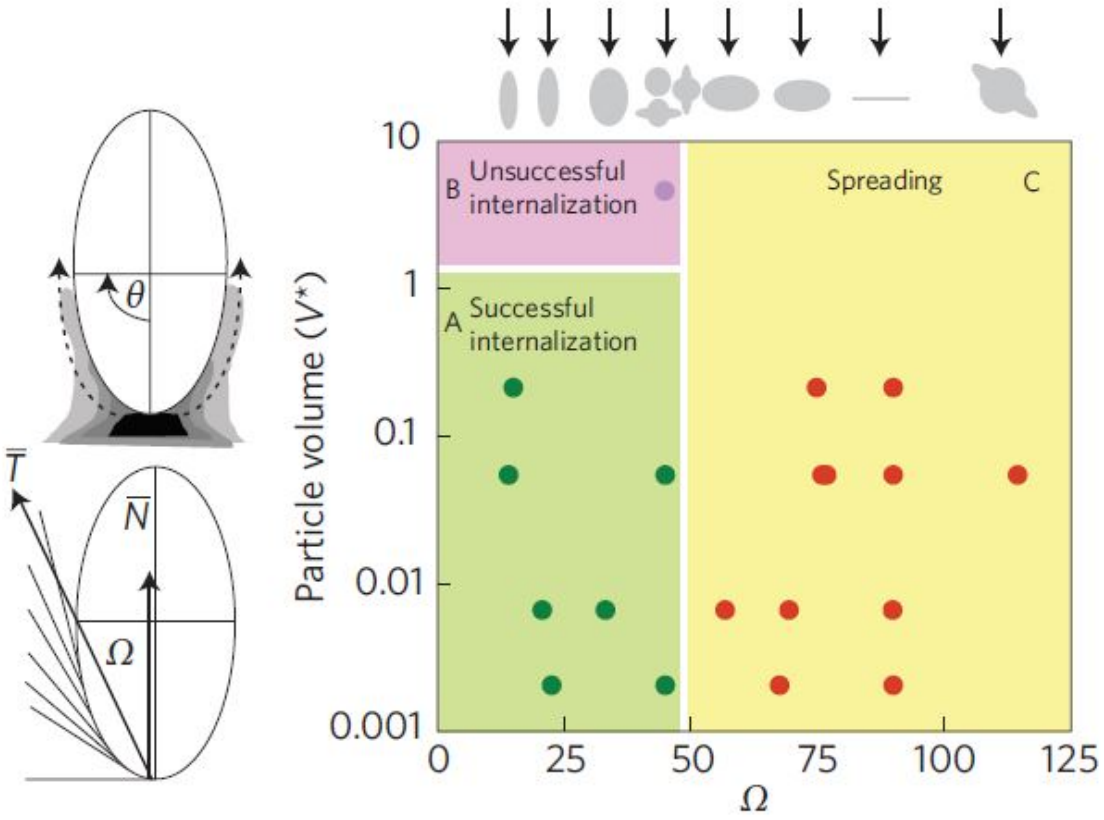

Figure 2.18: Phagocytosis phase diagram. The angle Ω as shown on the *left* and the dimensionless volume V^* defined as the volume of the particles divided by the volume of the macrophage (assuming a radius of 7.5 μm) may be used to predict if a nanoparticle will be phagocytosed by a macrophage. Region A predicts successful phagocytosis of the nanoparticle. Region B predicts no phagocytosis of the nanoparticle. Region C predicts wrapping of the macrophage membrane around the nanoparticle without successful phagocytosis. Reprinted with permission from [169], copyright 2009 Nature Publishing Group.

jection, the study found that the silicon content of these organs dropped over time [173]. This indicated that silica nanoparticles could be biodegraded or cleared from liver, spleen, lung, and kidney. Silica nanorods with aspect ratio of 5.0 (NLR) had a faster clearance rate when compared to silica nanorods with aspect ratio of 1.5 (NSR). Furthermore, the study found that PEG modification of NSR (NSR-PEG) and NLR (NLR-PEG) decreased the clearance rate of silica nanorods in organs. This

results showed that PEGylation of nanoparticles may further increase the circulation half-life on top of the extended circulation gain from having an ellipsoidal shape [174].

Based on the shape effects on phagocytosis, a long-circulating nanoparticle should have an ellipsoidal shape with aspect ratio between 1.5 and 2.0. Taken together with the conclusions from the effects of size and surface properties on nanoparticle circulation, the optimal design for a long-circulating nanoparticle should have the optimal size range between 30 nm and 200 nm, the surface PEGylated, and an ellipsoidal shape with aspect ratio between 1.5 and 2.0.

Chapter 3

Nanoparticle Design for Amino Acid Depletion in Cancer Therapy

As discussed in the previous chapter, the complexity of cancer biology and cancer treatments is nontrivial. There is probably not a single cancer treatment using nanotechnology that can achieve all the different desired distributions of therapeutic agents at the different desired dose in different tumor types. Instead of attempting to design a "magic bullet" to cure all cancers, this chapter focuses on a disease-driven approach to design and develop a nanotechnology-based delivery system to exploit a specific difference between cancer cells and normal cells for a specific cancer patient population. A disease-driven approach is built on understanding a specific cancer biology and the defined challenges with the current standard-of-care in order to design a delivery system to exploit the pathophysiology and mitigate adverse side effects such as excessive toxicity to healthy tissues or improve pharmacokinetic

profile of the therapeutic agents. In contrast, a formulation-driven approach focuses on developing a delivery system first, and then tries to fit it to solve an existing clinical problem [12].

This chapter discusses the different approaches and limitations of amino acid depletion therapy for cancer treatment that drive the design of a silica-based nanoparticle for the delivery of therapeutic enzymes for amino acid depletion treatment of cancer patients.

3.1 Amino Acid Depletion in Cancer Treatment

The previous chapter briefly discussed a cancer treatment strategy of starving cancer cells with nutrient deprivation. This strategy relies on the altered metabolism of cancer cells that sustain higher proliferation rates than normal cells. A cell needs to grow in size and replicate its DNA for cell division. This process requires large amounts of energy in the form of adenosine triphosphate (ATP) and building blocks such as amino acids, lipids, and nucleotides. Therefore, the amino acid metabolic pathways have become interesting targets for cancer therapies [175].

Amino acids are the building blocks of proteins. Of the twenty amino acids, nine are considered essential because humans cannot synthesize them *de novo*. These amino acids are phenylalanine, valine, threonine, tryptophan, methionine, leucine, isoleucine, lysine, and histidine; and they must be obtained from diet. The remaining non-essential amino acids are potential therapeutic targets. Depleting non-essential

amino acids will not have adverse side effects on normal cells since they can synthesize enough of these amino acids to meet their demand, while cancer cells may not.

Therefore, a possible targeting strategy is to exploit the alterations in amino acid synthesis or salvage pathways displayed by cancer cells. Due to the lack of self-sufficiency in certain amino acids through mutations or other reasons, cancer cells become dependent on the bloodstream to supply these amino acids to meet their demand for rapid growth and proliferation. Cancer cells that are auxotrophic for a particular amino acid can be targeted with amino acid deprivation. Since the normal cells have functioning amino acid synthesis or salvage pathways, they are not affected by amino acid deprivation. Amino acid deprivation can be achieved with enzymes that convert the targeted amino acid to other harmless biomolecules.

The use of enzymes for cancer treatment was proposed over fifty years ago. Enzymes can systemically deplete amino acids that are essential to the growth and proliferation of cancer cells (i.e. amino acid depletion therapy) or target tumor sites to activate non-toxic prodrug into toxic drug at a high and localized concentration to kill cancer cells (i.e. enzyme-prodrug therapy). However, enzymes with potential therapeutic effects are usually derived from non-human sources, which are highly immunogenic and have circulating half-life too short to achieve clinical efficacy [176].

Several non-essential amino acids have been identified for depletion to treat certain cancers. There has been preclinical data supporting anti-cancer effects with depletion of serine [177] and glutamine [178]. There are clinical trials currently being conducted with arginine depletion for treating melanoma and hepatocellular

carcinoma. Finally, asparagine depletion is an FDA-approved therapy for treating childhood acute lymphoblastic leukemia.

3.1.1 Arginine Depletion

Arginine is one of the non-essential amino acids that shows anti-cancer effects when depleted. The *de novo* biosynthesis of arginine involves two enzymatic steps [179]. The first step uses argininosuccinate synthetase to convert citrulline and aspartic acid to argininosuccinate. The second step uses argininosuccinate lyase to convert argininosuccinate to arginine and fumaric acid. The first step is the rate-limiting step in the biosynthesis of arginine. Argininosuccinate synthetase is found in all normal cells, but expressed at different levels in different normal cell types. Furthermore, the expression level of argininosuccinate synthetase differs between cancer cells and their normal counterparts. Ovarian, stomach, and colon cancers are reported to have higher expression level of argininosuccinate synthetase. In contrast, melanoma, hepatocellular carcinoma, mesotheliomas, renal cell carcinoma, and prostate cancers are found to have lower or lack of expression of the same enzyme [180]. For cancer cells lacking in argininosuccinate synthetase activity, they are unable to survive and proliferate if the systemic supply of arginine is depleted (i.e. auxotrophic for arginine).

Therefore, arginine depletion is a promising strategy to target cancer cells auxotrophic for arginine. Two enzymes have been developed for depleting arginine: arginine deiminase (ADI) and arginase. ADI catalyzes the conversion of arginine

to citrulline and ammonia, while arginase converts arginine to ornithine. Unfortunately, ADI has a short circulation half-life of around four hours and is highly immunogenic because it is a bacterial enzyme [181]. Therefore, a formulation with 20 kDa polyethylene glycol molecules conjugated to ADI (ADI-PEG20) was developed to improve its circulation half-life to about seven days [106] and minimize its immunogenicity. ADI-PEG20 is currently in different stages of clinical trials for treating hepatocellular carcinoma and melanoma [182]. It is typically administered weekly via intramuscular injection in clinical trials.

Initial results from multiple clinical trials showed efficacy of ADI-PEG20 in treating melanoma and hepatocellular carcinoma. A 35% response rate with ADI-PEG20 compared to 20% with current standard treatment is observed in patients with metastatic melanoma [179]. A better survival rate is observed in patients with more than four weeks of sustained arginine depletion than patients with less than 4 weeks of arginine depletion [183]. However, 75.9% of patients developed antibodies against the enzyme after two weeks of treatment with ADI-PEG20. The percentage increased to 93.5% after eight weeks of treatment [184]. Despite PEGylation, a similar immunogenic response is observed with unresectable and metastatic hepatocellular carcinoma patients, with antibody development occurring around 50 days into the treatment [185].

Because of the immunogenicity of ADI-PEG20, recombinant human arginase (rhArg1) is developed [179]. Although rhArg1 is non-immunogenic, it has significantly less affinity for arginine, which makes it less potent and requiring a higher dose

to be efficacious. In addition, the circulation half-life of rhArg1 is only a few minutes. This motivated the development of PEGylated rhArg1 (PEG-rhArg1), which has a longer circulation half-life of about three days [186]. Clinical trials conducted in Asia showed sustained arginine depletion with no development of neutralizing antibodies throughout the treatment [183]. More clinical studies are needed to determine the efficacy of PEG-rhArg1.

3.1.2 Asparagine Depletion

The most successful example of amino acid depletion therapy is the use of bacterial asparaginase to systemically deplete the amino acid asparagine to treat patients with childhood acute lymphoblastic leukemia (ALL) [187]. Leukemic lymphoblasts and certain cancer cells have low or lack asparagine synthetase activity [188]. Asparagine synthetase is involved in the *de novo* biosynthesis of asparagine from aspartic acid, with glutamine also required as the amine donor. Similar to argininosuccinate synthetase, asparagine synthetase is also ubiquitous in its distribution in all normal cell types. Since cancer cells lacking in asparagine synthetase activity are unable to synthesize asparagine *de novo*, they depend on exogenous supply of asparagine from the plasma to survive and proliferate. Asparagine depletion results in selective killing of these cancer cells while sparing normal cells with functioning asparagine synthetase. Conversely, increased asparagine synthetase expression has been observed in cancer cells resistant to asparagine depletion [189]. This is evident in B-lineage ALL positive for TEL-AML1 or hyperdiploidy, which has

lower asparagine synthetase expression than T-lineage ALL, being more sensitive to asparagine depletion than T-lineage ALL [190].

Asparaginase is an enzyme that catalyzes the conversion of asparagine to aspartic acid and ammonia, resulting in the depletion of asparagine in the plasma and the death of leukemic cells. Asparaginase is also enzymatically active against glutamine, albeit at a much lower affinity [190]. Since asparagine synthetase uses glutamine in the *de novo* biosynthesis of asparagine, reduction of glutamine level in the plasma by asparaginase may further aid in sustaining asparagine depletion. The effectiveness of asparaginase in treating ALL is observed in the complete remission in 30 to 65% of patients treated with asparaginase as a single therapeutic agent [191]. Taken in combination with other chemotherapeutics, asparaginase resulted in a 71% event-free survival versus 31% event-free survival without asparaginase after a median of 9.4 years [192]. In fact, the event-free survival rate is currently around 80% for childhood ALL with optimized dosing, treatment schedule, and combination therapy. In contrast, the long-term survival rate is only 38 to 50% for adult [193]. The poor patient outcome is most likely due to the higher incidence of allergic reactions, antibody formation, and reduction in enzyme activity observed in adult patients. Studies have shown that early and sustained asparagine depletion for at least the first 30 weeks of therapy is critical in the positive patient outcome [194]

There are currently three forms of asparaginase approved for clinical use: asparaginase from *E. coli* (marketed as Elspar®), asparaginase from *Erwinia chrysanthemi* (marketed as *Erwinia*), and polyethylene glycol conjugated asparaginase from

E. coli (marketed as Oncaspar®) [195]. The treatment for ALL typically consists of three phases: a remission-induction phase, an intensification or consolidation phase, and a continuation phase [196]. The purpose of the remission-induction phase is to destroy almost all of the initial leukemic cells in the attempt to return hemopoiesis back to normal. The standard remission-induction treatment regimen includes a glucocorticoid, vincristine, and asparaginase for two weeks. The consolidation or intensification phase is designed to destroy drug-resistant residual leukemic cells to reduce the risk of relapse. Different treatment regimens are employed, including high-dose methotrexate and mercaptopurine, same treatment as the remission-induction phase, and vincristine and corticosteroid with high-dose asparaginase for 20 to 30 weeks. The continuation treatment usually includes daily mercaptopurine and weekly methotrexate for 2 to 2.5 years.

Since all three forms of asparaginase are bacterial proteins, they are able to elicit immune response against them, leading to hypersensitivity. About 25% of patients treated with foreign proteins experienced hypersensitivity ranging from mild allergic reactions to anaphylactic shocks because of protein immunogenicity [197]. Asparaginase-associated toxicities are either related to immunological reactions to the foreign protein or the inhibition of protein synthesis due to asparagine depletion [197]. Acute hypersensitivity reactions ranging from mild local allergic reactions to fatal anaphylactic shocks usually occurs within a few hours of asparaginase administration [190]. In fact, 10 to 30% of patients experienced hypersensitivity reactions to Elspar® treatment [195]. Up to 80% incidence of hypersensitivity is reported fol-

lowing additional asparaginase exposure during intensification or re-induction treatment after relapse [191]. Hypersensitivity has been reported in 3 to 37% of the patients treated with *Erwinia* [195]. With Oncaspar®, the rate of allergic reactions is lower at 3 to 24% [195]. Other asparaginase-associated toxicities include hyperglycemia, thrombosis, hypertriglyceridemia, myelosuppression, hepatocellular dysfunction, neurotoxicity, and pancreatitis [195]. Neurotoxicity has been reported in 25% of adult patients treated with Elspar®. Study has shown that patients who tolerated more than 25 weekly doses of asparaginase had a better event-free survival than those who received 25 or fewer doses [193]. These dose-limiting toxicities hinder the effectiveness of asparaginase treatment.

In addition, the development of neutralizing antibodies against foreign proteins can lead to rapid clearance of the foreign proteins known as "silent inactivation" [198]. Up to 70% of children and 80% of adult patients develop antibodies against asparaginase eventually when treated with Elspar® [194]. With Oncaspar®, up to 12% of children and 15% of adult patients without prior exposure to asparaginase still develop antibodies against the enzyme [190]. PEGylation appears to reduce the immunogenicity of asparaginase, but does not completely eliminate it. There is evidence linking production of antibodies against asparaginase with shorter half-life of asparaginase, higher plasma levels of asparagine, and reduced efficacy of the treatment [191]. Therefore, development of antibodies against asparaginase can lead to resistance to asparaginase therapy.

The PEGylated form of asparaginase is a modification to the enzyme to not

just reduce its immunogenicity, but also improve its circulation half-life. The circulation half-life of the different forms of asparaginase in children with ALL are about 1.24 days, about 0.65 days, and 5.73 days for Elspar®, *Erwinia*, and Oncaspar®, respectively [194], [199]. Since Elspar® half-life is about 1.2 days in patients, the therapeutic enzymes must be administered every 2 to 5 days to achieve sustained asparagine depletion. Oncaspar®, with a half-life of 5.7 days, only needs to be administered once every 2 weeks to achieve the same effect [197]. However, when the patients develop antibodies against asparaginase, the enzyme circulation half-life is significantly reduced. Circulation half-life of Oncaspar® is reported to drop to 1.82 days in patients previously treated with the native form of the enzyme; these patients also developed hypersensitivity [190]. This shows cross-reactivity between antibodies against Elspar® and Oncaspar®. However, there are no evidence of cross-reactivity between antibodies against Elspar® and *Erwinia* [193]. Hypersensitive patients are usually switched to *Erwinia* or put on increased dosing frequency of Oncaspar®. However, the optimal dose and duration of *Erwinia* is not well-established [190].

Both arginine and asparagine depletion with non-human enzymes appear to encounter the same limitations, even with PEGylation. Incidence of hypersensitivity, development of neutralizing antibodies against the enzyme, and reduction of enzyme circulation half-life are the three main challenges. In addition, there are clinical studies supporting correlation between sustained amino acid depletion for weeks with improved patient outcomes. Therefore, for non-human enzymes to have clinical efficacy, they must be delivered in a non-immunogenic manner for an extended period

of time. For non-human enzyme to be a viable clinical option for cancer treatment, nanotechnology may be applied to engineer a nanoparticle-assisted delivery vehicle to carry non-human enzymes within these nanoparticles to protect them from the immune systems and enhance their circulation half-life [200].

3.2 Current Enzyme Delivery Technology

The previous section describes the successes and challenges of systemic depletion of cancer-essential amino acids in treating cancer patients. Unfortunately, depletion through dietary restriction is generally insufficient to attain a level that is therapeutically relevant. Because of the high affinity and specificity of enzymes, enzymatic depletion of amino acids has become the main approach. However, the human genome does not encode enzymes with the required affinity and specificity for therapeutic purposes [201]. As a results, the use of heterologous enzymes such as *E. coli*-derived asparaginase and *Mycoplasma arginini*-derived arginine deiminase is unavoidable. In addition to being susceptible to degradation by circulating proteases, heterologous enzymes are also immunogenic. They can elicit adverse immune responses such as development of neutralizing antibody against the enzyme and hypersensitivity reactions. Neutralizing antibodies cause rapid clearance of the enzymes, leading to enzyme inactivation. This is undesirable since clinical studies showed that amino acid depletion must last for weeks to show efficacy. Hypersensitivity reactions may lead to reduce dosage or treatment termination.

The current therapeutic enzyme delivery systems focus on solving these two major challenges. Blood proteases, neutralizing antibodies, and renal clearance contribute to the short circulation half-life of therapeutic enzymes [202]. Immunogenic epitopes of the heterologous enzymes elicits hypersensitivity reactions. Therefore, the designs for enzyme delivery system generally attempt to protect the enzymes from proteases and mask the immunogenic epitopes from immune cells. Both challenges may be addressed with enzyme stabilization and enzyme encapsulation.

3.2.1 Enzyme Stabilization

The strategies for enzyme stabilization include protein engineering and chemical modification [203]. Protein engineering includes directed evolution, site-directed mutagenesis, peptide chain extensions, post-translation modifications, and utilization of fusion partners to improve protein properties such as efficacy, stability, specificity, immunogenicity, and pharmacokinetics [204].

Chemical modification includes intramolecular or intermolecular crosslinking of the peptide chain for enzyme stabilization. Another chemical modification is the conjugation of enzymes to water-soluble and biocompatible polymers. Polymers such as polyethylene glycol (PEG), chitosan, alginate, cellulose, and hyaluronate have become popular in recent years.

The most common strategy is to chemically attach PEG molecules to a therapeutic enzyme to increase its circulation half-life and reduce its immunogenicity. Adding a PEG layer can increase the size of the therapeutic enzymes to avoid renal

filtration, sterically shield the therapeutic proteins from proteases and antibodies, and mask certain immunogenic epitopes [201]. Amino acids are small molecules that can still easily cross the PEG layer to reach the active site on the enzymes [202]. The PEG layer is proven to be successful in extending the circulation half-life of PEGylated asparaginase (i.e. Oncaspar®) and PEGylated arginine deiminase (i.e. ADI-PEG20). In fact, the dosage has been reduced 2.4 times from 6000 IU/m^2 dose of native asparaginase to 2500 IU/m^2 dose of the PEGylated version. The dosing frequency is also reduced from 15 doses of the native asparaginase to 3 doses of the PEGylated version due to the extended circulation half-life [202].

However, the PEG layer may only partially or transiently reduce the immunogenicity of the therapeutic enzymes. As evident in the case of Oncaspar® and ADI-PEG20, a majority of patients still develop neutralizing antibodies against these heterologous enzymes. In addition, the process of attaching PEG molecules is random and may negatively affect the enzyme binding site. It was reported that 50% of the arginine deiminase activity was lost after attachment of PEG molecules [202].

3.2.2 Enzyme Encapsulation

Because of persistent immunogenicity and loss of activity of therapeutic enzymes after PEGylation, other delivery systems in the form of enzyme-encapsulated nanoparticles have been developed. The strategies for enzyme encapsulation usually involved loading enzymes within nanoparticle carriers. The potential advantages of using nanoparticles as enzyme carriers may include improved enzyme stability, re-

duced immunogenicity, and fewer toxicity. In addition, varying the material, size, shape, and surface functional groups of the nanoparticles may further extend the circulation half-life of the nanoparticles and the corresponding enzymes.

The most common type of nanoparticles studied for therapeutic enzyme delivery are liposomes, polymeric nanoparticles, and silica nanoparticles [205]. Polymeric and liposomal nanoparticles have been discussed in the previous chapter. Silica nanoparticles will be discussed in the next section. Although there is potential for success in applying these nanoparticles to therapeutic enzyme delivery, none of these enzyme-encapsulated nanoparticles have been tested in clinical trials yet.

3.3 Silica Nanoparticles

Although PEGylating therapeutic enzymes has gained some clinical success in improving the performance of enzyme therapy, there are still some limitations associated with immunogenicity and short circulating half-life. Nanoparticles as delivery vehicles for therapeutic enzymes may be able to solve these issues. In designing nanoparticles as carriers for therapeutic enzyme delivery for systemic amino acid depletion, there are a few important considerations. First, the material of the nanoparticles must be biocompatible to avoid causing toxicity to organs. Second, the synthesis process of the enzyme-loaded nanoparticles must not affect the enzyme activity. Third, the nanoparticles must protect the enzymes from degradation by proteases and recognition by the immune system. Fourth, the nanoparticles must

have long circulating half-life in blood in order for the enzymes to have sustained effects. Finally, the material must be biodegradable to avoid accumulation that leads to long-term toxicity.

3.3.1 Synthesis

Silica nanoparticles are one of the potential delivery systems for therapeutic enzyme delivery that can be designed to meet all the criteria. Currently, there are three different methods developed for the synthesis of silica nanoparticles. The first two methods involve using a template for silicification to occur and the subsequent template removal to create pores for loading therapeutic agents. The last method involves a dissolution and regrowth process to create silica nanoparticles without the need for templates. Regardless of the synthesis methods, all approaches involve silica formation and share very similar physiochemical properties of silica such as ease of functionalization with surface silanol groups.

In bulk solution, silica precursors such as tetraethyl orthosilicate (TEOS) or tetramethyl orthosilicate (TMOS) are first hydrolyzed in the presence of water very quickly, followed by the relatively slower formation of silica nucleation sites. Subsequently, the preferential reaction of residual silica precursors with the surface silanols on the nuclei contributes to the growing size of the final silica nanoparticles [206]. This growth of silica is known as the condensation reaction. At pH above its isoelectric point of 2.0, silicates are negatively charged. The condensation rate increases with increasing negative charge of the silicates until it reaches a maximum

at pH around 7.5 [207]. Since the silicates tend to condense onto positively-charged surfaces via electrostatic attraction and hydrogen-bonding interaction, the templates for synthesizing silica nanoparticles are usually cationic. When surface silanols are participating in the condensation reaction to form the bonds between silicon and oxygen, there is a high tendency for fusion between silica nanoparticles, resulting in irreversible aggregates. Furthermore, the silicates may self-condense to form solid silica beads in addition to forming silica on the templates. By conducting the reaction in a highly diluted solution, the self-condensation rate can be suppressed and the tendency to form aggregates can be reduced [208]. The result is the formation of a stable colloidal solution of uniform silica nanoparticles.

At physiological pH, the silanol groups on silica surfaces are deprotonated and contribute to the intrinsic negative charge of silica nanoparticles [209]. Many commercially available silanes such as aminosilanes and PEG-silanes can be condensed onto the silica surface to modify the silica surface with positive amine groups or neutral PEG layer, respectively. Alternatively, cationic polymers or lipids can be coated onto the surface of silica nanoparticles by electrostatic interaction [210]. To retain therapeutic enzymes within the silica nanoparticles, the enzymes must either be strongly adsorbed within the inner surface of the particles or be "sealed" with a cationic polymer coating or lipid bilayers after the enzymes are loaded [209].

The first method of synthesizing silica nanoparticles was developed in the 1990s [174]. Mesoporous silica nanoparticles (MSN) are synthesized using cationic surfactants as templates to produce silica with high surface area, tunable pore size,

and controllable particle size. In general, MSNs are synthesized at room temperature by hydrolysis and condensation of TEOS in aqueous alkaline solutions containing cetyltrimethylammonium bromide (CTABr) surfactant. At concentration higher than the critical micelle concentration, the surfactant molecules self-assemble into micelles [209]. Silica condensation on the self-assembled structure forms an amorphous silica mold of the micelles. Removal of the surfactant by extraction or calcination results in the final spherical particle that is composed of ordered hexagonally-arranged cylindrical channels (also referred to as mesopores) [207]. MSNs that are 70 to 500 nm in diameter have been synthesized [211]. These MSNs can have specific surface area as high as 700 m^2/g and pore size between 1.6 to 10 nm, which is useful for loading small therapeutic molecules [174]. By introducing swelling agents, these mesopores can be synthesized to be as large as 10 to 30 nm for loading larger therapeutic agents such as nucleic acids and enzymes [212], [213]. In addition, elongated nanoparticles like silica nanorods can be synthesized using different ratio of cationic surfactant and silica precursors and changing the pH of the reaction [207]. Tunable size, shape, and pore size are a few of the features of MSNs. However, the main challenges in using MSN for therapeutic enzyme delivery are the low loading capacity of MSNs because of the limited pore volume and the concern for residual CTABr because of its toxicity [214].

Following the emergence of MSNs, another synthesis method was developed to form hollow mesoporous silica nanoparticles (HMSN) by using soft or hard templates as opposed to a single surfactant in the synthesis of MSNs [207]. For HMSN

synthesis with soft templates, two or more surfactants are used to create a complex template with pore forming agents on the surface to generate a mesoporous shell, while forming a hollow interior. Soft templates includes micelle-polymer aggregates [215]; oil-in-water [216], water-in-oil [217], or water-in-oil-in-water emulsions [218]; and other vesicles [219]. Because of the use of large amount and different types of surfactants to create the soft templates, the control over uniform size and shell thickness and the removal of all potentially toxic surfactants is difficult [174]. Hard templates include polymer beads (e.g. polystyrene and polymethyl methacrylate), metal nanoparticles (e.g. gold and silver), and metal oxide nanoparticles (e.g. iron oxide). Of all the templates, polymer beads are the most suitable templates for HMSN synthesis because they are commercially available in a wide ranges of surface functional groups and sizes from sub-100 nm to micrometer, are inexpensive, and are easily removed by calcination. Metal and metal oxide templates require hazardous corrosive acid solution for removal. The main advantage of HMSN is its increased loading capacity since the hollow interior of the nanoparticle is available for carrying therapeutic agents [207]. Increased loading capacity may lead to reduced doses and dosing frequency. However, these HMSNs typically have pore sizes ranging from 1 to 8 nm. The small pore size may not be an issue for loading small therapeutic agents, but it limits the loading of most enzymes, which are typically larger than 10 nm.

The last method is the formation of HMSN without templates. First, monodispersed amorphous solid silica beads are synthesized using the Stöber process, which involves the hydrolysis of tetraalkyl silicates in a mixture of alcohol, water, and am-

monia as the reaction catalyst [220]. Next, these silica particles are dispersed in an aqueous solution of sodium borohydride ($NaBH_4$), where they undergo dissolution of the core and regrowth of the shell to form HMSNs. At higher reaction temperature, the grain size and pore size of the silica shell increase. Therefore, modulating the reaction temperature can tune the shell porosity, which is important for applications requiring size-selective transportation of molecules through the shell [221]. However, the process may not be compatible with the synthesis of non-spherical HMSN.

3.3.2 Biocompatibility

A biocompatible material should not cause unacceptable cytotoxicity, toxicity to organs, or changes of cells and organs at molecular, cellular, and histological levels. Toxicity is further differentiated between acute toxicity from single administration and chronic toxicity from repeated administrations. Silica is generally considered a biocompatible material because of its low toxicity. However, silica type, concentration, route of administration, size, and surface properties may influence its biocompatibility.

Using 110 nm unmodified MSNs, a study found that MSNs have low toxicity when injected intravenously at a single dose or repeated doses in mice [222]. The median lethal dose (LD50) of 110 nm MSNs was higher than 1000 mg/kg. Repeated dosing of 110 nm MSN at 20 mg/kg for 14 days showed no adverse effect. The maximum tolerated dose for MSNs was reported to be 30 mg/kg when given intravenously [223]. There is also a difference between MSN and non-porous silica nanoparticles.

While the LD50 of 110 nm MSNs was found to be higher than 1000 mg/kg, the LD50 of similar size non-porous silica nanoparticles was found to be about 260 mg/kg when given intravenously [224].

Furthermore, toxicity of silica is dependent on the route of administration with intravenous and intraperitoneal injection requiring lower dosage than subcutaneous injection [225], [226]. Subcutaneous injections of 150 nm, 800 nm, and 4 μm MSN showed no toxicity. In contrast, intraperitoneal and intravenous injection in mice resulted in fatal response due to thrombosis [225].

Blood compatibility is a concern because of the potential of silica nanoparticles causing hemolysis. Unmodified silica are negatively charged and may interact electrostatically with positively charged trimethylammonium groups on red blood cell membranes to potentially cause hemolysis. However, studies have found than MSNs have reduced hemolytic effects as compared to non-porous silica due to the reduced silanol density [227]. Furthermore, any hemolytic effects from MSNs may be eliminated with PEGylation [228]. Geometry does not appear to influence the cellular toxicity and hemolytic activity of silica nanoparticles [229].

Cytotoxicity associated with reactive oxygen species (ROS) is another concern with silica nanoparticles. The hydroxyl radical on silica surface may react with water to form ROS [209] and degradation of silica nanoparticles in phagosomes may also produce ROS. ROS can cause cell death by disrupting cell membranes or triggering apoptosis. However, amorphous silica may have a less significant effect on ROS-associated adverse biological effects than crystalline silica [226]. In cell culture

studies, silica appears to be associated with increased ROS level in a size and dose-dependent manner. However, there is no direct evidence correlating increased ROS level with increased cytotoxicity [230].

In general, silica concentration, size, and surface properties can influence the biocompatibility of silica nanoparticles [231]. Taken together, these *in vitro* and *in vivo* toxicity results suggests silica nanoparticles are considered biocompatible, with PEGylation further improving their biocompatibility. With the first silica-based diagnostic nanoparticles approved by the FDA for human clinical trials, the understanding of silica biocompatibility in humans will be further advanced [232].

3.3.3 Biodegradability of Silica Nanoparticles

Ideally, silica nanoparticles should eventually be degraded and excreted from the body without accumulation in healthy tissues. The rate of biodegradation of silica nanoparticles are highly dependent on their synthesis method (e.g. amorphous or crystalline, calcinated or non-calcinated), surface properties, size, and shape [233]. Non-functionalized silica have exposed surface silanol groups that cause them to dissolve fairly rapidly in simulated body fluid under physiological conditions to form soluble non-toxic silicic acid species [234]. Conversely, PEGylated MSNs have slower degradation because the PEG layers delayed phagocytosis by macrophages and degradation in the phagosomes.

Since MSNs are the most widely studied silica nanoparticles, most of the elimination studies focus on them. It was reported that *in vitro* degradation of non-

calcinated MSNs in simulated body fluids occurs in three phases [235]. The first degradation phase is fast and occurs quickly, within hours. The second degradation phase slows down because calcium and magnesium silicate start forming on the surface of the MSNs. The final degradation phase is slow and occurs for days, with the complete dissolution of the MSNs in about two weeks. However, calcinated MSNs do not exhibit this three-phase degradation. In fact, minimal degradation was observed for calcinated MSNs after two weeks. Low degradation rate may result in accumulation and long-term toxicity.

As for *in vivo* degradation, there are data supporting excretion of MSNs through the renal system and hepatobiliary system. Studies on *in vivo* degradation of MSNs showed both MSNs and PEGylated MSNs could be excreted through the renal system of mice [234]. Silica degradation products were detected in urine as early as 30 minutes after intravenous injection of MSNs and PEGylated MSNs of sizes ranging from 80 to 360 nm. The highest excretion, at 45% of the injected dose, was from the largest tested MSNs at 360 nm in diameter. The lowest excretion, at 15% of the injected dose, was from the smallest tested PEGylated MSNs at 80 nm in diameter. In general, PEGylated MSNs showed reduced excretion of silica degradation products when compared to their unmodified counterpart within the tested size range. Similarly, smaller sized MSNs have lower excretion through the renal system compared to larger sized MSNs. Therefore, renal excretion is dependent on size and surface modifications. There are also studies that found dysfunctions of glomerular filtration and biliary excretion caused by MSNs may allow larger intact

MSNs to be excreted without degrading into smaller products [173].

Because of the wide variety of silica nanoparticles that are synthesized (e.g. MSN, HMSN, size, shape, surface modifications) and the lack of standardization in experimental design, it is difficult to make comparisons among different silica nanoparticles from different research groups. It is necessary to evaluate each type of silica nanoparticles for toxicity and degradation in order to understand its behavior *in vivo*.

3.3.4 Proposed Silica Nanoparticles

There are still several limitations faced by the current enzyme delivery systems that need to be addressed. Although PEGylated enzymes have been approved for clinical use, there is still a persist immunogenicity and loss of enzymatic activity after the PEGylation process. Silica nanoparticles may be a good replacement for therapeutic enzyme delivery based on its biocompatibility, ease of surface functionalization, and biodegradability. In addition, silica nanoparticles have high internal surface area and pore volume for increased loading capacity, tunable particle and pore sizes, and colloidal stability. Although current silica nanoparticles may be able to address the limitations of PEGylated enzymes, there is a need for a silica delivery system that has all of the following features: a small particle size (preferably between 30 and 200 nm), a high pore volume for high loading capacity (preferably hollow silica nanoparticles), a large pore size for loading large enzymes (preferably greater than 10 nm), non-spherical shape (preferably with aspect ratio greater than

1.5), and surface modified (preferably with PEG) for extended circulation half-life. A novel technique for synthesizing silica nanoparticle that is developed to meet these features will be introduced in the next chapter to serve as an alternative to the current enzyme delivery systems. To verify the extended circulation half-life of the proposed nanoparticles, a spherical version of the nanoparticles within the proposed size range will be developed for comparison.

Chapter 4

Synthesis of Hollow Mesoporous Silica Nanoparticles

Using a disease-driven approach outlined in the previous chapter, a new hollow mesoporous silica nanoparticle (HMSNP) is designed for therapeutic enzyme delivery for amino acid depletion in the treatment of certain cancers. To take into account the lessons learned from other nanoparticles described in Chapter 2 and the limitations of the current enzyme delivery systems described in Chapter 3, the proposed HMSNP is designed to have size below 200 nm, ellipsoidal shape, and PEGylated. The general approach to the HMSNP synthesis method is first outlined in this chapter, then the development and optimization of the intermediate steps is described in detail in the subsequent sections.

4.1 Characterization

The characterizations of the polystyrene templates, the polystyrene masks, and the HMSNP include counts, size, and surface charge. The counts of all particles were measured on ViewSizer® 3000 from Manta Instruments, Inc. The hydrodynamic size and poly-dispersity of all particles were measured using the dynamic light scattering technique with Zetasizer Nano ZSP from Malvern Instruments Ltd. The zeta potential of all particles were measured using the dynamic electrophoretic mobility technique with the same Zetasizer Nano ZSP.

A scanning electron microscope (SEM), FEI XL30-SFEG, was used to characterize the silica morphology and the mesopore size of the hollow mesoporous silica nanospheres (HMSNS) and nanorods (HMSNR). The silica samples were diluted with water, dried on a silicon wafer, and sputter-coated prior to imaging with the SEM. Carbon and gold coating were deposited on silica nanoparticles with EM ACE600 from Leica Microsystems. Iridium coating was deposited with Emitech K575X Sputter Coater.

The coating of non-conductive materials such as silica is necessary to enable SEM to image these samples. Coating a conductive layer on the sample inhibits charging, reduces thermal damages, and improves the secondary electron signal used to examine the topography of the sample in the SEM. Three types of coating materials were tested for compatibility with silica for imaging in the SEM. The same sample of 100-nm HMSNS were coated with different materials. Carbon layer ap-

pears transparent to the electron beam, but is conductive to avoid charging of the sample. However, carbon coating thickness ranging from 5 to 10 nm did not produce SEM images with adequate clarity to discern the mesopores on the silica nanoparticles. Gold coating thickness ranging from 5 to 10 nm produced high resolution SEM images, but the grain size of the sputtered gold was too coarse and covered the mesopores. Finally, iridium coating thickness ranging from 2 to 4 nm produced the best SEM images with visible mesopores. The SEM images of the 100-nm HMSNS with carbon, gold, and iridium coatings are shown in Figure 4.1.

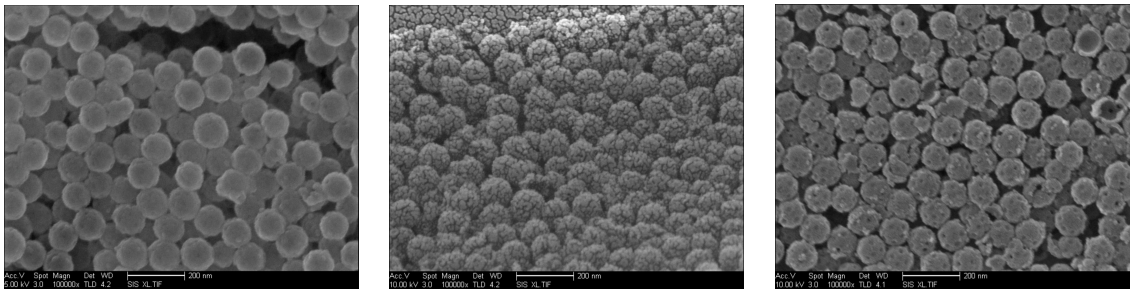

Figure 4.1: Scanning electron micrographs of 100-nm hollow mesoporous silica nanospheres with different coatings for imaging. A 10-nm carbon coating (*left*) did not suppress charging sufficiently to provide the resolution needed to discern the mesopores. A 5-nm gold coating (*middle*) produced grains so coarse that the mesopores were covered. A 4-nm iridium coating (*right*) produced a sufficiently thin layer that suppressed charging without blocking the mesopores to capture the best image.

4.2 Proposed Synthesis of Hollow Mesoporous Silica Nanoparticles

This section describes the general approach to the synthesis of the proposed hollow mesoporous silica nanoparticles (HMSNP). The synthesis uses a nanomasking technology and a modified Stöber process to selectively form silica on the polystyrene beads that function as templates, but not on the polystyrene beads that function as masks. The Stöber process is the chemical reaction of tetraesters of silicic acid with certain solvents. The most common process involves the hydrolysis and condensation of alkoxysilanes, such as tetramethyl orthosilicate (TMOS) or tetraethyl orthosilicate (TEOS), in aqueous alcohols, such as methanol or ethanol, and in the presence of ammonia [220].

A schematic diagram of the synthesis of HMSNP, the loading of enzymes within the HMSNP, and the sealing of the mesopores on the HMSNP is shown in Figure 4.2.

First, the polystyrene templates (shown in grey) are mixed with polystyrene masks (shown in green). The masks are attracted to the templates via electrostatic interaction. Next the silica precursors tetramethyl orthosilicate (TMOS) and 3-aminopropyl trimethoxysilane (APTMS) are added in the presence of ethanol to limit the amount of water in the reaction. If water is in excess, solid silica beads may form in the bulk solution. The mixture is allowed to react for two hours at room temperature while under constant shaking.

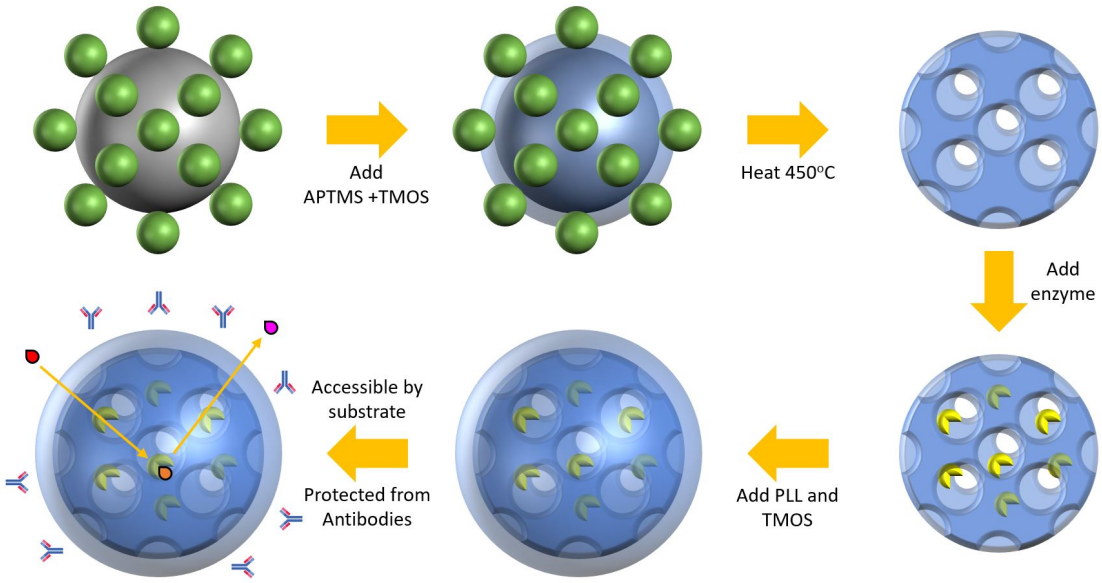

Figure 4.2: A schematic diagram of the synthesis of an enzyme-encapsulated hollow mesoporous silica nanoparticle. (1) Polystyrene template (*grey*) and masks (*green*) are electrostatically attracted. (2) Silica precursors are added to form silica on the template. (3) Particle is calcined at 450°C for 12 hours to remove the template and masks. (4) Enzymes are incubated with the particle and loaded by passive diffusion. (5) Cationic polymers are added to form a coating over the mesopores and silica precursors are added to form silica on the cationic polymers. (6) The final "sealed" enzyme-encapsulated hollow mesoporous silica nanoparticle protects the enzymes from their environment while the nanoporous silica allows small molecules to diffuse in and out of the particle.

The silica formation described here involves TMOS and APTMS. The reaction occurs in three steps: (1) the hydrolysis of TMOS and APTMS, (2) the hydrogen bond formation, and (3) the silanol condensation. APTMS has a positively charged amine group, which is necessary for silica formation on the negatively charged carboxylate groups on the surface of the polystyrene templates. The positively charged amino group from APTMS is attracted to the negatively charged polystyrene surface to initiate silica formation on the surface. The reaction steps in silica formation are shown in Figure 4.3 [236].

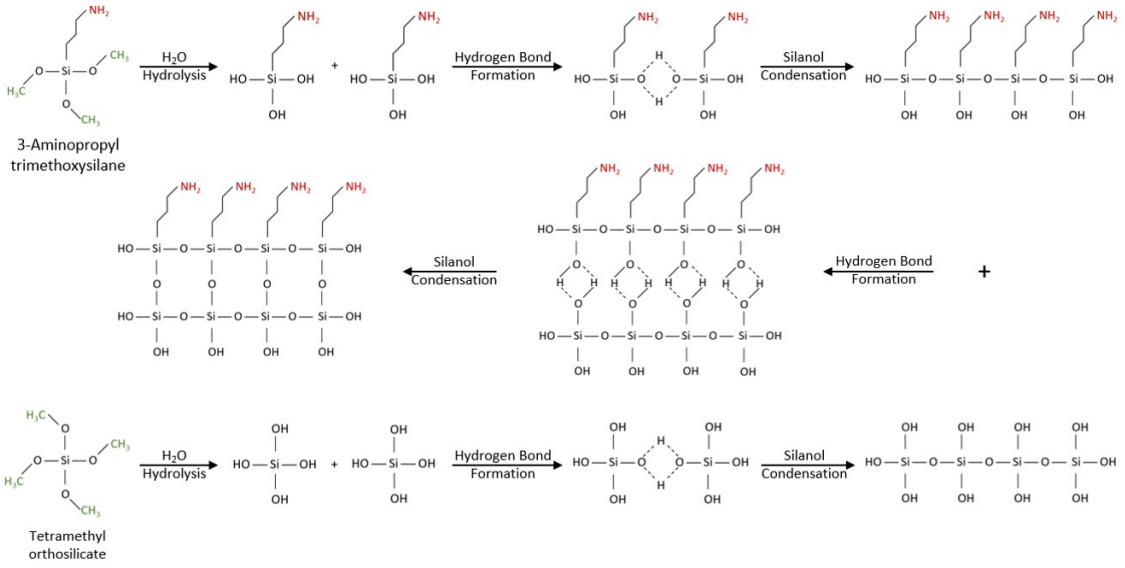

Figure 4.3: The reaction steps in silica formation by hydrolysis and condensation of alkoxysilanes. (1) Silica precursors APTMS and TMOS are hydrolyzed in the presence of water to form reactive silanols. (2) Silanols hydrogen-bond with each other. (3) Condensation reaction forms covalent bond between the silanols. (4) A network of covalent bonds among silanols forms silica.

After the silica formation reaction is completed, the mixture is washed multiple times in ethanol to remove any unreacted silica precursors. The washing step is accomplished by pelleting the silica-coated polystyrene beads via centrifugation at 14,000 rpm for 5 minutes and discarding the supernatant each time to remove any unreacted reagents. The mixture is dried on glass coverslips and calcined at 450°C on a hotplate for at least 12 hours. The polystyrene liquefies and burns off, leaving the silica shell that is spherical and hollow with large pores (i.e. mesopores). The particle and pore size of the HMSNP can be modulated by using different sizes, templates and masks as described in the subsequent section. The HMSNP recovered from the glass coverslips and transferred into water may be kept in 4°C refrigeration for long-term storage.

Next, the desired enzymes may be loaded into the HMSNP by incubating the nanoparticles with the enzymes overnight while under constant shaking. The enzymes will passively diffuse through the mesopores into the nanoparticles over time.

To seal the enzymes within the HMSNP, a layer of sol-gel silica is formed over the calcinated silica. This sealing sol-gel silica layer is formed by first adding positively charged polymer such as poly-L-lysine (PLL). This positively charged polymer is attracted to the negatively charged silica nanoparticles to form a coating over the mesopores. Next, silica precursor TMOS is added to form a silica sol-gel layer over the PLL and to seal the enzymes within the nanoparticles.

Now the enzymes are encapsulated within the sealed HMSNP and prevented from escaping by the sealing layer. The sealing layer also prevents antibodies from entering the nanoparticles to interact with the enzymes; thus, shielding the immunogenic enzymes from the immune system and from clearance. The silica formed is amorphous and intrinsically nanoporous, so small molecules such as enzyme substrates are still able to diffuse into the nanoparticles to react with the encapsulated enzymes and products are able to diffuse out of the nanoparticles.

4.3 Selection and Characterization of Templates

To test the proposed hypothesis of the size and shape dependency on blood circulation half-life, three different types of HMSNP will be evaluated. They are 100-

nm HMSNS (100NS), 200-nm HMSNS (200NS), and elongated HMSNR (100NR) that are nanorods with an aspect ratio of 1.5 (i.e. long axis divided by short axis) and dimensions between 30 and 200 nm.

This section describes the selection of the polystyrene template used to synthesize the three types of silica nanoparticles. For the spherical nanoparticles, two different types of spherical polystyrene beads were evaluated as templates for silica formation. One polystyrene template was amine-functionalized to create a net positive charge for the silica precursor TMOS to react on during silica formation. The other was carboxylate-functionalized to create a net negative charge for the silica precursors APTMS to attract to the beads and TMOS to react on during silica formation.

The amine-functionalized polystyrene beads were purchased from Polysciences, Inc. (Warrington, PA). Two sizes were tested: 0.10 μm and 0.20 μm Polybead® Amino Microspheres at 2.5% solids (w/v) in an aqueous suspension. For the 100-nm amine-functionalized polystyrene spherical template, the average hydrodynamic diameter and average zeta potential were measured with Malvern Zetasizer Nano ZSP instrument. The average hydrodynamic diameter is 119 +/- 37 nm as shown in Figure 4.4. The average zeta potential is -32.5 +/- 7.5 mV as shown in Figure 4.5. The zeta potential was not positive as expected, indicating possible insufficient amine groups on the polystyrene surface.

The 100-nm amine-functionalized polystyrene spherical templates were tested by (1) adding TMOS and water, (2) coating the beads with PLL first before adding

		Size (d.nm):	% Intensity:	St Dev (d.nm):
Z-Average (d.nm): 109.1	Peak 1:	119.3	100.0	37.34
PdI: 0.105	Peak 2:	0.000	0.0	0.000
Intercept: 0.940	Peak 3:	0.000	0.0	0.000
Result quality : Good				

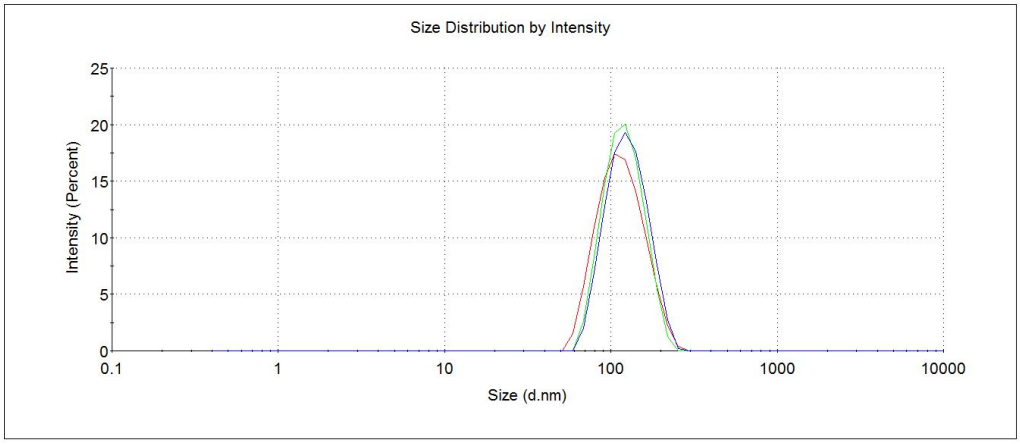

Figure 4.4: The average hydrodynamic diameter of 100-nm amine-functionalized polystyrene spherical beads measured by dynamic light scattering. The average hydrodynamic diameter is 119 +/- 37 nm.

		Mean (mV)	Area (%)	St Dev (mV)
Zeta Potential (mV): -37.2	Peak 1:	-32.5	100.0	7.45
Zeta Deviation (mV): 26.9	Peak 2:	0.00	0.0	0.00
Conductivity (mS/cm): 0.0274	Peak 3:	0.00	0.0	0.00
Result quality : Good				

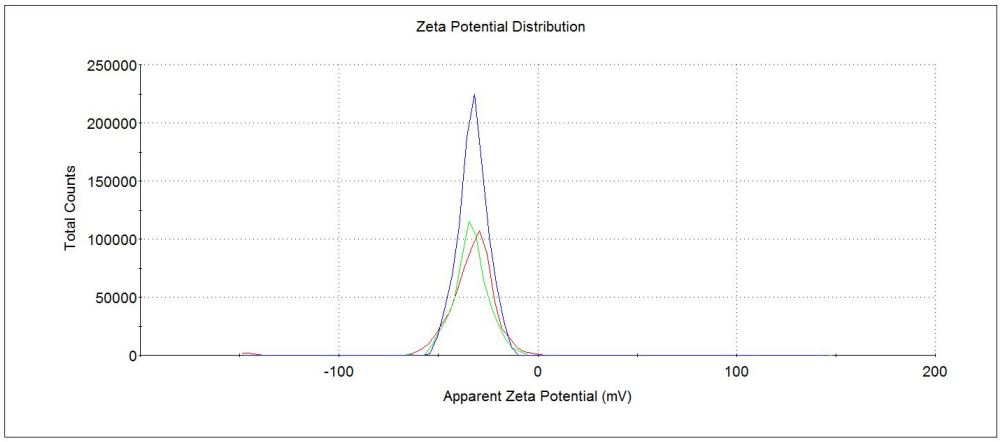

Figure 4.5: The average zeta potential of 100-nm amine-functionalized polystyrene spherical beads measured by dynamic electrophoretic mobility. The average zeta potential is -32.5 +/- 7.5 mV.

TMOS and water, and (3) adding APTMS, TMOS, and water. All three type of silica reactions were conducted in ethanol.

Silica formation was incomplete over the entire surface of the 100-nm amine-functionalized polystyrene template, as shown in the scanning electron micrographs in Figure 4.6, when only TMOS is used. The "popcorn-like" silica formation indicates the positive charge on the polystyrene beads may be insufficient to attract enough TMOS to form a continuous layer of silica on the surface of the template.

To test this hypothesis, the highly positive PLL polymer was first coated on the polystyrene template to convert the surface charge to positive before adding TMOS. The silica formation over the PLL-coated polystyrene beads was uniform over the entire surface of the template as shown in Figure 4.6. However, adding PLL to the template may affect the attraction of the masks to the templates in the subsequent step as the PLL may dissociate from the template and coat over the masks to cause undesirable silica formation on the masks.

Finally, using both APTMS (with positive amine group) and TMOS in the silica reaction appeared to form a uniform silica layer on the surface of the polystyrene template. However, there was also formation of solid silica beads about 200-nm in diameter in the bulk solution as shown in Figure 4.6. The formation of solid silica beads indicates excess of silica precursors. Reducing the APTMS and TMOS reagents produced some incomplete silica shells and/or thin silica shells that break during the synthesis process. Since none of the synthesis methods produced the desired results, the amine-functionalized polystyrene was not a good template for silica formation.

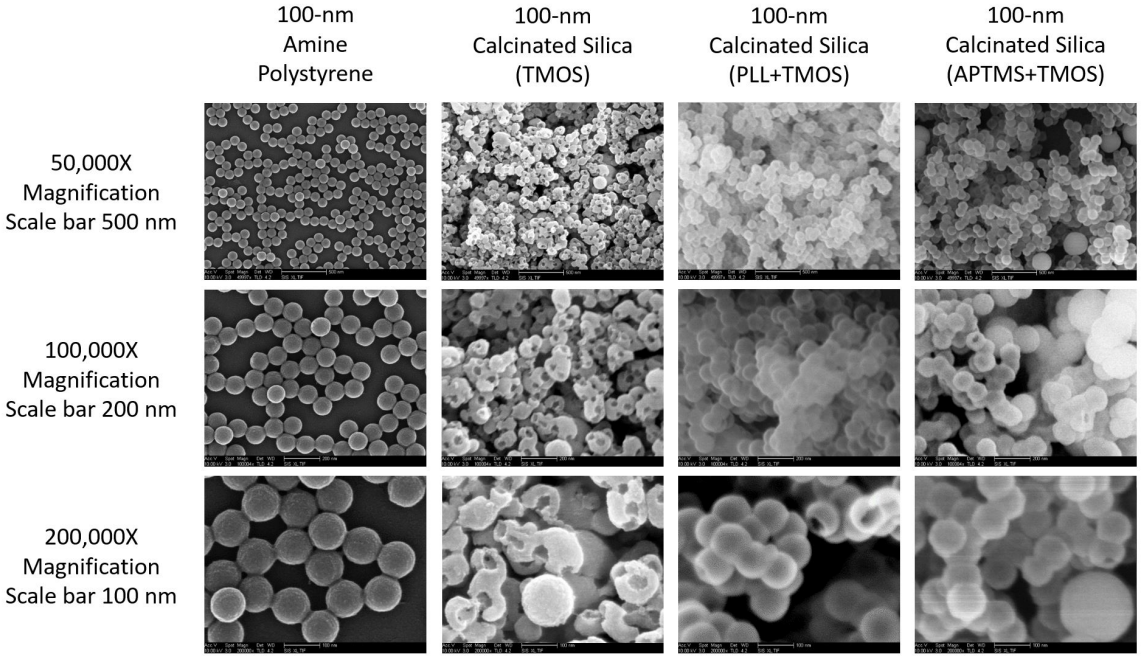

Figure 4.6: Scanning electron micrographs of 100-nm amine-functionalized polystyrene beads and silica formation with different reagents. The unmodified 100-nm amine-functionalized polystyrene beads are shown on the left. The calcinated silica formed with TMOS only showed incomplete silica shells (*second left*). The calcinated silica formed with PLL and TMOS showed the desired complete silica shells (*third left*). The calcinated silica formed with APTMS and TMOS showed the desired complete silica shells, but also the undesired solid silica beads about 200 nm in diameter (*right*).

For the 200-nm amine-functionalized polystyrene spherical template, the average hydrodynamic diameter and average zeta potential were also measured with Malvern Zetasizer Nano ZSP instrument. The average hydrodynamic diameter is 257 +/- 58 nm as shown in Figure 4.7. The average zeta potential is -35.9 +/- 9.2 mV as shown in Figure 4.8. Again, the zeta potential was not positive as expected, indicating possible insufficient amine groups on the polystyrene surface as observed in the 100-nm amine-functionalized polystyrene beads. Hence, the 200-nm amine-functionalized polystyrene beads were not selected as templates for silica formation.

		Size (d.nm):	% Intensity:	St Dev (d.nm):
Z-Average (d.nm): 243.3	Peak 1:	257.0	100.0	58.31
PdI: 0.061	Peak 2:	0.000	0.0	0.000
Intercept: 0.922	Peak 3:	0.000	0.0	0.000
Result quality : Good				

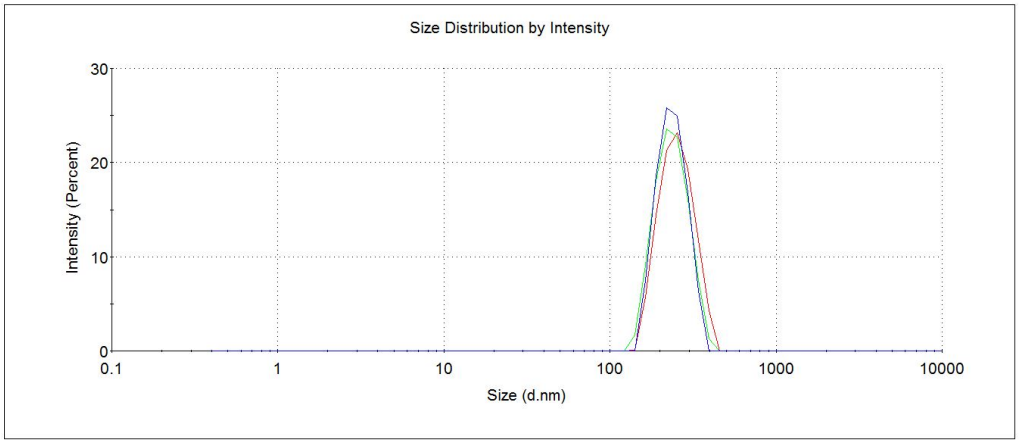

Figure 4.7: The average hydrodynamic diameter of 200-nm amine-functionalized polystyrene spherical beads measured by dynamic light scattering. The average hydrodynamic diameter is 257 +/- 58 nm.

		Mean (mV)	Area (%)	St Dev (mV)
Zeta Potential (mV): -38.5	Peak 1:	-35.9	100.0	9.15
Zeta Deviation (mV): 22.8	Peak 2:	0.00	0.0	0.00
Conductivity (mS/cm): 0.0472	Peak 3:	0.00	0.0	0.00
Result quality : Good				

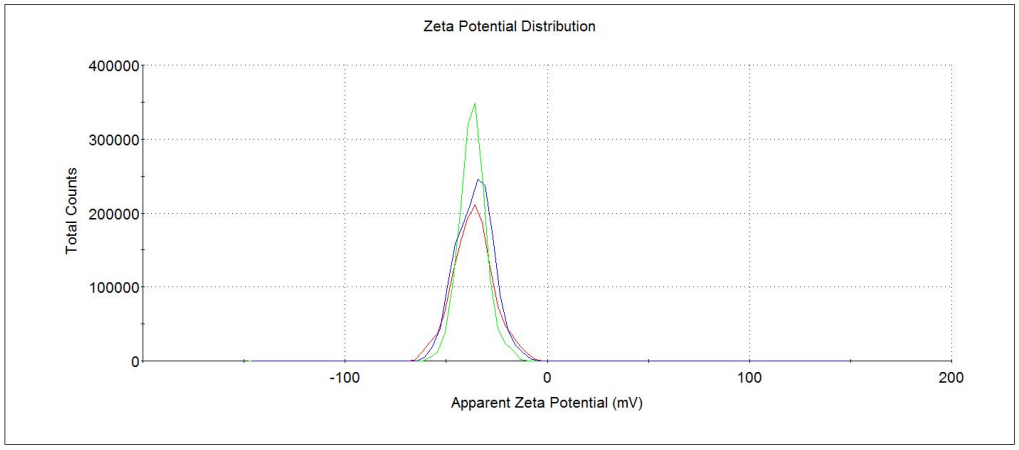

Figure 4.8: The average zeta potential of 200-nm amine-functionalized polystyrene spherical beads measured by dynamic electrophoretic mobility. The average zeta potential is -35.9 +/- 9.2 mV.

Since the amine-functionalized polystyrene spherical beads were not good templates for silica formation, a different type of polystyrene beads were tested. Carboxylate-functionalized polystyrene beads were purchased from Invitrogen^{TM} (a part of Thermo Fisher Scientific, Waltham, MA). Two sizes were tested: 0.1 μm and 0.2 μm carboxylate modified latex (CML) beads at 4% solids (w/v) in an aqueous suspension. For the 100-nm CML spherical template, the average hydrodynamic diameter and average zeta potential were measured with Malvern Zetasizer Nano ZSP instrument. The average hydrodynamic diameter is 114 +/- 26 nm as shown in Figure 4.9. The average zeta potential is -34.0 +/- 6.5 mV as shown in Figure 4.10. The zeta potential was negative as expected from the carboxylate groups on the polystyrene surface.

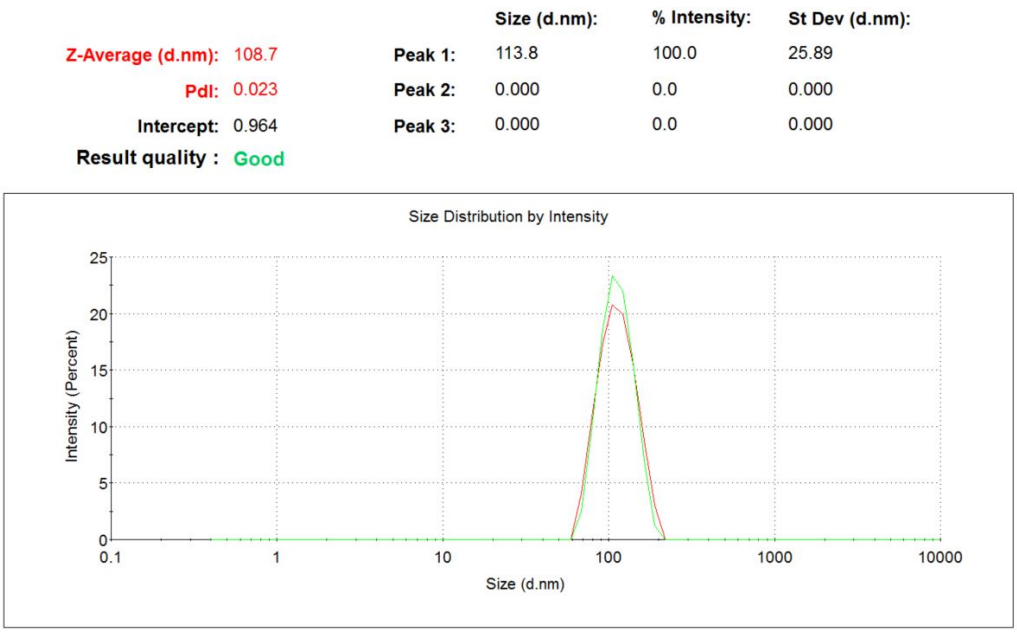

Figure 4.9: The average hydrodynamic diameter of 100-nm carboxylate-modified latex spherical beads measured by dynamic light scattering. The average hydrodynamic diameter is 114 +/- 26 nm.

		Mean (mV)	Area (%)	St Dev (mV)
Zeta Potential (mV): -35.7	Peak 1:	-34.0	100.0	6.47
Zeta Deviation (mV): 18.8	Peak 2:	0.00	0.0	0.00
Conductivity (mS/cm): 0.00349	Peak 3:	0.00	0.0	0.00

Result quality : Good

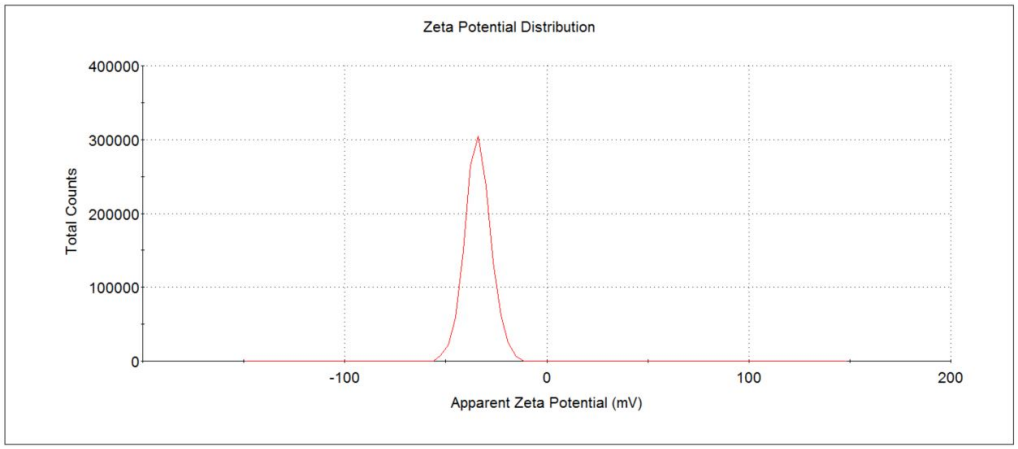

Figure 4.10: The average zeta potential of 100-nm carboxylate-modified latex spherical beads measured by dynamic electrophoretic mobility. The average zeta potential is -34.0 +/- 6.5 mV.

The silica shell formation was complete when APTMS and TMOS were used in the reaction, as shown in the scanning electron micrographs in Figure 4.11.

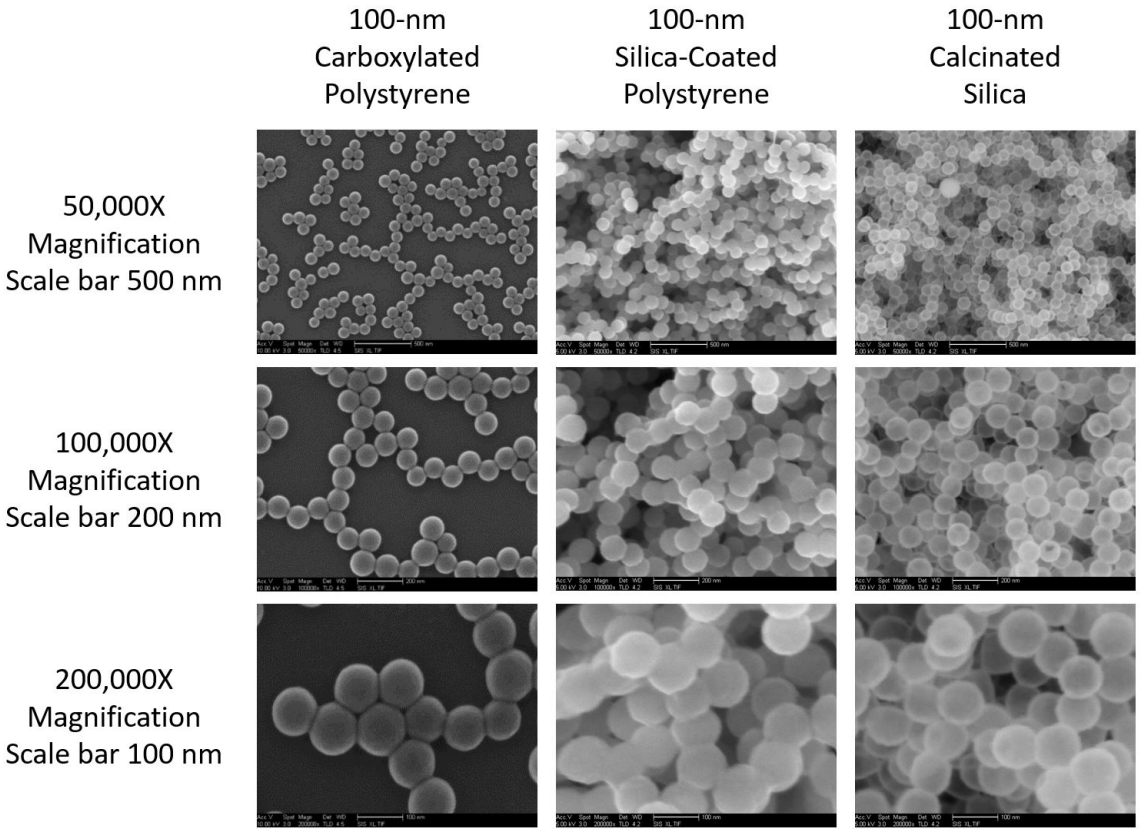

Figure 4.11: Scanning electron micrographs of 100-nm carboxylate-modified latex spherical beads and silica formation with APTMS and TMOS. The unmodified 100-nm carboxylate-modified latex spherical beads are shown on the *left*. The silica formed on the beads with APTMS and TMOS before calcination are shown in the *center*. The calcinated silica formed with APTMS and TMOS showed the desired complete silica shells (*right*).

For the 200-nm CML spherical template, the average hydrodynamic diameter and average zeta potential were measured with Malvern Zetasizer Nano ZSP instrument. The average hydrodynamic diameter is 201 +/- 42 nm as shown in Figure 4.12. The average zeta potential is -43.7 +/- 5.7 mV as shown in Figure 4.13. The zeta potential was negative as expected from the carboxylate groups on the polystyrene surface.

		Size (d.nm):	% Intensity:	St Dev (d.nm):
Z-Average (d.nm): 192.8	Peak 1:	201.0	100.0	42.25
PdI: 0.027	Peak 2:	0.000	0.0	0.000
Intercept: 0.965	Peak 3:	0.000	0.0	0.000
Result quality : Good				

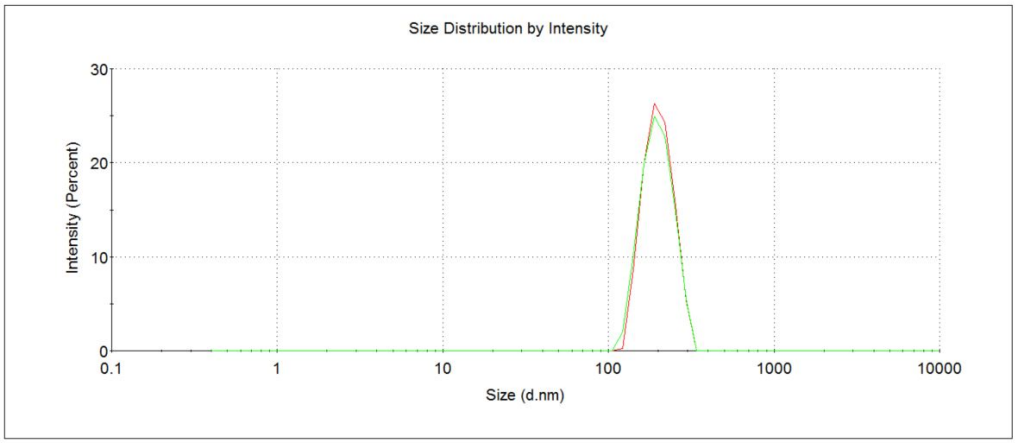

Figure 4.12: The average hydrodynamic diameter of 200-nm carboxylate-modified latex spherical beads measured by dynamic light scattering. The average hydrodynamic diameter is 201 +/- 42 nm.

		Mean (mV)	Area (%)	St Dev (mV)
Zeta Potential (mV): -43.7	Peak 1:	-43.7	100.0	5.69
Zeta Deviation (mV): 5.69	Peak 2:	0.00	0.0	0.00
Conductivity (mS/cm): 0.00410	Peak 3:	0.00	0.0	0.00
Result quality : Good				

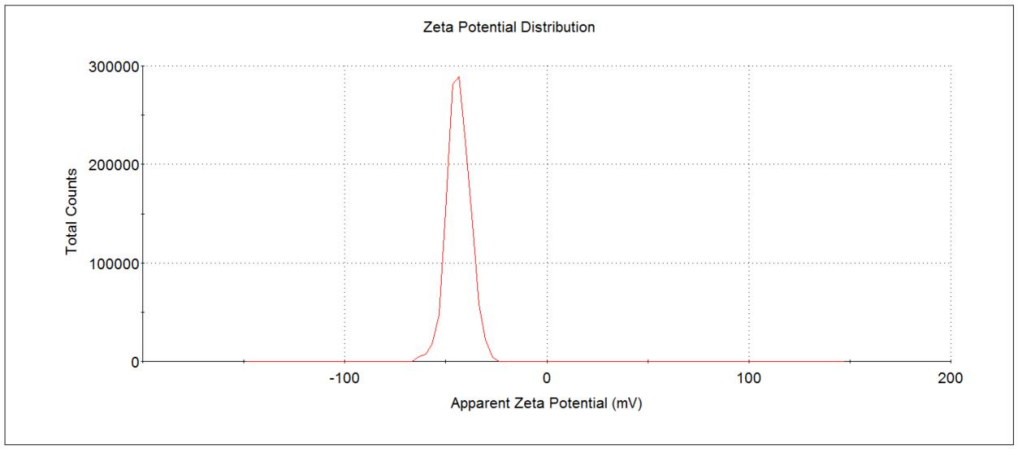

Figure 4.13: The average zeta potential of 200-nm carboxylate-modified latex spherical beads measured by dynamic electrophoretic mobility. The average zeta potential is -43.7 +/- 5.7 mV.

The silica shell formation was complete when APTMS and TMOS were used in the reaction, as shown in the scanning electron micrographs in Figure 4.14. The carboxylate-functionalized polystyrene was selected as the template because silica formation appears to be complete and uniform over the entire surface of the polystyrene with the use of both APTMS and TMOS as silica precursors.

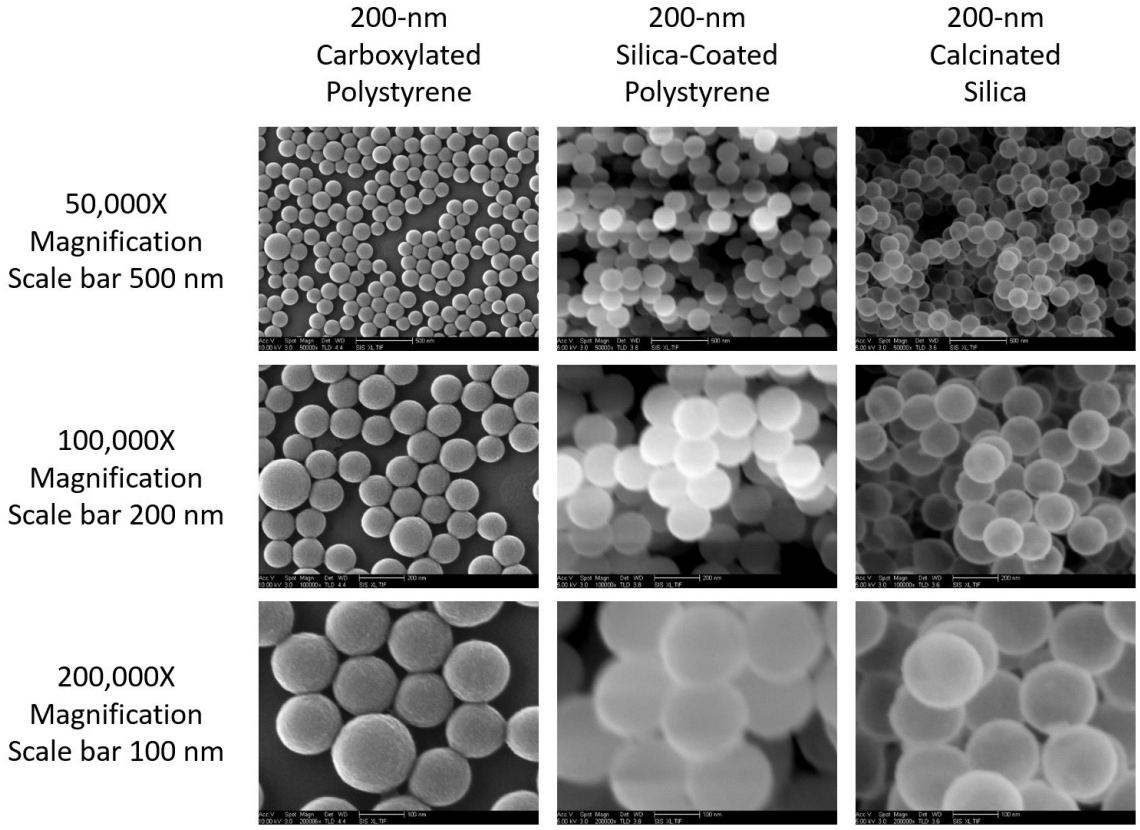

Figure 4.14: Scanning electron micrographs of 200-nm carboxylate-modified latex spherical beads and silica formation with APTMS and TMOS. The unmodified 200-nm carboxylate-modified latex spherical beads are shown on the *left*. The silica formed on the beads with APTMS and TMOS before calcination are shown in the *center*. The calcinated silica formed with APTMS and TMOS showed the desired complete silica shells (*right*).

4.4 Fabrication of Elongated Templates

To synthesize nanorods, the same nanomasking technique is used, except with an elongated polystyrene template instead of a spherical one. The materials used for the synthesis of the elongated polystyrene templates are the following: carboxylate modified latex (CML) beads at 4% solids (w/v) in an aqueous suspension of 0.1 μm mean diameter were purchased from Invitrogen^{TM} (part of Thermo Fisher Scientific, Waltham, MA), poly(vinyl) alcohol (PVA) with molecular weight between 85,000 and 124,000 was purchased from Sigma-Aldrich Co. LLC. (St. Louis, MO), isopropanol was purchased from Acros Organics (part of Thermo Fisher Scientific, Waltham, MA) and Super-Slippery Tape made with Teflon® PTFE for heat resistant with dimension .0045" thick and 4" width x 15' length was purchased from McMaster-Carr Supply Co. (Los Angeles, CA). All materials were used as received.

The elongated polystyrene template is fabricated from spherical poly-styrene beads. First, the spherical polystyrene beads are mixed into a PVA solution. The mixture is allowed to air dry on a flat surface to form a thin film. Next, the PVA film containing the polystyrene beads is stretched to form ellipsoidal voids around the polystyrene beads. Finally, the film is heated beyond the polystyrene glass transition temperature (T_g) to liquefy the polystyrene beads and fill the ellipsoidal-shaped void around them. When the polystyrene beads are cooled, they solidify into the ellipsoidal shape. A schematic diagram of the stretching process is shown in Figure 4.15 [27], [237], [238], [239], [240], [241], [242].

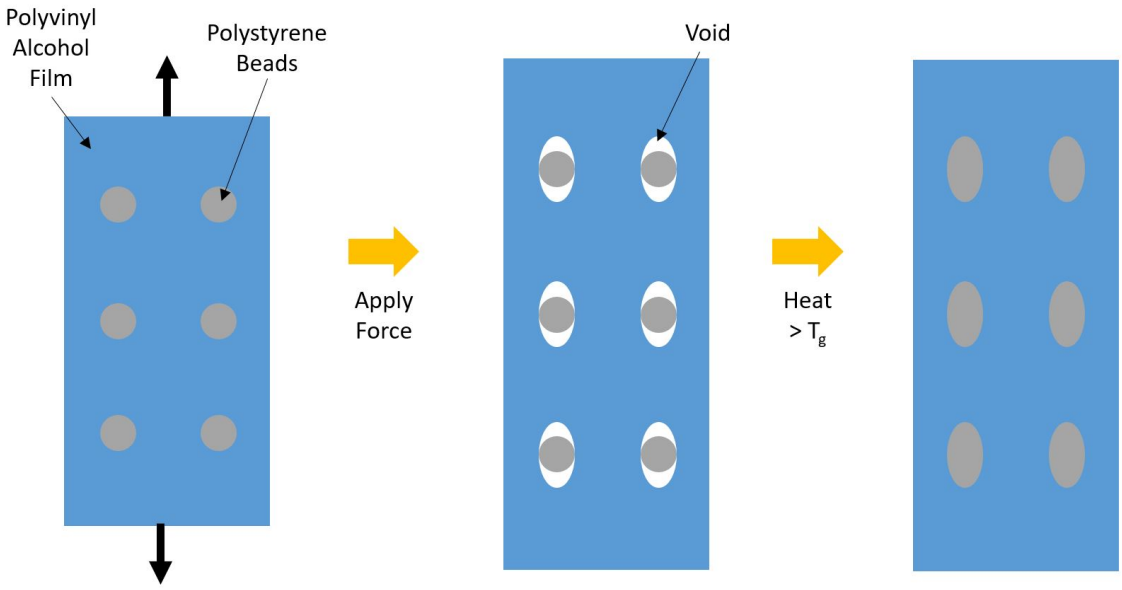

Figure 4.15: A schematic diagram of the synthesis of elongated polystyrene templates. (1) 100-nm carboxylate-modified latex spherical beads are mixed into a polyvinyl alcohol solution and dried on a flat surface to form a thin film. (2) The film is stretched to create ellipsoidal voids around the polystyrene beads. (3) The film is heated beyond the glass transition temperature of polystyrene to liquefy the polystyrene beads such that they fill the voids to assume the ellipsoidal shape.

Elongated polystyrene templates fabricated from stretching the film before or after heating showed no obvious differences. However, it was easier to stretch the film after heating. The polystyrene is recovered from the PVA film by dissolving the PVA film in a 30% isopropanol solution, pelleting the elongated polystyrene with ultracentrifugation, and washing them into water. At this point, the recovered elongated polystyrene templates may be kept in 4°C refrigeration for long-term storage.

To experimentally determine the glass transition temperature of the 100-nm CML spherical beads, the beads were heated to different temperature using a hot-plate. The heated beads were then imaged on the SEM. Based on the scanning electron micrographs shown in Figure 4.16, the polystyrene beads appear to liquefy between 120°C and 140°C.

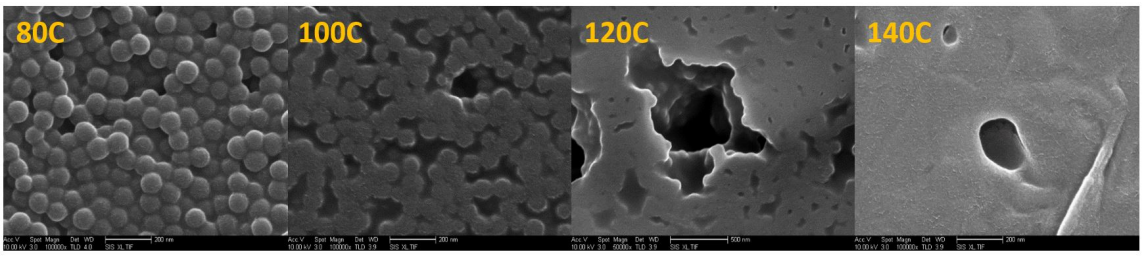

Figure 4.16: Scanning electron micrographs of 100-nm carboxylate-modified latex spherical beads heated to different temperatures. The beads were heated to 80°C, 100°C, 120°C, and 140°C. The glass transition temperature of polystyrene is between 120°C and 140°C, where the beads appeared to liquefy.

The fabrication process of the PVA film containing the 100-nm CML spherical beads is optimized to have sufficient thickness for ease of handling and stretching. It is also optimized for maximum bead density within the PVA film without the beads being so close that they fuse together during the heating and stretching process.

The final design to meet both criteria was to mix the 100-nm CML spherical beads with a 5% PVA solution to maintain a sufficient stiffness to withstand the applied force during the stretching process without tearing. Specifically, 5% and 10% PVA by weight is dissolved in water by heating the mixtures to 85°C under constant stirring at 400 rpm for an hour. The two PVA solutions are cooled to room temperature. 200 μL of the 100-nm CML beads is mixed into 5 mL of the 5% PVA

solution. The 10% PVA solution is used to form the two ends of the film to make the film stiffer for ease of handling. A flat metal sheet that is 10 x 20 cm is used as a mold for casting and drying the PVA film.

Next, the 5 mL of the 5% PVA solution mixed with 100-nm CML beads is dispensed onto the middle of the metal sheet. Then, 15 mL of the 10% PVA solution is dispensed onto the two ends of the metal sheet (i.e. 7.5 mL of 10% PVA solution on each end). The two ends of the film are made from 10% PVA solution to provide resistance to the stretching of the PVA film and sufficient strength to be fixed onto the stretching device with a heat-resistant adhesive tape. Finally, the PVA film is air dried overnight for at least 12 hours. Grid lines are drawn on the portion of the PVA film containing the 100-nm CML beads in order to determine the stretch ratio (i.e. ratio of the stretched PVA film length to its original length). Figure 4.17 shows an image of the final PVA film with 100-nm CML beads embedded.

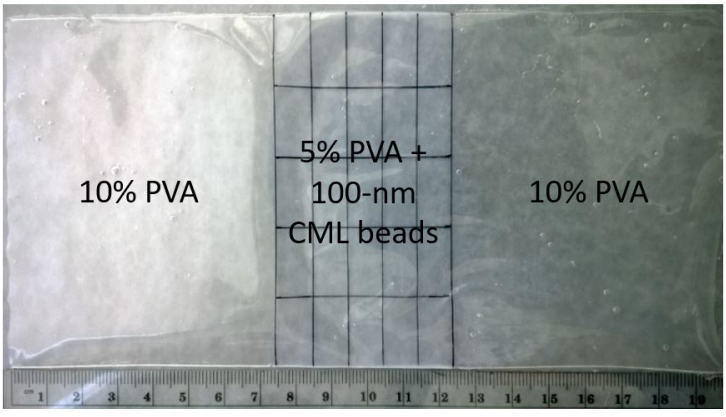

Figure 4.17: Polyvinyl alcohol (PVA) film with 100-nm carboxylate-modified latex (CML) beads embedded. The beads are suspended within the 5% PVA region of the film. Gridlines are drawn on that region for measurements before and after the film is stretched. The 10% PVA regions function as stretch-resistant regions of the film and as attachment sites for the stretching device.

To stretch the PVA film, a stretching device was designed such that the PVA film can be attached with heat-resistant adhesive tapes to the device. The device consists of two metal cylinders for uniform heat conduction. Two screws were drilled into the cylinders such that when the screws are moved toward each other, the cylinders are rotated in opposite direction to stretch the PVA film attached to them. Figure 4.18 shows an image of the stretching device with a PVA film attached with heat-resistant adhesive tapes.

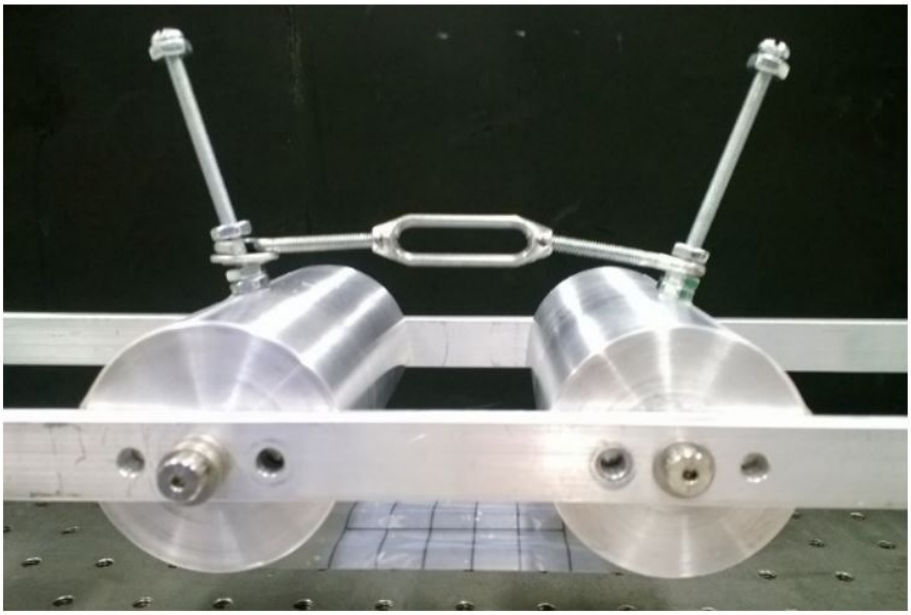

Figure 4.18: A design of the stretching device. The device consists of two metal cylinders for uniform heat conduction. Each end of the PVA film is attached to a cylinder with heat-resistant adhesive tape. When the two screws are moved towards each other, the cylinders rotate in opposite direction to stretch the attached film.

The process of stretching the PVA films containing 100-nm CML beads is described next. First, the stretching device is placed into canola cooking oil that have been pre-heated to 125 +/- 5°C such that only the portion of the PVA film containing the 100-nm CML beads is fully submerged in the oil. The beads are allow to heat up

to the target temperature for 5 minutes before the PVA film is stretched at the rate of about 2 cm per minute. The stretched PVA film is kept at the target temperature in the oil for another minute to ensure the liquefied polystyrene has completely filled the void before removing the stretching device with the attached PVA film from the hot oil. The stretched PVA film is allowed to cool to room temperature while still attached to the stretching device for about 30 minutes. Figure 4.19 shows the configuration of the stretching device and PVA film before and after stretching.

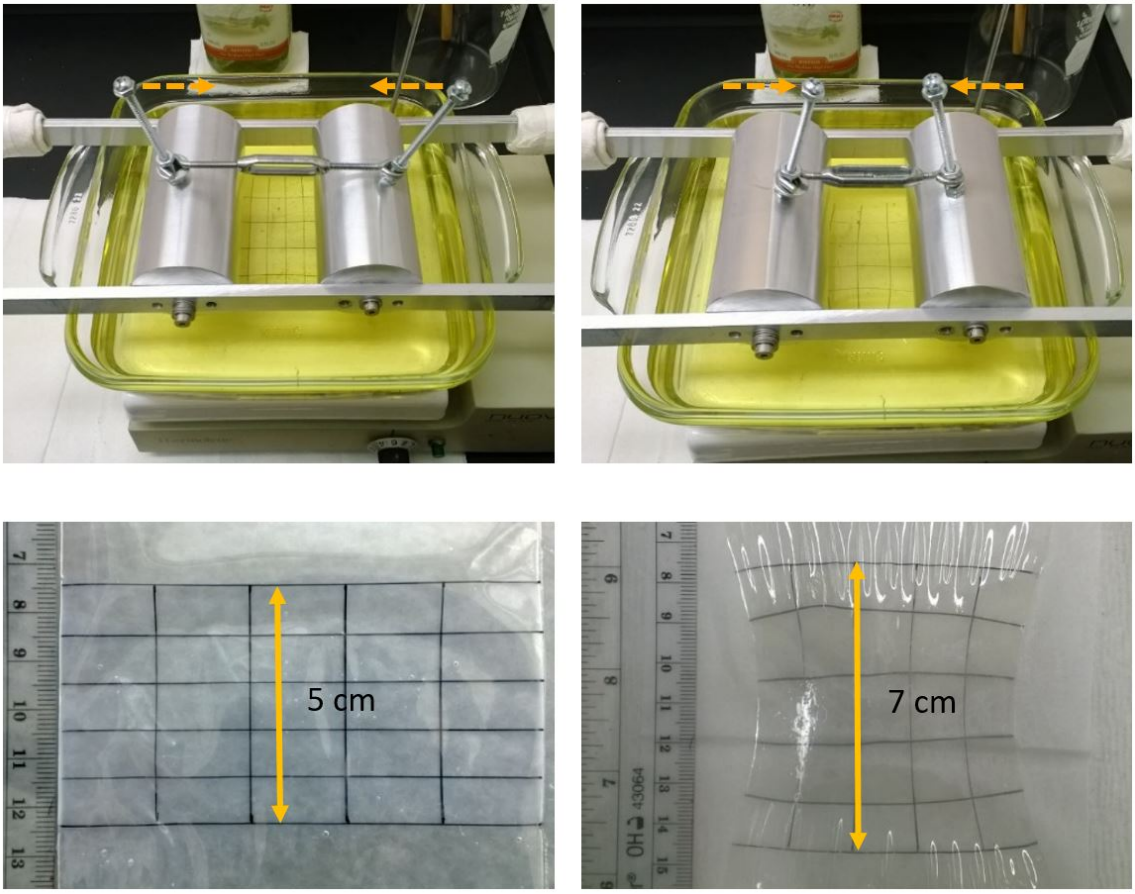

Figure 4.19: Stretching of a PVA film with 100-nm carboxylate-modified latex beads. The configuration of the stretching device in the hot oil bath before (*top left*) and after (*top right*) stretching. The PVA film before (*bottom left*) and after (*bottom right*) stretching.

Once the PVA film has been removed from the stretching device, the portions of the PVA film not containing the 100-nm CML beads are discarded. The grid lines on the portion of the PVA film containing the 100-nm CML beads are measured. Regions meeting the desired stretched ratio are selected for recovery of the elongated polystyrene templates. The dimension of the elongated polystyrene templates may be controlled within a tight tolerance with this grid system.

To recover the elongated polystyrene templates, the selected grids from the PVA film containing them are placed into a 30% isopropanol solution. The solution is heated to 65°C for 1 to 2 hours to dissolve the PVA film. Once the PVA film has been dissolved, the elongated polystyrene templates are washed to remove any residual PVA. The washing process is achieved by pelleting the elongated polystyrene templates using Beckman Coulter Optima™ L-90K Ultracentrifuge with SW 32 Ti rotor at maximum speed of 32,000 rpm (or 175,000 x g) for 2 hours at 25°C and discarding the supernatant. Fresh 30% isopropanol is added to resuspend the elongated polystyrene templates. This process is repeated three times.

Once the PVA residues are removed, the recovered elongated polystyrene templates are washed into water using the same washing process. Swelling of the elongated polystyrene templates will occur if they are stored in 30% isopropanol instead of water. Finally, the elongated polystyrene templates in water is ultrasonicated in an ice bath using Q125 Sonicator from Qsonica, LLC. at 40% amplitude (which output about 12W) for 4 minutes using a 4-second pulse on and 1-second pulse off cycle for a total of 2900 +/- 100 Joules of energy.

The aspect ratio or the ratio of the longer axis to the shorter axis of the elongated polystyrene templates can be modulated by stretching the PVA film to different stretch ratios. Figure 4.20 shows the images taken with the SEM of the elongated polystyrene templates with different aspect ratios. The 1.0 aspect ratio is the original 100-nm CML spherical beads. A 1.75 aspect ratio produces elongated polystyrene templates that are about 80-nm by 140-nm. A 2.0 aspect ratio produces elongated polystyrene templates that are about 80-nm by 160-nm. A 2.3 aspect ratio produces elongated polystyrene templates that are about 75-nm by 170-nm. Based on studies on nanoparticles shape and circulation, an aspect ratio of 1.75 is selected for subsequent *in vivo* circulation studies [173].

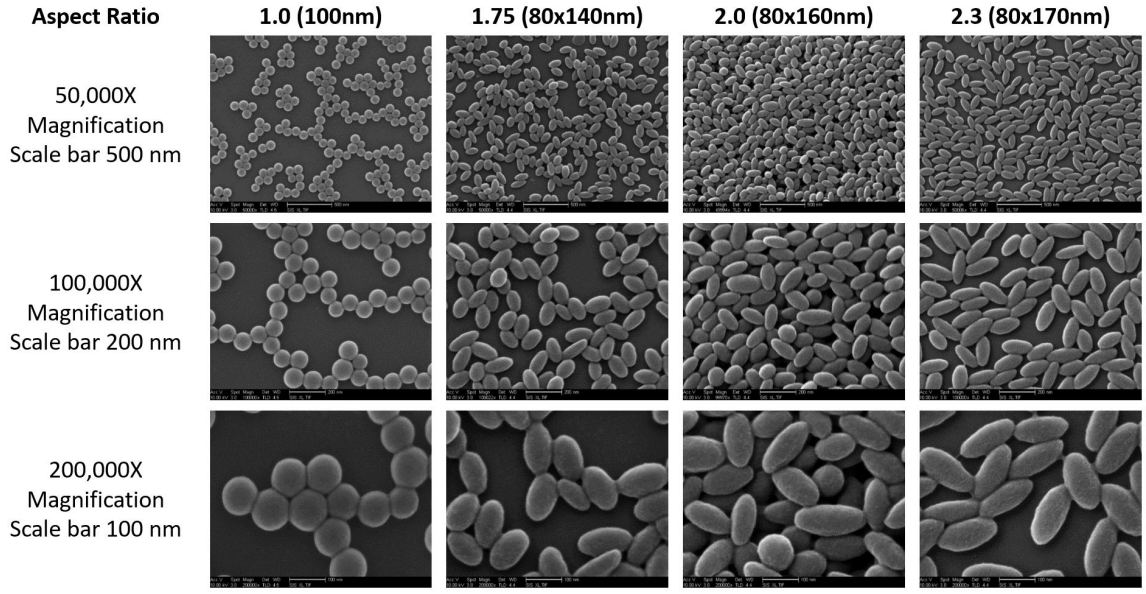

Figure 4.20: Scanning electron micrographs of elongated carboxylate-modified latex templates with different aspect ratios. Aspect ratio of 1.0 is the original 100-nm carboxylate-modified latex spherical beads. Elongated polystyrene templates with aspect ratio of 1.75, 2.0, and 2.3 has short and long axes measuring 80 nm by 140 nm, 80 nm by 160 nm, and 80 nm by 170 nm, respectively.

For the elongated polystyrene templates, the average hydrodynamic diameter and average zeta potential were measured with Malvern Zetasizer Nano ZSP instrument. The average hydrodynamic diameters of the elongated polystyrene templates with aspect ratio of 1.75, 2.0, and 2.3 are 153 +/- 45 nm (as shown in Figure 4.21), 180 +/- 54 nm (as shown in Figure 4.22), and 242 +/- 60 nm (as shown in Figure 4.23), respectively.

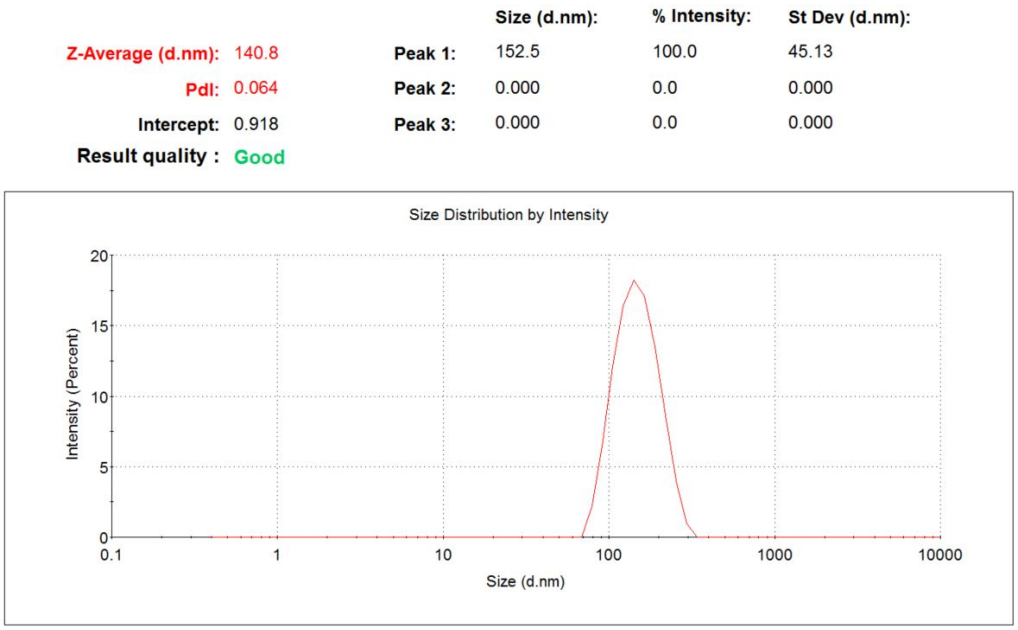

Figure 4.21: The average hydrodynamic diameter of elongated polystyrene templates with 1.75 aspect ratio measured by dynamic light scattering. The average hydrodynamic diameter is 153 +/- 45 nm.

		Size (d.nm):	% Intensity:	St Dev (d.nm):
Z-Average (d.nm): 164.1	Peak 1:	179.9	100.0	54.11
PdI: 0.077	Peak 2:	0.000	0.0	0.000
Intercept: 0.914	Peak 3:	0.000	0.0	0.000
Result quality : Good				

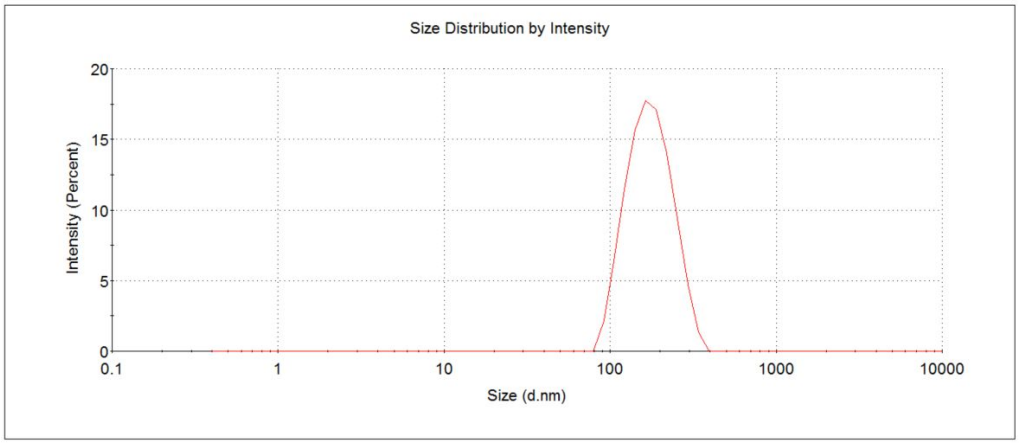

Figure 4.22: The average hydrodynamic diameter of elongated polystyrene templates with 2.0 aspect ratio measured by dynamic light scattering. The average hydrodynamic diameter is 180 +/- 54 nm.

		Size (d.nm):	% Intensity:	St Dev (d.nm):
Z-Average (d.nm): 229.2	Peak 1:	241.5	100.0	60.14
PdI: 0.022	Peak 2:	0.000	0.0	0.000
Intercept: 0.944	Peak 3:	0.000	0.0	0.000
Result quality : Good				

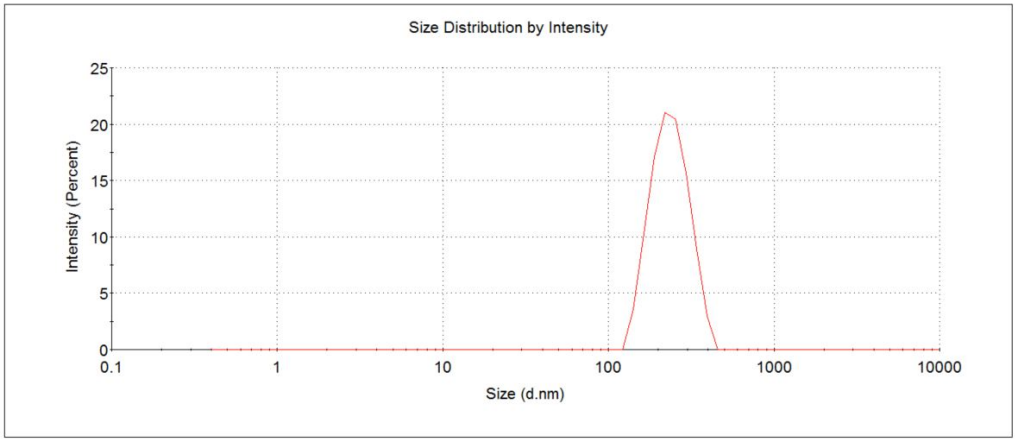

Figure 4.23: The average hydrodynamic diameter of elongated polystyrene templates with 2.3 aspect ratio measured by dynamic light scattering. The average hydrodynamic diameter is 242 +/- 60 nm.

There are discrepancies between the measurements observed in the SEM images versus that taken from the dynamic light scattering (DLS) technique. Samples for imaging in the SEM are prepared in a dried form, so the measurements are taken when the elongated polystyrene templates are dried. DLS measures the hydrodynamic diameter and assumes a spherical shape. For aspect ratio of 1.75, the SEM image showed the short and long axis to be about 80 nm and 140 nm, while the DLS reported a spherical diameter of about 153 nm. For aspect ratio of 2.0, the SEM image showed the short and long axis to be about 80 nm and 160 nm, while the DLS reported a spherical diameter of about 180 nm. For aspect ratio of 2.3, the SEM image showed the short and long axis to be about 80 nm and 170 nm, while the DLS reported a spherical diameter of about 242 nm.

The average zeta potential of the elongated polystyrene templates with aspect ratio of 1.75, 2.0, and 2.3 are -32.0 +/- 4.5 mV (as shown in Figure 4.24), -24.4 +/- 8.6 mV (as shown in Figure 4.25), and -20.4 +/- 9.2 mV (as shown in Figure 4.26), respectively. The drop in zeta potential as the aspect ratio of the template increases is most likely due to the increase in exposed hydrophobic polystyrene polymer as the template surface area increases with increased aspect ratio. Consequently, the carboxylate group density decreases.

		Mean (mV)	Area (%)	St Dev (mV)
Zeta Potential (mV): -32.0	Peak 1:	-32.0	100.0	4.49
Zeta Deviation (mV): 4.49	Peak 2:	0.00	0.0	0.00
Conductivity (mS/cm): 0.00343	Peak 3:	0.00	0.0	0.00

Result quality : Good

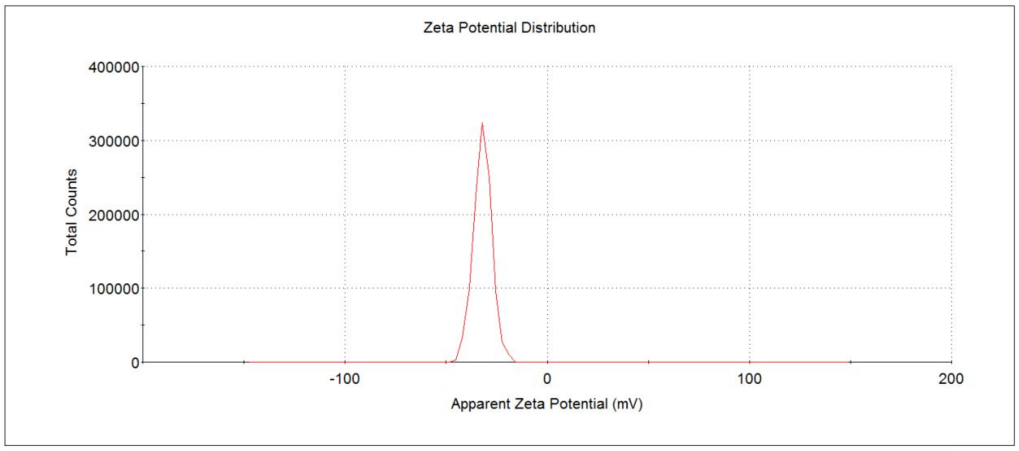

Figure 4.24: The average zeta potential of elongated polystyrene template with aspect ratio of 1.75 measured by dynamic electrophoretic mobility. The average zeta potential is -32.0 +/- 4.5 mV.

		Mean (mV)	Area (%)	St Dev (mV)
Zeta Potential (mV): -25.0	Peak 1:	-24.4	100.0	8.60
Zeta Deviation (mV): 13.9	Peak 2:	0.00	0.0	0.00
Conductivity (mS/cm): 0.00223	Peak 3:	0.00	0.0	0.00

Result quality : Good

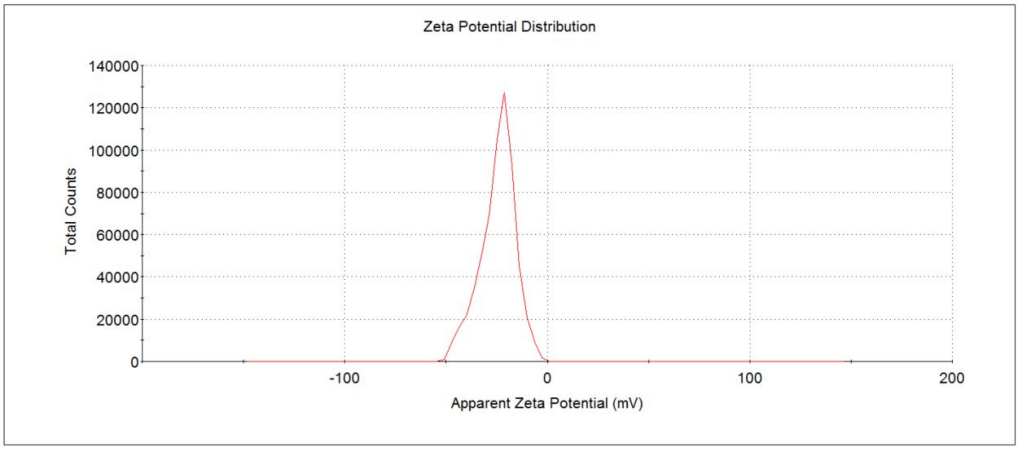

Figure 4.25: The average zeta potential of elongated polystyrene template with aspect ratio of 2.0 measured by dynamic electrophoretic mobility. The average zeta potential is -24.4 +/- 8.6 mV.

		Mean (mV)	Area (%)	St Dev (mV)
Zeta Potential (mV): -22.8	Peak 1:	-20.4	100.0	9.18
Zeta Deviation (mV): 21.5	Peak 2:	0.00	0.0	0.00
Conductivity (mS/cm): 0.00213	Peak 3:	0.00	0.0	0.00

Result quality : Good

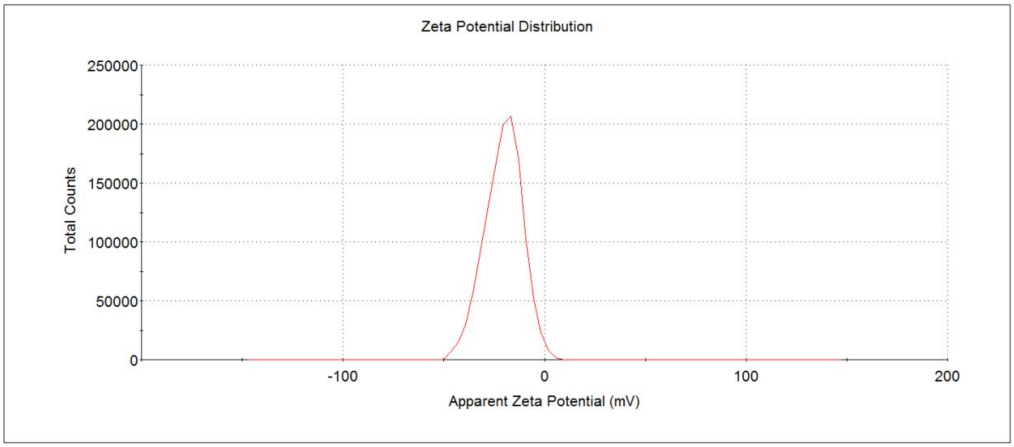

Figure 4.26: The average zeta potential of elongated polystyrene template with aspect ratio of 2.3 measured by dynamic electrophoretic mobility. The average zeta potential is -20.4 +/- 9.2 mV.

4.5 Selection and Characterization of Masks

With the selection of the carboxylate modified latex (CML) beads as the template for silica formation, the next step is to select polystyrene masks that will be electrostatically attracted to the templates and do not have the surface properties conducive to silica formation. Several different types of masks were evaluated. Two types of masks were found to be compatible. One type of masks that works well with the 100-nm and 200-nm CML spherical templates was the unfunctionalized polystyrene beads at 10% solids (w/v) in an aqueous suspension of varying diameters (42 nm, 62 nm, and 77 nm) purchased from Bangs Laboratories, Inc. (Fishers, IN).

The other type of masks that works well with the elongated polystyrene templates was the Nanobead NIST Traceable Particle Size Standard polystyrene microspheres at 1% solids (w/v) in an aqueous suspension of 50 nm mean diameter purchased from Polysciences, Inc. (Warrington, PA).

The SEM images of the 100-nm CML templates and the 42-nm, 62-nm, and 77-nm unfunctionalized polystyrene masks are shown in Figure 4.27.

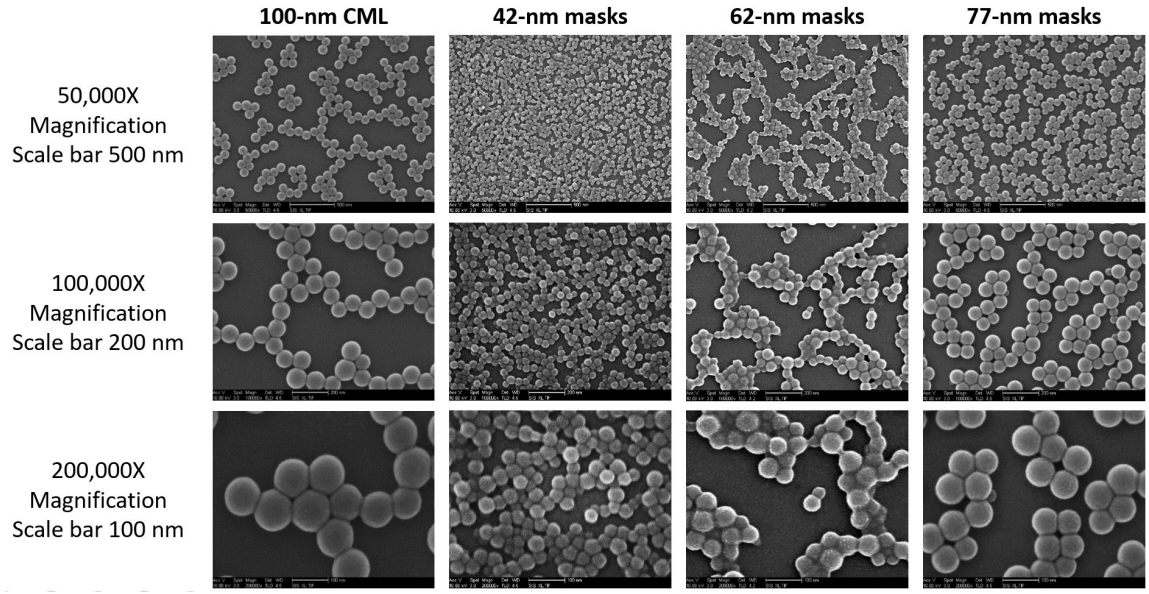

Figure 4.27: Scanning electron micrographs of spherical templates and masks of different sizes. The templates selected are the 100-nm carboxylate-modified latex beads. The masks selected are the 42-nm, 62-nm, and 77-nm unfunctionalized polystyrene beads.

For the 42-nm, 62-nm, and 77-nm unfunctionalized polystyrene masks, the average hydrodynamic diameters were measured with Malvern Zetasizer Nano ZSP instrument. The average hydrodynamic diameters of the 42-nm, 62-nm, and 77-nm masks are 46.0 +/- 11.6 nm (as shown in Figure 4.28), 68.6 +/- 15.7 nm (as shown in Figure 4.29), and 88.4 +/- 20.0 nm (as shown in Figure 4.30), respectively.

		Size (d.nm):	% Intensity:	St Dev (d.nm):
Z-Average (d.nm): 43.32	Peak 1:	45.96	100.0	11.57
PdI: 0.047	Peak 2:	0.000	0.0	0.000
Intercept: 0.912	Peak 3:	0.000	0.0	0.000
Result quality : Good				

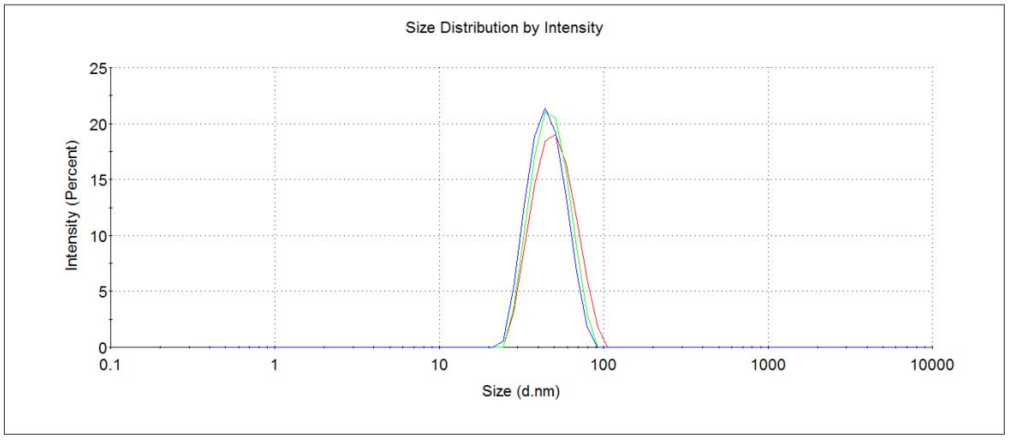

Figure 4.28: The average hydrodynamic diameter of 42-nm unfunctionalized polystyrene spherical beads measured by dynamic light scattering. The average hydrodynamic diameter is 46.0 +/- 11.6 nm.

		Size (d.nm):	% Intensity:	St Dev (d.nm):
Z-Average (d.nm): 65.55	Peak 1:	68.57	100.0	15.67
PdI: 0.021	Peak 2:	0.000	0.0	0.000
Intercept: 0.936	Peak 3:	0.000	0.0	0.000
Result quality : Good				

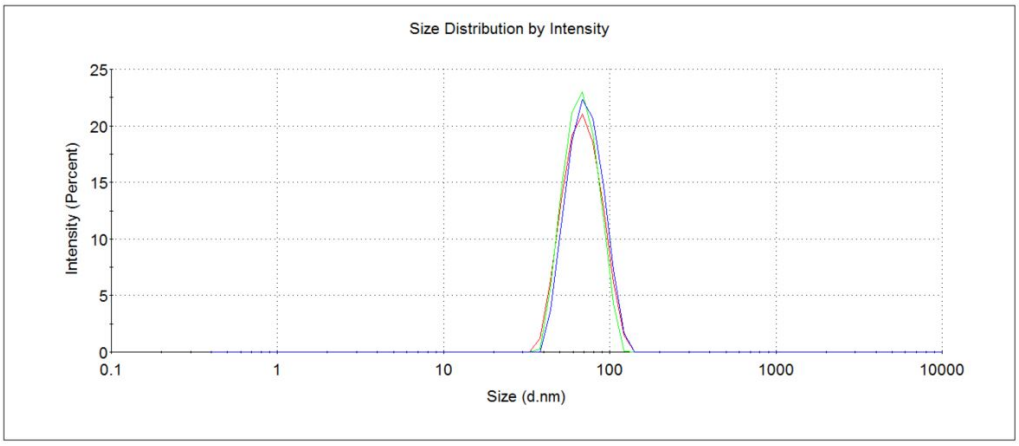

Figure 4.29: The average hydrodynamic diameter of 62-nm unfunctionalized polystyrene spherical beads measured by dynamic light scattering. The average hydrodynamic diameter is 68.6 +/- 15.7 nm.

			Size (d.nm):	% Intensity:	St Dev (d.nm):
Z-Average (d.nm):	84.52	Peak 1:	88.35	100.0	19.83
PdI:	0.021	Peak 2:	0.000	0.0	0.000
Intercept:	0.911	Peak 3:	0.000	0.0	0.000
Result quality :	Good				

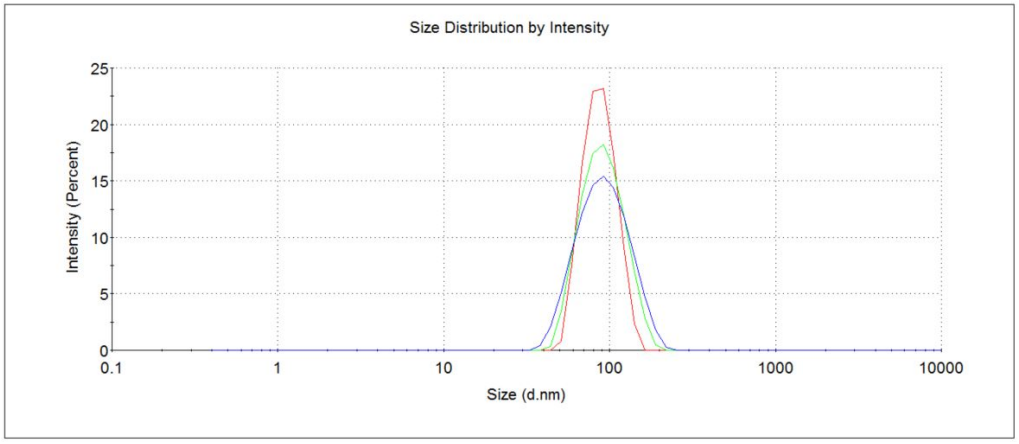

Figure 4.30: The average hydrodynamic diameter of 77-nm unfunctionalized polystyrene spherical beads measured by dynamic light scattering. The average hydrodynamic diameter is 88.4 +/- 20.0 nm.

4.6 Optimization of Silica Precursor Ratio

The optimization of the ratio of silica precursors was necessary to have the optimal silica shell thickness. Reagents required for the optimization experiment are 200 Proof ethanol, tetramethyl orthosilicate (TMOS), and (3-Aminopropyl) trimethoxysilane (APTMS) that were supplied by Sigma-Aldrich Co. LLC. (St. Louis, MO). All materials were used as received.

An optimization experiment was conducted to vary the volume of APTMS at 0.25 μL, 0.50 μL, and 1.00 μL and TMOS at 0.50 μL, 1.50 μL, and 2.50μL. First, 35 μL of 4% (w/v) 100-nm CML templates were added dropwise into 65 μL of 10%

(w/v) 42-nm unfunctionalized polystyrene masks while shaking. The template-and-mask mixture was mixed for at least 12 hours at 3000 rpm and at room temperature. At this point, the template-and-mask mixture may be kept in 4°C refrigeration for long-term storage.

Next, the template-and-mask mixture is added into 1 mL of ethanol while shaking. Immediately, APTMS was added followed by TMOS. The silica reaction with APTMS, TMOS, and water (from the templates and masks aqueous suspension) on the surface of the template was carried out at room temperature for 2 hours while shaking at 3000 rpm.

After that, the sample was washed three times with ethanol by centrifugation at 14,000 rpm for 5 minutes each time to remove any unreacted reagents. After the final wash, the sample was resuspended in 100 to 200uL ethanol and air dried on a 22 x 22 mm No. 1.5 glass coverslip. The sample on the coverslip was heated at 450°C for 12 hours to remove the polystyrene and calcine the silica. The HMSNS were recovered from the coverslip by washing them into a micro-centrifuge tube and resuspending into 35uL of distilled water. Finally, the HMSNS were ultrasonicated in an ice bath using Q125 Sonicator from Qsonica, LLC. at 40% amplitude (which output about 12W) for 4 minutes using a 4-second pulse on and 1-second pulse off cycle for a total of 2900 +/- 100 Joules of energy. The final silica nanoparticles were imaged with the SEM. Figure 4.31 shows the calcinated silica nanospheres formed from using different APTMS to TMOS ratio.

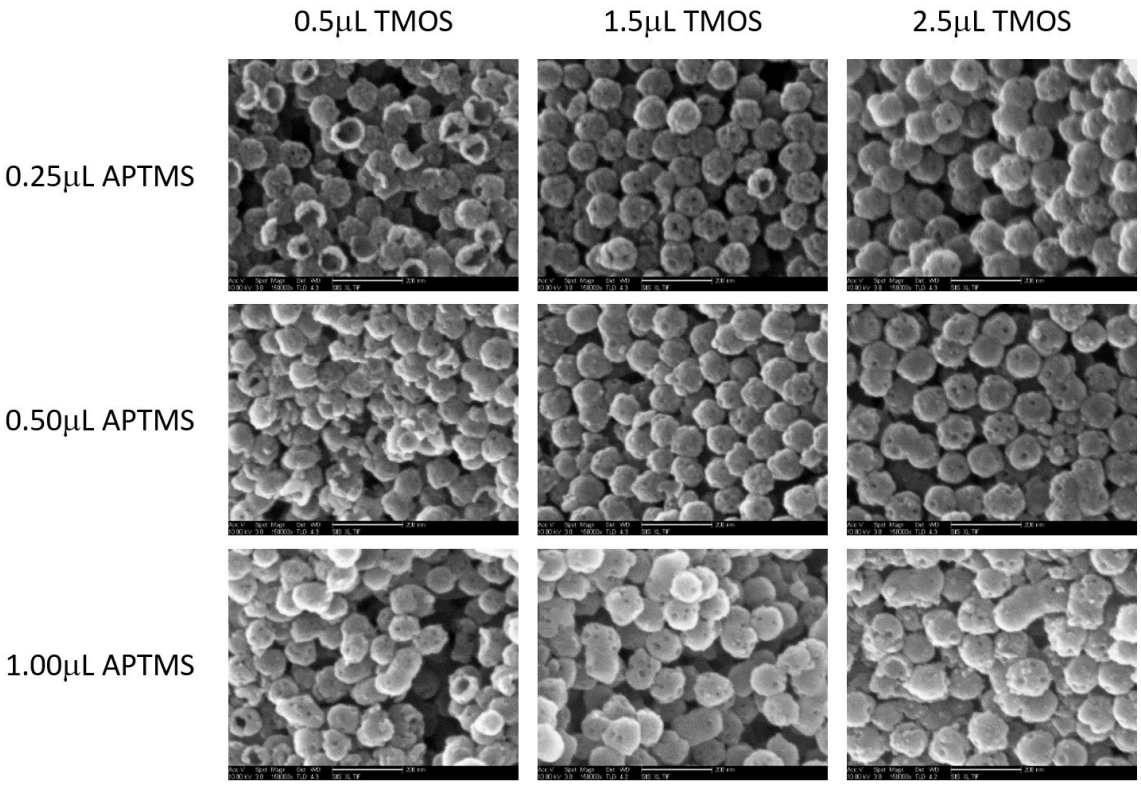

Figure 4.31: Scanning electron micrographs of silica nanospheres synthesized from different silica precursor ratios. The hollow mesoporous silica nanospheres are synthesized from 100-nm carboxylate-modified latex templates and 42-nm unfunctionalized polystyrene masks using different APTMS to TMOS ratio. The optimal silica nanospheres are formed with a 1:5 APTMS to TMOS ratio (or 0.50 μL APTMS and 2.5 μL TMOS).

At low volume of APTMS and TMOS, the silica shell thickness is too thin to have sufficient structural integrity such that the shells are broken during the calcination process. At high volume of APTMS and TMOS, the silica shell thickness is too thick and there are too much reagents such that silica nanoparticles began to fuse together to form dimers. Based on the SEM images, the optimal ratio was selected to be 1:5 ratio of APTMS to TMOS.

4.7 Optimization of Reaction Sequence

Once the ratio of APTMS to TMOS is optimized and selected to be 1:5 ratio, the next step is to optimize the reaction time and sequence for APTMS and TMOS to pre-hydrolyze before adding the templates and masks for silica formation. The experiment was conducted such that 0.5 μL of APTMS and 2.5 μL of TMOS was first added to 1 mL of 95% ethanol, then premixed template and mask was either added immediately or after 15 seconds, 5 minutes, 15 minutes, 30 minutes, 1 hour, 2 hour, or 4 hours after the APTMS and TMOS has time to react with the water in the ethanol.

The SEM images of this experiment are shown in Figure 4.32. The images showed that when the template-and-mask mixture was added immediately to the APTMS, TMOS, and ethanol mixture, the pores were smaller. However, when the template-and-mask mixture was added after 15 seconds to 30 minutes, the pores were larger and the silica surface appears smoother. When the template-and-mask mixture was added after 1 hour, the silica surface appears rougher.

The observation of smaller pores may be due to the hydrolysis of the APTMS and TMOS in the presence of the polystyrene template and already pre-forming on the template even between the contact points of the templates and masks. As a results, a thin layer of silica is able to grow further into the contact area of the templates and mask, causing the pore size to shrink.

The observation of the rougher silica surfaces is most likely due to the absence

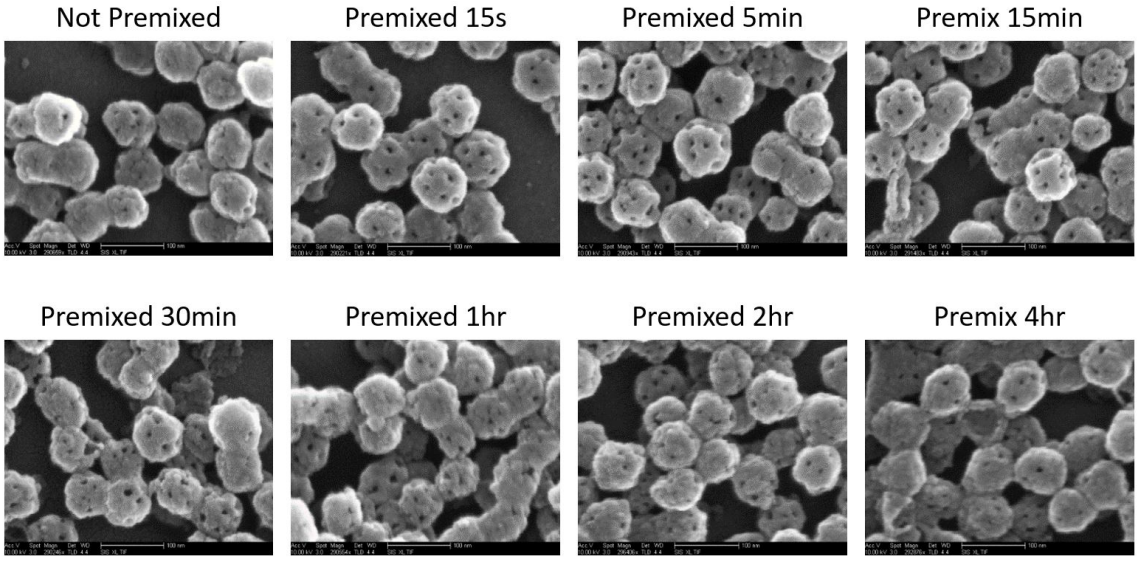

Figure 4.32: Scanning electron micrographs of silica nanospheres synthesized from different premixing time of silica precursors. The hollow mesoporous silica nanospheres are synthesized from 100-nm carboxylate-modified latex templates and 42-nm unfunctionalized polystyrene masks using different premixing time of APTMS and TMOS. The optimal silica nanospheres are formed with 15 seconds to 30 minutes of premixing APTMS and TMOS.

of templates for silica to grow on such that silica nucleation sites are allowed to grow in size in the bulk solution before the templates are introduced. With longer reaction time, these solid silica nanoparticles in the bulk solution grow to a larger size (possibly < 10 nm) before they are attracted onto the polystyrene surfaces and fused together to form the appearance of a rougher silica surfaces. When sufficient time (between 15 seconds to 30 minutes) is given for the APTMS and TMOS to hydrolyze and form smaller solid silica nuclei (possibly < 5 nm), these smaller solid silica are attracted onto the template surface and fused together to form a smoother silica surface as silanol condensation reaction continues.

4.8 Modulation of Mesopore Size

To synthesize silica nanoparticles with different mesopore size, masks of different sizes were used. The hollow mesoporous silica nanospheres were prepared by first adding 35 μL of 4% (w/v) 100-nm CML templates dropwise into 65 μL of 42-nm, 165 μL of 62-nm, or 215 μL of 77-nm unfunctionalized polystyrene masks at 10% (w/v) while vortexing. The template-and-mask mixture was mixed for at least 12 hours at 3000 rpm and at room temperature. Next, 0.5 μL of APTMS and 2.5 μL of TMOS were premixed with 1 mL of ethanol for about 15 seconds before adding the template-and-mask mixture in a dropwise manner while vortexing.

When 42-nm, 62-nm, and 77-nm unfunctionalized polystyrene masks are used with 100-nm CML templates during the synthesis of the hollow mesoporous silica nanospheres, the mesopore size is about 5 nm, 8 nm, and 11 nm, respectively. This shows that the mesopore size can be modulated depending on the enzyme size. Larger enzyme will need larger mesopores in order for enzyme loading to be possible. When the mask size increases, the number of mesopores forming on each silica nanospheres decreases because of steric hindrance. Figure 4.33, 4.34, and 4.35 show the different mesopore size when 42-nm, 62-nm, and 77-nm mask sizes are used, respectively.

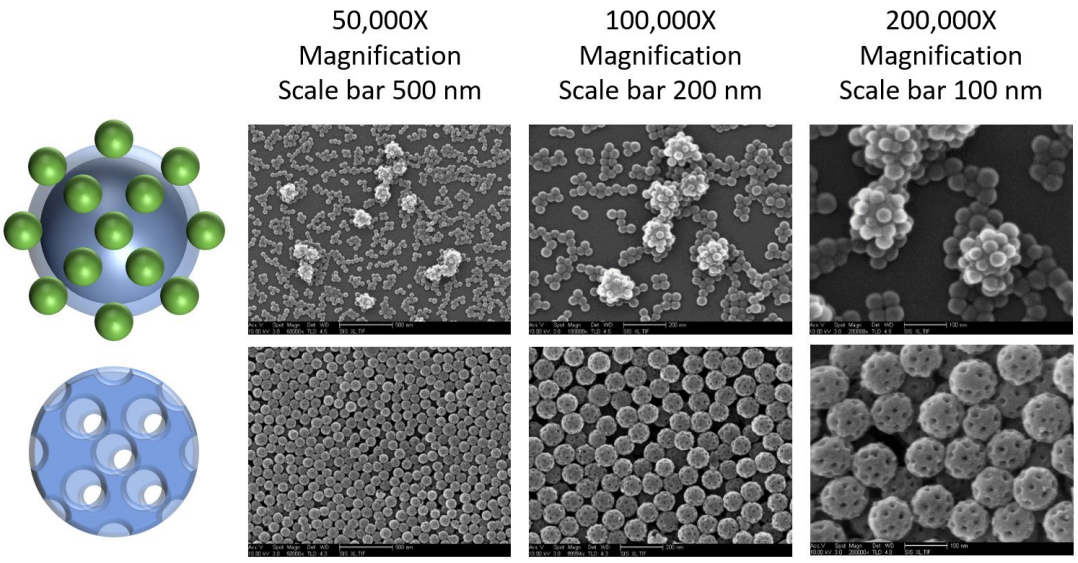

Figure 4.33: Scanning electron micrographs of hollow mesoporous silica nanospheres using 42-nm masks. The hollow mesoporous silica nanospheres are synthesized from 100-nm carboxylate-modified latex templates and 42-nm unfunctionalized polystyrene masks. The template-and-mask mixture before (*top row*) and after formation and calcination of silica (*bottom row*) are shown. The mesopore size is about 5 nm.

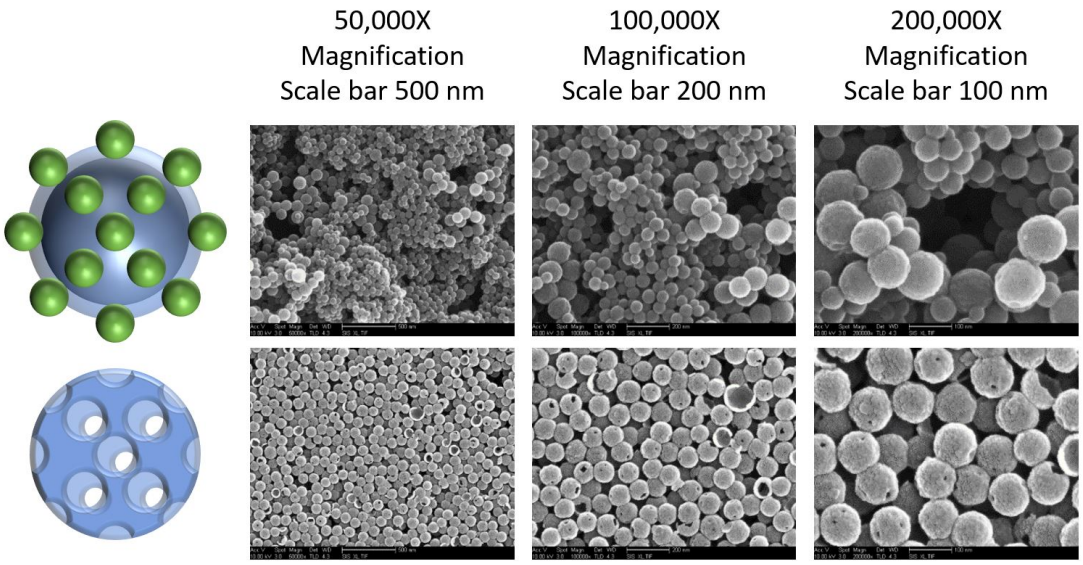

Figure 4.34: Scanning electron micrographs of hollow mesoporous silica nanospheres using 62-nm masks. The hollow mesoporous silica nanospheres are synthesized from 100-nm carboxylate-modified latex templates and 62-nm unfunctionalized polystyrene masks. The template-and-mask mixture before (*top row*) and after formation and calcination of silica (*bottom row*) are shown. The mesopore size is about 8 nm.

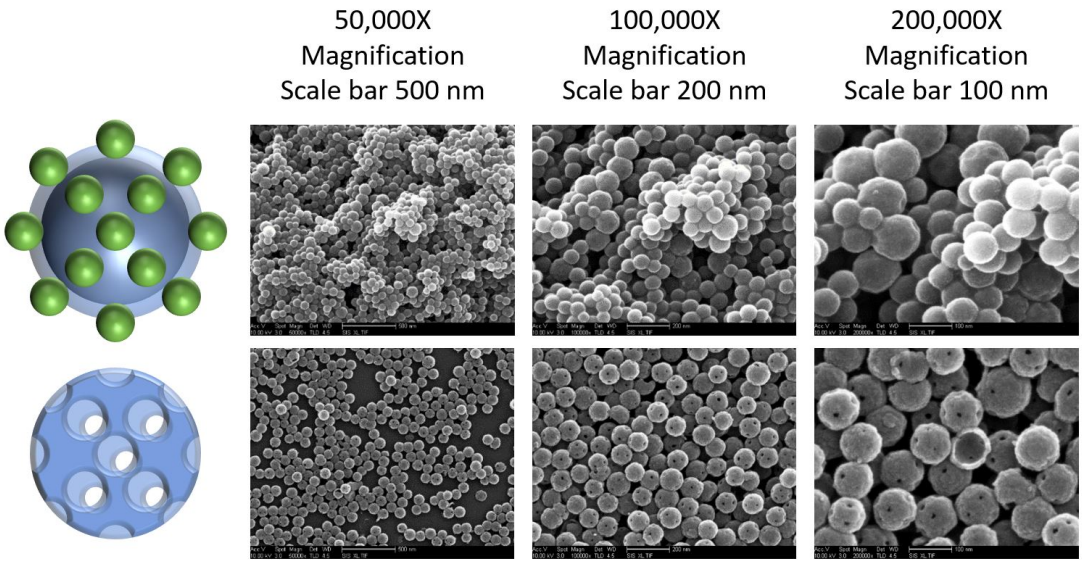

Figure 4.35: Scanning electron micrographs of hollow mesoporous silica nanospheres using 77-nm masks. The hollow mesoporous silica nanospheres are synthesized from 100-nm carboxylate-modified latex templates and 77-nm unfunctionalized polystyrene masks. The template-and-mask mixture before (*top row*) and after formation and calcination of silica (*bottom row*) are shown. The mesopore size is about 11 nm.

4.9 Synthesis of Hollow Mesoporous Silica Nano Rods

The hollow mesoporous silica nanorods (HMSNR) were prepared using the same method as the nanospheres, except the 35 μL of 4% (w/v) of elongated polystyrene templates in water were used instead of the 100-nm CML templates. Similar optimization experiments on masks selection and silica precursor concentrations selection were conducted.

For the mask selection, three different types of masks were evaluated. First, 65 μL of the same masks used with the 100-nm CML beads to make spherical nanopar-

ticles was tested (i.e. unfunctionalized polystyrene beads at 10% solids (w/v) in an aqueous suspension of 42-nm diameter purchased from Bangs Laboratories, Inc. (Fishers, IN)). The second type of masks tested was the Polybead® Microspheres at 2.5% solids (w/v) in an aqueous suspension of 50 nm mean diameter purchased from Polysciences, Inc. (Warrington, PA). A volume of 185 μL of the Polybead® Microspheres were used. The last type of masks tested was the Nanobead NIST Traceable Particle Size Standard polystyrene microspheres at 1% solids (w/v) in an aqueous suspension of 50 nm mean diameter also purchased from Polysciences, Inc. (Warrington, PA). A volume of 465 μL of the 50-nm NIST polystyrene was used.

The SEM images of the HMSNR synthesized from the elongated polystyrene templates and the three different masks are shown in Figure 4.36. Without masks, silica reaction on the elongated polystyrene templates successfully formed hollow silica nanorods with complete and uniform silica shell. Using the 42-nm masks from Bangs Laboratories, hollow mesoporous silica nanorods were formed. However, the silica surface appears to be rough. With the 50-nm masks from Polysciences, silica formed over both the templates and the masks and no mesopores were formed. The 50-nm NIST masks from Polysciences formed hollow mesoporous silica nanorods with the desired smooth silica surface and large mesopores around 15 nm. Based on the SEM images, the Nanobead NIST Traceable Particle Size Standard polystyrene microspheres at 1% solids (w/v) in an aqueous suspension of 50 nm mean diameter was selected as the masks for the synthesis of HMSNR.

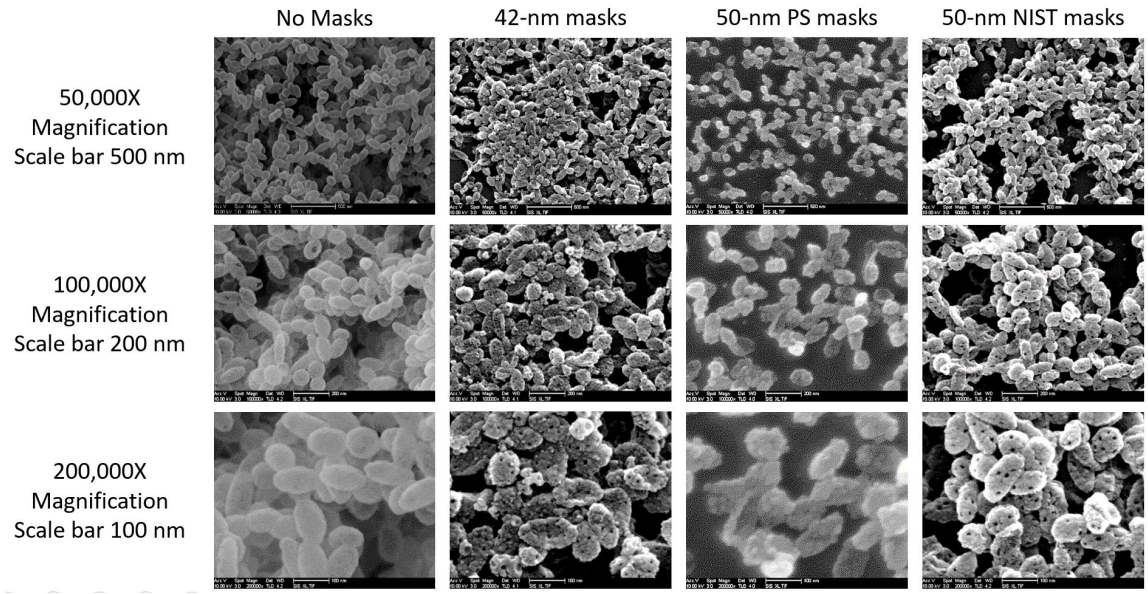

Figure 4.36: Scanning electron micrographs of hollow mesoporous silica nanorods using different masks. The silica nanorods are synthesized from the elongated polystyrene templates without masks (*left*), with 42-nm unfunctionalized polystyrene masks (*second left)*, with 50-nm polystyrene masks (*third left)*, and 50-nm NIST polystyrene mask (*right*) after silica formation and calcination. Based on the criteria of forming a complete and uniform silica shell and large mesopores (around 15 nm), the 50-nm NIST polystyrene masks were selected.

Next, the ratio of APTMS to TMOS is evaluated. The optimization experiment was conducted to vary the volume of APTMS at 0.25 μL and 0.50 μL and TMOS at 1.0 μL and 2.50μL. At low amount of APTMS and TMOS, the silica shell is too thin and breaks during the synthesis. The highest amount of APTMS and TMOS formed the optimal HMSNR as shown in Figure 4.37. Therefore, 0.5 μL APTMS and 2.5 μL TMOS for every 35 μL of elongated polystyrene templates was selected. The APTMS to TMOS ratio selected to synthesize the silica nanorods is the same as the ratio selected to synthesize the silica nanospheres.

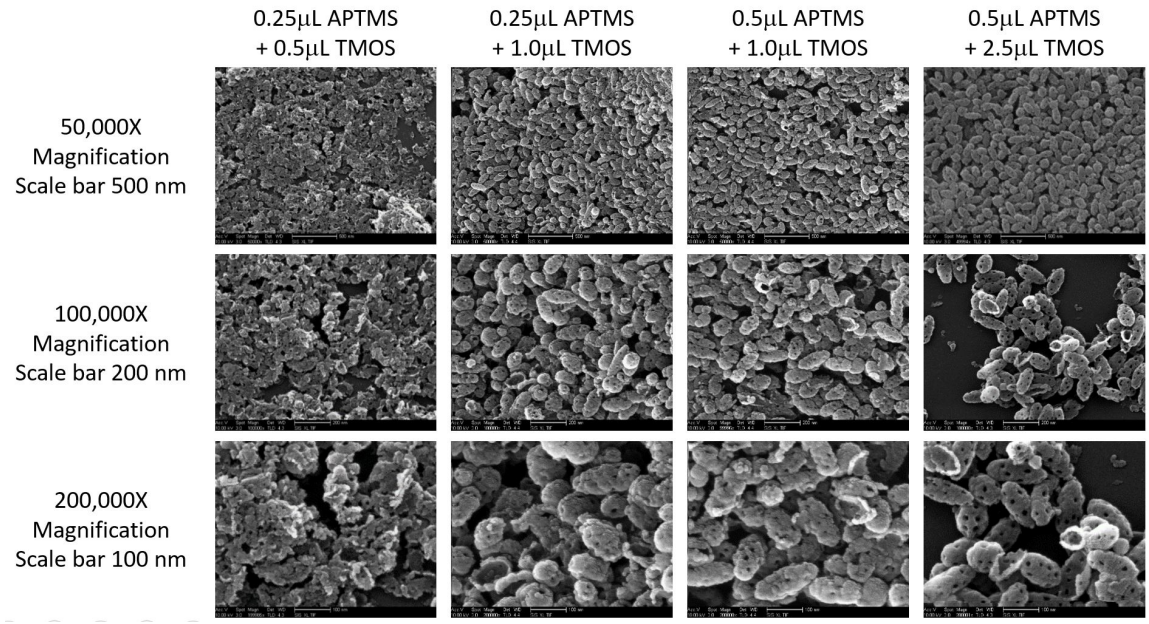

Figure 4.37: Scanning electron micrographs of silica nanorods synthesized from different silica precursor ratio. The hollow mesoporous silica nanorods are synthesized from the elongated polystyrene templates and 50-nm NIST polystyrene masks using different APTMS to TMOS ratio. The optimal silica nanorods are formed with a 1:5 APTMS to TMOS ratio (or 0.50 μL APTMS and 2.5 μL TMOS).

4.10 Optimized Synthesis Methods

The final optimized synthesis methods for 100-nm hollow mesoporous silica nanospheres (100NS), elongated hollow mesoporous silica nanorods (100NR), and 200-nm hollow mesoporous silica nanospheres (200NS) is described in this section.

The materials for synthesizing all three types of silica nanoparticles are listed next. For the use as templates for silica formation of 100NS and 200NS, carboxylate modified latex (CML) beads at 4% solids (w/v) in an aqueous suspension of 0.1 μm and 0.2 μm mean diameter were purchased from Invitrogen^{TM} (part of Thermo Fisher Scientific, Waltham, MA). For the use as templates for silica formation of 100NR, the same templates for 100NS are used and elongated using the process described

in the previous section. For the use as masks to create the mesopores in 100NS and 200NS, unfunctionalized polystyrene beads at 10% solids (w/v) in an aqueous suspension of varying diameters (42 nm, 62 nm, and 77 nm) were purchased from Bangs Laboratories, Inc. (Fishers, IN). For the use as masks to create the mesopores in 100NR, Nanobead NIST Traceable Particle Size Standard polystyrene microspheres at 1% solids (w/v) in an aqueous suspension of 50 nm mean diameter were purchased from Polysciences, Inc. (Warrington, PA). For silica formation, the chemical reagents tetramethyl orthosilicate (TMOS), 3-Aminopropyl trimethoxysilane (APTMS), and 200 Proof ethanol were purchased from Sigma-Aldrich Co. LLC. (St. Louis, MO). For silica calcination, 22 x 22 mm No. 1.5 glass coverslips were purchased from VWR International, LLC. (Radnor, PA). All materials were used as received.

To synthesize 100NS or 200NS, 35 μL of the 100-nm or 200-nm CML templates are added dropwise into 65 μL of 42-nm masks or 165 μL of 62-nm masks or 215 μL of 77-nm masks while vortexing. To synthesize 100NR, 35 μL of the elongated polystyrene templates are added dropwise into 465 μL of 50-nm masks. The template-and-mask mixture are mixed for at least 12 hours at 3000 rpm and at room temperature. At this point, the template-and-mask mixture may be kept in 4^{o}C refrigeration for long-term storage.

Next, 0.5 μL of APTMS and 2.5 μL of TMOS are added into 1 mL of ethanol. The mixture is mixed for about 15 seconds. While shaking, the entire template-and-mask mixture is added to the ethanol mixture containing the silica precursors. The silica reaction and formation on the surface of the templates are carried out at room

temperature for 2 hours while shaking at 3000 rpm.

After the reaction is completed, the samples are washed three times with ethanol by pelleting the nanoparticles with centrifugation at 14,000 rpm for 5 minutes and discarding the supernatant each time to remove any unreacted reagents. Fresh ethanol is added after each wash. After the final wash, the nanoparticles are resuspended in 100 to 200 μL of ethanol and air dried on a 22 x 22 mm No. 1.5 glass coverslip. The nanoparticles on the coverslip are heated at 450°C on a hotplate placed inside a fume hood for 12 hours to remove the polystyrene and calcine the silica to form the mesoporous hollow silica nanoparticles. The silica nanoparticles are recovered from the glass coverslips by washing them with ethanol into a microcentrifuge tube. The silica nanoparticles are washed again into water using the same washing process as described before and resuspended into 35uL of distilled water. Finally, the hollow mesoporous silica nanoparticles are ultrasonicated in an ice bath using Q125 Sonicator from Qsonica, LLC. at 40% amplitude (which output about 12W) for 4 minutes using a 4-second pulse on and 1-second pulse off cycle for a total of 2900 +/- 100 Joules of energy. At this point, the hollow mesoporous silica nanoparticles may be kept in 4°C refrigeration for long-term storage.

4.11 Acknowledgements

Chapter 4, in part is currently being prepared for submission for publication of the material. Yeh, Ya-San; Sadik, Esener C. "Synthesis of Spherical and Elongated

Hollow Mesoporous Silica Nanoparticles with Controlled Pore Size." The dissertation author was the primary investigator and author of this material.

Chapter 5

Synthesis of Enzyme Loaded Hollow Mesoporous Silica Nanoparticles

With the synthesis of hollow mesoporous silica nanospheres (HMSNS) and nanorods (HMSNR) optimized, the next steps are to optimize the loading of enzymes, sealing of the mesopores, and conjugating of polyethylene glycol molecules onto the surface of the final enzyme-encapsulated hollow mesoporous silica nanoparticles (HMSNP). This chapter describes the development and optimization of these steps and the *in vitro* evaluation of the effect of the silica nanoparticles on cells. Finally, a feasibility test on using ultrasound as an external trigger to activate the enzymes encapsulated in these silica nanoparticles is also briefly explored.

5.1 Optimization of Sealing Mesopores

In order to encapsulate enzymes within the HMSNP, the mesopores must be sealed. The strategy to seal the mesopores is to use a polymer to form a coating over the mesopores via electrostatic interaction between the polymer and the silica, then deposit another layer of silica onto the coating to form a sealed layer of silica that will not dissociate from the surface of the nanoparticles.

Since silica is terminated with hydroxyl groups, the surface charge of the HMSNP is negative. Therefore, positively charged polymers will be ideal materials for coating the surface of the silica nanoparticles and covering the mesopores. This positively charged coating is also ideal for attracting negatively charged TMOS when hydrolyzed to form silica on the coating.

There are many positively charged polymers such as poly-L-lysine (PLL) and polyethylenimine (PEI) that are suitable to form a coating on the surface of the HMSNP. The amount of polymers to use must be optimized. If the polymer concentration is too low, some mesopores may not be completely sealed. If the polymer concentration is too high, some polymers may begin to dissociate from the polymer-saturated silica surface and serve as templates for silica to form in the bulk solution.

Once the positively charged polymers have coated onto the surface of the nanoparticles to cover the mesopores and trap the enzymes within, the silica formation has to be relatively fast on the polymer coating before the polymers dissociate from the surface, leading to the mesopores being unsealed. To mitigate the risk of

not sealing the mesopores, a pre-reacted form of silica precursor is evaluated. TMOS is pre-hydrolyzed in a hydrochloric acid (HCl) solution into silicic acid before adding to the polymer-coated silica nanoparticles. Specifically, 15 μL of TMOS is mixed with 85 μL of 1 mM HCl for a minute to form silicic acid before immediate use.

An optimization experiment was conducted to determine the appropriate concentration of polymers. Poly-L-lysine hydrobromide with molecular weight of >300,000 in lyophilized powder form that is γ-irradiated and suitable for cell culture was purchased from Sigma-Aldrich Co. LLC. (St. Louis, MO). A 1% PLL (w/v) solution was prepared in water. To vary the PLL concentration, different volume (1 μL, 2.5 μL, and 5 μL) of the 1% PLL solution was added to 35 μL of 100NS in phosphate buffer saline (PBS). Then, 25 μ of the prepared silicic acid was added. The silica reaction to form the sealing layer was conducted for 2 hours while the mixture was shaken at 3000 rpm and at room temperature. After the reaction, the sealed nanoparticles are washed three times into PBS. The washing process was accomplished by pelleting the sealed nanoparticles using centrifugation at 14,000 rpm for 5 minutes and removing any unreacted reagents in the supernatant. After the final wash, the sample was resuspended in 50 μL of water for SEM. The SEM images of the sealed 100-nm silica nanospheres are shown in Figure 5.1. Based on the images, the optimal volume of 1% PLL solution to seal 100NS is 5 μL. However, the images also showed silica forming in the bulk solution even at the lowest PLL concentration.

To confirm that the highly reactive silicic acid is forming silica in the bulk solution, 25 μL of silicic acid only and 25 μL of silicic acid with 1 μL of PLL were

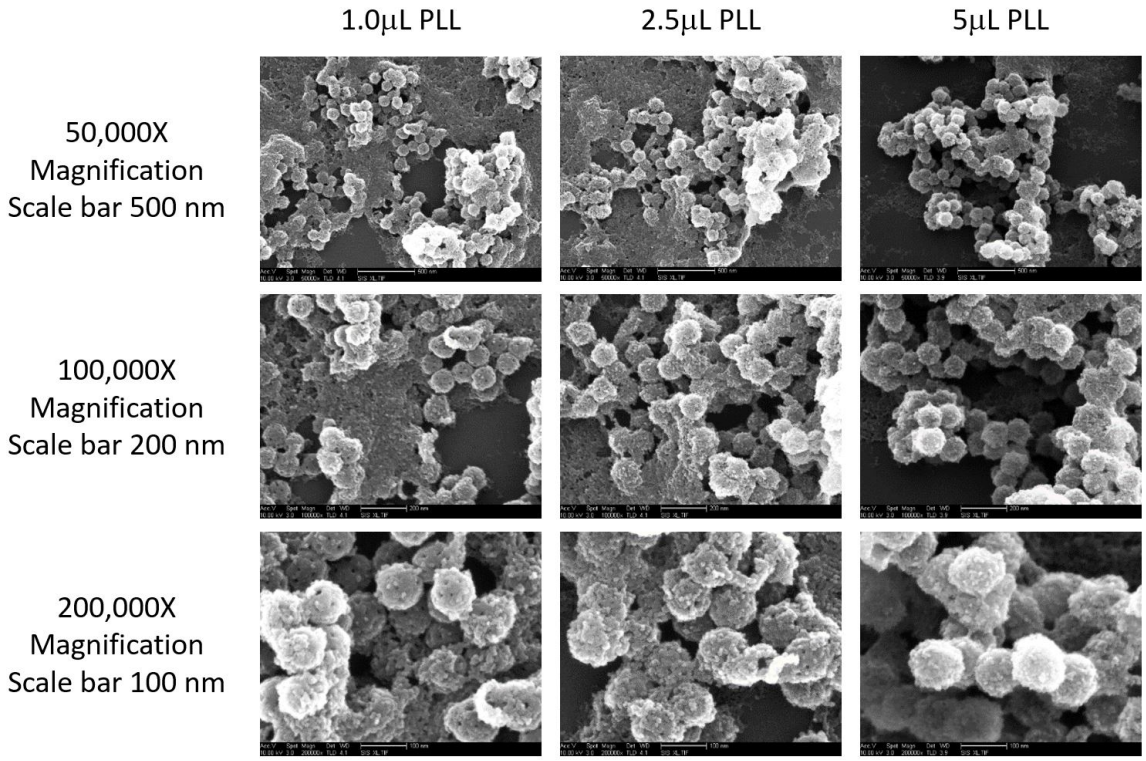

Figure 5.1: Scanning electron micrographs of 100-nm hollow mesoporous silica nanospheres sealed with different polymer concentrations and silica. Different volumes of 1% poly-L-lysine polymers solution (PLL) and silicic acids were used to seal the mesopores of 100NS. At 1 μL of PLL, most of the mesopores were not sealed (*left*). At 2.5 μL of PLL, some of the mesopores were still not sealed (*center*). At 5 μL, all the mesopores appeared to be sealed (*right*). All samples showed undesired solid silica formation in the bulk solution in addition to the desired silica formation on the 100NS.

mixed in 1 mL of PBS for 2 hours, without silica nanoparticles. The particles formed are imaged and compared with the previous experiment where 1 μL of PLL with 25 μL of silicic acid reacted with the 100NS. Figure 5.2 shows the SEM images from all three experiments. Since the images confirmed that silicic acid forms free silica in the bulk solution even without PLL, silicic acid is not selected as the silica precursor to form the silica sealing layer. Instead, TMOS is evaluated next.

To optimize the sealing process with TMOS, solutions with different ionic

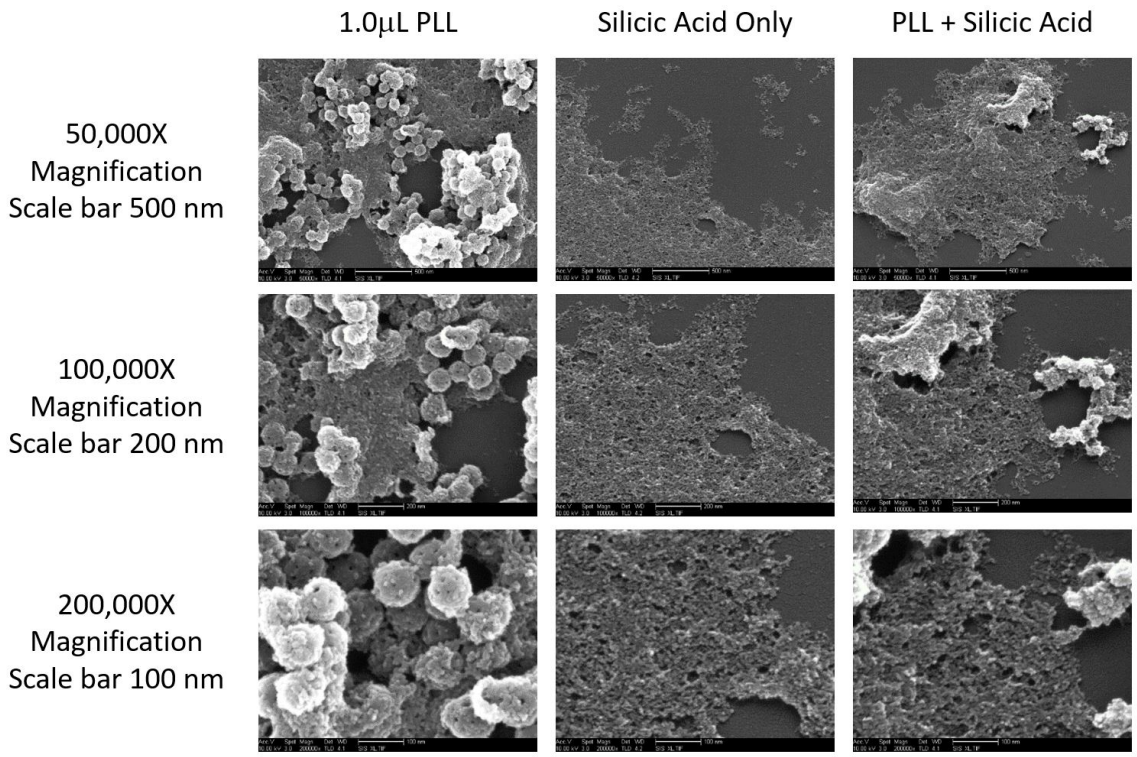

Figure 5.2: Scanning electron micrographs of silica formation with silicic acids. Sealing 100-nm hollow mesoporous silica nanospheres with 1 μL of poly-L-lysine (PLL) and silicic acid showed the formation of free silica in the bulk solution (*left*). Silicic acid alone is reactive enough to form free silica ($<$ 10 nm) in the bulk solution (*center*). Silicic acid with PLL also showed formation of free silica and larger silica aggregates in the bulk solution (*right*).

strength such as water, 0.05X PBS, and 1X PBS were tested. Based on the previous experiment, 5 μL of 1% PLL was selected. In each reaction, 5 μL of TMOS is used. When water was used as the reaction medium, silica did not form on the surface of 100NS and the mesopores were not sealed after 2 hours of reaction. When 1X PBS was used as the reaction medium, the mesopores were sealed but free silica again formed in the bulk solution after 2 hours of reaction. The optimum process appears to be using 0.05X PBS as the reaction medium. The mesopores were sealed and no free silica formation in the bulk solution was observed when the reaction was

conducted in 0.05X PBS for 2 hours as shown in Figure 5.3. In retrospect, the silicic acid may be optimized for the sealing process by lowering the ionic strength of the reaction medium.

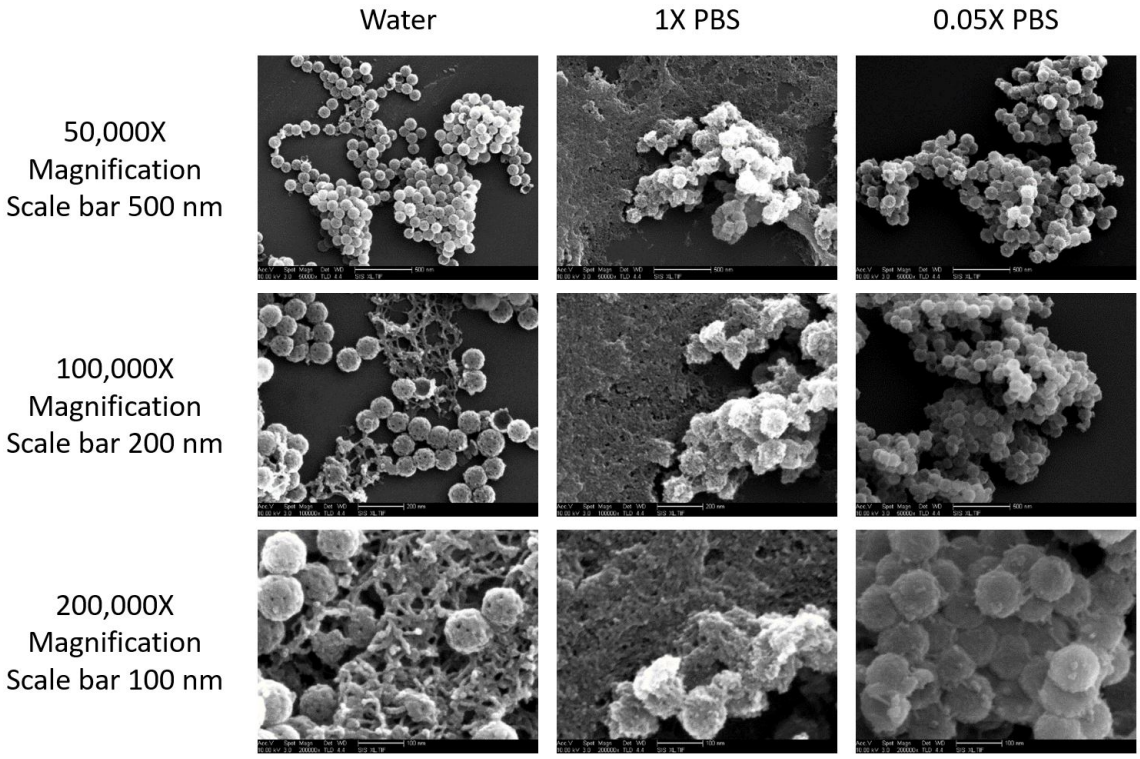

Figure 5.3: Scanning electron micrographs of silica formation with different ionic strength solution. Sealing 100-nm hollow mesoporous silica nanospheres (100NS) with 5 μL of poly-L-lysine (PLL) and 5 μL of TMOS in water for 2 hours showed no formation of silica sealing layer on the nanospheres (*left*). Sealing 100NS with the same conditions but in 1X PBS showed sealed mesopores and formation of free silica in the bulk solution (*center*). Sealing 100NS with the same condition but in 0.05X PBS showed sealed mesopores and no formation of free silica in the bulk solution (*right*).

Based on the optimization experiments, the final process for sealing the three types of nanoparticles was determined. A volume of 35 μL of each type of hollow mesoporous silica nanoparticles are incubated with 15 μL of the desired concentration of enzymes for at least 12 hours while shaking at 3000 rpm and at 4°C. Next 5 μL

of 1% PLL is added to the nanoparticle-and-enzyme mixture while mixing for 15 minutes for the PLL coating to form. Then 1 mL of 0.05X PBS is added to the mixture before adding 5 μL of TMOS to start the silica reaction on the polymer coating. The silica reaction is conducted for 2 hours while shaking at 3000 rpm and at room temperature.

After the reaction, the sealed nanoparticles are washed into 1X PBS by pelleting the sealed nanoparticles using centrifugation at 14,000 rpm for 5 minutes and removing any unreacted reagents in the supernatant. After the final wash, the sample was resuspended in 50 μL of 1X PBS or water for SEM imaging. The SEM images of the different stages of synthesis (i.e. template, template-and-mask mixture, hollow mesoporous silica nanoparticles, sealed nanoparticles) for 100-nm spherical nanoparticles, elongated nanoparticles, and 200-nm spherical nanoparticles are shown in Figure 5.4, 5.5, and 5.6, respectively.

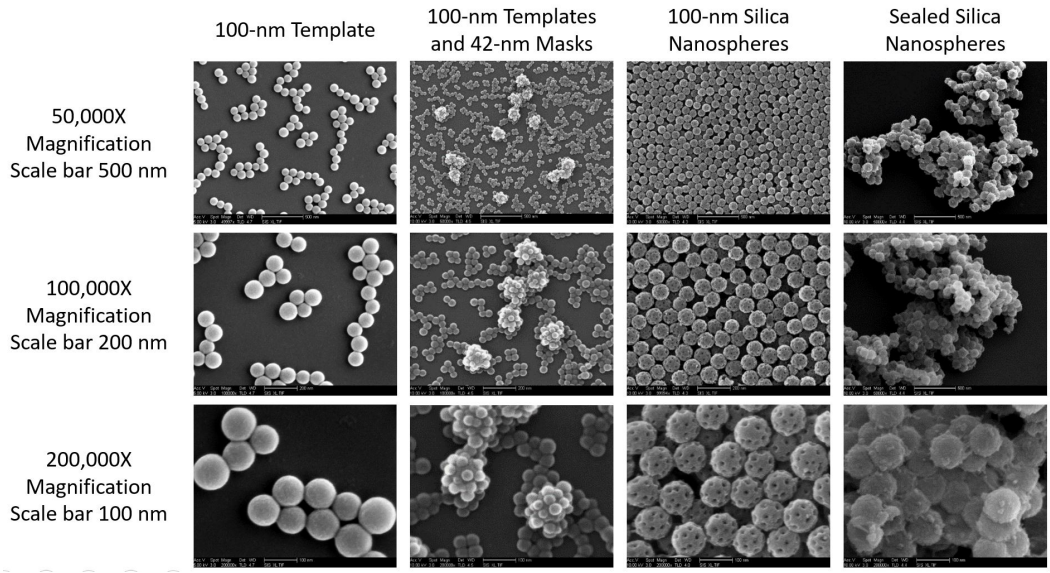

Figure 5.4: Scanning electron micrographs of the different stages of the synthesis process of the 100-nm sealed silica nanospheres. The 100-nm carboxylate-modified latex spherical templates are shown on the *left*. The templates mixed with 42-nm unfunctionalized polystyrene masks are shown on the *second left*. The 100-nm hollow mesoporous silica nanospheres are shown on the *third left*. The final 100-nm sealed silica nanospheres are shown on the *right*.

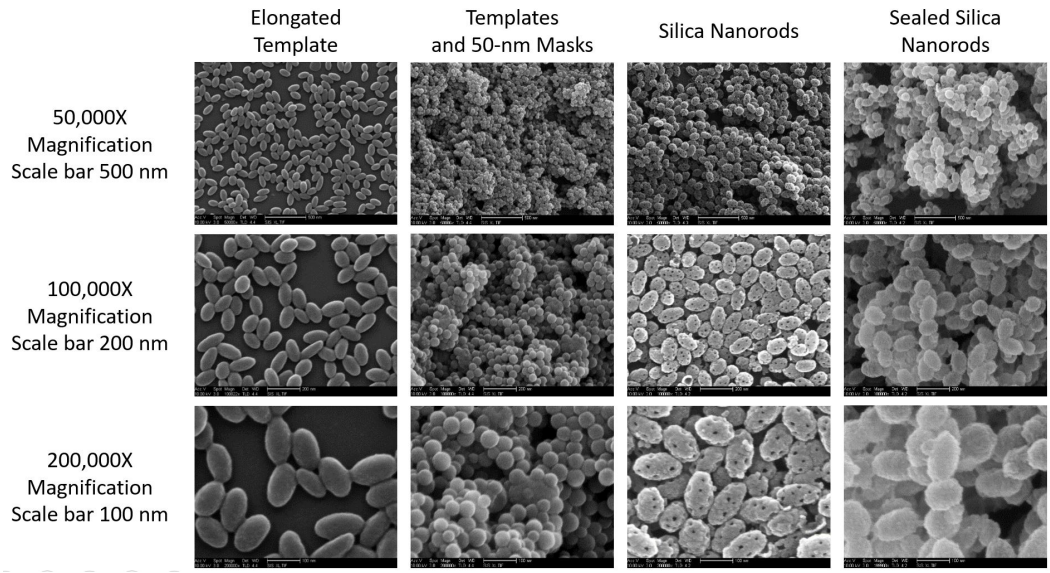

Figure 5.5: Scanning electron micrographs of the different stages of the synthesis process of the sealed silica nanorods. The elongated polystyrene templates are shown on the *left*. The templates mixed with 50-nm NIST polystyrene masks are shown on the *second left*. The hollow mesoporous silica nanorods are shown on the *third left*. The final sealed silica nanorods are shown on the *right*.

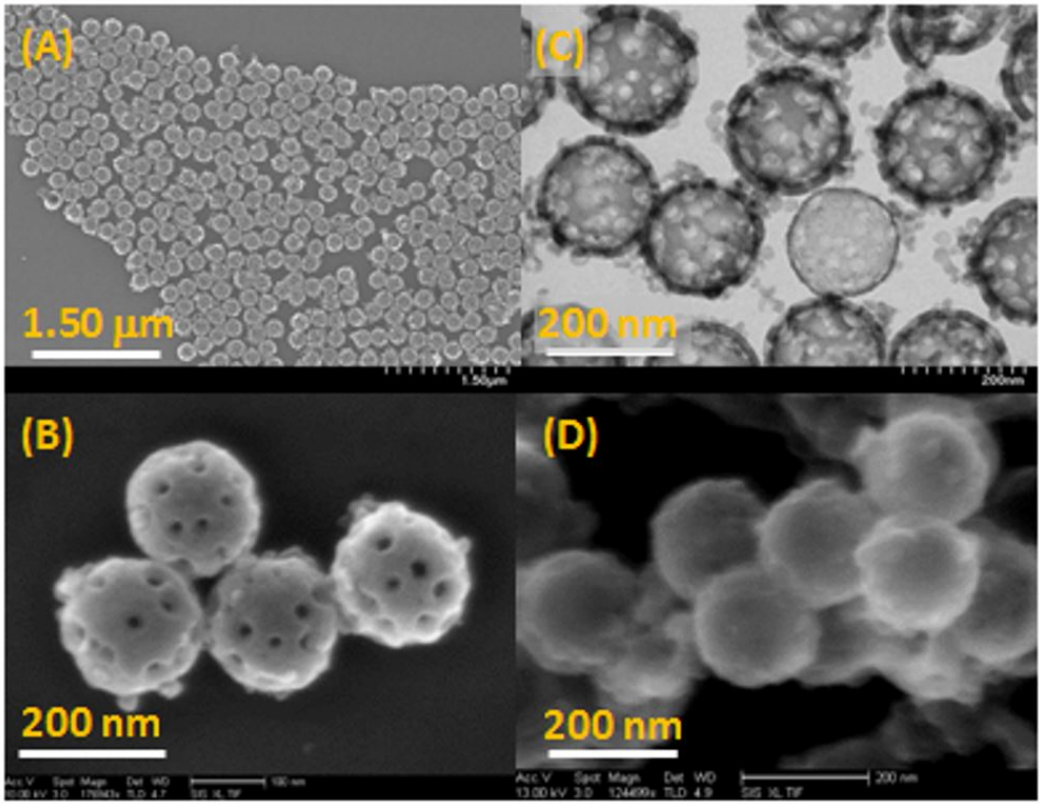

Figure 5.6: Scanning electron micrographs of the different stages of the synthesis process of the 200-nm sealed silica nanospheres. (A) The 200-nm hollow mesoporous silica nanospheres in low magnification. (B) The 200-nm hollow mesoporous silica nanospheres in high magnification. (C) The transmission electron micrograph of the 200-nm hollow mesoporous silica nanospheres. (D) The final 200-nm sealed silica nanospheres.

5.2 Characterization of Loading, Sealing, and PE-Gylation

In order to track the nanoparticles *in vivo*, the nanoparticles are labeled with fluorescent dyes. Generally, the fluorescent dyes are conjugated to the surface of the nanoparticles. However, surface dyes may detach from the nanoparticles *in*

vivo or may be affected by the physiological conditions such as pH or enzymes that quenches the fluorescent signal [173]. Furthermore, conjugating the fluorescent dye on the surface may change the surface properties of the nanoparticles and affects their circulation life-half and biodistribution *in vivo*. Therefore, the hollow mesoporous silica nanoparticles are labeled with fluorescent dyes prior to enzyme loading, sealing, and PEGylating.

The reagents used included Alexa Fluor™ 594 NHS Ester (Succinimidyl Ester) purchased from Molecular Probes® (part of Thermo Fisher Scientific, Waltham, MA), horseradish peroxidase purchased from Pierce™ (part of Thermo Fisher Scientific, Waltham, MA), and anhydrous dimethyl sulfoxide and sodium bicarbonate purchased from Sigma-Aldrich Co. LLC. (St. Louis, MO).

The process of loading the enzymes, sealing the mesopores, and PEGylating the nanoparticle surface can be characterized with the zeta potential of the nanoparticles after each step. The surface of silica nanoparticles are terminated with silanol groups that produce a negative zeta potential between -20 mV to -30 mV. Since many commercially available dyes are designed for labeling the primary amines of proteins using N-hydroxysuccinimide (NHS) esters chemistry, the surface of the silica nanoparticles will be first functionalized with primary amines group in order to conjugate to dyes with reactive NHS esters. To functionalize the surface of silica nanoparticles, APTMS are hydrolyzed and condensed on the silanol groups on the silica surface. The amine-functionalized silica nanoparticles produce a positive charge between +30mV to +40mV. Once the surface is amine-functionalized, the

silica nanoparticles are ready to react with any fluorescent dyes with reactive NHS esters. The NHS ester reaction with primary amine to form a stable amide bond is depicted in Figure 5.7.

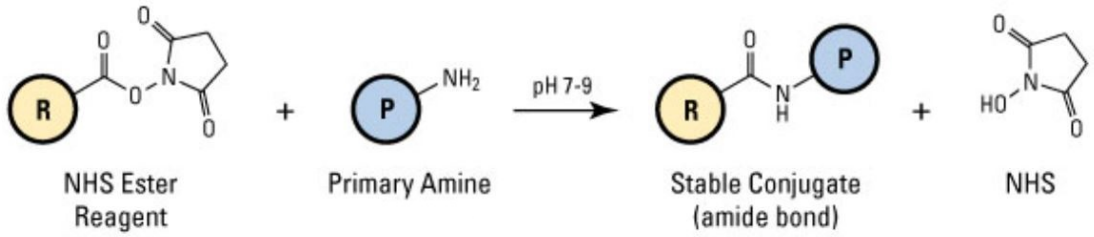

Figure 5.7: The N-hydroxysuccinimide (NHS) ester reaction with primary amine to form a stable amide bond. The NHS ester is conjugated to a fluorescent dye represented by the yellow circle (R). An amine-functionalized silica nanoparticle is represented by the blue circle (P). The amide bond covalently binds the fluorescent dye to the silica nanoparticle [243].

The fluorescent dyes, Alexa Fluor 594 NHS, are conjugated onto the silica nanoparticles by adding 10^{10} silica nanoparticles in 0.5 mL water to 0.5 mL of 0.2M sodium bicarbonate, then adding 5 mg of the dye in 100 μL anhydrous dimethyl sulfoxide (DMOS) and mixing the mixtures for an hour at room temperature. After conjugation of the fluorescent dyes, the zeta potential of the silica nanoparticles remains positive.

Next, the fluorescent-labeled nanoparticles are incubated with enzymes. Horse radish peroxidase (HRP) enzyme is chosen because it is a small (44 kDa) and neutral enzyme for proof-of-concept. After incubating with HRP, the zeta potential of the silica nanoparticles become less positive. This indicates that some enzymes may be adsorbed onto the surface of the silica nanoparticles, reducing their surface charge.

Addition of 1% (w/v) poly-L-lysine (PLL) polymer to silica nanoparticles

seals the mesopores of the nanoparticles and converts their surfaces into highly positive with zeta potential between +40 mV to +50 mV. This highly positive surface is desirable for silica sol-gel formation. TMOS is added to the mixture of fluorescent-labeled silica nanoparticles, HRP, and PLL in 0.05X PBS for two hours.

The successful formation of silica sol-gel layer on the silica nanoparticles will convert the nanoparticle surface to negative charge since silanol groups are negatively-charged. The zeta potential of nanoparticles sealed with silica sol-gel layers is between -15 mV to -25 mV.

Finally, the sealed nanoparticles are PEGylated by mixing them with 100 mg/mL of 5kDa PEG-silane in a 1:1 volume ratio and reacting for at least 12 hours at 4^{o}C. PEGylated nanoparticles should have neutral to slightly negative charge. The zeta potential of PEGylated silica nanoparticles is between -15 mv to 0 mV.

Figure 5.8, 5.9, and 5.10 show the average hydrodynamic diameter and average zeta potentials of 100-nm silica nanospheres (100NS), silica nanorods (100NR), and 200-nm silica nanospheres (200NS) after each step of the process, respectively. All measurements were performed with Malvern Zetasizer Nano ZSP instrument.

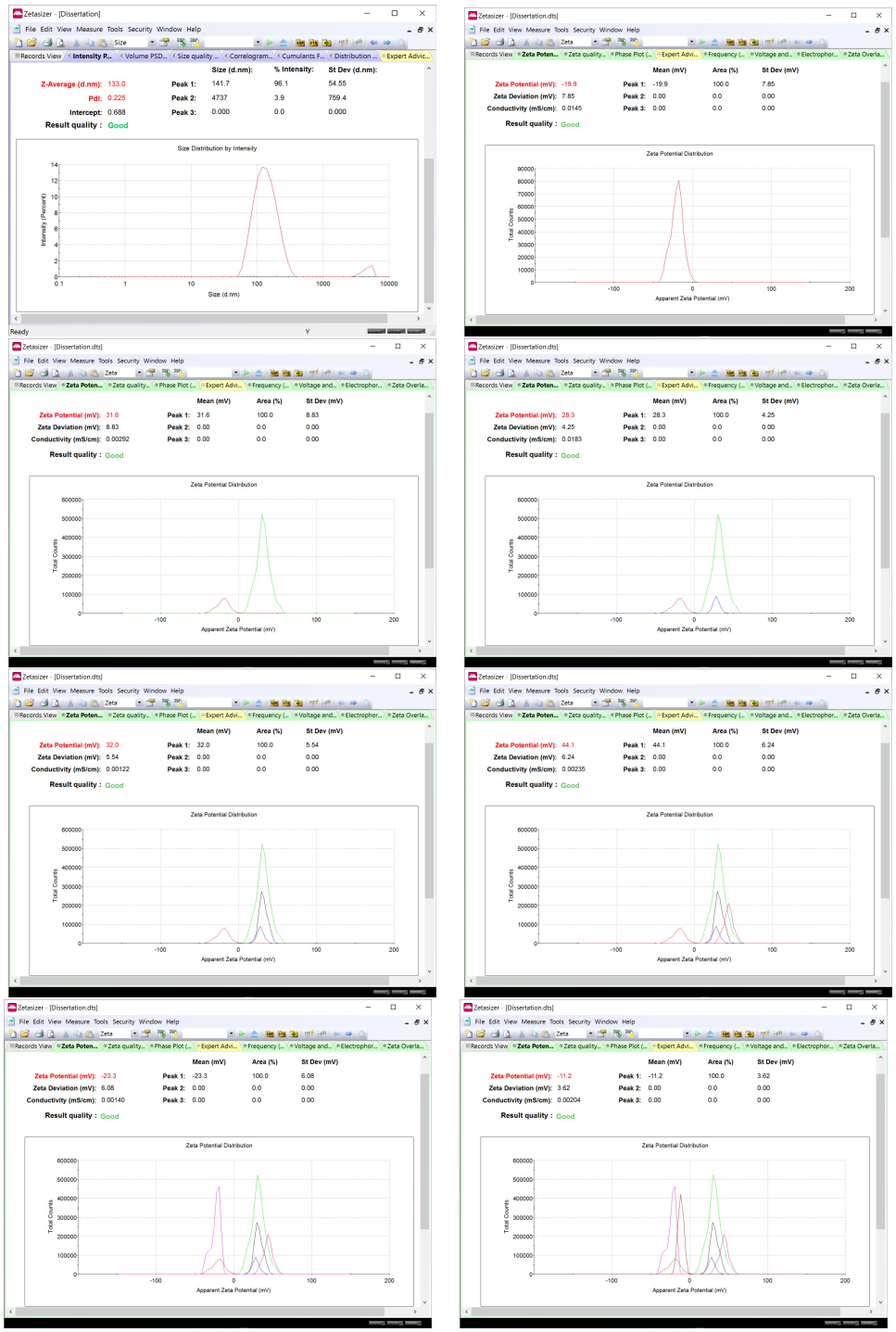

Figure 5.8: The average hydrodynamic diameter of 100NS measured by dynamic light scattering (*top left*). The average zeta potential of 100NS measured by dynamic electrophoretic mobility after each of the following steps (from *left to right and top to bottom*): unmodified silica, amine-functionalized, fluorescent-labeled, HRP loaded, PLL coated, silica sealed, and PEGylated.

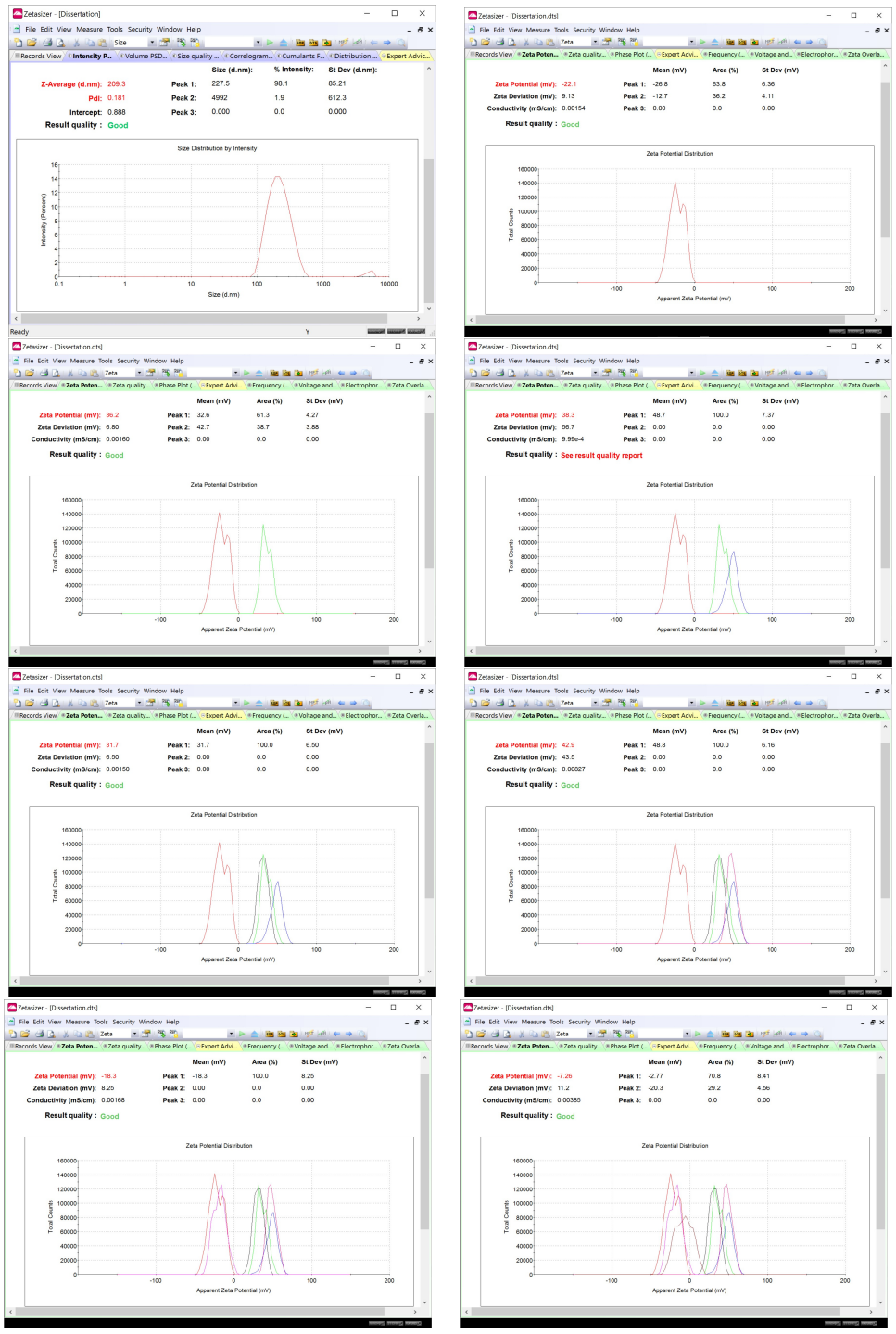

Figure 5.9: The average hydrodynamic diameter of 100NR measured by dynamic light scattering (*top left*). The average zeta potential of 100NR measured by dynamic electrophoretic mobility after each of the following steps (from *left to right and top to bottom*): unmodified silica, amine-functionalized, fluorescent-labeled, HRP loaded, PLL coated, silica sealed, and PEGylated.

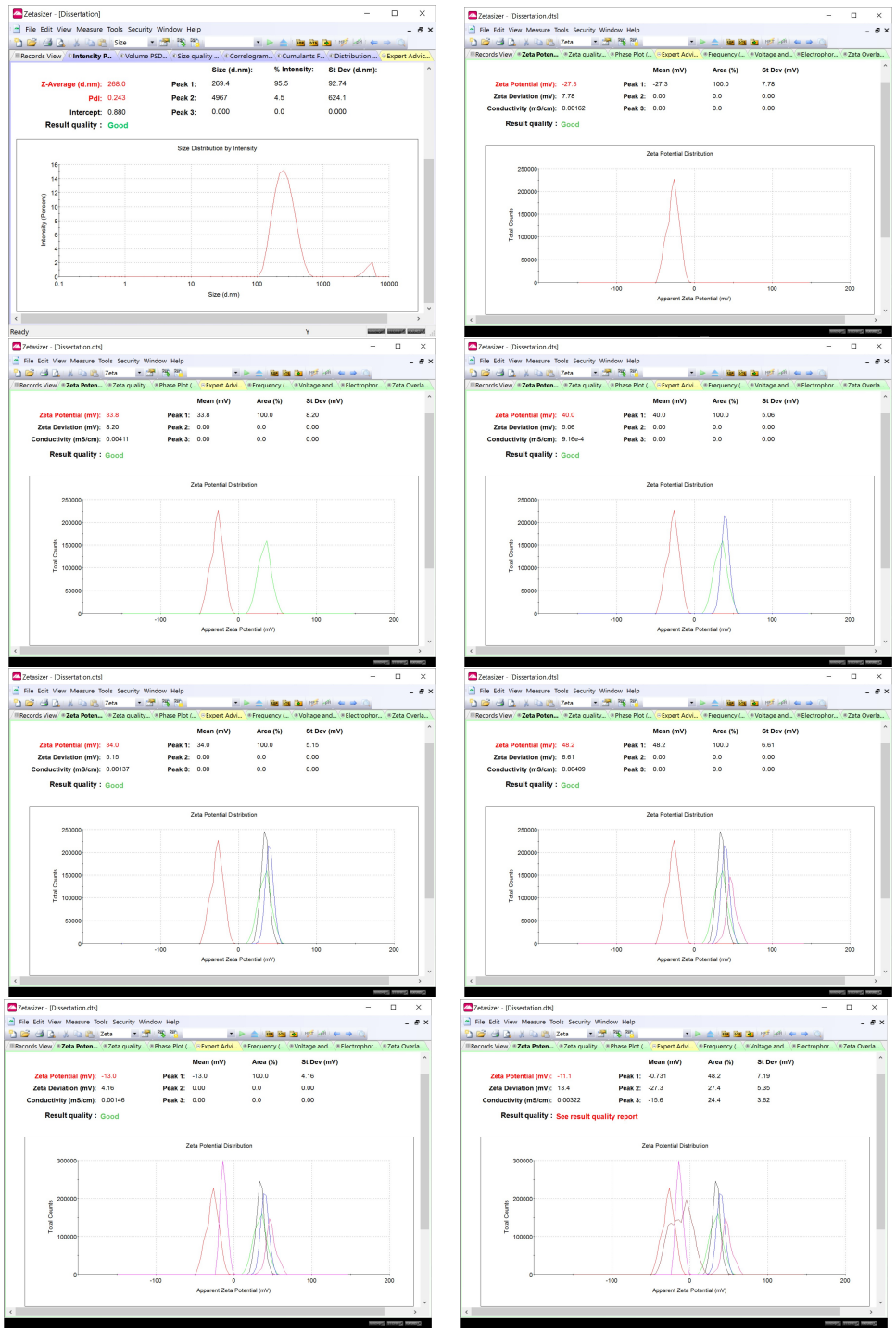

Figure 5.10: The average hydrodynamic diameter of 200NS measured by dynamic light scattering (*top left*). The average zeta potential of 200NS measured by dynamic electrophoretic mobility after each of the following steps (from *left to right and top to bottom*): unmodified silica, amine-functionalized, fluorescent-labeled, HRP loaded, PLL coated, silica sealed, and PEGylated.

5.3 Effects of Nanoparticles on Cell Viability

Since phagocytosis by macrophages is the main clearance mechanism that nanoparticles are removed from the circulation system, understanding the effect of nanoparticles on macrophage cell viability is important. The MTT (3-(4,5-dimethylthiazol-2-yl)-2,5-diphenyl tetrazolium bromide) assay is a colorimetric assay to quantify cell viability based on active metabolism of the cells and does not directly measure cell proliferation. Cell-based assays such as the MTT assay are useful to determine if a test compound have any dose-dependent or exposure time-dependent effects on cell proliferation or causes cell death.

The principle of the MTT assay is that the mitochondrial activity of viable cells is constant; therefore, any increase or decrease in the number of viable cells is linearly related to the mitochondrial activity [244]. When MTT is incubated with cells, viable cells with mitochondrial activity will be able to convert MTT into formazan product. The cellular mechanism of MTT reduction into formazan most likely involves reducing molecules such as NADH that transfer electrons to MTT. Formazan is purple in color and generates a maximum absorbance around 540 nm that is detectable by a spectrophotometer. This absorbance signal is proportional to the number of viable cells. Dying cells rapidly lose the ability to convert MTT into formazan, causing a drop in the absorbance signal. Therefore, the color formation attributed to formazan formation serves as a marker of viable cells.

However, the formazan product is an insoluble precipitate and accumulates

inside viable cells or on the cell surface after exocytosis. The precipitates of formazan must be solubilized before accurate absorbance measurements can be taken. Formazan precipitates may be solubilized using acidified isopropanol, dimethyl sulfoxide (DMOS), dimethylformamide, sodium dodecyl sulfate, or a combination of detergent and organic solvent.

Because the conversion of MTT to formazan by viable cells is time dependent, longer incubation of viable cells with MTT will increase the amount of formazan formed. More formazan will increase the absorbance signal and the sensitivity of the assay. However, MTT is also cytotoxic since the reduction of MTT to formazan consumes energy from the cell. Therefore, the optimum concentration and time for incubating cells with MTT are 0.2 to 0.5 mg/mL and 1 to 4 hours, respectively.

Conversion of MTT to formazan in a cell population that is in the log phase growth is generally linearly proportional to the number of metabolically active viable cells. However, any cell culture conditions that affect the metabolism of viable cells will result in a deviation from this linear behavior. For example, when the growth of adherent cells become contact inhibited due to high confluency, metabolism of viable cells may slow down and decreases the amount of MTT reduced per cell. Change in pH or depletion of essential nutrients are other adverse culture conditions that may suppress the reduction of MTT to formazan. Conversely, the formazan production may increase under certain conditions not related to cell metabolism. For example, extended exposure to direct light may cause an accelerated reduction of MTT and increase the absorbance level. Therefore, the MTT assay must be conducted with

non-confluent cells, conducive cell culture conditions, and in the dark. In addition, experimental controls such as culture medium with MTT only (i.e. no cells) should be measured to verify no interference is present in the cell culture.

Incorporating the considerations presented above, a cell viability assay using MTT was performed with a macrophage cell-line. The murine macrophage cell-line tested was RAW264.7 purchased from ATCC®. Cells were seeded at a density of 7500 cells per well in a 96-well plate overnight. Three types of silica nanoparticles with different sizes and shape are tested on the macrophages. They are 100-nm nanospheres, 200-nm nanospheres, and nanorods with aspect ratio of 1.75 and dimension of 80-nm by 140-nm. For each type of nanoparticles, different concentration of unmodified (silica surface produces negative charge), amine-functionalized (amine group produces positive charge), and PEGylated (PEG groups produces neutral charge) nanoparticles were incubated with the cells for 24 hours. After 24 hours, the media containing the nanoparticles was removed and fresh media containing MTT reagents were added. The cells were allowed to incubate with MTT for 4 hours. Finally, DMOS was added to solubilize the formazan crystals and the absorbance of each well was measured at 540-nm wavelength on a spectrophotometer, Spark® 20M from Tecan Trading AG, Switzerland.

Based on the MTT results, it is observed that the PEGylated nanoparticles are relatively non-toxic to the macrophages regardless of size or shape. The positively charged nanoparticles are the most toxic regardless of size or shape, followed by the negatively charged nanoparticles. The cell viability results of the 100-nm silica

nanospheres, silica nanorods, and 200-nm silica nanospheres are shown in Figure 5.11, 5.12, and 5.13, respectively. These observations are consistent with published literature as described in Chapter 2.

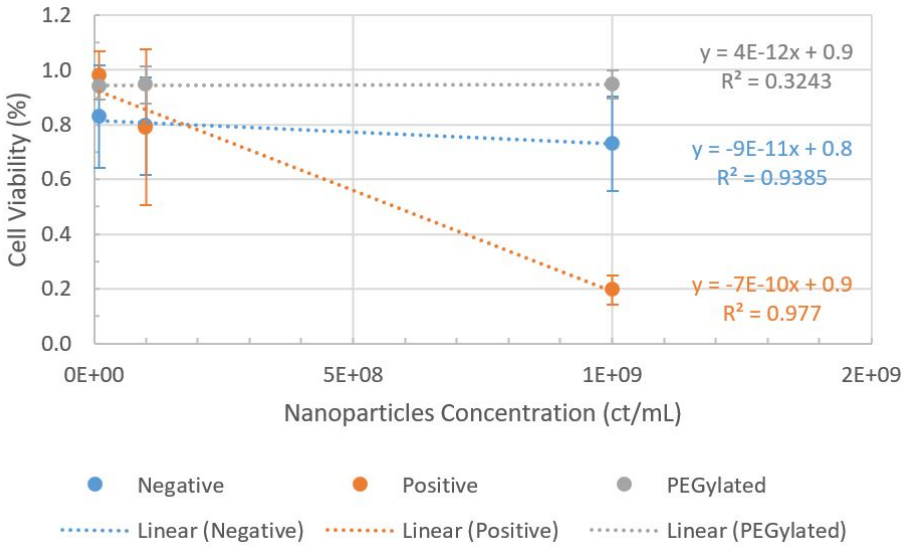

Figure 5.11: Macrophage cell viability when exposed to 100-nm silica nanospheres with different surface charges. Cell viability is inversely dependent on the dose of the amine-functionalized (positive) and unmodified (negative) 100-nm silica nanospheres, with the positively charged nanospheres being significantly more toxic to the cells. PEGylated nanospheres are non-toxic to the cells within the dose range tested.

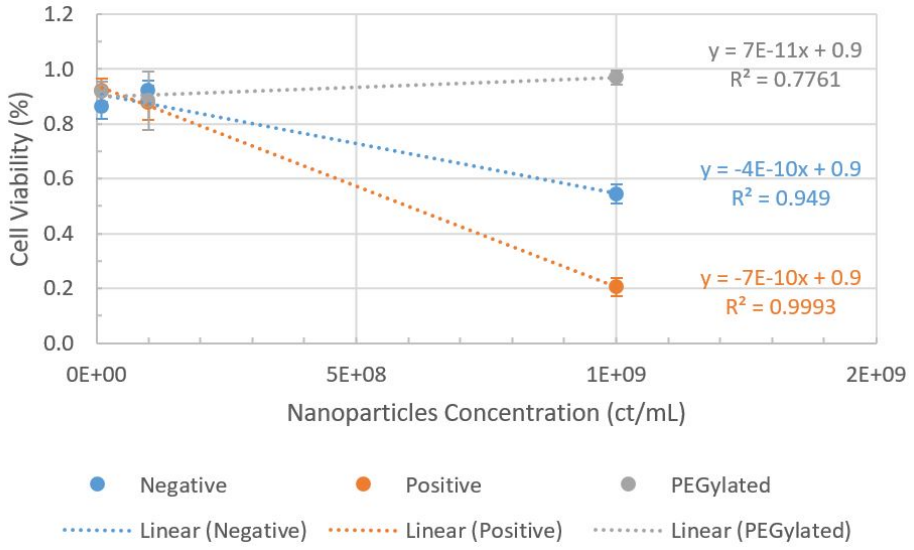

Figure 5.12: Macrophage cell viability when exposed to silica nanorods (aspect ratio of 1.75 and dimension of 80 nm by 140 nm) with different surface charges. Cell viability is inversely dependent on the dose of the amine-functionalized (positive) and unmodified (negative) silica nanorods, with the positively charged nanorods being significantly more toxic to the cells. PEGylated nanospheres are non-toxic to the cells within the dose range tested.

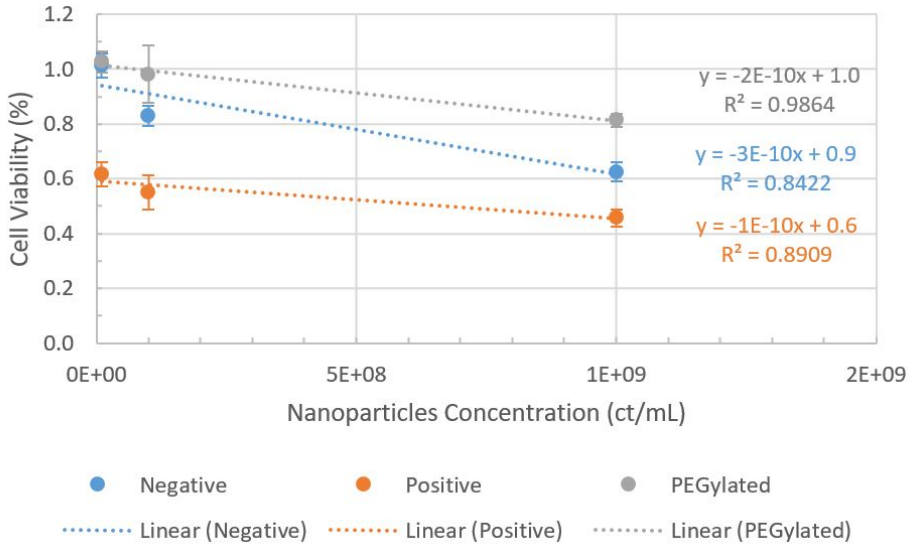

Figure 5.13: Macrophage cell viability when exposed to 200-nm silica nanospheres with different surface charges. Cell viability is inversely dependent on the dose of the amine-functionalized (positive), unmodified (negative), and PEGylated (neutral) 200-nm silica nanospheres, with the positively charged nanospheres being the most toxic and the neutrally charged nanospheres being the least toxic to the cells.

5.4 Ultrasound Targeting and Activation

To demonstrate the versatility of the silica nanoparticles as a platform for the delivery of therapeutic agents, the capability of activation by external triggers was incorporated into the design. This design adds a few more steps to the synthesis process. The reagents used include poly-L-lysine hydrobromide with molecular weight of >300,000 in lyophilized powder form that is γ-irradiated and suitable for cell culture, penicillinase from *Bacillus cereus* as lyophilized powder with 1500 to 3000 units/mg protein, nitrocefin, calcium chloride, trehalose, and mannitol that were purchased from Sigma-Aldrich Co. LLC. (St. Louis, MO). Perfluoro-n-pentane, minimum 98%, was purchased from Strem Chemicals, Inc. (Newburyport, MA).

Once the enzymes are encapsulated and sealed within the silica nanoparticles as described previously, another layer of calcium phosphate, $Ca_3(PO_4)_2$, is added. Briefly, 50 μL of the enzyme-encapsulated and sealed 200-nm silica nanospheres obtained as described in Section 5.1 is mixed with 5 μL of 1% poly-L-lysine solution for 15 minutes. Next, the mixture is diluted into 1 mL of 0.1X PBS, then 125 μL of 0.1M calcium chloride is added. The reaction is allowed to continue for 2 hours while shaking at 3000 rpm at room temperature for calcium phosphate shells to form over the nanospheres. The sample is washed three times into 1X PBS by pelleting the nanoparticles with centrifugation at 14,000 rpm for 5 minutes and discarding the supernatant each time to remove any unreacted reagents. Fresh 1X PBS is added after each wash. After the final wash, the nanoparticles are resuspended in a solution

containing 50 mM mannitol and 100 mM trehalose for lyophilization with FreeZone Plus 6 Liter Cascade Console Freeze Dry Systems from Labconco Corporation. Trehalose and mannitol are used as enzyme protectants during lyophilization to stabilize the enzyme conformation.

After lyophilization, the interior volume of the nanospheres are filled with perfluoro-n-pentane (PFP) by using a vacuum system to evacuate air from the sample, then pressurize the sample with PFP in a sealed chamber. After PFP gas is loaded into the interior of the nanospheres, degassed 1X PBS is added to rehydrate the silica nanoparticles. The hydrophobic PFP is designed to keep the water out of the interior volume of the silica nanospheres where the enzymes are located. Once an external force such as ultrasound is applied to the nanospheres, the PFP gas will be released and the encapsulated enzymes will be rehydrated and active.

To demonstrate the enzymes within the silica nanoparticles can be activated by ultrasound, a feasibility experiment is conducted with the enzyme penicillinase (BLA) encapsulated in 200-nm silica nanospheres that are sealed with a second layer of calcium phosphate and filled with PFP gas. The enzyme activity is measured before and after sonication and compared between single layer of silica shell and double layer of silica and calcium phosphate shells.

The BLA activity is determined with a colorimetric assay using the substrate nitrocefin that undergoes distinctive color change from yellow with maximum absorbance at 390-nm to red with maximum absorbance at 486-nm. The color change is caused by the amide bond in the β-lactam ring of nitrocefin being hydrolyzed

by BLA. The increase in absorbance at 486-nm wavelength directly correlates to the hydrolysis of nitrocefin and the activity of BLA. The absorbance at 486-nm wavelength is measured on a spectrophotometer, Spark® 20M from Tecan Trading AG, Switzerland. The sonication of the samples are performed in an ice bath using Q125 Sonicator from Qsonica, LLC. at 20% amplitude (which output about 3W) for different number of 1-second pulses.

The result is shown in Figure 5.14. The enzyme activity for silica nanospheres with a single-shell layer (yellow bars) appears to increase as the number of pulses increased and peaked at 20 pulses. After 20 pulses, the enzyme activity dropped and stabilizes. The maximum increase of 25% in enzyme activity is between no pulses to 20 pulses for the single-shell layer nanospheres. Similarly, the enzyme activity for the silica nanospheres with double-shell layer (blue bars) shows the same trend. The maximum increase of 80% in enzyme activity is between no pulses to 20 pulses for the double-shell layer nanospheres.

The number of pulses required to fully release all PFP gas from all nanospheres is probably 20 pulses. Beyond 20 pulses, the enzymes may be adversely affected by the sonication and cause the slight drop in activity. Comparing the maximum increase in enzyme activity from no pulse to 20 pulses, the double-shell layer silica nanospheres showed a higher increase than the single-shell layer silica nanospheres. The low 25% increase in enzyme activity observed in the single-shell layer silica nanospheres is due to the high enzyme activity of the sample before sonication. Most of the PFP gas may have already escaped from the silica nanospheres because the

single-shell layer was not able to keep the gas within the nanospheres. In contrast, the double-shell layer silica nanospheres has a much lower activity before sonication. Most of the PFP gas may still be retained within the silica nanospheres because the second layer of calcium phosphate shell is able to keep the gas from escaping. The enzyme activity before sonication may be further suppressed by optimizing the calcium phosphate thickness.

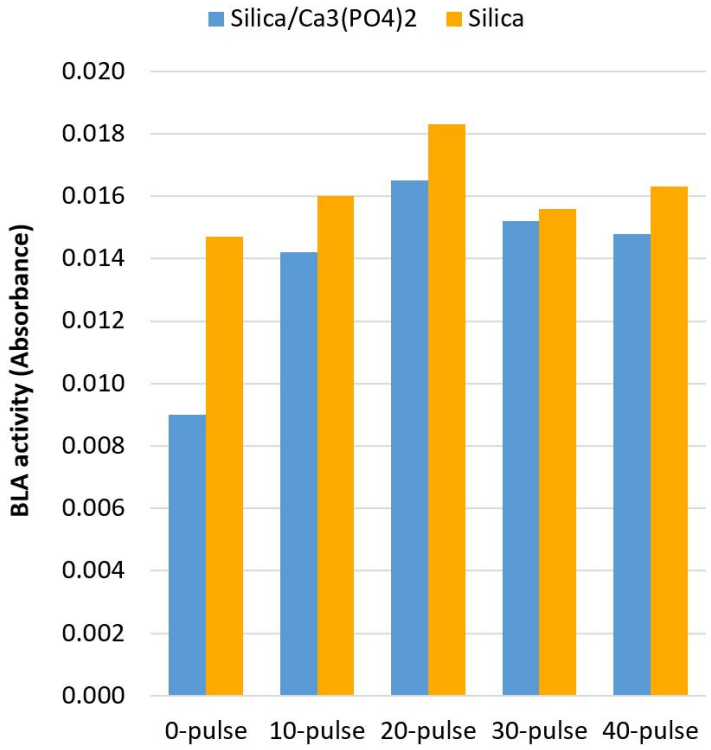

Figure 5.14: The enzyme activity from penicillinase encapsulated in 200-nm silica nanospheres with a single sealing shell or double sealing shells before and after sonication. The penicillinase (BLA) activity increased by 25% after 20 pulses from silica nanospheres with a single silica sealing shell (yellow bars). The penicillinase (BLA) activity increased by 80% after 20 pulses from silica nanospheres with double sealing shell consisting of silica and calcium phosphate (blue bars). Calcium phosphate appears to be able to retain the PFP gas to suppress the enzyme activity until triggered by sonication.

5.5 Acknowledgements

Chapter 5, in part is currently being prepared for submission for publication of the material. Yeh, Ya-San; Vaidyanathan, Mukanth; Sadik, Esener C. "Synthesis of Ultrasound-Activated Enzyme-Loaded Silica Nanoparticles for Targeted Cancer Therapy." The dissertation author was the co-investigator and co-author of this material.

Chapter 6

In vivo Enzyme Protection, Circulation, and Biodistribution

The previous two chapters described the synthesis process of three types of hollow mesoporous silica nanoparticles that differ in size (i.e. 100-nm and 200-nm) and shape (i.e. spherical and ellipsoidal) for therapeutic enzyme delivery. All three types of silica nanoparticles will be PEGylated in order to study the effect of size and shape on circulation and biodistribution. The hypothesis is that the silica nanoparticles will be able to protect the enzymes from neutralizing antibodies, but the ellipsoidal silica nanorods will have the longest time in circulation. Since nanoparticles have the tendency to accumulate in the liver and the spleen, the experimental results presented in this chapter will confirm if the biodistribution of these silica nanoparticles is also concentrated to the liver and spleen.

6.1 Protection of Enzyme *In Vivo*

To demonstrate the activity, protection from neutralizing antibodies, and efficacy in inhibiting tumor growth of non-human enzymes within the silica nanoparticles, the following experiments were performed. The enzymes used in the experiments are native asparaginase (Elspar®) gifted by the Durden group in University of California San Diego Moores Cancer Center. In addition, 200-nm silica nanospheres were synthesized as described in Chapter 4 and 5 with native asparaginase encapsulated. Since the nanospheres were injected intramuscularly, PEGylation was not necessary.

To determine if the enzymes still retain activity *in vivo* after encapsulation, an experimental group of three mice were injected intramuscularly with a single dose of 5 IU of enzyme-encapsulated 200-nm silica nanospheres (i.e. silica Elspar®). The control group of three mice were injected intramuscularly with a single dose of 5 IU of native enzymes (i.e. free Elspar®). All mice were BALB/C not previously exposed to asparaginase, so they do not have antibodies against asparaginase (i.e. naïve mice). The asparagine level in the serum of each mice were monitored over 8 days using high-performance liquid chromatography. The result of the serum asparagine level in naïve mice after treatment with free or silica Elspar® is shown in Figure 6.1(a) [245].

For the control group given the free Elspar®, the serum asparagine was depleted within 30 minutes of injection and sustained at an undetectable level for at least two days. The serum asparagine level reached about 80% of the normal level af-

ter 5 days and returned to the normal level after 8 days. Since the serum asparagine level was not measured daily, it is possible that serum asparagine was depleted for two to four days with free Elspar®. For the experimental group given the silica Elspar®, the serum asparagine dropped about 30% within 30 minutes of injection. By the second day, the serum asparagine level was depleted and sustained at an undetectable level for at least three days. The serum asparagine level returned to normal after 8 days. Since the serum asparagine level was not measured daily, it is possible that serum asparagine was depleted for three to six days with silica Elspar®.

The rapid depletion by the free Elspar® within 30 minutes of injection is probably due to a faster diffusion of the enzymes into the blood circulation, allowing for more access to the asparagine in blood. The diffusion of silica Elspar® into the blood circulation is probably slower due to the size of the nanospheres, causing limited access to asparagine in blood. In addition, asparagine molecules have to diffuse through the layer of silica to interact with the enzyme, which may delay the depletion effect. Even though the serum asparagine depletion profiles differ slightly between free and silica Elspar®, both forms of Elspar® were able to deplete asparagine for a few days. Therefore, the silica nanosphere synthesis process is successful in encapsulating enzymes without losing their activities.

To determine if the silica nanospheres are able to protect the encapsulated enzymes from neutralizing antibodies, all mice were first passively immunized by injecting them with antibodies against asparaginase before 5 IU of free or silica Elspar® were injected intramuscularly in three mice per treatment. Again, the serum

asparagine level of each mice were monitored over 8 days using high-performance liquid chromatography. The result of the serum asparagine level in passively immunized mice after treatment with free or silica Elspar® is shown in Figure 6.1(b) [245].

For the control group given the free Elspar® in the presence of antibodies, the serum asparagine was not depleted. There was a slight drop in serum asparagine level within 30 minutes of injection, but the level returned to normal within a day. The serum asparagine depletion profile observed in the immunized mice is in contrast to that observed in the naïve mice. This observation confirms that the antibodies were able to neutralize the free Elspar® and remove them from circulation. For the experimental group given the silica Elspar® in the presence of antibodies, the serum asparagine dropped about 20% within 30 minutes of injection. The serum asparagine was depleted within a day and sustained at an undetectable level for at least four days. After 8 days, the serum asparagine level returned to normal. The serum asparagine depletion profile observed in the immunized mice is similar to that observed in the naïve mice. This result confirms that the silica nanospheres were able to protect the enzymes from neutralizing antibodies.

In order to show efficacy in tumor inhibition, an experiment to compare tumor growth in mice treated with silica Elspar® with untreated mice was conducted. First, six BALB/C mice were injected with asparagine-sensitive PancO2 cancer cells subcutaneously. The tumors were allowed to grow for 8 days before starting the treatment. Based on the previous serum asparagine depletion profiles of mice treated with silica Elspar®, the intramuscular dosing frequency of once every five days with

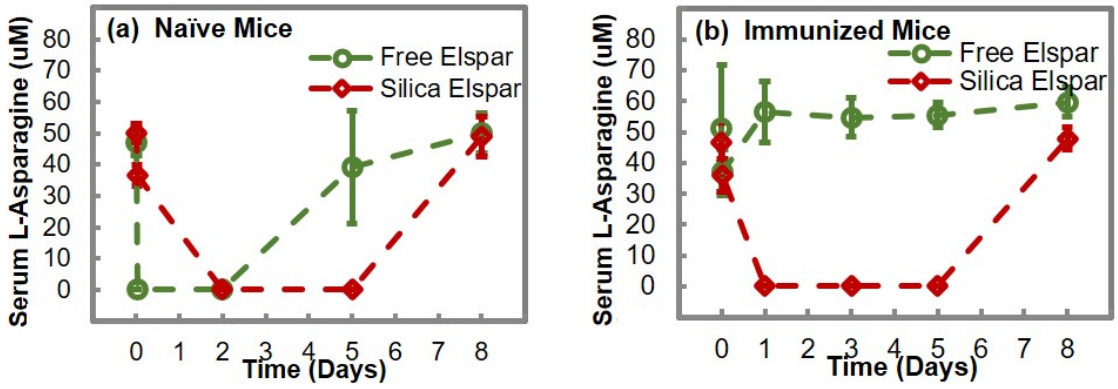

Figure 6.1: Enzyme activity and protection in the (a) absence and (b) presence of neutralizing antibodies (n = 3). (a) In the absence of neutralizing antibodies, both the free asparaginase (i.e. free Elspar® shown in green) and the asparaginase encapsulated in 200-nm silica nanospheres (i.e. silica Elspar® shown in red) were able to deplete serum asparagine for at least two to three days. This result confirms the intact activity of encapsulated Elspar® after the synthesis process. (b) In the presence of neutralizing antibodies, the free Elspar® was unable to deplete serum asparagine, while the silica Elspar® showed the same serum asparagine depletion profile as that without neutralizing antibodies. This result confirms that the neutralizing antibodies have no effects on the encapsulated enzymes and shows that the enzymes are protected by the silica nanospheres.

silica Elspar® was determined to ensure sustained depletion of serum asparagine. After repeated dosing for over 25 days, the tumor size of the mice treated with silica Elspar® appeared to be inhibited as shown in Figure 6.2 [245]. In contrast, the untreated group given phosphate buffer saline showed continued tumor growth. This result confirms the ability of systemic asparagine depletion to inhibit the growth of asparagine-sensitive tumor with repeated localized intramuscular injections of silica Elspar®.

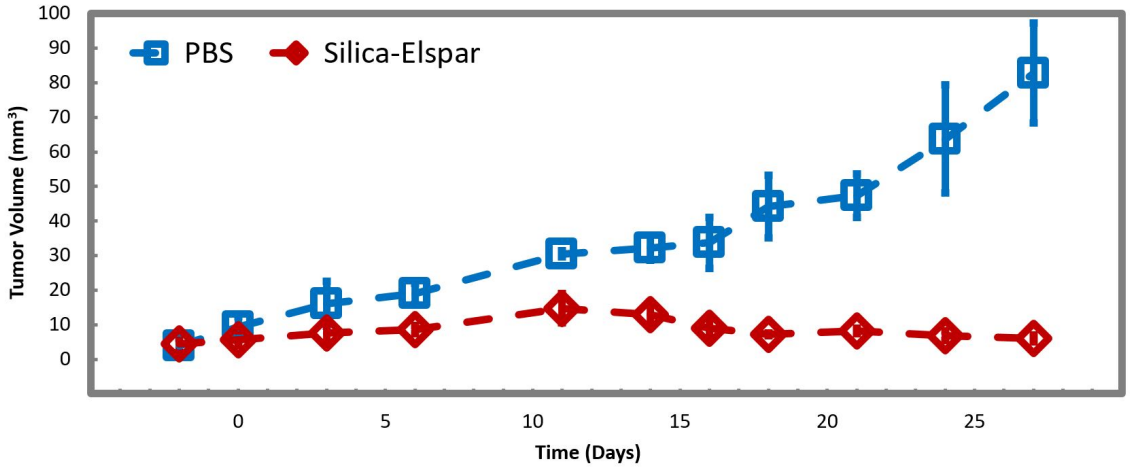

Figure 6.2: Growth inhibition of asparagine-sensitive tumor with systemic asparagine depletion using asparaginase-encapsulated silica nanospheres. BALB/C mice were injected with asparagine-sensitive PancO2 cells eight days prior to intramuscular injection with PBS or asparaginase-encapsulated 200-nm silica nanospheres (i.e. silica Elspar®) every five days (n=3). The tumor volume monitored over 25 days showed a steady increase in tumor volume in the control mice given PBS. In contrast, the tumor volume showed a slight increase then decrease in the mice treated with silica Elspar®. The result confirms the ability of systemic asparagine depletion to inhibit the growth of asparagine-sensitive tumor with repeated localized intramuscular injections of silica Elspar®.

6.2 Circulation of Nanoparticles

With the confirmation that encapsulating enzymes within the sealed hollow mesoporous silica nanoparticles retains the enzyme activity and protects the enzyme from neutralizing antibodies, the next step is to determine if the nanoparticles are able to circulate for an extended period of time. The two often used methods of administering nanoparticles directly into the blood circulation are intravenous (IV) and intraperitoneal (IP) injections. For mouse studies, IV injection is the injection of nanoparticles into the tail vein, while IP injection is the injection of nanoparticles into the peritoneal cavity.

With IV injection, the nanoparticles enter the blood stream and are first exposed to blood proteins while on route to the lung. Opsonic proteins in the blood include different subclasses of antibodies that facilitate the recognition of foreign bodies by different macrophage Fc receptors and complement activation molecules such as C3b and iC3b that label the surface of foreign entities for recognition by macrophage complement receptors. Therefore, opsonization of nanoparticles by certain blood proteins may induce nanoparticles recognition and clearance from the blood by circulating phagocytes and tissue macrophages that come in direct contact with the blood. The tissue macrophages are mainly the Kupffer cells in the liver and the marginal zone and red-pulp macrophages in the spleen. Surface adsorption of blood proteins onto the nanoparticles may induce aggregation. If the nanoparticles aggregates are greater than a micron, they will be trapped in the lung [9].

The peritoneal cavity is contained within a thin serous membrane known as the peritoneum. The peritoneum is made up of an outer monolayer of mesothelial cells, an inner basement membrane, and a network of vascularized connective tissue, fibroblasts, and macrophages. The intraperitoneal organs include the stomach, appendix, liver, transverse colon, first part of the duodenum, small intestines, tail of the pancreas, the upper third of the rectum, sigmoid colon, and spleen. One of the main function of the peritoneum is to recognize and remove bacteria. Mesothelial cells secrete opsonins to trigger destruction of foreign organisms, express CD40 for antigen presentation, and express intercellular adhesion molecules 1 (ICAM-1) and vascular cell adhesion molecule 1 (VCAM-1) for attachment and activation of

lymphocytes, granulocytes, and monocytes to destroy infectious pathogens [246].

It is proposed that nanoparticles injected intraperitoneally enter the blood circulation via the mesentery. The mesentery is formed from a fused, double layer of peritoneum surrounding the blood vessels, nerves, and lymphatics to the abdominal organs [247]. Therefore, the mesentery serves as the main route for arterial, venous, lymphatic, and neural structures in the peritoneal cavity [248].

The mesentery blood circulation system then transports the nanoparticles to the hepatic portal vein into the liver where the resident macrophages or Kupffer cells may remove the nanoparticles from circulation. A summary of the fate of nanoparticles *in vivo* is shown in Figure 6.3. At the injection site, there is possible nanoparticle aggregation in the stomach serous membrane and the mesentery. The remaining nanoparticles then enter the mesentery blood circulation. The superior mesenteric vein and the splenic vein feed into the hepatic portal vein and transport the nanoparticles to the liver and spleen, which are organs of the MPS [249].

To challenge the circulation ability of the sealed hollow mesoporous silica nanoparticles, intraperitoneal injection is selected to ensure the liver is the first organ the nanoparticles encounter after being administered. All three types of nanoparticles were synthesized with fluorescent labels, Alexa Fluor 594 dyes (AF594), in order to monitor their location and quantity. The nanoparticles are also PEGylated to minimize clearance. In addition, fluorescent-labeled proteins, horse radish peroxidase (HRP), are used as a surrogate for free enzymes. The fluorescent-labeled nanoparticles and HRP were spiked into control blood in serial dilution and measured on a

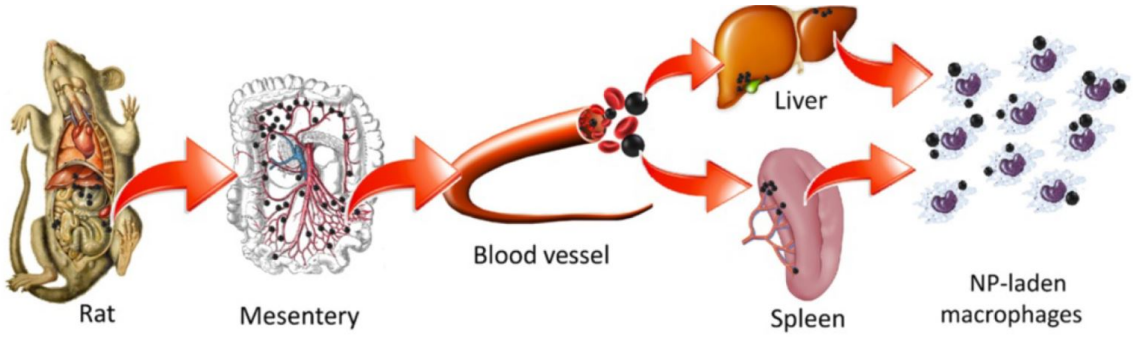

Figure 6.3: Fate of nanoparticles *in vivo* after intraperitoneal injection. It is proposed that after intraperitoneal injection, some nanoparticles may aggregate near the injection site in the stomach serous membrane and the mesentery. The remaining nanoparticles are transported to the liver and spleen via the superior mesenteric vein that feeds into the hepatic portal vein. The liver and spleen make up part of the mononuclear phagocytic system, which is involved in the sequestration and clearance of nanoparticles. Reprinted from [249], no permission required.

spectrophotometer, Spark® 20M from Tecan Trading AG, Switzerland, to generate a fluorescent standard curve for HRP and each type of nanoparticles: 100-nm sealed and PEGylated hollow mesoporous silica nanospheres (100NS), sealed and PEGylated hollow mesoporous silica nanorods with aspect ratio of 1.75 and dimension of 80 nm by 140 nm (100NR), and 200-nm sealed and PEGylated hollow mesoporous silica nanospheres (200NS). The fluorescent standard curves shown in Figure 6.4 are used to estimate the amount of HRP and nanoparticles circulating in the blood over the course of 9 days.

Based on the median lethal dose (LD50) reported for 110 nm MSNs being higher than 1000 mg/kg [222] and the average weight of a mouse at 20 g, no more than 20 mg of silica per mouse will be used in the animal studies. In addition, the circulation experiment will be conducted with numbers of silica nanoparticles in the same order of magnitude across the different types of silica nanoparticles. The dose

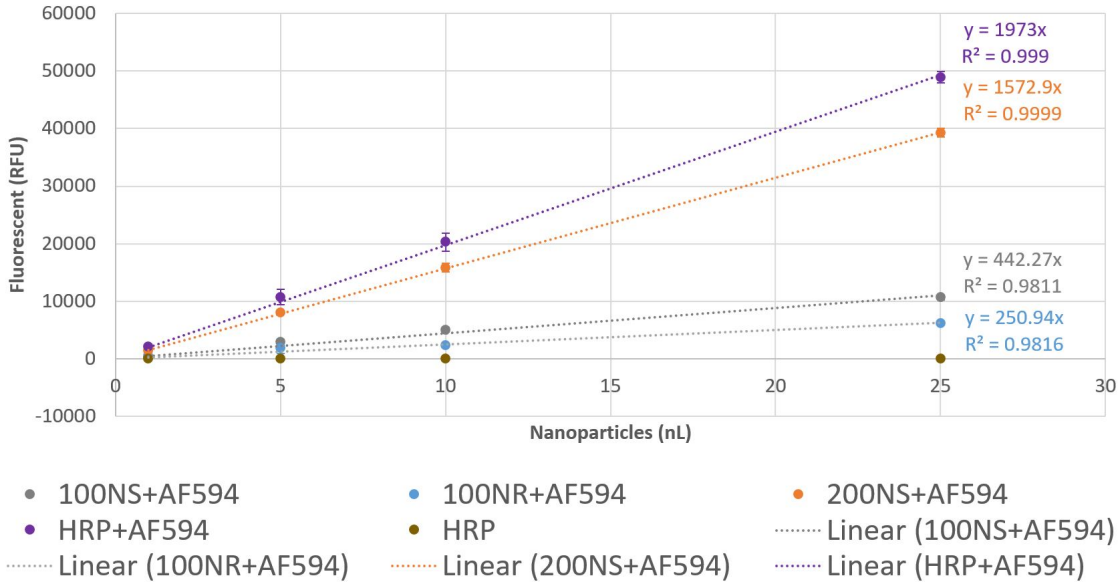

Figure 6.4: Fluorescent standard curves for enzymes and silica nanoparticles labeled with fluorescent dyes. The horseradish peroxidase (HRP), 100-nm sealed and PEGylated hollow mesoporous silica nanospheres (100NS), sealed and PEGylated hollow mesoporous silica nanorods with aspect ratio of 1.75 and dimensions of 80 nm by 140 nm (100NR), and 200-nm sealed and PEGylated hollow mesoporous silica nanospheres (200NS) were labeled with Alexa Fluor 594 dyes (AF594). The fluorescent signals are measured for all nanoparticles after serial dilution to generate the fluorescent standard curves. Unlabeled HRP was used as negative control.

effect will also be investigated by using a high dose and a low dose injection for each type of silica nanoparticles. Concentration of each type of silica nanoparticles was measured with ViewSizer® 3000 from Manta Instruments, Inc. and shown in Figure 6.5. For the high dose experiments, 1 mL of each type of nanoparticles were concentrated down to 100 μL for IP injection. Therefore, the total number of particles injected was about $4.88\text{x}10^{11}$ for 100NS (*left*), $2.34\text{x}10^{11}$ for 100NR (*middle*), and $3.23\text{x}10^{11}$ for 200NS (*right*). At this number of silica nanoparticles, the total silica weight is between 5 to 10 mg per injection. For the low dose experiment, 50 μL of the nanoparticles were used, which is half of the high dose.

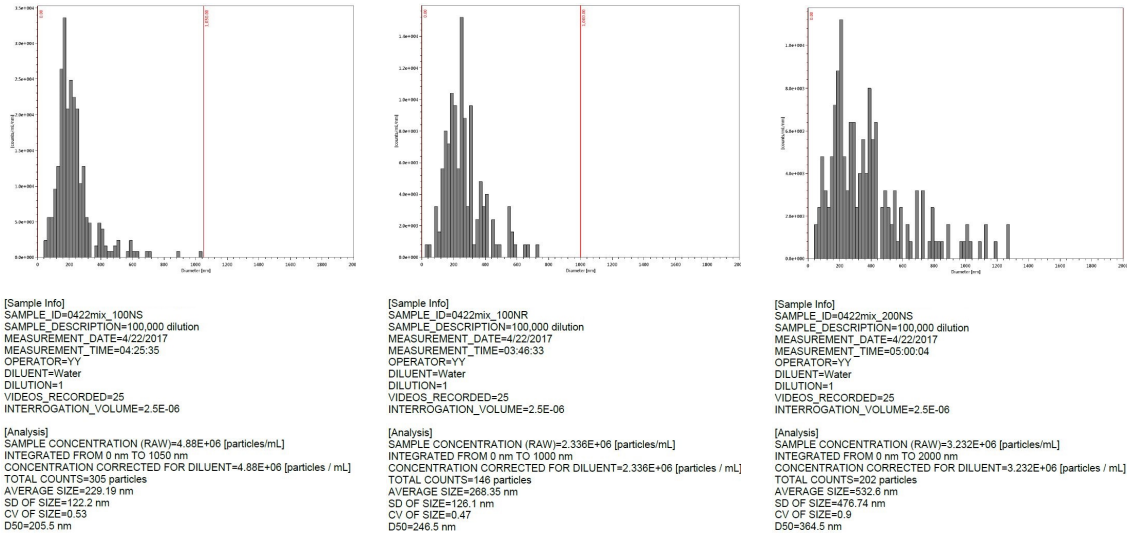

[Sample Info]
SAMPLE_ID=0422mix_100NS
SAMPLE_DESCRIPTION=100,000 dilution
MEASUREMENT_DATE=4/22/2017
MEASUREMENT_TIME=04:25:35
OPERATOR=YY
DILUENT=Water
DILUTION=1
VIDEOS_RECORDED=25
INTERROGATION_VOLUME=2.5E-06

[Analysis]
SAMPLE CONCENTRATION (RAW)=4.88E+06 [particles/mL]
INTEGRATED FROM 0 nm TO 1050 nm
CONCENTRATION CORRECTED FOR DILUENT=4.88E+06 [particles / mL]
TOTAL COUNTS=305 particles
AVERAGE SIZE=229.19 nm
SD OF SIZE=122.2 nm
CV OF SIZE=0.53
D50=205.5 nm

[Sample Info]
SAMPLE_ID=0422mix_100NR
SAMPLE_DESCRIPTION=100,000 dilution
MEASUREMENT_DATE=4/22/2017
MEASUREMENT_TIME=03:46:33
OPERATOR=YY
DILUENT=Water
DILUTION=1
VIDEOS_RECORDED=25
INTERROGATION_VOLUME=2.5E-06

[Analysis]
SAMPLE CONCENTRATION (RAW)=2.336E+06 [particles/mL]
INTEGRATED FROM 0 nm TO 1000 nm
CONCENTRATION CORRECTED FOR DILUENT=2.336E+06 [particles / mL]
TOTAL COUNTS=146 particles
AVERAGE SIZE=268.35 nm
SD OF SIZE=126.1 nm
CV OF SIZE=0.47
D50=246.5 nm

[Sample Info]
SAMPLE_ID=0422mix_200NS
SAMPLE_DESCRIPTION=100,000 dilution
MEASUREMENT_DATE=4/22/2017
MEASUREMENT_TIME=05:00:04
OPERATOR=YY
DILUENT=Water
DILUTION=1
VIDEOS_RECORDED=25
INTERROGATION_VOLUME=2.5E-06

[Analysis]
SAMPLE CONCENTRATION (RAW)=3.232E+06 [particles/mL]
INTEGRATED FROM 0 nm TO 2000 nm
CONCENTRATION CORRECTED FOR DILUENT=3.232E+06 [particles / mL]
TOTAL COUNTS=202 particles
AVERAGE SIZE=532.6 nm
SD OF SIZE=476.74 nm
CV OF SIZE=0.9
D50=364.5 nm

Figure 6.5: Concentration of different silica nanoparticles measured with ViewSizer® 3000 from Manta Instruments, Inc. For the low dose experiments, 1 mL of each type of nanoparticles were concentrated down to 100 μL for IP injection. Therefore, the total number of particles injected was about $4.88\text{x}10^{11}$ for 100NS (*left*), $2.34\text{x}10^{11}$ for 100NR (*middle*), and $3.23\text{x}10^{11}$ for 200NS (*right*). Half of the high dose is used in the low dose experiments.

The C57Bl6 mice IP injected with high dose of the nanoparticles all lost between 10% and 16% of their original weight by the second day, but gained the weight back to almost their baseline weight after nine days. The mice IP injected with low dose of the nanoparticles and free enzymes all lost between 1% and 5% of their original weight. The weight loss results are shown in Figure 6.6 and indicate possible toxicity of the nanoparticles.

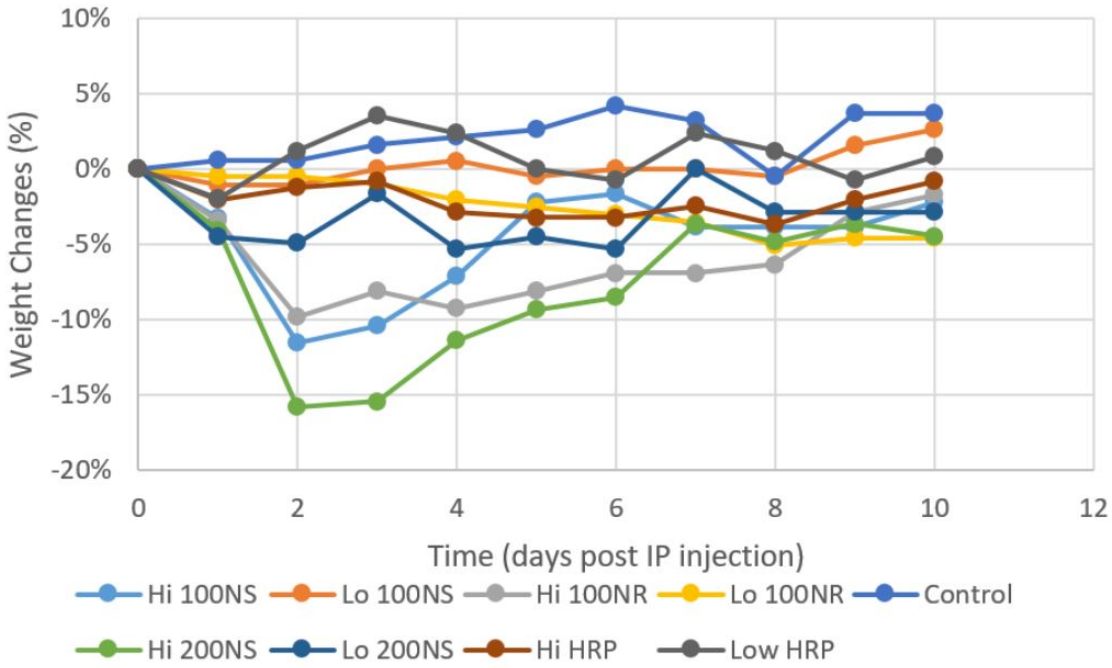

Figure 6.6: Weight loss of C57Bl6 mice injected with different silica nanoparticles and free enzymes at two doses (n = 1). The mice given the high dose nanoparticles (100NS Hi, 100NR Hi, and 200NS Hi) lost the most weight, ranging from 10% to 16% of their original weight. The mice given the low dose nanoparticles (100NS Lo, 100NR Lo, and 200 NS Lo) and either dose of HRP (HRP Hi and HRP Lo) lost between 1% and 5% of their baseline weight. The weight loss indicates possible toxicity of the silica nanoparticles.

The circulation of the nanoparticles were determined by the blood fluorescent signal. The fluorescent signal from whole blood drawn from each mouse and diluted in 1X PBS was measured on a spectrophotometer, Spark® 20M from Tecan Trading AG, Switzerland. The excitation and emission wavelength used were 580-nm and 625-nm, respectively. All fluorescent signals were normalized to the baseline blood fluorescent before the injection (i.e. day 0). The fluorescent signal threshold was set at three standard deviation of the average fluorescent signal from the blood of the mouse given PBS. Fluorescent signals below this threshold level was considered

below the detection limit.

For the high dose experiment, each mouse was given high dose of 100NS (100NS Hi), 100NR (100NR Hi), 200NS (200NS Hi), 0.5 mg of HRP (HRP Hi), or PBS (control) via IP injection. The fluorescent signal from 100NS Hi and 100NR Hi were below the detection limit between day 3 and 4, while that of the 200NS Hi and HRP Hi were below detection limit between day 2 and 3 as shown in Figure 6.7. The two other negative controls are PBS only and empty well to confirm there is no fluorescent interference from the PBS or the well.

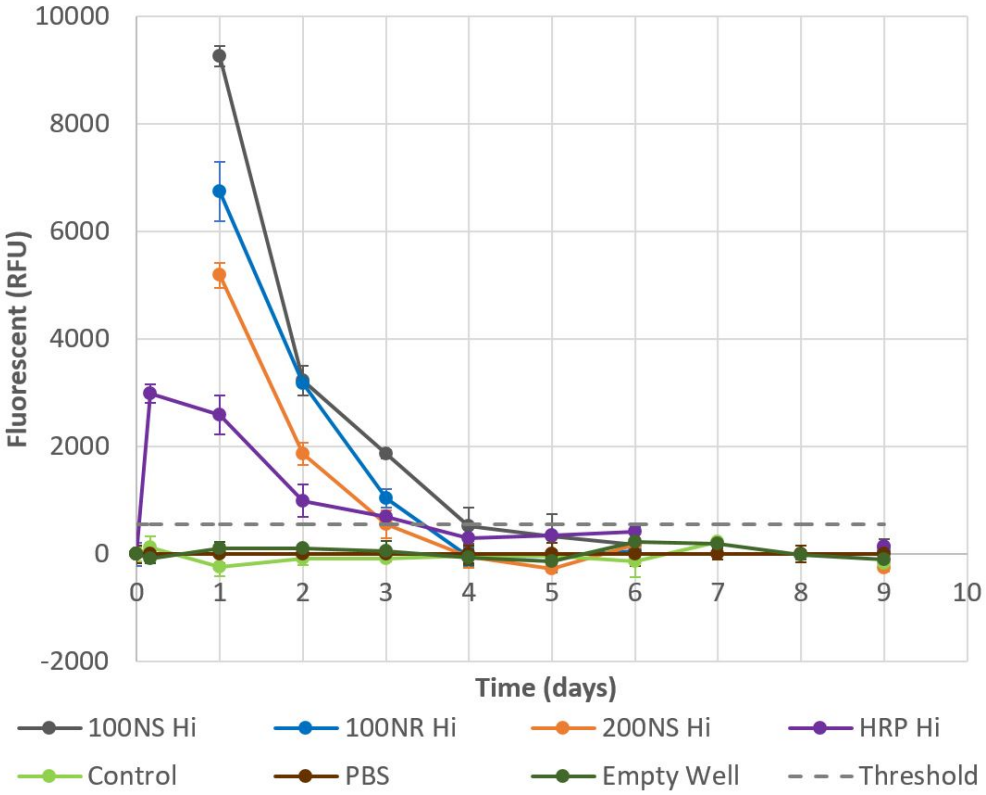

Figure 6.7: Blood fluorescent level of C57Bl6 mice injected with fluorescent-labeled 100NS, 100NR, and 200NS at a high dose (about 2.4 to 4.8 x 10^{11} nanoparticles and 0.5 mg HRP). The fluorescent signals from 100NS Hi and 100NR Hi dropped below the threshold detection limit (dotted line) by day 4, while that of 200NS Hi and HRP Hi dropped below the limit by day 3.

For the low dose experiment, each mouse was given low dose of 100NS (100NS Lo), 100NR (100NR Lo), 200NS (200NS Lo), 0.25 mg of HRP (HRP Lo), or PBS (control) via IP injection. The fluorescent signals from 100NR Lo lasted the longest for up to 9 days, followed by 100NS Lo for 8 days, and 200NS Lo for 5 days as shown in Figure 6.8. The HRP Lo fluorescent signal was undetectable by the second day.

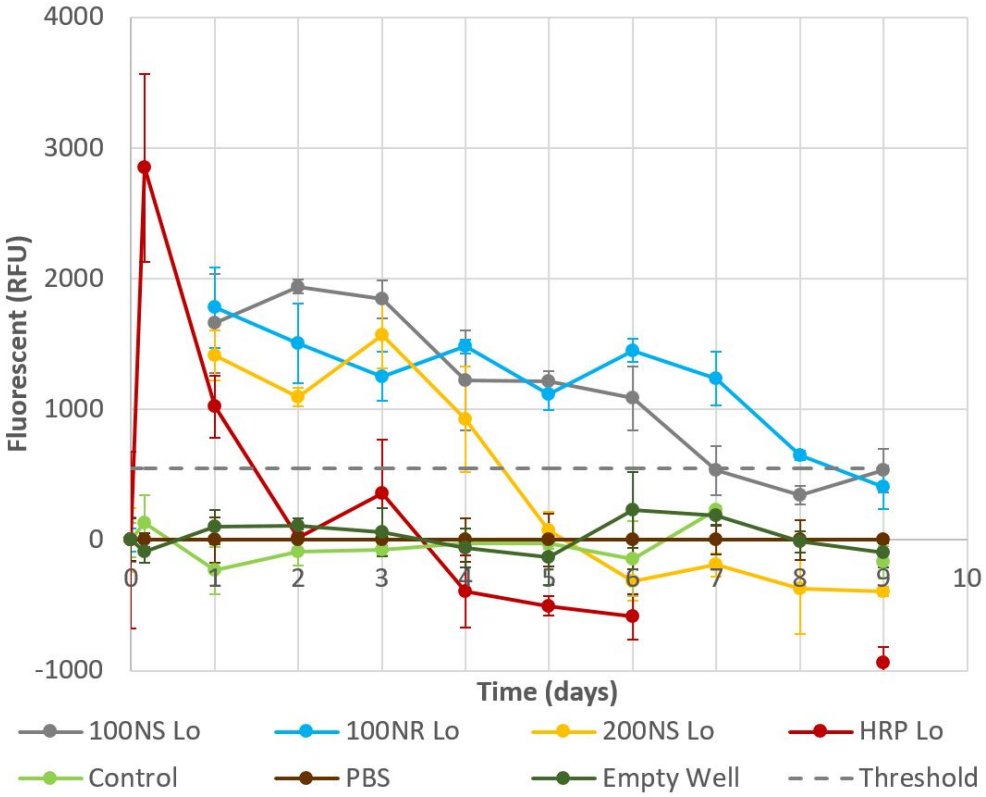

Figure 6.8: Blood fluorescent level of C57Bl6 mice injected with fluorescent-labeled 100NS, 100NR, and 200NS at a low dose (about 1.2 to 2.4 x 10^{11} nanoparticles and 0.25 mg HRP). The fluorescent signals from 100NR Lo lasted the longest for up to 9 days, followed by 100NS Lo for 8 days, 200NS Lo for 5 days, and HRP Lo for 2 days.

The results showed that free enzymes (i.e. HRP) are cleared from the circulation the fastest, followed by larger nanoparticles (i.e. 200-nm silica nanospheres)

regardless of dose. Reducing the size of the nanoparticles (i.e. 100-nm silica nanospheres) and changing the shape of the nanoparticles to ellipsoidal (i.e. silica nanorods with aspect ratio of 1.75 and dimensions < 200 nm) appear to enhance the circulation time of the nanoparticles. In addition, there is a dose-dependent effect on the nanoparticle circulation. Administering higher dose resulted in diminished circulation time of the nanoparticles. One possible explanation is that high dose injection may lead to higher chance of nanoparticles aggregating in the blood. These aggregates are more likely to be cleared by the MPS quickly.

6.3 Biodistribution of Nanoparticles

The circulation results confirmed the ability to increase the nanoparticle circulation time in the blood by reducing the nanoparticle size below 200-nm and changing the nanoparticle shape to ellipsoidal. The next focus is on the biodistribution of these nanoparticles once they exit systemic circulation. As reviewed in Chapter 2, most nanoparticles end up in the liver and spleen. Therefore, after nine days when the fluorescent signals from all nanoparticles are below detection limits, the organs from the mice were examined macroscopically with a fluorescent imaging system, *Iv Vivo* Imaging System (IVIS) Lumina XRMS from PerkinElmer Inc., and microscopically with a fluorescent microscope. The liver and spleen were expected to show sequestration of the nanoparticles. The kidney was expected to show low level of fluorescent signal if the nanoparticles have been degraded and excreted through the

renal system. The heart and lung were not expected to show any fluorescent signal since microparticles are usually the ones to accumulate in the lung, but these nanoparticles are not expected to aggregate to micron in size.

For accurate comparison, all IVIS images are taken with the same exposure time and excitation and emission wavelengths. The fluorescent signal from the unprocessed images are shown in auto scale. To eliminate artifact and tissue autofluorescence, the images were processed. The processed images have their fluorescent signals fixed with a lower threshold that eliminates any signals from the control group since no fluorescence is expected from the organs of the mouse injected with PBS only. The processed image is shown with a fixed scale next to the unprocessed image. This fixed scale is applied to all subsequent processed images. Figure 6.9 shows the organs from the two control mice displayed as unprocessed image (auto scale) and processed image (fixed scale).

For the mice injected with free HRP enzyme, no fluorescent signal was detected in the processed image as shown in Figure 6.10. Since the blood fluorescent signals were undetectable after day 2 and day 3 for the low dose and high dose HRP, respectively, it is possible that the free enzymes have been cleared through the renal system by the time the organs were examined on day 9.

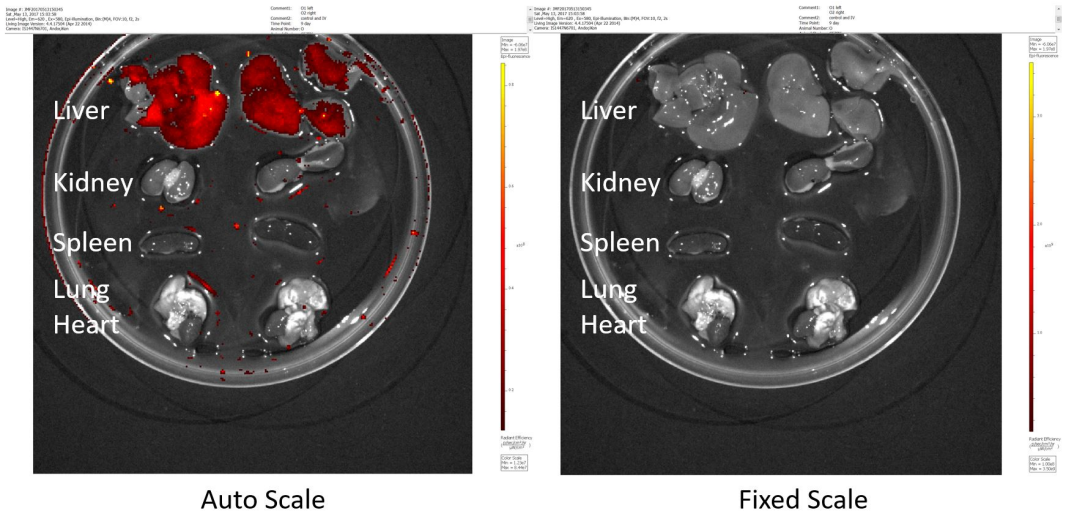

Figure 6.9: Unprocessed and processed images from *In Vivo* Imaging System of the organs from two C57Bl6 mice IP injected with PBS (control group). The unprocessed image with auto fluorescent scale is shown on the *left*. Since the organs from the control group should not have any fluorescent signal from the nanoparticles, the lower threshold is increased until there is no signal in the processed image as shown on the *right*. This fixed scale is used for all other processed images.

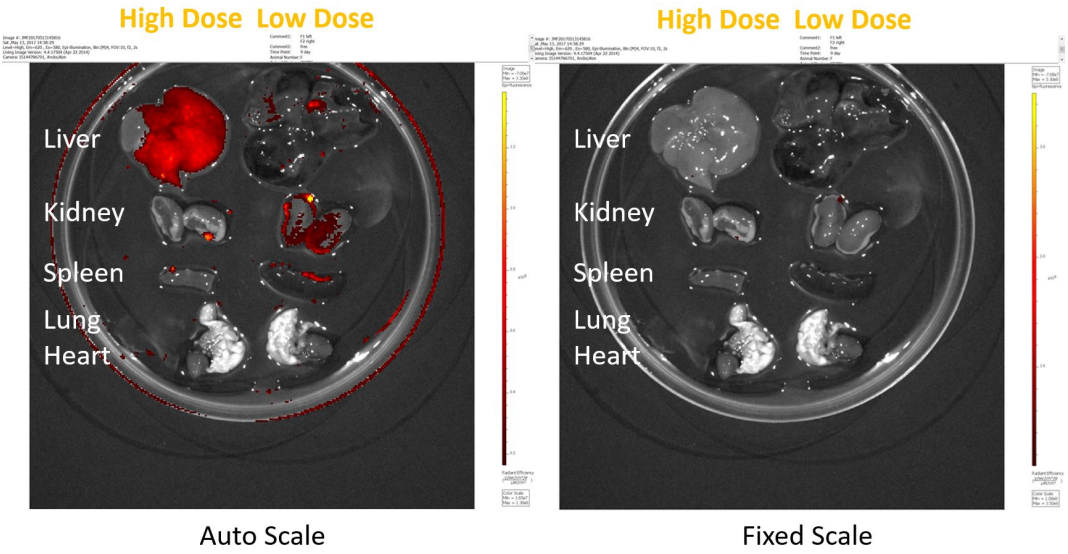

Figure 6.10: Unprocessed and processed images from *In Vivo* Imaging System of the organs from the C57Bl6 mouse IP injected with HRP at high and low dose (free enzyme group). The unprocessed image with auto fluorescent scale is shown on the *left*. After image processing, no fluorescent signal is visible as shown on the *right*. Since the blood fluorescent signals were undetectable after day 2 and day 3 for the low dose and high dose HRP, respectively, it is possible that the free enzymes have been cleared via the renal system by the time the organs were examined on day 9.

For the mice injected with fluorescent-labeled, sealed, and PEGylated 100-nm hollow mesoporous silica nanospheres (100NS) at a high dose, fluorescent signals are visible in the liver, spleen, and kidney in the processed image as shown in Figure 6.11. Since the blood fluorescent signal was undetectable after day 4 for high dose 100NS, this observation is consistent with the nanospheres being sequestered in the liver and spleen and possible degraded for excretion through the kidney by day 9. Low level fluorescent signal is detected only in the liver for low dose 100NS, which may be explain by the nanospheres exiting the circulation by day 8 and the inadequate sensitivity of the imaging system.

For the mice injected with fluorescent-labeled, sealed, and PEGylated hollow mesoporous silica nanorods with an aspect ratio of 1.75 and dimensions of 80 nm by 140 nm (100NR) at a high dose, weak fluorescent signals are visible in the liver and kidney in the processed image as shown in Figure 6.12. Since the blood fluorescent signal was undetectable after day 4 for both high dose 100NS and 100NR, the biodistribution of the nanorods was expected to be similar to the 100-nm nanospheres, where they were sequestered in the liver and spleen, and degraded for excretion through the kidney by day 9. However, only weak fluorescent signals were observed in the liver and kidney for high dose 100NR. This result may imply that the elimination route of 100NR differs from that of 100NS. One possible explanation is that the nanorods were excreted through the renal system without degradation. There are report of intact nanorods larger than the glomerular filtration limits of the renal system (i.e. < 25 nm) being excreted through the kidney [173]. No fluorescent signal

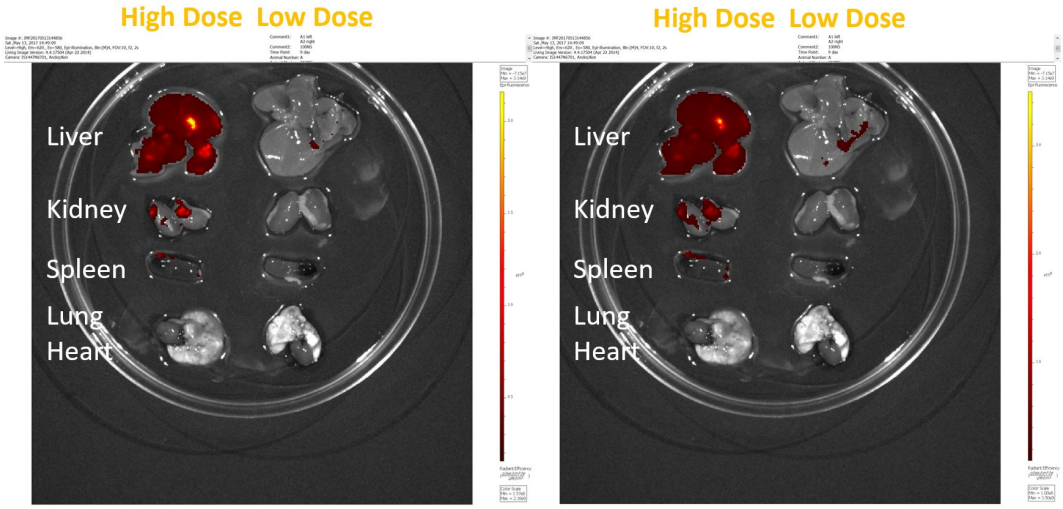

Figure 6.11: Unprocessed and processed images from *In Vivo* Imaging System of the organs from the C57Bl6 mouse IP injected with 100-nm silica nanospheres at high and low dose (100NS group). The unprocessed image with auto fluorescent scale is shown on the *left*. After image processing, fluorescent signals are visible in the liver, spleen, and kidney for high dose 100NS, while only low level signal is visible in the liver for low dose 100NS as shown on the *right*. Since the blood fluorescent signal was undetectable after day 4 for high dose 100NS, this observation is consistent with the nanospheres being sequestered in the liver and spleen and possibly degraded for excretion through the kidney by day 9. Low level fluorescent signal is detected only in the liver for low dose 100NS, which may be explained by the nanospheres exiting the circulation by day 8 and the inadequate sensitivity of the imaging system.

is detected for low dose 100NR, which may be explain by the nanorods exiting the circulation by day 9 and the inadequate sensitivity of the imaging system.

For the mice injected with fluorescent-labeled, sealed, and PEGylated 200-nm hollow mesoporous silica nanospheres (200NS) at a high dose, fluorescent signals are visible in the liver, spleen, and kidney in the processed image as shown in Figure 6.13. Since the blood fluorescent signal was undetectable after day 3 for high dose 200NS, this observation is consistent with the nanospheres being sequestered in the liver and spleen and possible degraded for excretion through the kidney by day 9.

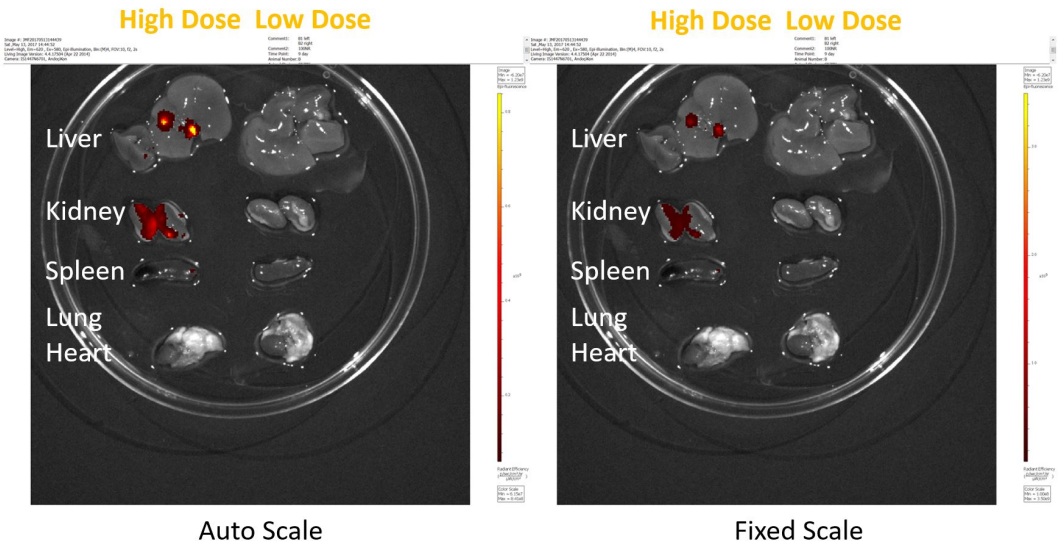

Figure 6.12: Unprocessed and processed images from *In Vivo* Imaging System of the organs from the C57Bl6 mouse IP injected with silica nanorods at high and low dose (100NR group). The unprocessed image with auto fluorescent scale is shown on the *left*. After image processing, low level fluorescent signals are visible in the liver and kidney for high dose 100NR, while no signal is visible in all organs for low dose 100NR as shown on the *right*. Since the blood fluorescent signal was undetectable after day 4 for high dose 100NS, the nanorods were expected to be sequestered in the liver and spleen, and possibly degraded for excretion through the kidney by day 9. However, only weak fluorescent signals were observed in the liver and kidney. No fluorescent signal is detected in all organs for low dose 100NR, which may be explain by the nanorods exiting the circulation by day 9 and the inadequate sensitivity of the imaging system.

No fluorescent signal is detected for low dose 200NS, which may be explain by the inadequate sensitivity of the imaging system.

A side-by-side comparison of the processed image of the organs from the high dose injection of all three types of nanoparticles is shown in Figure 6.14. The 200NS showed the highest and uniform fluorescent signal in the liver, indicating clearance by the liver. Furthermore, only the spleen from the mouse given the high dose 200NS showed fluorescent signal. These results are attributed to the larger size of

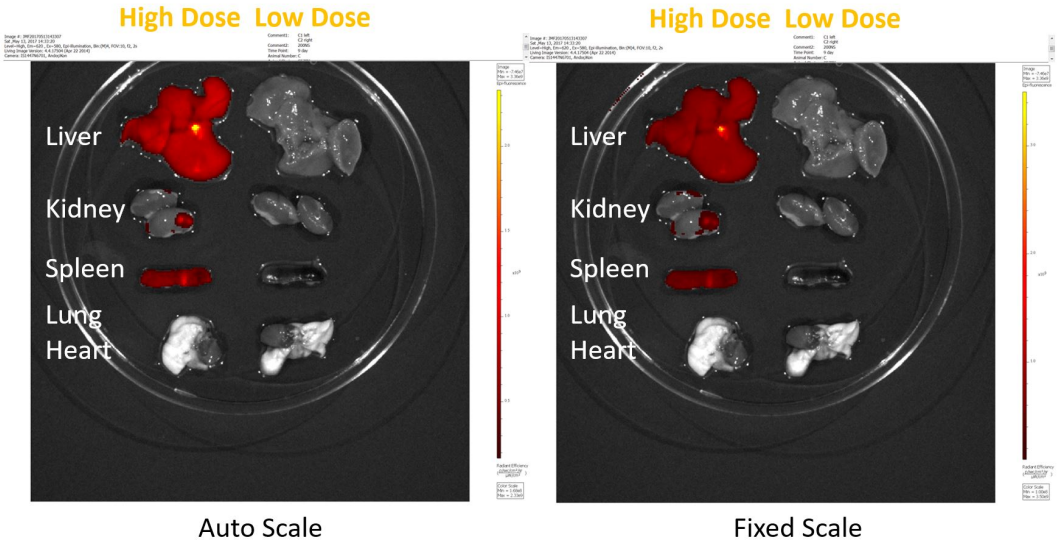

Figure 6.13: Unprocessed and processed images from *In Vivo* Imaging System of the organs from the C57Bl6 mouse IP injected with 200-nm silica nanospheres at high and low dose (200NS group). The unprocessed image with auto fluorescent scale is shown on the *left*. After image processing, strong fluorescent signals are visible in the liver and spleen, and weak signal in the kidney for high dose 200NS, while no signal is visible in all organs for low dose 200NS as shown on the *right*. Since the blood fluorescent signal was undetectable after day 3 for high dose 200NS, this observation is consistent with the nanospheres being sequestered in the liver and spleen and possibly degraded for excretion through the kidney by day 9. No fluorescent signal is detected in all organs for low dose 200NS, which may be explained by the inadequate sensitivity of the imaging system.

the 200NS. Nanoparticles larger than 200-nm has been reported to be sequestered in both the spleen and the liver as reviewed in Chapter 2. The strong fluorescent signal observed in the liver and the lack of fluorescent signal in the spleen from the mouse given the high dose 100NS are expected since the nanoparticles is just below the cut-off limit of the splenic filtration and around that of the liver sequestration. A single localized fluorescent signal in the liver from the mouse given the high dose 100NR was unexpected. Since the blood fluorescent level from both high dose 100NS and 100NR dropped below the detection limit around the same time, the biodistribution of both

nanospheres and nanorods will be similar if the clearance mechanisms are the same. Therefore, it is likely that the nanorods are cleared with a different mechanism.

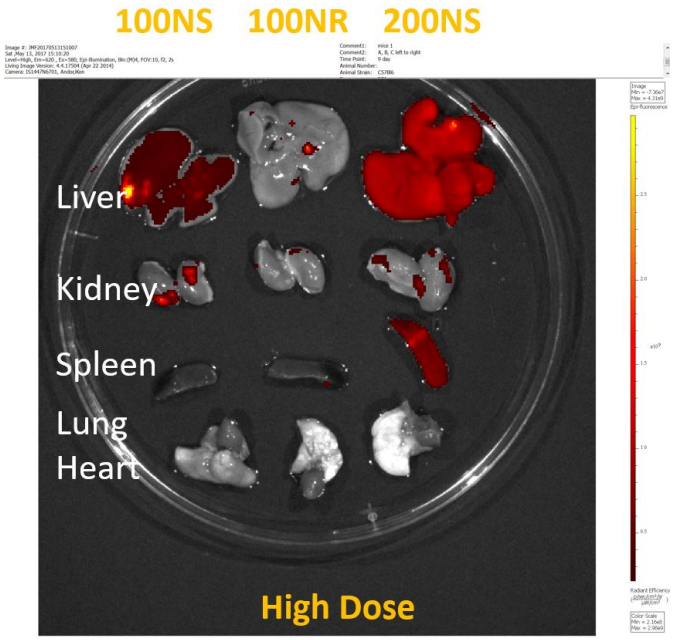

Figure 6.14: Processed image from *In Vivo* Imaging System of the organs from the C57Bl6 mice IP injected with high dose nanoparticles. The strong fluorescent signal from the liver and spleen of the mouse injected with high dose 200NS indicates clearance by the liver and spleen. The strong fluorescent signal from the liver of the mouse injected with high dose 100NS indicates clearance by the liver. The single localized fluorescent signal in the liver of the mouse injected with high dose 100NR indicates a different clearance mechanism.

A side-by-side comparison of the processed image of the organs from the low dose injection of all three types of nanoparticles is shown in Figure 6.15. None of the organs showed fluorescent signals. This may be partly explained by the inadequate sensitivity of the IVIS at this low level of fluorescent. A whole tissue examination with a fluorescent microscope will be used for confirmation.

The whole tissue fluorescent microscopy images of the organs injected with high dose nanoparticles are shown in Figure 6.16. For high dose 100NS and 200NS,

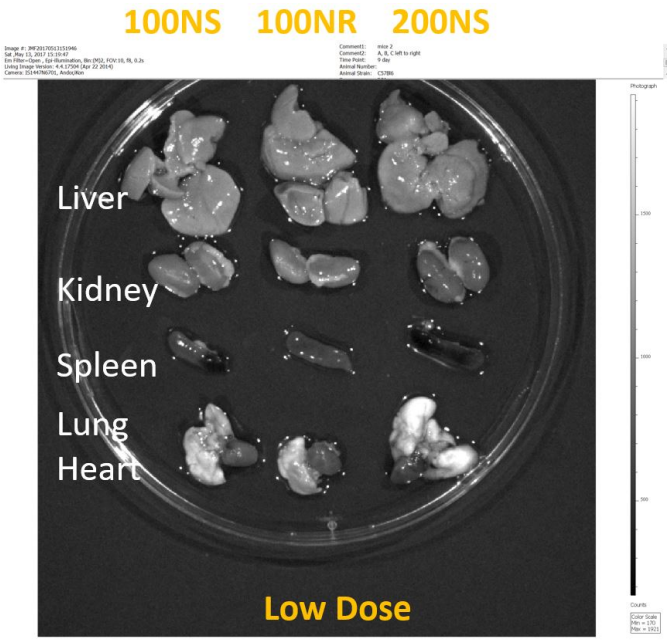

Figure 6.15: Processed image from *In Vivo* Imaging System of the organs from the C57Bl6 mice IP injected with low dose nanoparticles. None of the organs showed fluorescent signals.

the fluorescent signals appear to be spread outward from the portal vein toward the central vein. This pattern indicates the entrance of the nanoparticles from the peritoneal cavity through the mesentery into the portal vein and exiting the liver through the central vein to the heart. The highest fluorescent is located near the portal vein in the sinuous where the Kupffer cells reside, indicating clearance of the nanoparticles from circulation by the Kupffer cells. Furthermore, the fluorescent signal appears more diffused for the liver with high dose 200NS, indicating more 200-nm nanospheres are being sequestered. However, the fluorescent signal appears to be localized to one lobule for the liver with high dose 100NR. It is possible that most of the nanorods escaped clearance by the Kupffer cells. The captured nanorods may be a sub-population with lower PEGylation density or lower aspect ratio since PEGylation

and the template stretching processes do not produce homogeneous nanorods.

In addition, there are weak fluorescent signals detected in the spleens from mice injected with all three types of nanoparticles even though the IVIS images did not show any fluorescent signal from two of the spleens. This points to the inadequate sensitivity of the IVIS. Finally, fluorescent signals are detected in all kidneys. The excretion of nanoparticles through the renal system is desired to ensure no accumulation in the body. However, it is unclear if the nanoparticles have been degraded and the released fluorescent dyes were excreted or the nanoparticles are being excreted as intact particles.

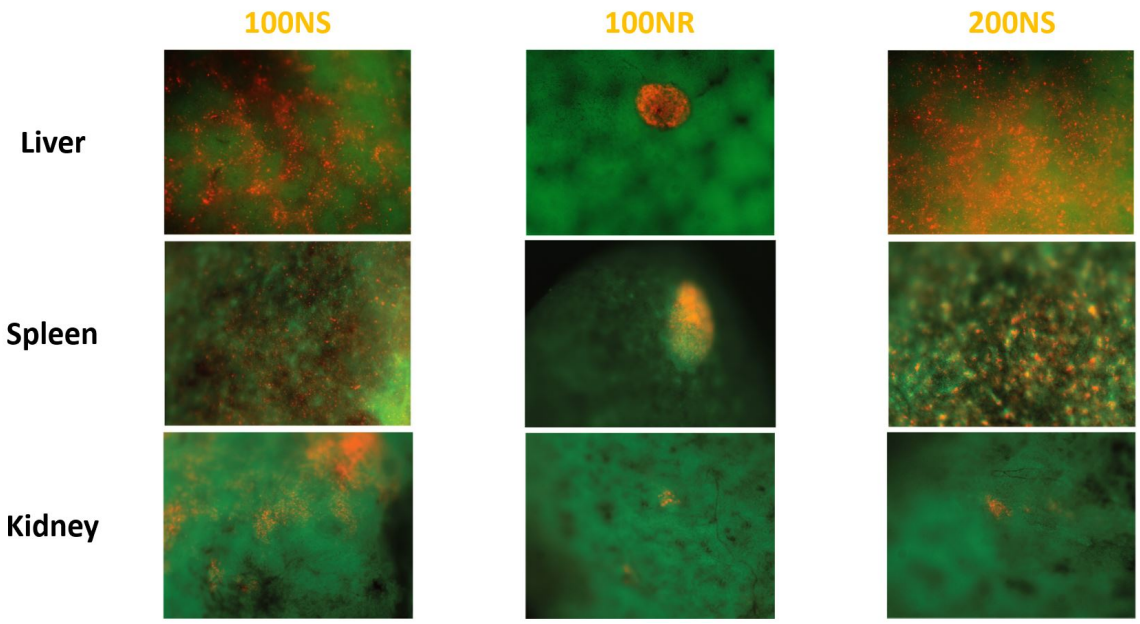

Figure 6.16: Fluorescent microscope images of whole organs from the C57Bl6 mice IP injected with high dose nanoparticles. The pattern of the fluorescent signals from 100NS and 200NS resembles the lobules of the liver, indicating that the nanospheres entered the liver through the portal veins and many were sequestered by the Kupffer cells in the sinuous as they traveled towards the central vein. More 200NS were sequestered than 100NS since the fluorescent signals were more diffused and cover a larger area of the liver. The single localized fluorescent signal from 100NR resembles one lobule, indicating a different clearance mechanism for 100NR. All spleens and kidneys showed fluorescent signal in varying intensity, indicating clearance of some nanoparticles by the spleen and kidney.

Chapter 7

Conclusions and Future Directions

7.1 Conclusions

In conclusion, this dissertation has described the synthesis of hollow mesoporous silica nanoparticles that are of different shapes and sizes, different surface functionalization, and different pore sizes. The silica nanoparticles have been shown to be protective of immunogenic enzymes *in vivo* and capable of inhibiting tumor growth. In addition, the silica nanoparticles can be loaded with perfluorocarbon gas to inactivate the enzymes until an ultrasound is applied to release the gas and rehydrate the enzymes to return their enzymatic activity. Finally, the *in vivo* circulation results showed that the circulation of the nanoparticles may be extended by reducing the nanoparticle size from 200 nm to 100 nm and by changing the nanoparticle shape from spherical to ellipsoidal with an aspect ratio of 1.75 and dimension of 80 by 140 nm.

The scientific contribution of this work includes designing and developing a flexible nanoparticle-assisted delivery vehicle platform that can (1) protect immunogenic enzymes from antibody neutralization which enables possible revival of previously failed enzyme therapy due to immunogenicity and possible elimination of the need to engineer de-immunizing proteins, (2) extend enzyme circulation half-life without modifications which enables possible revival of previously failed enzyme therapy due to low enzyme activity from enzyme modifications, and (3) enable passive and active targeting with simple silica surface modifications which enables possible revival of previously failed enzyme therapy due to low enzyme activity from enzyme modification or inadequate enzyme accumulation at target sites.

7.2 Future Directions

Some of the future work to be conducted includes quantifying nanoparticle biodistribution in the organs of the mice, investigate the nanoparticle clearance mechanisms, and study tumor shrinkage with the three types of nanoparticles with immunized mice.

In addition, it is important to conduct studies to understand the excretion of these nanoparticles to ensure the safety of such therapy. The assumption is that the poly(ethylene glycol) molecules will shed from the surface of the nanoparticles eventually and be excreted via the renal system. However, not much is known about the acute and chronic pharmacological effects of these PEG polymers. There are con-

cerns that these polymers may cause complement activation-related pseudoallergy, modulation of gene activation, enzyme activity, and signal transduction [144].

Another interesting consideration is the complement activating nature of stealth particles. Although complement activation may not necessarily lead to the clearance of PEGylated nanoparticles from the blood, complement activation is associated with the release of anaphylatoxins. Anaphylatoxins may be responsible for the observed pseudoallergic reaction following intravenous injection of PEGylated nanoparticles. In fact, complement activation is associated with the activation of other proteolytic plasma cascades which may cause other adverse side effects [144].

The degradation and excretion of both the sol-gel silica layer and the calcinated silica layer will need to be studied as well for safety. If they cannot be degraded by the phagocytes, these nanoparticles will accumulate in the MPS organs, which will most likely be in the liver and spleen. Long term accumulation of these nanoparticles may lead to toxicity and other adverse side effects.

There is evidence that silica can be degraded and excreted via the renal system in urine and the biliary system in feces [173]. One study using uncalcinated silica was able to detect silicon content in kidney and urine two hours after the uncalcinated silica nanoparticles were injected to indicate renal clearance. Silicon content was detected in liver two hours after injection, but was only detected in high level in feces at seven days after injection. The suggested explanation is that the hepatic processing and biliary excretion after liver uptake is a much slower clearance route than the renal clearance route. Since the nanoparticles are consisted of an uncalci-

nated layer over a calcinated silica layer, the excretion time and long-term toxicity will need to be evaluated.

Finally, the characterization of the silica nanoparticles described here will need to meet the standards for pre-clinical studies as defined by the National Cancer Institute (NCI), National Institute of Standards and Technology (NIST), and FDA. The three groups have established the Nanotechnology Characterization Lab (NCL) to run standardized tests to provide physiochemistry, toxicology, pharmacology, efficacy studies of nanoparticles in *in vitro* and pre-clinical *in vivo* settings and to provide standardized reporting formats to better prepare nanotechnology products for the clinical approval process [42]. The goal for these standardized tests is to identify and characterize the important parameters involved in the absorption, distribution, metabolism, and excretion (also known as ADME) of a nanoparticle [12].

Bibliography

[1] Ferrari, M. (2005). Cancer nanotechnology opportunities and challenges. *Nature Reviews Cancer*, 5(3), 161-171.

[2] LaVan, D. A., McGuire, T., and Langer, R. (2003). Small-scale systems for in vivo drug delivery. *Nature biotechnology*, 21(10), 1184-1191.

[3] Mantripragada, S. (2002). A lipid based depot (DepoFoam® technology) for sustained release drug delivery. *Progress in lipid research*, 41(5), 392-406.

[4] Li, K. C., Pandit, S. D., Guccione, S., and Bednarski, M. D. (2004) Molecular imaging applications in nanomedicine. *Biomedical microdevices*, 6(2), 113-116.

[5] Parveen, S., Misra, R., and Sahoo, S. K. (2012). Nanoparticles: a boon to drug delivery, therapeutics, diagnostics and imaging. *Nanomedicine: Nanotechnology, Biology and Medicine*, 8(2), 147-166.

[6] Bertrand, N., Wu, J., Xu, X., Kamaly, N., and Farokhzad, O. C. (2014). Cancer nanotechnology: the impact of passive and active targeting in the era of modern cancer biology. *Advanced drug delivery reviews*, 66, 2-25.

[7] Wicki, A., Witzigmann, D., Balasubramanian, V., and Huwyler, J. (2015). Nanomedicine in cancer therapy: challenges, opportunities, and clinical applications. *Journal of controlled release*, 200, 138-157.

[8] Duncan, R. (2006). Polymer conjugates as anticancer nanomedicines. *Nature Reviews Cancer*, 6(9), 688-701.

[9] Moghimi, S. M., Hunter, A. C., and Andresen, T. L. (2012). Factors controlling nanoparticle pharmacokinetics: an integrated analysis and perspective. *Annual review of pharmacology and toxicology*, 52, 481-503.

[10] Chidambaram, M., Manavalan, R., and Kathiresan, K. (2011). Nanotherapeutics to overcome conventional cancer chemotherapy limitations. *Journal of pharmacy & pharmaceutical sciences*, 14(1), 67-77.

[11] Gelderblom, H., Verweij, J., Nooter, K., and Sparreboom, A. (2001). Cremophor EL: the drawbacks and advantages of vehicle selection for drug formulation. *European journal of cancer*, 37(13), 1590-1598.

[12] Hare, J. I., Lammers, T., Ashford, M. B., Puri, S., Storm, G., and Barry, S. T. (2017). Challenges and strategies in anti-cancer nanomedicine development: An industry perspective. *Advanced drug delivery reviews*, 108, 25-38.

[13] Decuzzi, P., Pasqualini, R., Arap, W., and Ferrari, M. (2009). Intravascular delivery of particulate systems: does geometry really matter?. *Pharmaceutical research*, 26(1), 235.

[14] Estanqueiro, M., Amaral, M. H., Conceio, J., and Lobo, J. M. S. (2015). Nanotechnological carriers for cancer chemotherapy: the state of the art. *Colloids and surfaces B: Biointerfaces*, 126, 631-648.

[15] Illum, L., and Davis, S. S. (1982). The targeting of drugs parenterally by use of microspheres. *PDA Journal of Pharmaceutical Science and Technology*, 36(6), 242-248.

[16] Chen, L. T. (1978). Microcirculation of the spleen: and open or closed circulation?. *Science*, 201(4351), 157-159.

[17] Shukla, S., Ablack, A. L., Wen, A. M., Lee, K. L., Lewis, J. D., and Steinmetz, N. F. (2012). Increased tumor homing and tissue penetration of the filamentous plant viral nanoparticle Potato virus X. *Molecular pharmaceutics*, 10(1), 33-42.

[18] Chauhan, V. P., Popovic, Z., Chen, O., Cui, J., Fukumura, D., Bawendi, M. G., and Jain, R. K. (2011). Fluorescent nanorods and nanospheres for realtime in vivo probing of nanoparticle shapedependent tumor penetration. *Angewandte Chemie International Edition*, 50(48), 11417-11420.

[19] Decuzzi, P., and Ferrari, M. (2007). The role of specific and non-specific interactions in receptor-mediated endocytosis of nanoparticles. *Biomaterials*, 28(18), 2915-2922.

[20] Kojić, M., Filipović, N., Stojanović, B., and Kojić, N. (2008). Computer Modeling in Bioengineering: Theoretical background, examples and software. John Wiley & Sons.

[21] Perkins, S. J., Nealis, A. S., Sutton, B. J., and Feinstein, A. (1991). Solution structure of human and mouse immunoglobulin M by synchrotron X-ray scattering and molecular graphics modelling: a possible mechanism for complement activation. *Journal of molecular biology*, 221(4), 1345-1366.

[22] Tasciotti, E., Liu, X., Bhavane, R., Plant, K., Leonard, A.D., Price, B.K., Cheng, M.M.C., Decuzzi, P., Tour, J.M., Robertson, F. and Ferrari, M. (2008). Mesoporous silicon particles as a multistage delivery system for imaging and therapeutic applications. *Nature nanotechnology*, 3(3), 151-157.

[23] Souza, G.R., Christianson, D.R., Staquicini, F.I., Ozawa, M.G., Snyder, E.Y., Sidman, R.L., Miller, J.H., Arap, W. and Pasqualini, R. (2006). Networks of gold nanoparticles and bacteriophage as biological sensors and cell-targeting agents. *Proceedings of the National Academy of Sciences*, 103(5), 1215-1220.

[24] Illing, A., Unruh, T., and Koch, M. H. (2004). Investigation on particle self-assembly in solid lipid-based colloidal drug carrier systems. *Pharmaceutical research*, 21(4), 592-597.

[25] van Dillen, T., van Blaaderen, A., and Polman, A. (2004). Shaping colloidal assemblies. *Materials Today*, 7(7), 40-46.

[26] Kohli, P., and Martin, C. R. (2005). Smart nanotubes for biotechnology. *Current pharmaceutical biotechnology*, 6(1), 35-47.

[27] Champion, J. A., Katare, Y. K., and Mitragotri, S. (2007). Making polymeric micro-and nanoparticles of complex shapes. *Proceedings of the National Academy of Sciences*, 104(29), 11901-11904.

[28] Stylianopoulos, T., Poh, M. Z., Insin, N., Bawendi, M. G., Fukumura, D., Munn, L. L., and Jain, R. K. (2010). Diffusion of particles in the extracellular matrix: the effect of repulsive electrostatic interactions. *Biophysical journal*, 99(5), 1342-1349.

[29] Bregoli, L., Movia, D., Gavigan-Imedio, J. D., Lysaght, J., Reynolds, J., and Prina-Mello, A. (2016). Nanomedicine applied to translational oncology: a future perspective on cancer treatment. *Nanomedicine: Nanotechnology, Biology and Medicine*, 12(1), 81-103.

[30] Fasol, U., Frost, A., Bchert, M., Arends, J., Fiedler, U., Scharr, D., Scheuenpflug, J. and Mross, K. (2011). Vascular and pharmacokinetic effects of EndoTAG-1 in patients with advanced cancer and liver metastasis. *Annals of oncology*, 23(4), 1030-1036.

[31] Beningo, K. A., and Wang, Y. L. (2002). Fc-receptor-mediated phagocytosis is regulated by mechanical properties of the target. *Journal of cell science*, 115(4), 849-856.

[32] Anselmo, A. C., Zhang, M., Kumar, S., Vogus, D. R., Menegatti, S., Helgeson, M. E., and Mitragotri, S. (2015). Elasticity of nanoparticles influences their blood circulation, phagocytosis, endocytosis, and targeting. *ACS nano*, 9(3), 3169-3177.

[33] Sun, T., Zhang, Y. S., Pang, B., Hyun, D. C., Yang, M., and Xia, Y. (2014). Engineered nanoparticles for drug delivery in cancer therapy. *Angewandte Chemie International Edition*, 53(46), 12320-12364.

[34] Hashizume, H., Baluk, P., Morikawa, S., McLean, J.W., Thurston, G., Roberge, S., Jain, R.K. and McDonald, D.M. (2000). Openings between defective endothelial cells explain tumor vessel leakiness. *The American journal of pathology*, 156(4), 1363-1380.

[35] Baban, D. F., and Seymour, L. W. (1998). Control of tumour vascular permeability. *Advanced drug delivery reviews*, 34(1), 109-119.

[36] Chauhan, V. P., and Jain, R. K. (2013). Strategies for advancing cancer nanomedicine. *Nature materials*, 12(11), 958-962.

[37] Hobbs, S. K., Monsky, W. L., Yuan, F., Roberts, W. G., Griffith, L., Torchilin, V. P., and Jain, R. K. (1998). Regulation of transport pathways in tumor vessels: role of tumor type and microenvironment. *Proceedings of the National Academy of Sciences*, 95(8), 4607-4612.

[38] Jain, R. K., and Stylianopoulos, T. (2010). Delivering nanomedicine to solid tumors. *Nature reviews Clinical oncology*, 7(11), 653-664.

[39] Leu, A. J., Berk, D. A., Lymboussaki, A., Alitalo, K., and Jain, R. K. (2000). Absence of functional lymphatics within a murine sarcoma: a molecular and functional evaluation. *Cancer research*, 60(16), 4324-4327.

[40] Matsumura, Y., and Maeda, H. (1986). A new concept for macromolecular therapeutics in cancer chemotherapy: mechanism of tumoritropic accumulation of proteins and the antitumor agent smancs. *Cancer research*, 46(12 Part 1), 6387-6392.

[41] Peer, D., Karp, J. M., Hong, S., Farokhzad, O. C., Margalit, R., and Langer, R. (2007). Nanocarriers as an emerging platform for cancer therapy. *Nature nanotechnology*, 2(12), 751-760.

[42] Etheridge, M. L., Campbell, S. A., Erdman, A. G., Haynes, C. L., Wolf, S. M., and McCullough, J. (2013). The big picture on nanomedicine: the state of investigational and approved nanomedicine products. *Nanomedicine: nanotechnology, biology and medicine*, 9(1), 1-14.

[43] Nicholson, R. I., Gee, J. M. W., and Harper, M. 2. (2001). EGFR and cancer prognosis. *European journal of cancer*, 37, 9-15.

[44] Danhier, F., Le Breton, A., and Preat, V. (2012). RGD-based strategies to target alpha (v) beta (3) integrin in cancer therapy and diagnosis. *Molecular pharmaceutics*, 9(11), 2961-2973.

[45] Farokhzad, O. C., Jon, S., Khademhosseini, A., Tran, T. N. T., LaVan, D. A., and Langer, R. (2004). Nanoparticle-aptamer bioconjugates. *Cancer research*, 64(21), 7668-7672.

[46] Farokhzad, O.C., Cheng, J., Teply, B.A., Sherifi, I., Jon, S., Kantoff, P.W., Richie, J.P. and Langer, R. (2006). Targeted nanoparticle-aptamer bioconjugates for cancer chemotherapy in vivo. *Proceedings of the National Academy of Sciences*, 103(16), 6315-6320.

[47] Xiao, Z., and Farokhzad, O. C. (2012). Aptamer-functionalized nanoparticles for medical applications: challenges and opportunities. *ACS nano*, 6(5), 3670-3676.

[48] Gu, F., Zhang, L., Teply, B.A., Mann, N., Wang, A., Radovic-Moreno, A.F., Langer, R. and Farokhzad, O.C. (2008). Precise engineering of targeted nanoparticles by using self-assembled biointegrated block copolymers. *Proceedings of the National Academy of Sciences*, 105(7), 2586-2591.

[49] Zwicke, G. L., Ali Mansoori, G., and Jeffery, C. J. (2012). Utilizing the folate receptor for active targeting of cancer nanotherapeutics. *Nano reviews*, 3(1), 18496.

[50] Leckband, D. (2011). Novel functions and binding mechanisms of carbohydrate-binding proteins determined by force measurements. *Current Protein and Peptide Science*, 12(8), 743-759.

[51] Mura, S., Nicolas, J., and Couvreur, P. (2013). Stimuli-responsive nanocarriers for drug delivery. *Nature materials*, 12(11), 991.

[52] Leung, S. J., and Romanowski, M. (2012). Light-activated content release from liposomes. *Theranostics*, 2(10), 1020.

[53] Swenson, C. E., Haemmerich, D., Maul, D. H., Knox, B., Ehrhart, N., and Reed, R. A. (2015). Increased duration of heating boosts local drug deposition during radiofrequency ablation in combination with thermally sensitive liposomes (ThermoDox) in a porcine model. *PloS one*, 10(10), e0139752.

[54] Chithrani, B. D., Ghazani, A. A., and Chan, W. C. (2006). Determining the size and shape dependence of gold nanoparticle uptake into mammalian cells. *Nano letter*, 6(4), 662-668.

[55] Lee, K. D., Oh, Y. K., Portnoy, D. A., and Swanson, J. A. (1996). Delivery of macromolecules into cytosol using liposomes containing hemolysin from Listeria monocytogenes. *Journal of Biological Chemistry*, 271(13), 7249-7252.

[56] Sapra, P., and Allen, T. M. (2002). Internalizing antibodies are necessary for improved therapeutic efficacy of antibody-targeted liposomal drugs. *Cancer Research*, 62(24), 7190-7194.

[57] Decuzzi, P., Lee, S., Bhushan, B., and Ferrari, M. (2005). A theoretical model for the margination of particles within blood vessels. *Annals of biomedical engineering*, 33(2), 179-190.

[58] Pundir, S., Badola, A., and Sharma, D. (2013). Sustained release matrix technology and recent advance in matrix drug delivery system: a review. *International Journal of drug research and technology*, 3(1), 8.

[59] Robitzki, A. A., and Kurz, R. (2010). Biosensing and drug delivery at the microscale. *Drug Delivery*, 87-112.

[60] Zilberman, M., and Grinberg, O. (2008). HRP-loaded bioresorbable microspheres: effect of copolymer composition and molecular weight on microstructure and release profile. *Journal of biomaterials applications*, 22(5), 391-407.

[61] Zuleger, S., and Lippold, B. C. (2001). Polymer particle erosion controlling drug release. I. Factors influencing drug release and characterization of the release mechanism. *International journal of pharmaceutics*, 217(1), 139-152.

[62] Tamada, J. A., and Langer, R. (1993). Erosion kinetics of hydrolytically degradable polymers. *Proceedings of the National Academy of Sciences*, 90(2), 552-556.

[63] Felber, A. E., Dufresne, M. H., and Leroux, J. C. (2012). pH-sensitive vesicles, polymeric micelles, and nanospheres prepared with polycarboxylates. *Advanced drug delivery reviews*, 64(11), 979-992.

[64] Kim, J. O., Kabanov, A. V., and Bronich, T. K. (2009). Polymer micelles with cross-linked polyanion core for delivery of a cationic drug doxorubicin. *Journal of Controlled Release*, 138(3), 197-204.

[65] Borchert, U., Lipprandt, U., Bilang, M., Kimpfler, A., Rank, A., Peschka-Süss, R., Schubert, R., Lindner, P. and Förster, S. (2006). pH-induced release from P2VP PEO block copolymer vesicles. *Langmuir*, 22(13), 5843-5847.

[66] Oishi, M., Hayashi, H., Iijima, M., and Nagasaki, Y. (2007). Endosomal release and intracellular delivery of anticancer drugs using pH-sensitive PEGylated nanogels. *Journal of Materials Chemistry*, 17(35), 3720-3725.

[67] Fleige, E., Quadir, M. A., and Haag, R. (2012). Stimuli-responsive polymeric nanocarriers for the controlled transport of active compounds: concepts and applications. *Advanced drug delivery reviews*, 64(9), 866-884.

[68] Zhu, L., Kate, P., and Torchilin, V. P. (2012). Matrix metalloprotease 2-responsive multifunctional liposomal nanocarrier for enhanced tumor targeting. *ACS nano*, 6(4), 3491-3498.

[69] Dorresteijn, R., Billecke, N., Schwendy, M., Pütz, S., Bonn, M., Parekh, S.H., Klapper, M. and Müllen, K. (2014). PolylactideblockPolypeptideblockPolylactide Copolymer Nanoparticles with Tunable Cleavage and Controlled Drug Release. *Advanced Functional Materials*, 24(26), 4026-4033.

[70] Harris, T.J., von Maltzahn, G., Lord, M.E., Park, J.H., Agrawal, A., Min, D.H., Sailor, M.J. and Bhatia, S.N. (2008). ProteaseTriggered Unveiling of Bioactive Nanoparticles. *small*, 4(9), 1307-1312.

[71] Kohane, D. S., and Langer, R. (2010). Biocompatibility and drug delivery systems. *Chemical Science*, 1(4), 441-446.

[72] Nazir, S., Hussain, T., Ayub, A., Rashid, U., and MacRobert, A. J. (2014). Nanomaterials in combating cancer: therapeutic applications and developments. *Nanomedicine: Nanotechnology, Biology and Medicine*, 10(1), 19-34.

[73] Yih, T. C., and AlFandi, M. (2006). Engineered nanoparticles as precise drug delivery systems. *Journal of cellular biochemistry*, 97(6), 1184-1190.

[74] Ho, D., Brown, N.S., Yen, A., Holmes, R., Keating, M., Abuchowski, A., Newman, R.A. and Krakoff, I.H. (1986). Clinical pharmacology of polyethylene glycol-L-asparaginase. *Drug metabolism and disposition*, 14(3), 349-352.

[75] Feng, Q., and Tong, R. (2016). Anticancer Nanoparticulate PolymerDrug Conjugate. *Bioengineering & Translational Medicine*, 1(3), 277-296.

[76] Kehrer, D. F., Yamamoto, W., Verweij, J., de Jonge, M. J., de Bruijn, P., and Sparreboom, A. (2000). Factors involved in prolongation of the terminal disposition phase of SN-38: clinical and experimental studies. *Clinical cancer research*, 6(9), 3451-3458.

[77] Awada, A., Garcia, A.A., Chan, S., Jerusalem, G.H., Coleman, R.E., Huizing, M.T., Mehdi, A., O'Reilly, S.M., Hamm, J.T., Barrett-Lee, P.J. and Cocquyt, V. (2013). Two schedules of etirinotecan pegol (NKTR-102) in patients with previously treated metastatic breast cancer: a randomised phase 2 study. *The lancet oncology*, 14(12), 1216-1225.

[78] Gradishar, W.J., Tjulandin, S., Davidson, N., Shaw, H., Desai, N., Bhar, P., Hawkins, M. and O'shaughnessy, J. (2005). Phase III trial of nanoparticle albumin-bound paclitaxel compared with polyethylated castor oilbased paclitaxel in women with breast cancer. *Journal of clinical oncology*, 23(31), 7794-7803.

[79] Zuckerman, J. E. and Davis, M. E. (2015). Clinical experiences with systemically administered siRNA-based therapeutics in cancer. *Nature Reviews Drug Discovery*, 14(12), 843.

[80] Davis, M.E., Zuckerman, J.E., Choi, C.H.J., Seligson, D., Tolcher, A., Alabi, C.A., Yen, Y., Heidel, J.D. and Ribas, A. (2010). Evidence of RNAi in humans from systemically administered siRNA via targeted nanoparticles. *Nature*, 464(7291), 1067.

[81] Torchilin, V. P. (2005). Recent advances with liposomes as pharmaceutical carriers. *Nature reviews Drug discovery*, 4(2), 145-160.

[82] Dawidczyk, C.M., Kim, C., Park, J.H., Russell, L.M., Lee, K.H., Pomper, M.G. and Searson, P.C. (2014). State-of-the-art in design rules for drug delivery platforms: lessons learned from FDA-approved nanomedicines. *Journal of Controlled Release*, 187, 133-144.

[83] Anselmo, A. C. and Mitragotri, S. (2014). An overview of clinical and commercial impact of drug delivery systems. *Journal of Controlled Release*, 190, 15-28.

[84] Gabizon, A., Shmeeda, H., and Barenholz, Y. (2003). Pharmacokinetics of pegylated liposomal Doxorubicin: review of animal and human studies. *Clinical Pharmacokinetics*, 42(5), 419-436.

[85] Libutti, S.K., Paciotti, G.F., Byrnes, A.A., Alexander, H.R., Gannon, W.E., Walker, M., Seidel, G.D., Yuldasheva, N. and Tamarkin, L. (2010). Phase I and pharmacokinetic studies of CYT-6091, a novel PEGylated colloidal gold-rhTNF nanomedicine. *Clinical cancer research*, clincanres-0978.

[86] Stern, J. M., Kibanov Solomonov, V. V., Sazykina, E., Schwartz, J. A., Gad, S. C., and Goodrich, G. P. (2016). Initial evaluation of the safety of nanoshell-directed photothermal therapy in the treatment of prostate disease. *International journal of toxicology*, 35(1), 38-46.

[87] Fortuin, A. S., Brggemann, R., Linden, J., Panfilov, I., Isral, B., Scheenen, T. W., and Barentsz, J. O. (2017). Ultrasmall superparamagnetic iron oxides for metastatic lymph node detection: back on the block. *Wiley Interdisciplinary Reviews: Nanomedicine and Nanobiotechnology*.

[88] Gillies, E. R., and Frechet, J. M. (2005). Dendrimers and dendritic polymers in drug delivery. *Drug discovery today*, 10(1), 35-43.

[89] Kukowska-Latallo, J.F., Candido, K.A., Cao, Z., Nigavekar, S.S., Majoros, I.J., Thomas, T.P., Balogh, L.P., Khan, M.K. and Baker, J.R. (2005). Nanoparticle targeting of anticancer drug improves therapeutic response in animal model of human epithelial cancer. *Cancer research*, 65(12), 5317-5324.

[90] Farokhzad, O. C., and Langer, R. (2009). Impact of nanotechnology on drug delivery. *ACS nano*, 3(1), 16-20.

[91] Prabhakar, U., Maeda, H., Jain, R.K., Sevick-Muraca, E.M., Zamboni, W., Farokhzad, O.C., Barry, S.T., Gabizon, A., Grodzinski, P. and Blakey, D.C. (2013). Challenges and key considerations of the enhanced permeability and retention effect for nanomedicine drug delivery in oncology. *Cancer Research*, 73(8), 2412-2417.

[92] Suzuki, M., Hori, K., Abe, I., Saito, S., and Sato, H. (1981). A New Approach to Cancer Chemotherapy: Selective Enhancement of Tumor Blood Flow With Angiotensin II. *Journal of the National Cancer Institute*, 67(3), 663-669.

[93] Choi, H. S., Liu, W., Liu, F., Nasr, K., Misra, P., Bawendi, M. G., and Frangioni, J. V. (2010). Design considerations for tumour-targeted nanoparticles. *Nature nanotechnology*, 5(1), 42-47.

[94] Wong, C., Stylianopoulos, T., Cui, J., Martin, J., Chauhan, V.P., Jiang, W., Popovi, Z., Jain, R.K., Bawendi, M.G. and Fukumura, D. (2011). Multistage nanoparticle delivery system for deep penetration into tumor tissue. *Proceedings of the National Academy of Sciences*, 108(6), 2426-2431.

[95] Wang, Y. C., Wang, F., Sun, T. M., and Wang, J. (2011). Redox-responsive nanoparticles from the single disulfide bond-bridged block copolymer as drug carriers for overcoming multidrug resistance in cancer cells. *Bioconjugate chemistry*, 22(10), 1939-1945.

[96] Cerqueira, B. B. S., Lasham, A., Shelling, A. N., and Al-Kassas, R. (2015). Nanoparticle therapeutics: Technologies and methods for overcoming cancer. *European Journal of Pharmaceutics and Biopharmaceutics*, 97, 140-151.

[97] Monsuez, J. J., Charniot, J. C., Vignat, N., and Artigou, J. Y. (2010). Cardiac side-effects of cancer chemotherapy. *International journal of cardiology*, 144(1), 3-15.

[98] Prendergast, G. C., and Jaffee, E. M. (Eds.). (2013). *Cancer immunotherapy: immune suppression and tumor growth*. Academic Press.

[99] Pabla, N., and Dong, Z. (2012). Curtailing side effects in chemotherapy: a tale of PKC in cisplatin treatment. *Oncotarget*, 3(1), 107.

[100] Monje, M., and Dietrich, J. (2012). Cognitive side effects of cancer therapy demonstrate a functional role for adult neurogenesis. *Behavioural brain research*, 227(2), 376-379.

[101] Pushparaj, P. N., Aarthi, J. J., Manikandan, J., and Kumar, S. D. (2008). siRNA, miRNA, and shRNA: in vivo applications. *Journal of dental research*, 87(11), 992-1003.

[102] Crombez, L., Morris, M.C., Dufort, S., Aldrian-Herrada, G., Nguyen, Q., Mc Master, G., Coll, J.L., Heitz, F. and Divita, G. (2009). Targeting cyclin B1 through peptide-based delivery of siRNA prevents tumour growth. *Nucleic acids research*, 37(14), 4559-4569.

[103] Iorio, M. V., and Croce, C. M. (2012). MicroRNA dysregulation in cancer: diagnostics, monitoring and therapeutics. A comprehensive review. *EMBO molecular medicine*, 4(3), 143-159.

[104] Resnier, P., Montier, T., Mathieu, V., Benoit, J. P., and Passirani, C. (2013). A review of the current status of siRNA nanomedicines in the treatment of cancer. *Biomaterials*, 34(27), 6429-6443.

[105] Vellard, M. (2003). The enzyme as drug: application of enzymes as pharmaceuticals. *Current Opinion in Biotechnology*, 14(4), 444-450.

[106] Ensor, C. M., Holtsberg, F. W., Bomalaski, J. S., and Clark, M. A. (2002). Pegylated arginine deiminase (ADI-SS PEG20, 000 mw) inhibits human melanomas and hepatocellular carcinomas in vitro and in vivo. *Cancer research*, 62(19), 5443-5450.

[107] Andtbacka, R.H., Kaufman, H.L., Collichio, F., Amatruda, T., Senzer, N., Chesney, J., Delman, K.A., Spitler, L.E., Puzanov, I., Agarwala, S.S. and Milhem, M. (2015). Talimogene laherparepvec improves durable response rate in patients with advanced melanoma. *Journal of clinical oncology*, 33(25), 2780-2788.

[108] Parato, K.A., Breitbach, C.J., Le Boeuf, F., Wang, J., Storbeck, C., Ilkow, C., Diallo, J.S., Falls, T., Burns, J., Garcia, V. and Kanji, F. (2012). The oncolytic poxvirus JX-594 selectively replicates in and destroys cancer cells driven by genetic pathways commonly activated in cancers. *Molecular Therapy*, 20(4), 749-758.

[109] Russell, S. J., Peng, K. W., and Bell, J. C. (2012). Oncolytic virotherapy. *Nature biotechnology*, 30(7), 658-670.

[110] Owen, S. C., Doak, A. K., Wassam, P., Shoichet, M. S., and Shoichet, B. K. (2012). Colloidal aggregation affects the efficacy of anticancer drugs in cell culture. *ACS chemical biology*, 7(8), 1429-1435.

[111] Garti, N., and Bisperink, C. (1998). Double emulsions: progress and applications. *Current Opinion in Colloid & Interface Science*, 3(6), 657-667.

[112] Conner, S. D., and Schmid, S. L. (2003). Regulated portals of entry into the cell. *Nature*, 422(6927), 37.

[113] Petros, R. A., and DeSimone, J. M. (2010). Strategies in the design of nanoparticles for therapeutic applications. *Nature reviews. Drug discovery*, 9(8), 615.

[114] Mayor, S., Parton, R. G., and Donaldson, J. G. (2014). Clathrin-independent pathways of endocytosis. *Cold Spring Harbor perspectives in biology*, 6(6), a016758.

[115] Fuller, J. E., Zugates, G. T., Ferreira, L. S., Ow, H. S., Nguyen, N. N., Wiesner, U. B., and Langer, R. S. (2008). Intracellular delivery of coreshell fluorescent silica nanoparticles. *Biomaterials*, 29(10), 1526-1532.

[116] Li, W., Nicol, F., and Szoka, F. C. (2004). GALA: a designed synthetic pH-responsive amphipathic peptide with applications in drug and gene delivery. *Advanced drug delivery reviews*, 56(7), 967-985.

[117] Mammen, M., Choi, S. K., and Whitesides, G. M. (1998). Polyvalent interactions in biological systems: implications for design and use of multivalent ligands and inhibitors. *Angewandte Chemie International Edition*, 37(20), 2754-2794.

[118] Mukherjee, S., Ghosh, R. N., and Maxfield, F. R. (1997). Endocytosis. *Physiological reviews*, 77(3), 759-803.

[119] Moghimi, S. M., Andersen, A. J., Ahmadvand, D., Wibroe, P. P., Andresen, T. L., and Hunter, A. C. (2011). Material properties in complement activation. *Advanced drug delivery reviews*, 63(12), 1000-1007.

[120] Carroll, Maria V., and Robert B. Sim. "Complement in health and disease." *Advanced drug delivery reviews* 63.12 (2011): 965-975.

[121] Haynes BF, Soderberg KA, Fauci AS. (2014). Introduction to the Immune System. In: Kasper D, Fauci A, Hauser S, Longo D, Jameson J, Loscalzo J. eds. *Harrison's Principles of Internal Medicine*, 19e New York, NY: McGraw-Hill.

[122] Lee LA. (2012). Chapter 37. Humoral Immunity and Complement. In: Goldsmith LA, Katz SI, Gilchrest BA, Paller AS, Leffell DJ, Wolff K. eds. *Fitzpatrick's Dermatology in General Medicine*, 8e New York, NY: McGraw-Hill.

[123] Levinson, W. (2016). Chapter 63. Complement. In: Levinson W. eds. *Review of Medical Microbiology and Immunology*, 14e New York, NY: McGraw-Hill.

[124] Ryan KJ, Ray C. (2014). Chapter 2. Immune Response to Infection. In: Ryan KJ, Ray C. eds. *Sherris Medical Microbiology*, 6e New York, NY: McGraw-Hill.

[125] Greidinger EL. (2012). Chapter 15. The Immune System. In: Janson LW, Tischler ME. eds. *The Big Picture: Medical Biochemistry*, New York, NY: McGraw-Hill.

[126] Akhtar, N., Rahman, R., Sultana, S., and Mawla, N. N. (2014). Complement Activation: The role in Health and Disease and Strategies of Therapeutic Complement Inhibition. *American Journal of Medical Sciences and Medicine*, 2(6), 115-121.

[127] Mescher AL. (2016) Connective Tissue. In: Mescher AL. eds. *Junqueira's Basic Histology*, 14e New York, NY: McGraw-Hill.

[128] Kibble JD, Halsey CR. (2014) Gastrointestinal Physiology. In: Kibble JD, Halsey CR. eds. *Medical Physiology: The Big Picture* New York, NY: McGraw-Hill.

[129] Barrett KE. (2014) Functional Anatomy of the Liver and Biliary System. In: Barrett KE. eds. *Gastrointestinal Physiology*, 2e New York, NY: McGraw-Hill.

[130] Morton DA, Foreman K, Albertine KH. (2011) Foregut. In: Morton DA, Foreman K, Albertine KH. eds. *The Big Picture: Gross Anatomy* New York, NY: McGraw-Hill.

[131] Turcotte S, Jarnagin WR. Liver & Portal Venous System. (2014) In: Doherty GM. eds. *CURRENT Diagnosis & Treatment: Surgery*, 14e New York, NY: McGraw-Hill.

[132] Lobules of liver (2009). In *Wikipedia*. Retrieved May 31st, 2017, from https://en. wikipedia.org/wiki/Lobules_of_liver

[133] Adams, D. H., and Eksteen, B. (2006). Aberrant homing of mucosal T cells and extra-intestinal manifestations of inflammatory bowel disease. Nature Reviews Immunology, 6(3), 244-251.

[134] Cheng EY, Zarrinpar A, Geller DA, Goss JA, Busuttil RW. (2015) Liver. In: Brunicardi F, Andersen DK, Billiar TR, Dunn DL, Hunter JG, Matthews JB, Pollock RE. eds. *Schwartz's Principles of Surgery*, 10e New York, NY: McGraw-Hill.

[135] Paulsen DF. (2010) Chapter 14. Lymphoid System. In: Paulsen DF. eds. *Histology & Cell Biology: Examination & Board Review*, 5e New York, NY: McGraw-Hill.

[136] Freud AG, Caligiuri MA. (2016) The Organization and Structure of Lymphoid Tissues. In: Kaushansky K, Lichtman MA, Prchal JT, Levi MM, Press OW, Burns LJ, Caligiuri M. eds. *Williams Hematology*, 9e New York, NY: McGraw-Hill.

[137] Mescher AL. (2016) The Immune System & Lymphoid Organs. In: Mescher AL. eds. *Junqueira's Basic Histology*, 14e New York, NY: McGraw-Hill.

[138] Douglas SD, Douglas AG. (2016) Production, Distribution, and Activation of Monocytes and Macrophages. In: Kaushansky K, Lichtman MA, Prchal JT, Levi MM, Press OW, Burns LJ, Caligiuri M. eds. *Williams Hematology*, 9e New York, NY: McGraw-Hill.

[139] Mebius, R. E., and Kraal, G. (2005). Structure and function of the spleen. *Nature Reviews Immunology*, 5(8), 606-616.

[140] Nie, S. M. (2010). Understanding and overcoming major barriers in cancer nanomedicine. *Nanomedicine*, 5, 523 528.

[141] Anderson, J. M., Rodriguez, A., and Chang, D. T. (2008, April). Foreign body reaction to biomaterials. *Seminars in immunology*, 20(2), 86-100.

[142] Mitchell, R.N. (2004) Innate and adaptive immunity: the immune response to foreign materials. In: Ratner, B.D., Hoffman, A.S., Schoen, F.J., Lemons, J.E. (Eds.), *Biomaterials Science: An Introduction to Materials in Medicine*. Elsevier Academic Press, Amsterdam.

[143] Carstensen, H., Muller, R.H., Muller, B.W. (1992) Particle-size, surface hydrophobicity and interaction with serum of parenteral fat emulsions and model-drug carriers as parameters related to RES uptake. *Clin. Nutr.* 11, 289297.

[144] Moghimi, S. M., and Szebeni, J. (2003). Stealth liposomes and nanoparticles: critical issues on protein-binding properties, activation of proteolytic blood cascades and intracellular fate. *Prog Lipid Res*, 42, 463-78.

[145] Toda, M., Kitazawa, T., Hirata, I., Hirano, Y., and Iwata, H. (2008). Complement activation on surfaces carrying amino groups. *Biomaterials*, 29(4), 407-417.

[146] Lundqvist, M., Stigler, J., Elia, G., Lynch, I., Cedervall, T., and Dawson, K. A. (2008). Nanoparticle size and surface properties determine the protein corona with possible implications for biological impacts. *Proceedings of the National Academy of Sciences*, 105(38), 14265-14270.

[147] Salvador-Morales, C., Zhang, L., Langer, R., and Farokhzad, O. C. (2009). Immunocompatibility properties of lipidpolymer hybrid nanoparticles with heterogeneous surface functional groups. *Biomaterials*, 30(12), 2231-2240.

[148] Albanese, A., Tang, P. S., and Chan, W. C. (2012). The effect of nanoparticle size, shape, and surface chemistry on biological systems. *Annual review of biomedical engineering*, 14, 1-16.

[149] Neal, J. C., Stolnik, S., Schacht, E., Kenawy, E. R., Garnett, M. C., Davis, S. S., and Illum, L. (1998). In vitro displacement by rat serum of adsorbed radiolabeled poloxamer and poloxamine copolymers from model and biodegradable nanospheres. *Journal of pharmaceutical sciences*, 87(10), 1242-1248.

[150] Brittain, W. J., and Minko, S. (2007). A structural definition of polymer brushes. *Journal of Polymer Science Part A: Polymer Chemistry*, 45(16), 3505-3512.

[151] Ayres, N. (2010). Polymer brushes: Applications in biomaterials and nanotechnology. *Polymer Chemistry*, 1(6), 769-777.

[152] Wattendorf, U. T. A., and Merkle, H. P. (2008). PEGylation as a tool for the biomedical engineering of surface modified microparticles. *Journal of pharmaceutical sciences*, 97(11), 4655-4669.

[153] Szebeni, J., Baranyi, L., Savay, S., Lutz, H. U., Jelezarova, E., Bunger, R., and Alving, C. R. (2000). The role of complement activation in hypersensitivity to pegylated liposomal doxorubicin (Doxil). *Journal of Liposome Research*, 10(4), 467-481.

[154] Szebeni, J., Baranyi, L., Savay, S., Milosevits, J., Bunger, R., Laverman, P., Metselaar, J.M., Storm, G., Chanan-Khan, A., Liebes, L. and Muggia, F.M. (2002). Role of complement activation in hypersensitivity reactions to doxil and hynic PEG liposomes: experimental and clinical studies. *Journal of liposome research*, 12(1-2), 165-172.)

[155] Elwing, H., Askendal, A., and Lundstrm, I. (1987). Competition between adsorbed fibrinogen and highmolecularweight kininogen on solid surfaces incubated in human plasma (the vroman effect): Influence of solid surface wettability. Journal of Biomedical Materials Research Part A, 21(8), 1023-1028.

[156] Pedersen, M.B., Zhou, X., Larsen, E.K.U., Sørensen, U.S., Kjems, J., Nygaard, J.V., Nyengaard, J.R., Meyer, R.L., Boesen, T. and Vorup-Jensen, T. (2010). Curvature of synthetic and natural surfaces is an important target feature in classical pathway complement activation. *The journal of immunology*, 184(4), 1931-1945.

[157] Gordon, D. L., Johnson, G. M., and Hostetter, M. K. (1986). Ligand-receptor interactions in the phagocytosis of virulent Streptococcus pneumoniae by polymorphonuclear leukocytes. *Journal of Infectious Diseases*, 154(4), 619-626.

[158] Cornacoff, J. B., Hebert, L. A., Smead, W. L., VanAman, M. E., Birmingham, D. J., and Waxman, F. J. (1983). Primate erythrocyte-immune complex-clearing mechanism. *Journal of Clinical Investigation*, 71(2), 236.

[159] Perry, J.L., Reuter, K.G., Kai, M.P., Herlihy, K.P., Jones, S.W., Luft, J.C., Napier, M., Bear, J.E. and DeSimone, J.M. (2012). PEGylated PRINT nanoparticles: the impact of PEG density on protein binding, macrophage association, biodistribution, and pharmacokinetics. *Nano letters*, 12(10), 5304-5310.

[160] Owens, D. E., and Peppas, N. A. (2006). Opsonization, biodistribution, and pharmacokinetics of polymeric nanoparticles. *International journal of pharmaceutics*, 307(1), 93-102.

[161] Sun, M., Deng, J., Tang, Z., Wu, J., Li, D., Chen, H., and Gao, C. (2014). A correlation study of protein adsorption and cell behaviors on substrates with different densities of PEG chains. *Colloids and Surfaces B: Biointerfaces*, 122, 134-142.

[162] Hamad, I., Hunter, A. C., Szebeni, J., and Moghimi, S. M. (2008). Poly(ethylene glycol) generates complement activation products in human serum through increased alternative pathway turnover and a MASP-2-dependent process. *Molecular immunology*, 46(2), 225-232.

[163] Li, S. D., and Huang, L. (2009). Nanoparticles evading the reticuloendothelial system: role of the supported bilayer. *Biochimica et Biophysica Acta (BBA)-Biomembranes*, 1788(10), 2259-2266.

[164] Gbadamosi, J. K., Hunter, A. C., and Moghimi, S. M. (2002). PEGylation of microspheres generates a heterogeneous population of particles with differential surface characteristics and biological performance. *FEBS letters*, 532(3), 338-344.

[165] Boylan, N. J., Suk, J. S., Lai, S. K., Jelinek, R., Boyle, M. P., Cooper, M. J., and Hanes, J. (2012). Highly compacted DNA nanoparticles with low MW PEG coatings: in vitro, ex vivo and in vivo evaluation. Journal of controlled release, 157(1), 72-79.

[166] Moore, N. W., and Kuhl, T. L. (2006). Bimodal polymer mushrooms: compressive forces and specificity toward receptor surfaces. *Langmuir*, 22(20), 8485-8491.

[167] Damodaran, V. B., Fee, C. J., and Popat, K. C. (2010). Prediction of protein interaction behaviour with PEG-grafted matrices using X-ray photoelectron spectroscopy. *Applied Surface Science*, 256(16), 4894-4901.

[168] Moghimi, S. M., Hedeman, H., Muir, I. S., Illum, L., and Davis, S. S. (1993). An investigation of the filtration capacity and the fate of large filtered sterically-stabilized microspheres in rat spleen. *Biochimica et Biophysica Acta (BBA)-General Subjects*, 1157(2), 233-240.

[169] Mitragotri, S., and Lahann, J. (2009). Physical approaches to biomaterial design. Nature materials, 8(1), 15-23.

[170] Ishida, T., Wang, X., Shimizu, T., Nawata, K., and Kiwada, H. (2007). PE-Gylated liposomes elicit an anti-PEG IgM response in a T cell-independent manner. *Journal of Controlled Release*, 122(3), 349-355.

[171] Wang, X., Ishida, T., and Kiwada, H. (2007). Anti-PEG IgM elicited by injection of liposomes is involved in the enhanced blood clearance of a subsequent dose of PEGylated liposomes. *Journal of Controlled Release*, 119(2), 236-244.)

[172] Meng, H., Yang, S., Li, Z., Xia, T., Chen, J., Ji, Z., Zhang, H., Wang, X., Lin, S., Huang, C. and Zhou, Z.H. (2011). Aspect ratio determines the quantity of mesoporous silica nanoparticle uptake by a small GTPase-dependent macropinocytosis mechanism. *ACS nano*, 5(6), 4434-4447.

[173] Huang, X., Li, L., Liu, T., Hao, N., Liu, H., Chen, D., and Tang, F. (2011). The shape effect of mesoporous silica nanoparticles on biodistribution, clearance, and biocompatibility in vivo. *ACS nano*, 5(7), 5390-5399.

[174] Tang, F., Li, L., and Chen, D. (2012). Mesoporous silica nanoparticles: synthesis, biocompatibility and drug delivery. *Advanced Materials*, 24(12), 1504-1534.

[175] Tennant, D. A., Duran, R. V., and Gottlieb, E. (2010). Targeting metabolic transformation for cancer therapy. *Nature reviews cancer*, 10(4), 267-277.

[176] Asselin, B. L., Whitin, J. C., Coppola, D. J., Rupp, I. P., Sallan, S. E., and Cohen, H. J. (1993). Comparative pharmacokinetic studies of three asparaginase preparations. *Journal of Clinical Oncology*, 11(9), 1780-1786.

[177] Maddocks, O. D., Berkers, C. R., Mason, S. M., Zheng, L., Blyth, K., Gottlieb, E., and Vousden, K. H. (2013). Serine starvation induces stress and p53-dependent metabolic remodelling in cancer cells. *Nature*, 493(7433), 542-546.

[178] Wise, D. R., and Thompson, C. B. (2010). Glutamine addiction: a new therapeutic target in cancer. *Trends in biochemical sciences*, 35(8), 427-433.

[179] Feun, L. G., Kuo, M. T., and Savaraj, N. (2015). Arginine deprivation in cancer therapy. *Current Opinion in Clinical Nutrition & Metabolic Care*, 18(1), 78-82.

[180] Dillon, B. J., Prieto, V. G., Curley, S. A., Ensor, C. M., Holtsberg, F. W., Bomalaski, J. S., and Clark, M. A. (2004). Incidence and distribution of argininosuccinate synthetase deficiency in human cancers. *Cancer*, 100(4), 826-833.

[181] Holtsberg, F. W., Ensor, C. M., Steiner, M. R., Bomalaski, J. S., and Clark, M. A. (2002). Poly (ethylene glycol)(PEG) conjugated arginine deiminase: effects of PEG formulations on its pharmacological properties. *Journal of controlled release*, 80(1), 259-271.

[182] Vander Heiden, M. G. (2011). Targeting cancer metabolism: a therapeutic window opens. *Nature reviews Drug discovery*, 10(9), 671-684.

[183] Phillips, M. M., Sheaff, M. T., and Szlosarek, P. W. (2013). Targeting arginine-dependent cancers with arginine-degrading enzymes: opportunities and challenges. *Cancer research and treatment: official journal of Korean Cancer Association*, 45(4), 251.

[184] Ott, P.A., Carvajal, R.D., Pandit-Taskar, N., Jungbluth, A.A., Hoffman, E.W., Wu, B.W., Bomalaski, J.S., Venhaus, R., Pan, L., Old, L.J. and Pavlick, A.C. (2013). Phase I/II study of pegylated arginine deiminase (ADI-PEG 20) in patients with advanced melanoma. *Investigational new drugs*, 31(2), 425-434.

[185] Glazer, E.S., Piccirillo, M., Albino, V., Di Giacomo, R., Palaia, R., Mastro, A.A., Beneduce, G., Castello, G., De Rosa, V., Petrillo, A. and Ascierto, P.A. (2010). Phase II study of pegylated arginine deiminase for nonresectable and metastatic hepatocellular carcinoma. *Journal of Clinical Oncology*, 28(13), 2220-2226.

[186] Cheng, P. N. M., Lam, T. L., Lam, W. M., Tsui, S. M., Cheng, A. W. M., Lo, W. H., and Leung, Y. C. (2007). Pegylated recombinant human arginase (rhArg-peg5, 000mw) inhibits the in vitro and in vivo proliferation of human hepatocellular carcinoma through arginine depletion. *Cancer research*, 67(1), 309-317.

[187] Chen, S.H., Yang, W., Fan, Y., Stocco, G., Crews, K.R., Yang, J.J., Paugh, S.W., Pui, C.H., Evans, W.E. and Relling, M.V. (2011). A genome-wide approach identifies that the aspartate metabolism pathway contributes to asparaginase sensitivity. *Leukemia*, 25(1), 66-74.

[188] Kiriyama, Y., Kubota, M., Takimoto, T., Kitoh, T., Tanizawa, A., Akiyama, Y., and Mikawa, H. (1989). Biochemical characterization of U937 cells resistant to L-asparaginase: the role of asparagine synthetase. *Leukemia*, 3(4), 294-297.

[189] Aslanian, A. M., Fletcher, B. S., and Kilberg, M. S. (2001). Asparagine synthetase expression alone is sufficient to induce l-asparaginase resistance in MOLT-4 human leukaemia cells. *Biochemical Journal*, 357(1), 321-328.

[190] Zeidan, A., Wang, E. S., and Wetzler, M. (2009). Pegasparaginase: where do we stand?. *Expert opinion on biological therapy*, 9(1), 111-119.

[191] Kurtzberg, J., Asselin, B., Bernstein, M., Buchanan, G. R., Pollock, B. H., and Camitta, B. M. (2011). Polyethylene glycol-conjugated L-asparaginase versus native L-asparaginase in combination with standard agents for children with acute lymphoblastic leukemia in second bone marrow relapse: a Childrens Oncology Group Study (POG 8866). *Journal of pediatric hematology/oncology*, 33(8), 610.

[192] Stock, W., Douer, D., DeAngelo, D.J., Arellano, M., Advani, A., Damon, L., Kovacsovics, T., Litzow, M., Rytting, M., Borthakur, G. and Bleyer, A. (2011). Prevention and management of asparaginase/pegasparaginase-associated toxicities in adults and older adolescents: recommendations of an expert panel. *Leukemia & lymphoma*, 52(12), 2237-2253.

[193] Pieters, R., Hunger, S.P., Boos, J., Rizzari, C., Silverman, L., Baruchel, A., Goekbuget, N., Schrappe, M. and Pui, C.H. (2011). Lasparaginase treatment in acute lymphoblastic leukemia. *Cancer*, 117(2), 238-249.

[194] Patil, S., Coutsouvelis, J., and Spencer, A. (2011). Asparaginase in the management of adult acute lymphoblastic leukaemia: is it used appropriately?. *Cancer treatment reviews*, 37(3), 202-207.

[195] Hijiya, N., and van der Sluis, I. M. (2016). Asparaginase-associated toxicity in children with acute lymphoblastic leukemia. *Leukemia & lymphoma*, 57(4), 748-757.

[196] Pui, C. H., Robison, L. L., and Look, A. T. (2008). Acute lymphoblastic leukaemia. *The Lancet*, 371(9617), 1030-1043.

[197] Narta, U. K., Kanwar, S. S., and Azmi, W. (2007). Pharmacological and clinical evaluation of L-asparaginase in the treatment of leukemia. *Critical reviews in oncology/hematology*, 61(3), 208-221.

[198] Offman, M. N., Krol, M., Patel, N., Krishnan, S., Liu, J., Saha, V., and Bates, P. A. (2011). Rational engineering of L-asparaginase reveals importance of dual activity for cancer cell toxicity. *Blood*, 117(5), 1614-1621.

[199] Duval, M., Suciu, S., Ferster, A., Rialland, X., Nelken, B., Lutz, P., Benoit, Y., Robert, A., Manel, A.M., Vilmer, E. and Otten, J. (2002). Comparison of Escherichia coliasparaginase withErwinia-asparaginase in the treatment of childhood lymphoid malignancies: results of a randomized European Organisation for Research and Treatment of CancerChildren's Leukemia Group phase 3 trial. *Blood*, 99(8), 2734-2739.

[200] Xu, G., and McLeod, H. L. (2001). Strategies for enzyme/prodrug cancer therapy. *Clinical Cancer Research*, 7(11), 3314-3324.

[201] Cantor, J. R., Panayiotou, V., Agnello, G., Georgiou, G., and Stone, E. M. (2012). 12 Engineering Reduced-Immunogenicity Enzymes for Amino Acid Depletion Therapy in Cancer. *Methods in enzymology*, 502, 291.

[202] Pasut, G., and Veronese, F. M. (2009). PEG conjugates in clinical development or use as anticancer agents: an overview. *Advanced drug delivery reviews*, 61(13), 1177-1188.

[203] Moehlenbrock, M. J., and Minteer, S. D. (2011). Introduction to the field of enzyme immobilization and stabilization. *Enzyme Stabilization and Immobilization: Methods and Protocols*, 1-7.

[204] Marshall, S. A., Lazar, G. A., Chirino, A. J., and Desjarlais, J. R. (2003). Rational design and engineering of therapeutic proteins. *Drug discovery today*, 8(5), 212-221.

[205] Vertegel, A. A., Reukov, V., and Maximov, V. (2011). EnzymeNanoparticle Conjugates for Biomedical Applications. *Enzyme Stabilization and Immobilization: Methods and Protocols*, 165-182.

[206] Nakamura, T., Mizutani, M., Nozaki, H., Suzuki, N., and Yano, K. (2007). Formation mechanism for monodispersed mesoporous silica spheres and its application to the synthesis of core/shell particles. *The Journal of Physical Chemistry C*, 111(3), 1093-1100.

[207] Wu, S. H., Mou, C. Y., and Lin, H. P. (2013). Synthesis of mesoporous silica nanoparticles. *Chemical Society Reviews*, 42(9), 3862-3875.

[208] Fowler, C. E., Khushalani, D., Lebeau, B., and Mann, S. (2001). Nanoscale materials with mesostructured interiors. *Advanced Materials*, 13(9), 649-652.

[209] Tarn, D., Ashley, C. E., Xue, M., Carnes, E. C., Zink, J. I., and Brinker, C. J. (2013). Mesoporous silica nanoparticle nanocarriers: biofunctionality and biocompatibility. *Accounts of chemical research*, 46(3), 792-801.

[210] Ashley, C.E., Carnes, E.C., Epler, K.E., Padilla, D.P., Phillips, G.K., Castillo, R.E., Wilkinson, D.C., Wilkinson, B.S., Burgard, C.A., Kalinich, R.M. and Townson, J.L. (2012). Delivery of small interfering RNA by peptide-targeted mesoporous silica nanoparticle-supported lipid bilayers. *ACS nano*, 6(3), 2174-2188.

[211] Kim, T. W., Chung, P. W., and Lin, V. S. Y. (2010). Facile synthesis of monodisperse spherical MCM-48 mesoporous silica nanoparticles with controlled particle size. *Chemistry of Materials*, 22(17), 5093-5104.

[212] Kim, M.H., Na, H.K., Kim, Y.K., Ryoo, S.R., Cho, H.S., Lee, K.E., Jeon, H., Ryoo, R. and Min, D.H. (2011). Facile synthesis of monodispersed mesoporous silica nanoparticles with ultralarge pores and their application in gene delivery. *ACS nano*, 5(5), 3568-3576.

[213] Fan, J., Yu, C., Lei, J., Zhang, Q., Li, T., Tu, B., Zhou, W. and Zhao, D. (2005). Low-temperature strategy to synthesize highly ordered mesoporous silicas with very large pores. *Journal of the American Chemical Society*, 127(31), 10794-10795.

[214] He, Q., and Shi, J. (2011). Mesoporous silica nanoparticle based nano drug delivery systems: synthesis, controlled drug release and delivery, pharmacokinetics and biocompatibility. *Journal of Materials Chemistry*, 21(16), 5845-5855.

[215] Khanal, A., Inoue, Y., Yada, M., and Nakashima, K. (2007). Synthesis of silica hollow nanoparticles templated by polymeric micelle with core shell corona structure. *Journal of the American Chemical Society*, 129(6), 1534-1535.

[216] Li, J., Liu, J., Wang, D., Guo, R., Li, X., and Qi, W. (2010). Interfacially controlled synthesis of hollow mesoporous silica spheres with radially oriented pore structures. *Langmuir*, 26(14), 12267-12272.

[217] Lin, Y. S., Wu, S. H., Tseng, C. T., Hung, Y., Chang, C., and Mou, C. Y. (2009). Synthesis of hollow silica nanospheres with a microemulsion as the template. *Chemical Communications*, (24), 3542-3544.

[218] Fujiwara, M., Shiokawa, K., Sakakura, I., and Nakahara, Y. (2006). Silica hollow spheres with nano-macroholes like diatomaceous earth. *Nano letters*, 6(12), 2925-2928.

[219] Yeh, Y. Q., Chen, B. C., Lin, H. P., and Tang, C. Y. (2006). Synthesis of hollow silica spheres with mesostructured shell using cationic anionic-neutral block copolymer ternary surfactants. *Langmuir*, 22(1), 6-9.

[220] Stöber, W., Fink, A., and Bohn, E. (1968). Controlled growth of monodisperse silica spheres in the micron size range. *Journal of colloid and interface science*, 26(1), 62-69.

[221] Zhang, T., Ge, J., Hu, Y., Zhang, Q., Aloni, S., and Yin, Y. (2008). Formation of hollow silica colloids through a spontaneous dissolutionregrowth process. *Angewandte Chemie*, 120(31), 5890-5895.

[222] Liu, T., Li, L., Teng, X., Huang, X., Liu, H., Chen, D., Ren, J., He, J. and Tang, F. (2011). Single and repeated dose toxicity of mesoporous hollow silica nanoparticles in intravenously exposed mice. *Biomaterials*, 32(6), 1657-1668.

[223] Yu, T., Greish, K., McGill, L. D., Ray, A., and Ghandehari, H. (2012). Influence of geometry, porosity, and surface characteristics of silica nanoparticles on acute toxicity: their vasculature effect and tolerance threshold. *ACS nano*, 6(3), 2289-2301.

[224] Yu, Y., Li, Y., Wang, W., Jin, M., Du, Z., Li, Y., Duan, J., Yu, Y. and Sun, Z. (2013). Acute toxicity of amorphous silica nanoparticles in intravenously exposed ICR mice. *PloS one*, 8(4), e61346.

[225] Hudson, S. P., Padera, R. F., Langer, R., and Kohane, D. S. (2008). The biocompatibility of mesoporous silicates. *Biomaterials*, 29(30), 4045-4055.

[226] Mamaeva, V., Sahlgren, C., and Linden, M. (2013). Mesoporous silica nanoparticles in medicine recent advances. *Advanced drug delivery reviews*, 65(5), 689-702.

[227] Slowing, I. I., Wu, C. W., ViveroEscoto, J. L., and Lin, V. S. Y. (2009). Mesoporous silica nanoparticles for reducing hemolytic activity towards mammalian red blood cells. *Small*, 5(1), 57-62.

[228] Lin, Y. S., and Haynes, C. L. (2010). Impacts of mesoporous silica nanoparticle size, pore ordering, and pore integrity on hemolytic activity. *Journal of the American Chemical Society*, 132(13), 4834-4842.

[229] Yu, T., Malugin, A., and Ghandehari, H. (2011). Impact of silica nanoparticle design on cellular toxicity and hemolytic activity. *ACS nano*, 5(7), 5717-5728.

[230] Díaz, B., SánchezEspinel, C., Arruebo, M., Faro, J., de Miguel, E., Magadán, S., Yagüe, C., FernándezPacheco, R., Ibarra, M.R., Santamaría, J. and GonzálezFernández, Á. (2008). Assessing methods for blood cell cytotoxic responses to inorganic nanoparticles and nanoparticle aggregates. *Small*, 4(11), 2025-2034.

[231] He, Q., Zhang, Z., Gao, Y., Shi, J., and Li, Y. (2009). Intracellular Localization and Cytotoxicity of Spherical Mesoporous Silica Nanoand Microparticles. *Small*, 5(23), 2722-2729.

[232] Benezra, M., Penate-Medina, O., Zanzonico, P.B., Schaer, D., Ow, H., Burns, A., DeStanchina, E., Longo, V., Herz, E., Iyer, S. and Wolchok, J. (2011). Multimodal silica nanoparticles are effective cancer-targeted probes in a model of human melanoma. *The Journal of clinical investigation*, 121(7), 2768.

[233] Argyo, C., Weiss, V., Bräuchle, C., and Bein, T. (2013). Multifunctional mesoporous silica nanoparticles as a universal platform for drug delivery. *Chemistry of materials*, 26(1), 435-451.

[234] He, Q., Zhang, Z., Gao, F., Li, Y., and Shi, J. (2011). In vivo biodistribution and urinary excretion of mesoporous silica nanoparticles: effects of particle size and PEGylation. *small*, 7(2), 271-280.

[235] He, Q., Shi, J., Zhu, M., Chen, Y., and Chen, F. (2010). The three-stage in vitro degradation behavior of mesoporous silica in simulated body fluid. *Microporous and Mesoporous Materials*, 131(1), 314-320.

[236] Hermanson, GT. (2013). Chapter 13 Silane Coupling Agents. In: Hermanson, GT. eds. *Bioconjugate Techniques*, 3e Boston, MA: Academic Press.)

[237] Ho, C. C., Keller, A., Odell, J. A., and Ottewill, R. H. (1993). Preparation of monodisperse ellipsoidal polystyrene particles. *Colloid & Polymer Science*, 271(5), 469-479.

[238] Lu, Y., Yin, Y., and Xia, Y. (2001). Preparation and Characterization of MicrometerSized Egg Shells. *Advanced Materials*, 13(4), 271-274.

[239] Mohraz, A., and Solomon, M. J. (2005). Direct visualization of colloidal rod assembly by confocal microscopy. *Langmuir*, 21(12), 5298-5306.

[240] Shin, H., and Kim, C. (2012). Preparation of spheroidal and ellipsoidal particles from spherical polymer particles by extension of polymer film. *Colloid and Polymer Science*, 290(13), 1309-1315.

[241] Schneider, D., Beltramo, P.J., Mattarelli, M., Pfleiderer, P., Vermant, J., Crespy, D., Montagna, M., Furst, E.M. and Fytas, G. (2013). Elongated polystyrene spheres as resonant building blocks in anisotropic colloidal crystals. *Soft Matter*, 9(38), 9129-9136.

[242] Klein, M. K., Saenger, N. R., Schuetter, S., Pfleiderer, P., and Zumbusch, A. (2014). Shape-Tunable CoreShell Microparticles. *Langmuir*, 30(42), 12457-12464.

[243] NHS ester reaction chemistry. Retrieved from https://www.thermofisher.com/us/en/home/life-science/protein-biology/protein-biology-learning-center/protein-biology-resource-library/pierce-protein-methods/amine-reactive-crosslinker-chemistry.html

[244] van Meerloo, J., Kaspers, G. J., and Cloos, J. (2011). Cell sensitivity assays: the MTT assay. *Cancer cell culture: methods and protocols*, 237-245.

[245] Ortac, I. (2013). Synthetic Hollow Enzyme Loaded Nanospheres for Diagnostic and Therapeutic Applications. University of California, San Diego.

[246] Brady, M. and Mahoney, E. (2010). Peritoneal Cavity In Gerald M. Doherty (13th Ed.), *Current Diagnosis & Treatment: Surgery*. New York, NY: McGraw-Hill.)

[247] Morton D. A., Foreman K., and Albertine K. H. (2011) Chapter 8. Serous Membranes of the Abdominal Cavity. In: Morton D. A., Foreman K., Albertine K. H. eds. *The Big Picture: Gross Anatomy*, New York, NY: McGraw-Hill.

[248] Seymour N.E. and Bell R.L. (2015) Abdominal Wall, Omentum, Mesentery, and Retroperitoneum. In: Brunicardi F., Andersen D. K., Billiar T. R., Dunn D. L., Hunter J. G., Matthews J. B., Pollock R. E. eds. *Schwartz's Principles of Surgery*, 10e New York, NY: McGraw-Hill.

[249] Kurantowicz, N., Strojny, B., Sawosz, E., Jaworski, S., Kutwin, M., Grodzik, M., Wierzbicki, M., Lipiska, L., Mitura, K. and Chwalibog, A. (2015). Biodistribution of a high dose of diamond, graphite, and graphene oxide nanoparticles after multiple intraperitoneal injections in rats. *Nanoscale research letters*, 10(1), 398.